

Neuroscience Bulletin

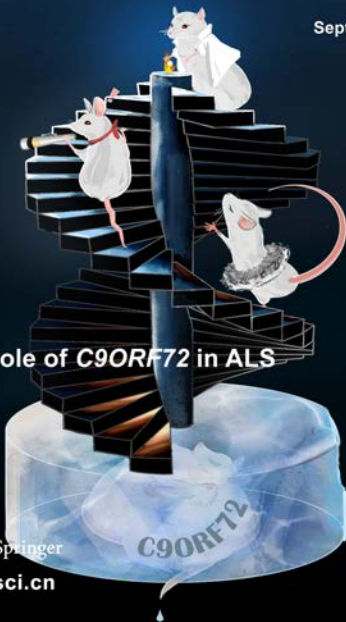
The Official Journal of The Chinese Neuroscience Society

神经科学通报

Volume 36

Number 9

September 2020



Essential Role of *C9ORF72* in ALS

STBS Springer

www.neurosci.cn

About the Cover

Amyotrophic lateral sclerosis (ALS) is clinically characterized by stiff muscles and progressive motor dysfunction. Hexanucleotide repeat expansion in the intron of the *C9ORF72* gene is the most common cause of ALS accounting for 37.6% of familial ALS and 21.1% of sporadic ALS. The cover illustrates that the hexanucleotide repeat expansion in *C9ORF72* results in a freezing phenotype in a rodent model of ALS. Recent advances uncover the role of *C9ORF72* in disease pathology and the attempts in therapeutics using animal models, which may “melt the ice” to free the frozen muscles and broaden the avenue to overcome ALS. See pages 1057–1070. (Cover image provided by Ms. Xiyang Wang)



Volume 36 Number 9
September 2020

Editorial

959 The First National Prevalence of Autism Spectrum Disorder in China

Zi Chao Zhang · Junhai Han

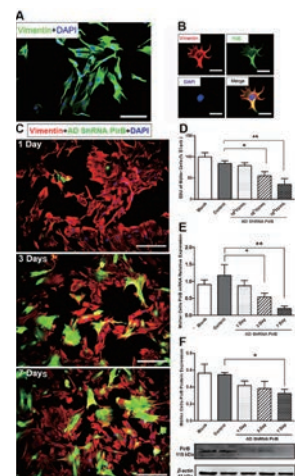
Original Articles

961 Prevalence of Autism Spectrum Disorder in China: A Nationwide Multi-center Population-based Study Among Children Aged 6 to 12 Years

Hao Zhou · Xiu Xu · Weili Yan · Xiaobing Zou · Lijie Wu · Xuerong Luo · Tingyu Li · Yi Huang · Hongyan Guan · Xiang Chen · Meng Mao · Kun Xia · Lan Zhang · Erzhen Li · Xiaoling Ge · Lili Zhang · Chunpei Li · Xudong Zhang · Yuanfeng Zhou · Ding Ding · Andy Shih · Eric Fombonne · Yi Zheng · Jisheng Han · Zhongsheng Sun · Yong-hui Jiang · Yi Wang · LATENT-NHC Study Team

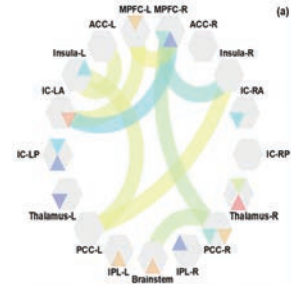
972 Paired Immunoglobulin-like Receptor B Inhibition in Müller Cells Promotes Neurite Regeneration After Retinal Ganglion Cell Injury *in vitro*

Rongdi Yuan · Mei Yang · Wei Fan · Jian Lan · Yuan-Guo Zhou



985 Neuroimage-Based Consciousness Evaluation of Patients with Secondary Doubtful Hydrocephalus before and After Lumbar Drainage

Jiayu Huo · Zengxin Qi · Sen Chen · Qian Wang · Xuehai Wu · Di Zang · Tanikawa Hiromi · Jiaying Tan · Lichi Zhang · Weijun Tang · Dinggang Shen



997 APPL2 Negatively Regulates Olfactory Functions by Switching Fate Commitments of Neural Stem Cells in Adult Olfactory Bulb via Interaction with Notch1 Signaling

Chong Gao · Tingting Yan · Xingmiao Chen · Kenneth K.Y. Cheng · Aimin Xu · Jiangang Shen

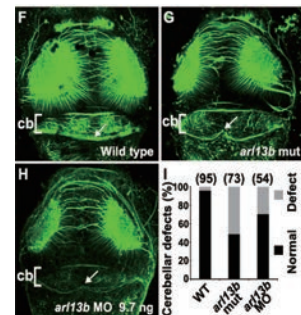
p 993

1009 Changes of Effective Connectivity in the Alpha Band Characterize Differential Processing of Audiovisual Information in Cross-modal Selective Attention

Weikun Niu · Yuying Jiang · Xin Zhang · Tianzi Jiang · Yujin Zhang · Shan Yu

1023 The Joubert Syndrome Gene *arll3b* is Critical for Early Cerebellar Development in Zebrafish

Jian Zhu · Han-Tsing Wang · Yu-Rong Chen · Ling-Ya Yan · Ying-Ying Han · Ling-Yan Liu · Ying Cao · Zhi-Zhi Liu · Hong A. Xu



1035 Macrophage–NLRP3 Inflammasome Activation Exacerbates Cardiac Dysfunction after Ischemic Stroke in a Mouse Model of Diabetes

Hong-Bin Lin · Guan-Shan Wei · Feng-Xian Li · Wen-Jing Guo · Pu Hong · Ya-Qian Weng · Qian-Qian Zhang · Shi-Yuan Xu · Wen-Bin Liang · Zhi-Jian You · Hong-Fei Zhang

p1026

Letters to the Editor

1046 Comparing GWAS and Brain Structure-Specific Gene Expression Profiles Identifies Psychiatric Disorder-Related Brain Structures at Different Developmental Stages

Xin Qi · Cuiyan Wu · Yanan Du · Shiqiang Cheng · Yan Wen · Mei Ma · Chujun Liang · Li Liu · Bolun Cheng · Lu Zhang · Ping Li · Feng Zhang

1051 Molecular Basis for Cephalic Mechanosensitivity of *Drosophila* Larvae

Zhenyu Zhang · Zhiyuan Li · Ting Liu · Wei Zhang

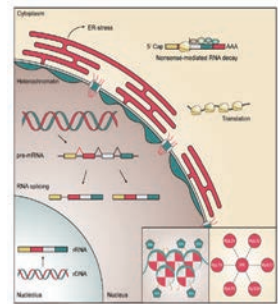
Reviews

1057 Role of the C9ORF72 Gene in the Pathogenesis of Amyotrophic Lateral Sclerosis and Frontotemporal Dementia

Zongbing Hao · Rui Wang · Haigang Ren · Guanghui Wang

1071 Inflammation in Mental Disorders: Is the Microbiota the Missing Link?

Sophie Ouabbou · Ying He · Keith Butler · Ming Tsuang



Research Highlights

p1064

1085 Microglia Interact with Neurons by Forming Somatic Junctions

Yongjie Wang · Zhihui Huang

1089 The Visual Pathway for Binocular Integration

Na Li · Yu Gu

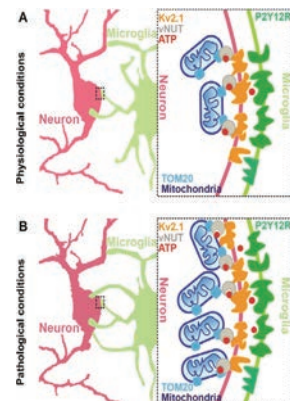
Corrections

1092 Correction to: Microglia Interact with Neurons by Forming Somatic Junctions

Yongjie Wang · Zhihui Huang

1093 Correction to: Projection from the Anterior Cingulate Cortex to the Lateral Part of Mediodorsal Thalamus Modulates Vicarious Freezing Behavior

Chaowen Zheng · Yanwang Huang · Binshi Bo · Lei Wei · Zhifeng Liang · Zuoren Wang



p1086



The First National Prevalence of Autism Spectrum Disorder in China

Zi Chao Zhang¹ · Junhai Han¹

Received: 12 June 2020 / Accepted: 28 June 2020 / Published online: 29 August 2020
© Shanghai Institutes for Biological Sciences, CAS 2020

Autism spectrum disorder (ASD) is a complex developmental disability characterized by impaired social interaction and communication, restricted interests, and stereotypical behaviors [1, 2]. In addition to these core diagnostic features, children with ASD frequently present with a host of associated behavioral issues, such as intellectual disability and epilepsy, as well as feeding and sleep problems. The prevalence of ASD in the United States is about 1/59, with a significantly higher proportion in males [3]. Therefore, ASD is no longer a rare disorder.

An estimate of national or local ASD prevalence rates is critical for governments to determine the financial and health services provided to support ASD patients and their families. Moreover, it also helps to identify geographical and environmental risk factors in ASD [4, 5]. The prevalence of ASD in different countries or areas varies from 0.019% to 1.16% [6–12]. These variations mostly come from methodological differences in the case definition and case-finding procedures [13, 14]. So far, the national prevalence of ASD in China is still not available. Several small-scale studies have estimated the prevalence of ASD in particular regions in China [15–18]. For example, an ASD assessment performed in 2014 in toddlers (3.8–4.8 years of age) who attended mainstream kindergarten in Shenzhen estimated the ASD prevalence at 2.62% [16]. In 2015, another evaluation in children aged 6 to 11 years from two mainstream schools in Beijing estimated the prevalence at 1.19% [15]. The sample size

and catchment area may also affect prevalence estimation [19]. In the current work by Zhou *et al.*, the first national prevalence of ASD in Chinese children was estimated at 0.70%, close to those in western countries.

The prevalence of ASD estimated by Zhou *et al.* is of considerable reliability for several reasons. First, they used a total of 125,806 samples, which is much larger than other ASD prevalence studies conducted in China. Second, they chose children aged 6–12 years from eight main cities in China. The multicenter epidemiological study largely reduced the effects of catchment areas, ensured a high participation rate, and enhanced maneuverability. Third, this study's sampling strategy was based on households and used the most comprehensive registration system. Compared with the sampling framework of a school population, the sampling scheme used in this study ensured the maximal coverage of the target population. Finally, this study used a combination of tools, including MC-ASRS (Modified Chinese Autism Spectrum Rating Scale) for screening, DSM-5 (Diagnostic and Statistical Manual of Mental Disorders, Fifth Edition) for diagnosis, and ADOS (Autism Diagnostic Observation Schedule) and ADI-R (Autism Diagnostic Interview-Revised) for in-depth diagnostic evaluation. Taken together, these significant strengths in design and execution enhanced the accuracy of ASD prevalence.

The study by Zhou *et al.* has estimated a true national-wide prevalence of ASD in China. The last decade has witnessed a substantial increase in ASD prevalence, which necessitates growth in the availability of relevant services. Continual monitoring of the national-wide prevalence of ASD will be essential for the proper adjustment of service inputs in the future.

✉ Junhai Han
junhaihan@seu.edu.cn

¹ School of Life Science and Technology, Key Laboratory of Developmental Genes and Human Disease, Southeast University, Nanjing 210096, China

References

- American Psychiatric Association. Diagnostic and statistical manual of mental disorders. 5th ed. Washington DC: American Psychiatric Association Publishing, 2013.
- Qiu Z, Yuan B. Towards the framework of understanding autism spectrum disorders. *Neurosci Bull* 2019, 35: 1110–1112.
- Baio J, Wiggins L, Christensen DL, Maenner MJ, Daniels J, Warren Z, *et al.* Prevalence of autism spectrum disorder among children aged 8 years—autism and developmental disabilities monitoring network, 11 sites, United States, 2014. *MMWR Surveill Summ* 2018, 67: 1–23.
- Rice CE, Rosanoff M, Dawson G, Durkin MS, Croen LA, Singer A, *et al.* Evaluating changes in the prevalence of the autism spectrum disorders (ASDs). *Public Health Rev* 2012, 34: 1–22.
- Imm P, White T, Durkin MS. Assessment of racial and ethnic bias in autism spectrum disorder prevalence estimates from a US surveillance system. *Autism* 2019, 23: 1927–1935.
- Bachmann CJ, Gerste B, Hoffmann F. Diagnoses of autism spectrum disorders in Germany: time trends in administrative prevalence and diagnostic stability. *Autism* 2018, 22: 283–290.
- Mohammadi MR, Ahmadi N, Khaleghi A, Zarafshan H, Mostafavi SA, Kamali K, *et al.* Prevalence of autism and its comorbidities and the relationship with maternal psychopathology: a national population-based study. *Arch Iran Med* 2019, 22: 546–553.
- Al-Mamri W, Idris AB, Dakak S, Al-Shekaili M, Al-Harathi Z, Alnaamani AM, *et al.* Revisiting the prevalence of autism spectrum disorder among Omani children: a multicentre study. *Sultan Qaboos Univ Med J* 2019, 19: e305–e309.
- Kita Y, Ashizawa F, Inagaki M. Prevalence estimates of neurodevelopmental disorders in Japan: a community sample questionnaire study. *Psychiatry Clin Neurosci* 2020, 74: 118–123.
- Randall M, Sciberras E, Brignell A, Ihsen E, Efron D, Dis-sanayake C, *et al.* Autism spectrum disorder: presentation and prevalence in a nationally representative Australian sample. *Aust N Z J Psychiatry* 2016, 50: 243–253.
- Diallo FB, Fombonne E, Kisely S, Rochette L, Vasiliadis HM, Vanasse A, *et al.* Prevalence and correlates of autism spectrum disorders in quebec: prevalence et correlats des troubles du spectre de l'autisme au Quebec. *Can J Psychiatry* 2018, 63: 231–239.
- Maenner MJ, Shaw KA, Baio J, EdS, Washington A, Patrick M, *et al.* Prevalence of autism spectrum disorder among children aged 8 years—autism and developmental disabilities monitoring network, 11 sites, United States, 2016. *MMWR Surveill Summ* 2020, 69: 1–12.
- Li C, Zhou H, Wang T, Long S, Du X, Xu X, *et al.* Performance of the autism spectrum rating scale and social responsiveness scale in identifying autism spectrum disorder among cases of intellectual disability. *Neurosci Bull* 2018, 34: 972–980.
- Meng FC, Xu XJ, Song TJ, Shou XJ, Wang XL, Han SP, *et al.* Development of an autism subtyping questionnaire based on social behaviors. *Neurosci Bull* 2018, 34: 789–800.
- Sun X, Allison C, Matthews FE, Zhang Z, Auyeung B, Baron-Cohen S, *et al.* Exploring the underdiagnosis and prevalence of autism spectrum conditions in Beijing. *Autism Res* 2015, 8: 250–260.
- Yang W, Xia H, Wen G, Liu L, Fu X, Lu J, *et al.* Epidemiological investigation of suspected autism in children and implications for healthcare system: a mainstream kindergarten-based population study in Longhua District, Shenzhen. *BMC Pediatr* 2015, 15: 207.
- Huang JP, Cui SS, Han Y, Irva HP, Qi LH, Zhang X. Prevalence and early signs of autism spectrum disorder (ASD) among 18–36 month-old children of Tianjin in China. *Biomed Environ Sci* 2014, 27: 453–461.
- Sun X, Allison C, Wei L, Matthews FE, Auyeung B, Wu YY, *et al.* Autism prevalence in China is comparable to Western prevalence. *Mol Autism* 2019, 10: 7.
- Elsabbagh M, Divan G, Koh YJ, Kim YS, Kauchali S, Marcin C, *et al.* Global prevalence of autism and other pervasive developmental disorders. *Autism Res* 2012, 5: 160–179.



Prevalence of Autism Spectrum Disorder in China: A Nationwide Multi-center Population-based Study Among Children Aged 6 to 12 Years

Hao Zhou¹ · Xiu Xu² · Weili Yan³ · Xiaobing Zou⁴ · Lijie Wu⁵ · Xuerong Luo⁶ · Tingyu Li⁷ · Yi Huang⁸ · Hongyan Guan⁹ · Xiang Chen¹⁰ · Meng Mao¹¹ · Kun Xia¹² · Lan Zhang¹¹ · Erzhen Li⁹ · Xiaoling Ge¹³ · Lili Zhang¹ · Chunpei Li¹ · Xudong Zhang¹³ · Yuanfeng Zhou¹ · Ding Ding¹⁴ · Andy Shih¹⁵ · Eric Fombonne¹⁶ · Yi Zheng¹⁷ · Jisheng Han¹⁸ · Zhongsheng Sun¹⁹ · Yong-hui Jiang²⁰ · Yi Wang¹ · LATENT-NHC Study Team

Received: 25 December 2019 / Accepted: 6 April 2020 / Published online: 30 June 2020
© Shanghai Institutes for Biological Sciences, CAS 2020

Abstract This study aimed to obtain the first national estimate of the prevalence of autism spectrum disorder (ASD) in Chinese children. We targeted the population of 6 to 12-year-old children for this prevalence study by multistage convenient cluster sampling. The Modified Chinese Autism Spectrum Rating Scale was used for the

screening process. Of the target population of 142,086 children, 88.5% ($n = 125,806$) participated in the study. A total of 363 children were confirmed as having ASD. The observed ASD prevalence rate was 0.29% (95% CI: 0.26%–0.32%) for the overall population. After adjustment for response rates, the estimated number of ASD cases was 867 in the target population sample, thereby achieving an estimated prevalence of 0.70% (95% CI: 0.64%–0.74%). The prevalence was significantly higher in boys than in girls (0.95%; 95% CI: 0.87%–1.02% versus 0.30%; 95% CI: 0.26%–0.34%; $P < 0.001$). Of the 363 confirmed ASD cases, 43.3% were newly diagnosed, and most of those (90.4%) were attending regular schools, and 68.8% of the

Hao Zhou, Xiu Xu, Weili Yan contributed equally.

Members of the LATENT-NHC Study Team are listed in the Supplementary Materials.

Electronic supplementary material The online version of this article (<https://doi.org/10.1007/s12264-020-00530-6>) contains supplementary material, which is available to authorized users.

✉ Yi Wang
yiwang@shmu.edu.cn

- ¹ Department of Neurology, Children's Hospital of Fudan University, Shanghai 201102, China
- ² Child Health Care, Children's Hospital of Fudan University, Shanghai 201102, China
- ³ Department of Clinical Epidemiology, Children's Hospital of Fudan University, Shanghai 201102, China
- ⁴ Child Development Behavior Center, The Third Affiliated Hospital, Sun Yat-Sen University, Guangzhou 510630, China
- ⁵ Department of Children and Adolescent Health, School of Public Health, Harbin Medical University, Harbin 150081, China
- ⁶ Department of Psychiatry, The Second Xiangya Hospital of Central South University, Changsha 410011, China
- ⁷ Child Health Care, Children's Hospital of Chongqing Medical University, Chongqing 400014, China

- ⁸ Department of Psychiatry, West China Hospital of Sichuan University, Chengdu 610041, China
- ⁹ Capital Institute of Pediatrics, Beijing 100020, China
- ¹⁰ The Second Affiliated Hospital and Yuying Children's Hospital of Wenzhou Medical University, Wenzhou 325027, China
- ¹¹ Child Health Care, Chengdu Women and Children's Hospital, Chengdu 610091, China
- ¹² Center for Medical Genetics, School of Life Sciences, Central South University, Changsha 410013, China
- ¹³ Children's Hospital of Fudan University, Shanghai 201102, China
- ¹⁴ Huashan Hospital of Fudan University, Shanghai 200040, China
- ¹⁵ Autism Speaks, 1 East 33rd Street, New York, NY 10016, USA

children with ASD had at least one neuropsychiatric comorbidity. Our findings provide reliable data on the estimated ASD prevalence and comorbidities in Chinese children.

Keywords Autism spectrum disorder · Prevalence · Comorbidity · Autism Spectrum Rating Scale · China

Introduction

Autism spectrum disorder (ASD) is a group of neurodevelopmental dysfunctions characterized by impaired social communication and interaction as well as repetitive and stereotypical behaviors [1]. The World Health Organization (WHO) estimated that 0.76% of the world's children have ASD, based on studies in countries accounting for < 16% of the population [2]. The alarming increase in the prevalence of ASD reported over the last two decades also poses an important public health concern [3–8].

Various methods of case ascertainment and determination have been employed in ASD prevalence studies in different countries. In the USA, the estimated prevalence among 8-year-old children was 0.66% in 2002, 1.46% in 2012, and 1.68% in 2014 based on active surveillance and expert record review by the Centers for Disease Control and Prevention (CDC) [3, 9, 10]. Most recently, a prevalence of 2.47% was estimated for children aged 3–17 years based on parental reports of physicians' diagnoses from a representative sample of households included in the National Health Interview Survey [4, 11]. The estimated prevalence and the trends in prevalence over time have been reported for Finland and Denmark, where national registries are available [12]. A prevalence of 1.57% was reported based on a school-based survey in the UK in 2009 [13]. A total population survey (55,266) was conducted in South Korea in 2011, and an estimated prevalence of 2.64% for children aged 7–12 years was reported [14, 15]. An epidemiological survey with a large sample size administered through questionnaires and home visits was conducted in India in 2016, and the estimated

prevalence of ASD was 0.23% among those aged 1–30 years [16]. The association between indicators of socioeconomic status, ethnic background, and the prevalence of ASD in the USA in 2002 has also been reported [17]. Studies of ASD prevalence in developing countries are rare or generally of low quality due to a small sample size or the use of non-standard methods for case determination [5, 18].

China has ~ 22% of the world's population. Over the last decade, the medical and educational communities have witnessed and experienced a demand for services and concerns for children with ASD across the country [19]. A few small-scale studies have reported the prevalence of ASD in mainland China since 2003 using various methods of case ascertainment [20, 21]. A recent meta-analysis of 25 studies of ASD in Chinese children, mostly in China, found an estimated prevalence of 0.12% (95% CI: 0.08%–0.15%) in mainland China and 0.27% (95% CI: 0.19%–0.35%) in mainland China, Hong Kong, and Taiwan region [22]. These prevalence estimates are much lower than those reported in most population-based studies in other countries and are believed to be underestimates because of the methodologies used. These epidemiological surveys were conducted using non-representative samples and regions with non-standard methods of case ascertainment and diagnostic confirmation. Thus, reliable data on the national prevalence of ASD in China is not yet available.

To assess the medical and educational service needs of the growing number of children with ASD in China, medical professionals and public policy-makers count on reliable prevalence data. Thus, with support from the National Health Commission of the central government in China, we conducted the first nationwide population-based study with a large representative sample to investigate the prevalence of ASD and describe its comorbidities among children in China.

Methods

Study Sites and Recruitment Procedures

A pilot study was conducted from January to July 2014 at four sites (Shanghai, Guangzhou, Changsha, and Harbin) to develop a modified Chinese version of the Autism Spectrum Rating Scale (MC-ASRS) [23–25] (Supplementary Method A1). The main study was conducted from July 2014 to December 2016. We used a multi-stage convenience cluster sampling strategy and selected eight cities (Shanghai, Guangzhou, Changsha, Chongqing, Chengdu, Wenzhou, Beijing, and Harbin) from five provinces (Zhejiang, Hunan, Sichuan, Guangdong, and Heilongjiang) and three municipalities (Shanghai, Beijing, and

¹⁶ Oregon Health and Science University, Portland, OR 97239, USA

¹⁷ Beijing Anding Hospital, Capital Medical University, Beijing 100088, China

¹⁸ Neuroscience Research Institute, Peking University, Beijing 100191, China

¹⁹ Beijing Institutes of Life Science, Chinese Academy of Sciences, Beijing 100021, China

²⁰ Department of Genetics and Pediatrics, Yale School of Medicine, New Haven, CT 06520, USA

Table 1 Geographic characteristics of the eight study sites.

Site	Location	Area (km ²)	Total Population (million)	2016 PCI (Yuan)	Site Ranking	National Ranking (100 cities)
Shanghai	East	6,340	24	52,962	Top 1	1
Guangzhou	South	7,434	13.5	52,829	Top 3	7
Changsha	Middle	11,819	7.4	46,735	Top 5	20
Chengdu	Southwest	14,312	15.7	27,239	Top 6	47
Chongqing	Southwest	82,400	33.7	33,476	Top 8	100
Wenzhou	Southeast	12,061	8.1	39,961	Top 4	13
Beijing	North	16,410	21.7	30,978	Top 2	2
Harbin	Northeast	53,100	9.6	44,026	Top 7	64
Total	/	203,876 (2.1)	133.7 (10)	/	/	/

PCI, average per capita income in yuan (1 US dollar equals ~ 6.4 yuan); data from the National Bureau of Statistics of China 2016 (<http://www.stats.gov.cn/tjsj/pcsj/rkpc/6rp/indexch.htm>).

Table 2 Sampling strategy for the study population.

Study site	Number of selected districts	Names of selected districts	Number of selected streets	Names of selected streets	Number of regular schools
Shanghai	3 out of 16	Xuhui	2 out of 12	Tianping, Fenglin	11
		Minhang	1 out of 13	Qibao	4
		Qingpu	2 out of 11	Yingpu, Xiayang	8
Guangzhou	1 out of 11	Huangpu	9 out of 9	Huangpu, Hongshan, Yuzhu, Taisha, Wenchong, Nilian, Nangang, Huidong, Changzhou	21
Changsha	1 out of 8	Liuyang	4 out of 4	Huachuan, Jili, Hehua, Guankou	16
Harbin	3 out of 9	Pingfang	6 out of 6	Xingjian, Baoguo, Lianmeng, Youxie, Xinjiang, Xinwei	20
		Nangang	2 out of 18	Xinchun, Baojilu	72
		Daowai	4 out of 4	Nongchun, Juyuan, Yongyuan, Mingzhu	52
Beijing	2 out of 16	Dongchen	5 out of 17	Hepingli, Andingmen, Jiaodaokou, Tiyuguanlu, Longtan	38
		Daxing	6 out of 22	Huangxing, Tuanhe, Huangchun, Sunchun, Tiangongyuan, Guanyingshi	32
Chongqing	3 out of 26	Jiulongpo	3 out of 8	Jiulongpo, Yangjiaping, Shiping	5
		Changshou	1 out of 7	Fengcheng	5
		Fengdu	1 out of 2	Sanhe	2
Chengdu	2 out of 20	Pixian	3 out of 3	Pitong, Hezuo, Xiyuan	16
		Tianfu	31 out of 31	Huayang, Wanan, Xingnong, Zhengxing, Baisha, and others	31
Wenzhou	2 out of 11	Pingyang	2 out of 16	Xiaojiang, Shuitou	31
Total	17		82		364

Chongqing) as the study sites (Table 1 and Supplementary Method A2). Multistage convenience cluster sampling was applied at each site (Table 2). We selected one to three urban districts based on the size of the population and the proportion of the migrant population, information that was obtained from the local Public Security Bureau Household Registration System (PSBHSS) (Supplementary Method A2).

We used the local PSBHSS as a sampling frame; this covered all children in the targeted districts because every child born in China must be registered in the PSBHSS by law. The information documented by the PSBHSS includes each child’s full name, identity number, nationality, date of birth, sex, home address, and home phone number. Thus, the use of this system as a sampling frame was considered the best approach; it is superior to the use of other

registration systems such as the school registration system, the Disabled Persons' Federation (DPF) registry system, and hospital information systems, which have frequently been used for other prevalence studies in China [22]. Studies using the other registration systems for sampling might have missed children with ASD who do not attend special or regular schools and instead stay at home.

The sample-size calculation suggested that 15,000 participants were required for each site, with the assumption of a prevalence of 1%, an alpha of 0.05, and a power of at least 0.8 and allowing for 5/1000 error (Supplementary Method A3). All children born between January 1, 2002 and December 31, 2008 (aged 6–12 years) with local residency registration in the PSBHSS were eligible for the study (Supplementary Method A2). These children attended regular schools, special education schools or rehabilitation centers, or remained at home. After comparing the list from the PSBHSS with the school registration system and DPF registry system for each study site, we assigned each eligible child to one of the following: Source 1 indicated children studying in regular schools located within the sampled districts; Source 2 indicated children studying in regular schools located outside the sampled districts; Source 3 indicated children registered at special education schools, rehabilitation centers, or a DPF anywhere in the local city or children staying at home; and Source 4 indicated children who could not be located or assigned to one of the above sources. Comparison of the sources allowed us to identify children who were born in the sampled districts but had never lived in the area or had moved; these children were subsequently removed from the sample used for prevalence calculations.

This study was approved by the Institutional Ethics Committee at the Children's Hospital of Fudan University. Written informed consent was given by the parents of the participants.

ASD Screening and Diagnosis

The protocols for screening and diagnosing ASD were different for children from each of the four sources. For children attending regular schools (sources 1 and 2), we used a two-step screening protocol (Supplementary Method A4) because of the large sample size and the expected large number of children screened as positive by the MC-ASRS. Children registered at special education schools, rehabilitation centers, or the DPF registry or children staying at home (Source 3) were relatively few in number and were expected to be at high risk for ASD (Supplementary Method A5). All children in this category underwent direct diagnostic testing.

The Diagnostic and Statistical Manual of Mental Disorders, Fifth Edition (DSM-5) was used by a trained

team of clinicians to diagnose ASD (Supplementary Method A6). Additional clinical assessment procedures, including the Autism Diagnostic Observation Schedule (ADOS) and the Autism Diagnostic Interview-Revised (ADI-R) [26, 27], a cognitive assessment using the Wechsler Intelligence Scale for Children in Chinese (WISC-C) [28], and neuropsychiatric comorbidity assessment using the Chinese Mini International Neuropsychiatric Interview for Children and Adolescents–Parent Version (MINI kid) [29] were administered in a subset of ASD cases. A caregiver interview, growth and development measurements, family history data, and comprehensive physical examination were also obtained. All members of the clinical assessment team were trained in using standard protocols to ensure high quality in the administration of diagnostic evaluations. They were blinded to the MC-ASRS scores during assessments.

The diagnosis of confirmed ASD cases fell into the following four categories: (1) the diagnosis based on the DSM-5 was also supported by the ADI-R, the ADOS, or both; (2) the diagnosis based on the DSM-5 was not supported by either the ADI-R or the ADOS; (3) the diagnosis of ASD was made based on the DSM-5, but neither the ADI-R nor the ADOS were administered; and (4) in a small number of cases from Source 3, participants were not clinically assessed by the research team, but the diagnosis or description of ASD was documented in their medical records or reported by others, such as the DPF and the special education database. In this situation, the available medical records were reviewed, and the ASD diagnosis was made by more than two experienced clinicians on the study team.

Statistical Analysis and the Methods Used to Estimate Prevalence

We used the following two prevalence calculations for ASD: (1) the observed prevalence, i.e., a proportion based on the observed number of ASD cases; and (2) an estimated prevalence that took into account non-responses in different phases of the investigation (Supplementary Method A7). The number of ASD cases among the non-responders was estimated based on the assumption of a rate equal to that observed in the responders from the same survey phase. For students in regular schools outside the sampled districts (Source 2), the response to our mailed invitations to participate in the screening was poor. Thus, we estimated the number of ASD cases based on Source 1 data with an assumption that there was no significant difference in prevalence between the two sources.

The denominator used for prevalence calculations (125,806) was determined by the total number of eligible participants. The observed prevalence was calculated based

on the exact number of confirmed ASD cases from all study sites divided by the denominator. For the estimation of overall and sex-specific prevalence, we applied weights to adjust for varying participation rates by site during different survey phases. In addition, the 95% CI for the overall prevalence and site prevalence were determined based on the Poisson distribution.

The prevalence across study sites was compared using Mantel–Haenszel tests. Prior to these comparisons, standardization was performed to adjust for differences in sex stratification and the contributions of sites to the overall sample size of the study by using the whole study sample as a reference. The overall sex and age stratification of the study population across sites or in the included *versus* excluded populations were compared using the χ^2 and Mantel–Haenszel tests to evaluate possible selection bias due to the exclusion of untraceable participants. The clinical assessment scores were compared between previously-diagnosed and newly-diagnosed cases and between the sexes using Student's *t* test. We used Cohen's *d* to measure between-group differences, using thresholds for small ($d = 0.20$), medium ($d = 0.50$), or large ($d = 0.80$) effect sizes as a guide to make inferences [30].

Results

The flow chart of the study population at different sampling and assessment stages is shown in Figure 1. After exclusion of the 16,280 non-participants, 125,806 participants (88.5%) were included in the final prevalence analysis. The age and sex distribution of the entire study population and for each study site are listed in Table 3. The study population included 66,687 (53.0%) males (Table S1). The age (from 6 to 12 years) was relatively evenly distributed throughout the entire study population from the 8 sites (Table S2). The sex distribution of the included sample did not differ from that of the excluded sample (53.0% *vs* 53.7% for males, respectively); however, the age distributions did differ (Sources 1–3 *vs* Source 4; $P = 0.097$ for sex; $P < 0.001$ for age) (Tables S1 and S3).

In the regular school investigation (Source 1), MC-ASRS questionnaires were collected from a total of 110,416 (96.8%) parents and 108,689 (95.3%) teachers. A total of 37,500 (32.9%) students tested positive through either the parent or teacher rating; the proportion was significantly higher among boys than among girls (37.9% *vs* 27.2%; $P < 0.001$). A total of 634 children were identified from Source 3. All of these children were asked to participate in the full ASD diagnostic assessment in the clinics of local hospitals. A total of 10,913 (8.7%) children were eligible for the study but attended schools outside the sampled districts (Source 2). The MC-ASRS screening

questionnaires were mailed to these students; 44.7% ($n = 4,874$) of parents and teachers completed the MC-ASRS. A total of 1,870 (38.4%) students were positive for ASD according to either parent or teacher rating, and 11.8% ($n = 220$) participated in group face-to-face interviews in schools. Due to the poor response rate, we excluded this group from further participation in the study. The sex ratio and age distributions of children who attended the schools within or outside the sampled districts were comparable ($P = 0.09$).

In total, 363 participants were diagnosed with ASD according to the DSM-5 criteria; 222 (61.2%) were from regular schools and 157 (43.3%) were newly-diagnosed. The observed ASD prevalence rate was 0.29% (95% CI: 0.26%–0.32%) for the overall population, 0.44% (95% CI: 0.38%–0.49%) for boys, and 0.12% (95% CI: 0.09%–0.15%) for girls. The 363 children with ASD were aged 9.0 ± 2.0 years and the male-to-female ratio was 4.3:1.

The denominators and estimated numbers of ASD cases used for the prevalence estimation are shown by site and investigation source in Supplementary Method A7 and Table S4. The overall estimated prevalence of ASD was 0.70% (95% CI: 0.64%–0.74%) and was significantly higher in boys than in girls (0.95%; 95% CI: 0.87%–1.02% *vs* 0.30%; 95% CI: 0.26%–0.34%; $P < 0.001$); however, it did not significantly differ among ages ($P = 0.19$) (Table 4). Among the 867 estimated ASD cases, the contributions of Sources 1, 2, and 3 were 38.5% (334), 3.4% (29), and 58.1% (504), respectively.

ADOS and ADI-R assessments were offered to all 363 children who were diagnosed with ASD based on the DSM-5 criteria. Among them, 318 (87.6%) were assessed with the ADOS (164 children, 45.2%) and the ADI-R (154 parents, 42.4%). The agreement between the DSM-5-based diagnosis and a positive score on the secondary assessment was 91.5% for the ADOS, 90.3% for the ADI-R, and 96.4% for both the ADOS and the ADI-R. Among the 363 confirmed ASD cases, 185 (51.0%) children also received the WISC-C to evaluate their cognitive function.

Among the 185 children who received the WISC-C test, 35.7% had a normal cognitive performance with an intelligence quotient (IQ) ≥ 85 , 18.9% had a borderline IQ (70–85), 11.4% had mild intellectual disability (ID) (IQ, 50–69), and 34.0% had moderate or severe ID (IQ < 50) (Table S5). However, according to the WISC-C, boys with ASD had significantly higher IQs than girls with ASD (73.9 ± 28.7 *vs* 55.7 ± 20.9 , $P < 0.001$) (Table S6).

Among the 157 children newly diagnosed with ASD, 90.4% were attending regular schools (Sources 1 and 2), which was markedly higher than the proportion from Source 3 (9.6%; $P < 0.001$). The children newly diagnosed with ASD had significantly higher IQs (~ 1 SD higher; 79.1 ± 25.2 *vs* 58.4 ± 27.9 , $P < 0.001$) than the

Table 3 Age, sex, and site distributions of the study population by sampling source.

	Participants			Non-participants	Total <i>n</i> (%)
	Source 1 <i>n</i> (%)	Source 2 <i>n</i> (%)	Source 3 <i>n</i> (%)	Source 4 <i>n</i> (%)	
Sex					
Male	60,499 (52.9)	5,768 (52.9)	420 (66.3)	8,742 (53.7)	75,429 (53.1)
Female	53,760 (47.1)	5,145 (47.1)	214 (33.7)	7,538 (46.3)	66,657 (46.9)
Age (years)					
6	13,223 (11.6)	1,750 (16.0)	97 (15.3)	2,736 (16.8)	17,806 (12.5)
7	20,370 (17.8)	1,105 (10.1)	99 (15.6)	2,680 (16.5)	24,254 (17.1)
8	16,669 (14.6)	1,044 (9.6)	83 (13.1)	2,139 (13.1)	19,935 (14.0)
9	16,527 (14.5)	1,139 (10.4)	93 (14.7)	1,952 (12.1)	19,711 (13.9)
10	18,155 (15.9)	1,218 (11.2)	102 (16.1)	2,138 (13.1)	21,613 (15.2)
11	14,402 (12.6)	2,410 (22.1)	79 (12.4)	1,650 (10.1)	18,541 (13.1)
12	14,913 (13.0)	2,247 (20.6)	81 (12.8)	2,985 (18.3)	20,226 (14.2)
Site					
Shanghai	14,490 (12.7)	2,731 (25.0)	200 (31.6)	2,744 (16.9)	20,165 (14.2)
Guangzhou	12,398 (10.9)	403 (3.7)	186 (29.3)	1,707 (10.5)	14,694 (10.3)
Changsha	9,744 (8.5)	1,425 (13.1)	15 (2.4)	298 (1.8)	11,482 (8.1)
Harbin	22,376 (19.6)	811 (7.4)	51 (8.0)	1,245 (7.6)	24,483 (17.2)
Beijing	7,112 (6.2)	783 (7.2)	25 (3.9)	3,355 (20.6)	11,275 (7.9)
Chongqing	20,010 (17.5)	2,167 (19.8)	98 (15.5)	3,012 (18.5)	25,287 (17.8)
Chengdu	15,021 (13.1)	1,035 (9.5)	35 (5.5)	628 (3.9)	16,719 (11.8)
Wenzhou	13,108 (11.5)	1,558 (14.3)	24 (3.8)	3,291 (20.2)	17,981 (12.7)
Total	114,259 (100.0)	10,913 (100.0)	634 (100.0)	16,280 (100.0)	142,086 (100.0)

Source 1, children studying in regular schools within the sampled districts; Source 2, children studying in regular schools outside the sampled districts; Source 3, children registered at special education schools, rehabilitation centers, or a DPF anywhere in the local city or children staying at home; Source 4, children who could not be located or ascribed to one of the above sources.

Table 4 Prevalence of ASD in Chinese children aged 6 to 12 years (per 100).

Category	Sample size	ASD cases	Observed prevalence (95% CI)	Estimated prevalence (95% CI)
Sex				
Male	66,687	292	0.44 (0.38, 0.49)	0.95 (0.87, 1.02)
Female	59,119	71	0.12 (0.09, 0.15)	0.30 (0.26, 0.34)
Age (years)				
6	15,070	43	0.29 (0.20, 0.37)	/
7	21,574	69	0.32 (0.24, 0.40)	/
8	17,796	61	0.34 (0.26, 0.43)	/
9	17,759	44	0.25 (0.17, 0.32)	/
10	19,475	65	0.33 (0.25, 0.41)	/
11	16,891	36	0.21 (0.14, 0.28)	/
12	17,241	45	0.26 (0.18, 0.34)	/
Total	125,806	363	0.29 (0.26, 0.32)	0.70 (0.64, 0.74)
ASD case status				
Newly diagnosed	/	157 (43.3)		/
Previously diagnosed	/	206 (56.7)		/

ASD, autism spectrum disorder; CI, confidence interval. The estimated prevalence of ASD was higher in boys than in girls ($P < 0.001$) and did not differ among ages ($\chi^2 = 8.76, df = 6, P = 0.19$).

Discussion

We conducted the first nationwide and the largest cross-sectional epidemiological study of ASD using the total population of children aged 6 to 12 years residing in eight representative cities in China from 2014 to 2016. This study provided a national estimated ASD prevalence of 0.70% (95% CI: 0.64%–0.74%), corresponding to ~ 1 in 143 children. For the first time, we present a reliable estimate of the disease burden of ASD in China. The prevalence was estimated as 0.95% (1 in 105; 95% CI: 0.87%–1.02%) in boys and 0.30% (1 in 333; 95% CI: 0.26%–0.34%) in girls. Importantly, 43.3% of the children with ASD were newly diagnosed, had a milder presentation, attended regular schools at the time of the study, and 2/3 (68.8%) of them had at least one neuropsychiatric comorbidity. Our findings provide valuable guidance to the medical community and policy-makers to develop a strategic plan for the care of children with ASD and to support future research on ASD in China.

Our study has several major strengths. First, this study provides a national estimate of ASD prevalence in a population-based, multi-center, epidemiological study. To the best of our knowledge, ours was the largest sample (125,806) ever surveyed in China or in any published ASD prevalence study using similar methodology [20, 31]. Second, instead of restricting the sampling framework to a school population, as in most previous studies [22], our strategy was based on households and used the most inclusive registration system. This sampling scheme ensured maximal coverage of the target population. Third, we achieved a high response rate for the screening step (~ 90%); this rate was higher than that of any other published population-based study in the literature [4, 14, 16]. Fourth, we used a modified Chinese version of the ASRS for screening, the DSM-5 as the diagnostic tool, and the ADOS and ADI-R for in-depth diagnostic evaluations. In fact, this was the first large ASD prevalence study to use the DSM-5 since it was released in 2013 [32]. In addition, this was the first study to use a combination of screening and diagnostic tools, the MC-ASRS and the ADOS/ADI-R, in Chinese children. The multi-informant approach that combined parent and teacher ratings for the initial ASRS screening followed by a professional group interview is a unique feature of our study design that improved the quality of the screening process. Altogether, we believe that these significant strengths in design and execution have ensured the best estimate of ASD prevalence in China to date.

Our estimated prevalence rate of 0.70% is consistent with the results of several meta-analyses and individual reviews but is lower than the prevalence reported in several recent epidemiological studies that had prevalence rates

ranging from 1% to 2% [33, 34]. For instance, the estimated prevalence rate of 1.46% for children aged 8 years was from the CDC's monitoring network in 2014 [10] and 1.68% in a more recent report [3], and the estimate of 2.47% among children in the USA aged 3 to 17 years from 2014 to 2016 was from the National Health Interview [4]. A prevalence of 1.57% was found in a school-based survey in the UK [13], the prevalence was 2.5% in an Australian birth cohort aged 6–7 years [35], and a prevalence of 2.64% was obtained for South Korean children aged 7–12 years in a population-based survey [14].

Several explanations may account for the lower estimated prevalence in our study. First, the level of cultural and public awareness of ASD should be considered. Although studies have generally found that the clinical phenotypes of ASD show little variation with country or culture [36], a lower ASD prevalence has been consistently reported in Hispanic and African American populations and in populations associated with low socioeconomic status in the USA in surveys by the CDC surveillance program [17, 37], presumably due to less access to specialized medical care and educational services. It is possible that the specific cultural heritage and the level of awareness of ASD in China may have influenced the prevalence estimation in the present study. The first autism case report in China was published in 1987 [38], 40 years after Kanner's seminal report [39]. However, public awareness in China did not truly emerge until 2010 [40]. Further research may be warranted to assess the impact of these cultural factors. Second, the use of the DSM-5 may have contributed to a lower estimate of ASD prevalence, as suggested in two other population-based studies [41, 42]. These studies have shown that, other things being equal, the prevalence estimate is reduced by 15%–20% when the DSM-5 criteria are used instead of the DMS-IV-TR criteria for case determination. Finally, while the response rate for screening was very high and satisfactory (~ 90%), the participation rate of ~ 80% among children who were screened as positive by the MS-ARS during the in-person diagnostic assessment was slightly lower. The exact reasons why individuals failed to attend in-person assessment need to be fully investigated as it is unclear whether non-participation was more or less common among families with children with ASD. From a cultural standpoint, it is possible that some parents might be afraid of their child being diagnosed with ASD due to social stigma and the fear of being ridiculed by others [40].

In contrast, the 0.70% prevalence reported in this study is significantly higher than the ~ 0.12% (95% CI: 0.08%–0.15%) arising from 25 pooled studies of various age groups from 1987 to 2011 in mainland China [22]. The much lower prevalence in previous studies is likely due to methodological issues, such as the sampling procedures,

sample size, and diagnostic criteria used. However, it remains conceptually possible that the higher prevalence in this study may actually reflect a true increase in the incidence of ASD, as suggested in other countries [4, 43].

Consistent with the results reported in the literature [14, 34], the male-to-female ratio of children with ASD in our study was 4.3:1. Similar to the findings of some studies [34], females with ASD had significantly lower cognitive function and more severe impairment in social interactions and other autistic behaviors than males with ASD. Interestingly, children newly diagnosed with ASD had higher IQs than previously-diagnosed children. This is consistent with the fact that most of these newly-diagnosed children were attending regular schools and that their behavioral problems had not drawn sufficient attention from parents or teachers to lead to testing for ASD [14].

We included assessments of neuropsychiatric and medical comorbidity in our study. This is a first among all prevalence studies conducted in Chinese children in China or other regions in Asia. Over two-thirds of the children with ASD had at least one comorbid psychiatric disorder, including ADHD and social phobia. The overall pattern of comorbidity is similar to that found in other reports that used the same assessment tool, with one exception: the rate of anxiety disorder was much lower in our study than in a previous study [44]. Over 40% of the children with ASD had co-occurring medical conditions, such as GI problems. The pattern of medical comorbidity is similar to previous reports, except that the frequency of seizures is lower than the 20%–25% reported in other studies [45].

Limitations

The study has three major limitations. First, we deliberately selected the eight participating sites using several predetermined criteria, including prior research experience with ASD, the quality of infrastructure and facilities, and the level of collaboration between the school and medical communities to implement the study. Consequently, the survey population was mainly composed of urban residents, although there was a fair representation of diverse social and economic strata. Given the rapid urbanization of China over the last two decades, 60% of the population lived in urban areas between 2014 and 2016. Nevertheless, the results may not be generalizable to rural population. The inclusion of children living in rural regions should be considered in future national epidemiological studies when it is technically feasible. Second, the assumption of an equal risk of ASD in participants *versus* non-participants, particularly the children who failed to present in person for diagnostic assessment, may lead to bias in both directions. For instance, this assumption may underestimate the prevalence if parents of children with ASD were more

likely to be non-participants. However, without further investigation, it remains uncertain what impact the 10% and 20% non-response rates in the screening and diagnostic phases, respectively, could have had on the final prevalence estimate in this study. Finally, the response rates differed among sources 1, 2, and 3, although we adjusted for unequal participation from each source in our prevalence calculations.

Based on these limitations, the rural population should be included in future national epidemiological studies, in order to truly represent the prevalence in China. The propagation, extension, and awareness campaigns and science popularization by the ASD network are expanding the public awareness of ASD, and may increase the response rate in the target population.

Conclusions

We report an estimated 0.70% prevalence of ASD among 6- to 12-year-old children in the largest population-based study to date, with > 120,000 children from eight representative cities in China. This estimate translates into a total of ~ 700,000 children aged 6–12 years with ASD in China, based on the national census data for 2016 (<http://www.stats.gov.cn/tjsj/pcsj/rkpc/6rp/indexch.htm>). The finding that almost half of the confirmed ASD cases were previously-undiagnosed children attending regular schools has important implications for the medical community, the educational system, and society in China. Our findings support the rising public concern about and awareness of ASD over the last decade in China and provide, for the first time, valid and reliable data to inform public health and government agencies in their efforts to design evidence-based policies regarding the care of children with ASD in China.

Acknowledgements This work was supported by the National Health Commission of the People's Republic of China (201302002, Clinical Trial NCT02200679). We thank all the parents who participated in this study. For data collection, we would like to acknowledge the members of the National Health Commission listed in the supplement in the LATENT-NHC Study Team member list.

Conflict of interest The authors declare that there are no conflicts of interest.

References

1. Harris J. Leo Kanner and autism: a 75-year perspective. *Int Rev Psychiatry* 2018, 30: 3–17.
2. Baxter AJ, Brugha TS, Erskine HE, Scheurer RW, Vos T, Scott JG. The epidemiology and global burden of autism spectrum disorders. *Psychol Med* 2015, 45: 601–613.

3. Baio J, Wiggins L, Christensen DL, Maenner MJ, Daniels J, Warren Z, *et al.* Prevalence of autism spectrum disorder among children aged 8 years - autism and developmental disabilities monitoring network, 11 sites, United States, 2014. *MMWR Surveill Summ* 2018, 67: 1–23.
4. Xu G, Strathearn L, Liu B, Bao W. Prevalence of autism spectrum disorder among US children and adolescents, 2014–2016. *JAMA* 2018, 319: 81–82.
5. Lyall K, Croen L, Daniels J, Fallin MD, Ladd-Acosta C, Lee BK, *et al.* The changing epidemiology of autism spectrum disorders. *Annu Rev Public Health* 2017, 38: 81–102.
6. Maenner MJ, Durkin MS. Trends in the prevalence of autism on the basis of special education data. *Pediatrics* 2010, 126: e1018–e1025.
7. Rubenstein E, Daniels J, Schieve LA, Christensen DL, Van Naarden BK, Rice CE, *et al.* Trends in special education eligibility among children with autism spectrum disorder, 2002–2010. *Public Health Rep* 2018, 133: 85–92.
8. Mandell DS, Barry CL, Marcus SC, Xie M, Shea K, Mullan K, *et al.* Effects of autism spectrum disorder insurance mandates on the treated prevalence of autism spectrum disorder. *JAMA Pediatr* 2016, 170: 887–893.
9. Prevalence of autism spectrum disorders—autism and developmental disabilities monitoring network, 14 sites, United States, 2002. *MMWR Surveill Summ* 2007, 56: 12–28.
10. Christensen DL, Baio J, Van Naarden BK, Bilder D, Charles J, Constantino JN, *et al.* Prevalence and characteristics of autism spectrum disorder among children aged 8 years—autism and developmental disabilities monitoring network, 11 sites, United States, 2012. *MMWR Surveill Summ* 2016, 65: 1–23.
11. Xu G, Strathearn L, Liu B, Bao W. Corrected prevalence of autism spectrum disorder among US children and adolescents. *JAMA* 2018, 319: 505.
12. Schendel DE, Bresnahan M, Carter KW, Francis RW, Gissler M, Gronborg TK, *et al.* The International Collaboration for Autism Registry Epidemiology (iCARE): multinational registry-based investigations of autism risk factors and trends. *J Autism Dev Disord* 2013, 43: 2650–2663.
13. Baron-Cohen S, Scott FJ, Allison C, Williams J, Bolton P, Matthews FE, *et al.* Prevalence of autism-spectrum conditions: UK school-based population study. *Br J Psychiatry* 2009, 194: 500–509.
14. Kim YS, Leventhal BL, Koh YJ, Fombonne E, Laska E, Lim EC, *et al.* Prevalence of autism spectrum disorders in a total population sample. *Am J Psychiatry* 2011, 168: 904–912.
15. Charman T. The highs and lows of counting autism. *Am J Psychiatry* 2011, 168: 873–875.
16. Poovathinal SA, Anitha A, Thomas R, Kaniamattam M, Melempatt N, Anilkumar A, *et al.* Prevalence of autism spectrum disorders in a semiurban community in south India. *Ann Epidemiol* 2016, 26: 663–665.
17. Durkin MS, Maenner MJ, Baio J, Christensen D, Daniels J, Fitzgerald R, *et al.* Autism spectrum disorder among US children (2002–2010): Socioeconomic, Racial, and ethnic disparities. *Am J Public Health* 2017, 107: 1818–1826.
18. Rice CE, Lee LC. Expanding the global reach of research in autism. *Autism* 2017, 21: 515–517.
19. Huang AX, Jia M, Wheeler JJ. Children with autism in the People’s Republic of China: diagnosis, legal issues, and educational services. *J Autism Dev Disord* 2013, 43: 1991–2001.
20. Feng L, Li C, Chiu H, Lee TS, Spencer MD, Wong JC. Autism spectrum disorder in Chinese populations: a brief review. *Asia Pac Psychiatry* 2013, 5: 54–60.
21. Sun X, Allison C, Wei L, Matthews FE, Auyeung B, Wu YY, *et al.* Autism prevalence in China is comparable to Western prevalence. *Mol Autism* 2019, 10: 7.
22. Sun X, Allison C, Matthews FE, Sharp SJ, Auyeung B, Baron-Cohen S, *et al.* Prevalence of autism in mainland China, Hong Kong and Taiwan: a systematic review and meta-analysis. *Mol Autism* 2013, 4: 7.
23. Zhou H, Zhang L, Wu L, Zou X, Luo X, Xia K, *et al.* Validity and reliability analysis of the Chinese parent version of the Autism Spectrum Rating Scale (6–18 years). *Psychiatry Res* 2015, 230: 255–261.
24. Zhou H, Zhang L, Zou X, Luo X, Xia K, Wu L, *et al.* Chinese Norms for the Autism Spectrum Rating Scale. *Neurosci Bull* 2017, 33: 161–167.
25. Zhou H, Zhang L, Luo X, Wu L, Zou X, Xia K, *et al.* Modifying the Autism Spectrum Rating Scale (6–18 years) to a Chinese Context: An exploratory factor analysis. *Neurosci Bull* 2017, 33: 175–182.
26. Lord C, Rutter M, Le Couteur A. Autism Diagnostic Interview-Revised: a revised version of a diagnostic interview for caregivers of individuals with possible pervasive developmental disorders. *J Autism Dev Disord* 1994, 24: 659–685.
27. Lord C, Rutter M, Goode S, Heemsbergen J, Jordan H, Mawhood L, *et al.* Autism diagnostic observation schedule: a standardized observation of communicative and social behavior. *J Autism Dev Disord* 1989, 19: 185–212.
28. Li D, Jin Y, Vandenberg SG, Zhu YM, Tang CH. Report on Shanghai norms for the Chinese translation of the Wechsler Intelligence Scale for Children-Revised. *Psychol Rep* 1990, 67: 531–541.
29. Shen YM, Chan B, Liu JB, Zhou YY, Cui XL, He YQ, *et al.* The prevalence of psychiatric disorders among students aged 6–16 years old in central Hunan, China. *BMC Psychiatry* 2018, 18: 243.
30. Furukawa TA, Leucht S. How to obtain NNT from Cohen’s d: comparison of two methods. *PLoS One* 2011, 6: e19070.
31. Wong VC, Hui SL. Epidemiological study of autism spectrum disorder in China. *J Child Neurol* 2008, 23: 67–72.
32. McGuinness TM, Johnson K. DSM-5 changes in the diagnosis of autism spectrum disorder. *J Psychosoc Nurs Ment Health Serv* 2013, 51: 17–19.
33. Elsabbagh M, Divan G, Koh YJ, Kim YS, Kauchali S, Marciniak C, *et al.* Global prevalence of autism and other pervasive developmental disorders. *Autism Res* 2012, 5: 160–179.
34. Fombonne E. Epidemiology of pervasive developmental disorders. *Pediatr Res* 2009, 65: 591–598.
35. Randall M, Sciberras E, Brignell A, Ihsen E, Efron D, Disanayake C, *et al.* Autism spectrum disorder: Presentation and prevalence in a nationally representative Australian sample. *Aust N Z J Psychiatry* 2016, 50: 243–253.
36. Charman T, Loth E, Tillmann J, Crawley D, Wooldridge C, Goyard D, *et al.* The EU-AIMS Longitudinal European Autism Project (LEAP): clinical characterisation. *Mol Autism* 2017, 8: 27.
37. Pedersen A, Pettygrove S, Meaney FJ, Mancilla K, Gotschall K, Kessler DB, *et al.* Prevalence of autism spectrum disorders in Hispanic and non-Hispanic white children. *Pediatrics* 2012, 129: e629–e635.
38. Tao KT. Infantile autism in China. *J Autism Dev Disord* 1987, 17: 289–296.
39. Kanner L. Irrelevant and metaphorical language in early infantile autism. *Am J Psychiatry* 1946, 103: 242–246.
40. Tang L, Bie B. The stigma of autism in China: an analysis of newspaper portrayals of autism between 2003 and 2012. *Health Commun* 2016, 31: 445–452.
41. Kim YS, Fombonne E, Koh YJ, Kim SJ, Cheon KA, Leventhal BL. A comparison of DSM-IV pervasive developmental disorder and DSM-5 autism spectrum disorder prevalence in an

- epidemiologic sample. *J Am Acad Child Adolesc Psychiatry* 2014, 53: 500–508.
42. Maenner MJ, Rice CE, Arneson CL, Cunniff C, Schieve LA, Carpenter LA, *et al.* Potential impact of DSM-5 criteria on autism spectrum disorder prevalence estimates. *JAMA Psychiatry* 2014, 71: 292–300.
 43. Fombonne E. Estimated prevalence of autism spectrum conditions in Cambridgeshire is over 1%. *Evid Based Ment Health* 2010, 13: 32.
 44. Verheij C, Louwse A, van der Ende J, Eussen ML, Van Gool AR, Verheij F, *et al.* The stability of comorbid psychiatric disorders: A 7 year follow up of children with pervasive developmental disorder-not otherwise specified. *J Autism Dev Disord* 2015, 45: 3939–3948.
 45. Thomas S, Hovinga ME, Rai D, Lee BK. Brief report: Prevalence of co-occurring epilepsy and autism spectrum disorder: The U.S. National Survey of Children’s Health 2011–2012. *J Autism Dev Disord* 2017, 47: 224–229.



Paired Immunoglobulin-like Receptor B Inhibition in Müller Cells Promotes Neurite Regeneration After Retinal Ganglion Cell Injury *in vitro*

Rongdi Yuan^{1,2} · Mei Yang¹ · Wei Fan¹ · Jian Lan¹ · Yuan-Guo Zhou²

Received: 22 October 2019 / Accepted: 31 January 2020 / Published online: 22 May 2020
© Shanghai Institutes for Biological Sciences, CAS 2020

Abstract In the central nervous system (CNS), three types of myelin-associated inhibitors (MAIs) have major inhibitory effects on nerve regeneration. They include Nogo-A, myelin-associated glycoprotein, and oligodendrocyte-myelin glycoprotein. MAIs possess two co-receptors, Nogo receptor (NgR) and paired immunoglobulin-like receptor B (PirB). Previous studies have confirmed that the inhibition of NgR only results in a modest increase in regeneration in the CNS; however, the inhibitory effects of PirB with regard to nerve regeneration after binding to MAIs remain controversial. In this study, we demonstrated that PirB is expressed in primary cultures of retinal ganglion cells (RGCs), and the inhibitory effects of the three MAIs on the growth of RGC neurites are not significantly decreased after direct PirB knockdown using adenovirus PirB shRNA. Interestingly, we found that retinal Müller cells expressed PirB and that its knockdown enhanced the regeneration of co-cultured RGC neurites. PirB knockdown also activated the JAK/Stat3 signaling pathway in Müller cells and upregulated ciliary neurotrophic factor levels. These findings indicate that PirB plays a novel role in retinal Müller cells and that its action in these cells may

indirectly affect the growth of RGC neurites. The results also reveal that PirB in Müller cells affects RGC neurite regeneration. Our findings provide a novel basis for the use of PirB as a target molecule to promote nerve regeneration.

Keywords Neurite regeneration · Müller cell · Retina ganglion cell injury · Ciliary neurotrophic factor

Introduction

Determining a means of promoting the repair and regeneration of the injured central nervous system (CNS) has long been a research hotspot and a medical challenge. The optic nerve is a unique CNS component that has difficulty regenerating after damage. Active treatment methods for diseases that affect the optic nerve remain scarce, and this lack of options frequently results in visual dysfunction or even blindness in affected individuals [1]. Myelin-associated inhibitors (MAIs), which are abundant in the microenvironment, are responsible for the regeneration difficulties following optic nerve damage. Myelin sheaths typically surround optic nerve axons and are exposed to a large number of MAIs after damage. These MAIs specifically bind to receptors on the axons, resulting in an unstable cytoskeleton for the growth of cone-plate pseudopods and filopodia, ultimately hindering regeneration [2].

Among these MAIs, Nogo-A, myelin-associated glycoprotein (MAG), and oligodendrocyte-myelin glycoprotein (OMgp) play major roles in the inhibition of axon regeneration [3]. In the CNS, they have two known co-receptors, Nogo receptor (NgR) and paired immunoglobulin-like receptor B (PirB) [4–8]. The MAIs facilitate the collapse of neuronal growth cones after they bind to NgRs, ultimately resulting in actin depolymerization in cells.

Electronic supplementary material The online version of this article (<https://doi.org/10.1007/s12264-020-00510-w>) contains supplementary material, which is available to authorized users.

✉ Yuan-Guo Zhou
yuanguo.zhou@gmail.com; ygzhou@tmmu.edu.cn

¹ Department of Ophthalmology, Xinqiao Hospital, Army Medical University, Chongqing 400037, China

² The Molecular Biology Centre, State Key Laboratory of Trauma, Burn and Combined Injury, Research Institute of Surgery and Daping Hospital, Army Medical University, Chongqing 400042, China

Interestingly, myelin-associated inhibition of NgRs in the context of CNS regeneration is very limited. Indeed, the knockdown of NgR alone does not significantly reduce the inhibitory effects of MAIs on axon growth [9, 10].

PirB is widely expressed in a number of immune cells such as macrophages, B cells, and dendritic cells, and this protein functions as a major histocompatibility complex class I (MHC I) molecule receptor. After binding to MHC I molecules, PirB negatively regulates cells by recruiting the tyrosine protein phosphatase of Src oncogene homologous domains 1 and 2 (SHP-1 and SHP-2) to the intracellular immunoreceptor tyrosine-based inhibition motif segment [11, 12]. In the CNS, PirB is mainly expressed in the axons and synapses of neurons in the cerebral cortex, hippocampus, cerebellum, retina, and optic nerve [13, 14]. After binding to PirB, MAIs in the CNS inhibit axon growth through the PirB-SHP1/SHP2 and PirB-POSH (plenty of SH3s)-myosin IIA pathways [15, 16]. A previous study has demonstrated that antagonizing PirB reduces the inhibitory effect of Nogo-A on axon growth [8]; however, whether PirB promotes axonal regeneration after MAI inhibition in the optic nerve remains unclear.

In the retina, Müller cells are closely associated with retinal ganglion cells (RGCs). Müller cells constitute a “bridge” that provides a link between neurons and the microenvironment [17]. This contact allows retinal neurons to exchange substances with extracellular blood vessels, the vitreous cavity, and the subretinal space [18]. Many nerve growth factors secreted by Müller cells affect RGC axon growth [19–21]. Our preliminary study demonstrated that PirB is also expressed in Müller cells; however, its specific role remains unclear. In addition, it is unknown if PirB affects RGC axon growth.

In this study, we used adenovirus (AD) PirB shRNA to knock down PirB expression in primary RGCs and in Müller cells. Subsequently, we examined the growth of neurites after direct PirB silencing in RGCs, and monitored the indirect effect of the PirB-silenced Müller cells on co-cultured RGC neurites. We further investigated if the indirect effect of PirB in Müller cells was related to the promotion of endogenous ciliary neurotrophic factor (CNTF) expression, and the associated signaling pathways were also explored. The results clarify the role of PirB in Müller cells and provide a basis for studying regeneration after optic nerve damage by targeting PirB in Müller cells.

Experimental Procedures

Experimental Animals

Sprague-Dawley rat pups 1–2 days old were used for primary cell culture. All experimental animal procedures

complied with the Association for Research in Vision and Ophthalmology statement and were approved by the Medical Ethics Committee of Daping Hospital, Army Medical University. The animals were purchased from the Animal Center of Daping Hospital, Army Medical University.

Experimental Reagents

The reagents used in this study included fetal bovine serum (Gibco, Newcastle, Australia, Lot No: 10100147), Neurobasal culture medium (Gibco, NY, USA, Lot No: 2085380), B27 (Gibco, NY, USA, Lot No: 2042265), Nogo-A, MAG, OMgp (R&D, MN, USA), Rotenone (Sigma, St. Louis, USA, Lot No: MKBZ2534V), and an Ultra-high-sensitivity ECL kit (Medchem Express, Monmouth Junction, NJ, USA, Cat No: HY-K1005). The antibodies used are listed in Table 1.

Viruses and Sequences

The target sequences for Si-r-CNTF and AD PirB shRNA (with GFP tag) were GGCTTACCGTACCTTCCAA (Ribobio Co., Ltd., Guangzhou, China) and GGAGCC-GAACTTTATTGTCTCTATA (Hanbio Co., Ltd., Shanghai, China).

RGC Culture

Sprague-Dawley rats aged 1–2 days were euthanized by intraperitoneal injection of 2% pentobarbital. The retinas were separated under a high-power microscope and centrifuged at 1100 $\times g$ for 5 min. Digestion medium (0.2% papain, 10% DNase, and 1% glutamine) was added for digestion in an incubator containing 5% CO₂ at 37°C for 20 min. An appropriate amount of Neurobasal complete medium (Neurobasal medium supplemented with 2% B27, 1% glutamine, and 0.5% penicillin–streptomycin) was added to prepare a cell suspension, which was filtered using a 70- μm cell strainer. The cells were inoculated on plates coated with polylysine (PDL) at a density of 3×10^5 /mL and cultured in an incubator under 5% CO₂ at 37°C. Cell adherence was observed the next day, and the medium was replaced once for an additional 6–8 days of culture [22, 23].

Müller Cell Culture

Müller cells were extracted according to the previously reported methods [24, 25]. Briefly, retinas were digested in 0.25% trypsin for 15 min, and complete Dulbecco's modified Eagle's medium [DMEM; containing 1% penicillin–streptomycin and 10% fetal bovine serum (FBS)]

Table 1 List of primary and secondary antibodies used for western blot (WB), immunohistochemistry (IHC), and immunocytochemistry (ICC).

Antibody	Source	Lot/Cat No.	Dilution	
<i>Primary antibodies</i>			WB	IHC/ICC
Goat anti-PirB	R&D, MN, USA	AF2754	1:1000	1:100
Rabbit anti-phospho Stat3 Y705	Abcam, Cambridge, UK	ab76315	1:5000	
Mouse anti-GAPDH	Abcam	ab8245	1:5000	
Rabbit anti-SHP2	Abcam	ab187040	1:5000	
Rabbit anti-phospho SHP2 Y542	Abcam	ab17939	1:1000	
Rabbit anti-phospho SHP1 Tyr536	ThermoFisher, MA, USA	PA5-36682	1:750	
Rabbit anti-SHP1	Abcam	ab32559	1:1000	
Rabbit anti-CNTF	Abcam	ab175387	1:1000	
Rabbit anti-beta III tubulin	Abcam	ab18207		1:500
Mouse anti-beta III tubulin	Abcam	ab78078		1:500
Rabbit anti-vimentin	Abcam	ab92547		1:500
Mouse anti-glutamine synthetase	Abcam	ab64613		1:200
Mouse anti-CD90/Thy1	Abcam	Ab225		1:500
Mouse anti-Brn-3a	Merck Millipore, Watford, UK	MAB1585		1:50
<i>Secondary antibodies</i>				
HRP-labelled anti-mouse IgG	Invitrogen, Poole, UK	G-21040	1:10000	
HRP-labelled anti-rabbit IgG	Invitrogen	31460	1:10000	
HRP-labelled anti-donkey IgG	R&D	HAF109	1:1000	
Alexa488 anti-goat IgG	Invitrogen	A32814		1:300
Alexa488 anti-mouse IgG	Invitrogen	A32723		1:300
Alexa594 anti-rabbit IgG	Invitrogen	A32740		1:300

was added. The resulting cell suspension was filtered using a 70- μ m cell strainer. Cells at a density of 3×10^5 cells/mL were grown in medium under 5% CO₂ at 37°C. The next day, the medium was replaced prior to 6–8 days of continuous culture. Passaging was performed when the cell density reached 80%. Subsequent experiments were performed after cells were passaged 3–4 times.

Cellular Immunofluorescence

Cells were fixed in 4% paraformaldehyde for 15 min and then washed three times for 5 min with phosphate-buffered saline (PBS). The cells were permeabilized using 0.1% Triton for 15 min, and then blocked with 10% goat serum for 30 min. Primary antibodies (mouse anti- β -III tubulin, rabbit anti-vimentin, and mouse anti-Brn 3a) were added prior to incubation at 4°C overnight. After three PBS washes, fluorescent secondary antibodies were added and left at room temperature (20–22°C) for 1 h in the dark; this was followed by counterstaining with 4', 6-diamidino-2-phenylindole (DAPI) for 15 min. Five regions in each well were randomly selected and imaged under a fluorescence microscope (Leica, Wetzlar, Germany). The lengths of 20 neurites with adjacent RGCs were measured using Image-Pro plus 6.0 (Media Cybernetics, Maryland, USA) to assess their growth [26, 27]. Cells exhibiting positive vimentin or Brn3a expression were counted to determine the purity of

the primary cells. Müller/RGC purity = number of cells positive for vimentin or Brn3a expression / total number of cells positive for DAPI nuclear staining \times 100% [28, 29].

Transfection of Primary Cells with AD PirB shRNA

Müller cells and RGCs were seeded into 6- or 24-well plates at 3×10^5 cells/mL and cultured under 5% CO₂ at 37°C for 24 h. The medium was refreshed and AD PirB shRNA (with GFP tag) was added gradually according to the manufacturer's instructions to achieve final titers of 10^8 , 10^7 , and 10^6 plaque-forming units (PFU)/mL. The medium was not replaced during transfection. In addition, AD shRNA was added to the control group, and the blank group was left untreated. Three duplicate wells were used for each group. Cell growth and GFP expression were observed under a microscope at 1, 3, and 7 days after transfection. Müller cells and RGCs were transfected at 10^6 PFU/mL in all subsequent experiments.

Transfection of Müller Cells Using Si-r-CNTF

Müller cells were passaged 3–4 times and then seeded on a 24-well plate at a density of 3×10^5 cells/mL. These cells were then transfected with AD PirB shRNA. The next day, empty vector Si-r (control) and Si-r-CNTF were added at final concentrations of 10, 20, 30, 50, and 100 nmol/L. The

interference efficiency was assessed, and Si-r-CNTF was used at 50 nmol/L in all subsequent experiments. After 48 h–72 h of transfection, cells were repeatedly transfected with Si-r-CNTF to consolidate the interference effect.

EdU (5-ethynyl-2'-deoxyuridine) Assay of Müller Cells

Müller cells were passaged 3–4 times and then seeded into a 24-well plate at 3×10^5 cells/mL. These cells were divided into the following groups: blank (without treatment), control (with empty virus), and PirB shRNA (at 10^8 , 10^7 , and 10^6 PFU/mL). Three duplicate wells were used for each group, and cells were cultured in an incubator under 5% CO₂ at 37°C for 72 h. Based on the kit instructions, 300 µL medium containing EdU A solution was added to each well and left for 2 h. Then, the cells were fixed in 4% paraformaldehyde for 30 min, followed by neutralization with 2 mg/mL glycine for 15 min. The cells were permeabilized using 0.5% Triton at room temperature for 30 min, and this was followed by nuclear staining with F solution for 15 min, three PBS washes for 5 min each, and then imaging.

Inhibition of Primary RGCs by Nogo, MAG, and OMgp

RGCs were divided into the following groups: blank (culture plates coated with 0.1 mg/mL PDL), PBS (plates coated with 0.1 mg/mL PDL + PBS at an amount equal to that of the MAI group), and MAI (plates coated with 0.1 mg/mL PDL + Nogo, MAG, or OMgp in PBS). The concentrations of MAIs were 0.25, 0.5, 1.0, and 2.0 µg/mL. Three duplicate wells were prepared for 7 days of culture. Then, the culture medium was removed, and β-III tubulin was stained by immunofluorescence to assess the lengths of RGC neurites. In the MAI group, the coating concentrations of Nogo, OMgp, and MAG were 0.5, 0.5, and 1 µg/mL, respectively, in subsequent experiments.

Establishment of the RGC Injury Model

Rotenone is a mitochondrial complex 1 inhibitor that induces neuronal cytotoxicity and is commonly used to prepare injury models for *in vitro* assays [30]. Primary RGCs were cultured in 24-well plates for 3 days, the medium was then replaced and rotenone (100 nmol/L) was added as previously described [31]. After rotenone injury, the surviving RGCs were detected using an MTT assay (Solarbio, Beijing, China, Lot No:M1020) as directed by the manufacturer. Briefly, blank wells without cells were used for zero-adjustment, and the control and rotenone groups (injuring RGCs for 6 h, 12 h, 24 h, 48 h, and 72 h)

were prepared. Three duplicate wells were used for each group, and the culture supernatant was replaced with 360 µL fresh medium. Then, 40 µL MTT solution was added and left for 4 h. After careful removal of the supernatant, 490 µL dimethyl sulfoxide was added to each well to dissolve the formazan crystals. The cells were incubated on a shaker at low speed for 10 min, and the absorbance was measured at 490 nm. RGCs injured for 24 h were selected for subsequent experiments.

Co-culture of Müller Cells and RGCs

Müller cells were passaged, inoculated into transwell chambers, then transfected with AD PirB ShRNA or CNTF siRNA. After 3 days, the transwell chambers were extracted, the medium was removed, and the cells were washed three times with PBS. After adding fresh medium, the cells were transferred into RGC culture plates in the presence of renewed solution for co-culture [27]. Two duplicate wells were used for each group, and the experiment was repeated three times. Isolated Müller cells and RGCs were cultured separately. There was no contact between Müller cells and RGCs except *via* the culture medium. Using the 24-well plate as an example, Müller cells were cultured in the transwell, and 0.5 mL DMEM containing 10% FBS and 1% penicillin–streptomycin was added. Primary RGCs were cultured outside the transwell in 0.6 mL Neurobasal medium containing 2% B27, 1% glutamine, and 0.5% penicillin–streptomycin. The cells were co-cultured in an incubator under 5% CO₂ at 37°C.

Real-Time PCR

RNA was extracted as previously described [32] and reverse-transcribed into cDNA according to the kit instructions (TAKARA BIO. INC, Beijing, China, Lot No: RR047A). A total of 2 µL of nuclease-free and high-purity water, 5 µL of Mix and oligo (dT) 18 primers, 0.5 µL each of forward and reverse primers, and 2 µL of cDNA were used for the reaction. β-actin was used as an internal reference. The primers were designed based on GenBank and included: PirB, forward AGGATGGAGTGGAGCTGAAC and reverse TGATTGTTTGCTCCTTGCC; CNTF, forward CTTTCGCAGAGCAAACACCTC and reverse ACTGTGAGAGCTCTTGAAGGAC; and GAPDH, forward GACATCAAGAAGGTGGTGAAGC and reverse TGTCATTGAGAGGACCTGCCAGC. The qPCR conditions were pre-denaturation at 95°C for 10 min, denaturation at 95°C for 15 s (cycled 39 times), annealing at 57°C for 1 min, and extension at 65°C for 5 min. Relative quantification was performed to obtain real-time PCR results.

Western Blot

Immunoblotting was performed as previously described [33]. Briefly, equal amounts of protein (40 µg) were separated by 10% SDS-PAGE and transferred onto polyvinylidene fluoride membranes. After blocking with 5% skimmed milk for 2 h, primary antibodies were added prior to incubation on a shaker at 4°C overnight. Then, secondary antibodies were added and left at room temperature for 1 h. Enhanced chemiluminescence was used for development prior to detection on an Omega Lum G gel imager (Aplegen, Pleasanton, USA). Gray values were analyzed using ImageJ software (National Institutes of Health, Bethesda, Germany), and β-actin or GAPDH was used as an internal reference. The ratio of the gray value of the target strip to that of the internal reference was calculated.

Statistical Analysis

Data were analyzed using SPSS 19.0 (IBM, Armonk, USA). Cell counts are expressed as percentages. Continuous data are expressed as the mean ± SD. Student's *t* test or one-way ANOVA was used in cases with homogeneity of variance and normal distribution, and for all other cases, a nonparametric test was used. $P < 0.05$ was considered statistically significant.

Results

PirB Knockdown in RGCs does not Promote the Growth of Neurites

After primary culture of RGCs for 24 h, the cells were observed by microscopy to be adherent. Some cells aggregated, and a few single cells were scattered. After 7–8 days in culture, RGCs had large numbers of neurites. The RGCs were specifically labelled with Brn-3a, and they accounted for > 85% of all cells (RGC purity = Brn-3a / DAPI × 100%) (Fig. 1A). They also expressed PirB, and this expression occurred primarily in the cell bodies and neurites (Fig. 1B).

After transfection with AD, >55% of RGCs were GFP-positive. MTT assays showed no significant difference in cell number from that of the blank (negative control, 100% ± 20%, $P = 0.23$) and control (empty virus, 90% ± 13.45%, $P = 0.62$) groups when AD PirB shRNA was transfected at 10⁶ PFU/mL (83.33% ± 12.22%; Fig. 1C). Cytotoxicity against RGCs was enhanced, and the cell number was decreased at the final transfection concentrations of 10⁷ (67.33% ± 7.63%, $P = 0.048$) and 10⁸ PFU/mL (42% ± 21.66%, $P = 0.004$) compared to controls

(Fig. 1C). Subsequent experiments were performed using a transfection concentration of 10⁶ PFU/mL. As assessed by qPCR (Fig. 1D), the *PirB* mRNA levels in cells transfected with AD PirB shRNA at 10⁶ PFU/mL (59 ± 18.68) were significantly lower than those of the control groups (108 ± 13.11, $P = 0.014$).

The inhibitory effects of Nogo, MAG, and OMgp on RGC axonal growth were concentration-dependent. The growth of RGC neurites was significantly inhibited by Nogo and OMgp at 0.5 µg/mL and by MAG at 1 µg/mL (94.33 ± 13.65 µm, $P = 0.017$; 90.67 ± 21 µm, $P = 0.012$; 77.33 ± 10.26 µm, $P = 0.013$) compared to that of the PBS group (138.33 ± 23.63 µm, Fig. 1E). AD PirB shRNA reduced the PirB expression in RGCs but did not significantly promote the regeneration of neurites in RGCs treated with Nogo, MAG, or OMgp compared to the control group transfected with empty virus. In addition, the lengths of the neurites were not significantly different ($P > 0.05$, Fig. 1F, G).

PirB Knockdown in Müller Cells Increases CNTF Expression and Activates the Janus Kinase/Signal Transducer and Activator Of Transcription (JAK/Stat3) Signaling Pathway

After primary Müller cells were passaged three times, >95% of the cells expressed the Müller cell-specific protein vimentin and glutamine synthetase (Müller cell purity = vimentin / DAPI × 100%) (Fig. 2A and Fig. S1). We found for the first time that Müller cells expressed PirB, and this expression occurred primarily in the cell membrane and cytoplasm (Fig. 2B). EdU assays revealed that cell proliferation decreased with increasing transfected virus concentration. There was no significant effect on the proliferation of Müller cells at a viral PirB shRNA titer of 10⁶ PFU/mL (relative to blank at 100%; 79.33% ± 7.02%, $P = 0.516$). At transfection titers of 10⁷ PFU/mL (53.33% ± 10.02%, $P = 0.006$) and 10⁸ PFU/mL (35.34% ± 13.5%, $P = 0.001$), cell proliferation in the AD PirB shRNA groups decreased significantly compared to that of the control (empty virus, 84.67% ± 6.11%, Fig. 2D and Fig. S2).

After the cells were transfected with AD at a final titer of 10⁶ PFU/mL for 1 day, scattered green fluorescence (GFP) was observed, and this increased significantly at 3 days (30%–40%), and 7 days (50%–60%) (Fig. 2C). After Müller cells were transfected with viruses for 1 day (0.87 ± 0.16), the *PirB* mRNA levels were lower than those of the control group (1.18 ± 0.32). The decrease at 3 days was statistically significant (0.54 ± 0.11, $P < 0.028$), and the lowest level was reached at 7 days (0.20 ± 0.07, $P = 0.007$) (Fig. 2E). Compared to the level in the control group (0.55 ± 0.02), PirB protein expression significantly decreased to

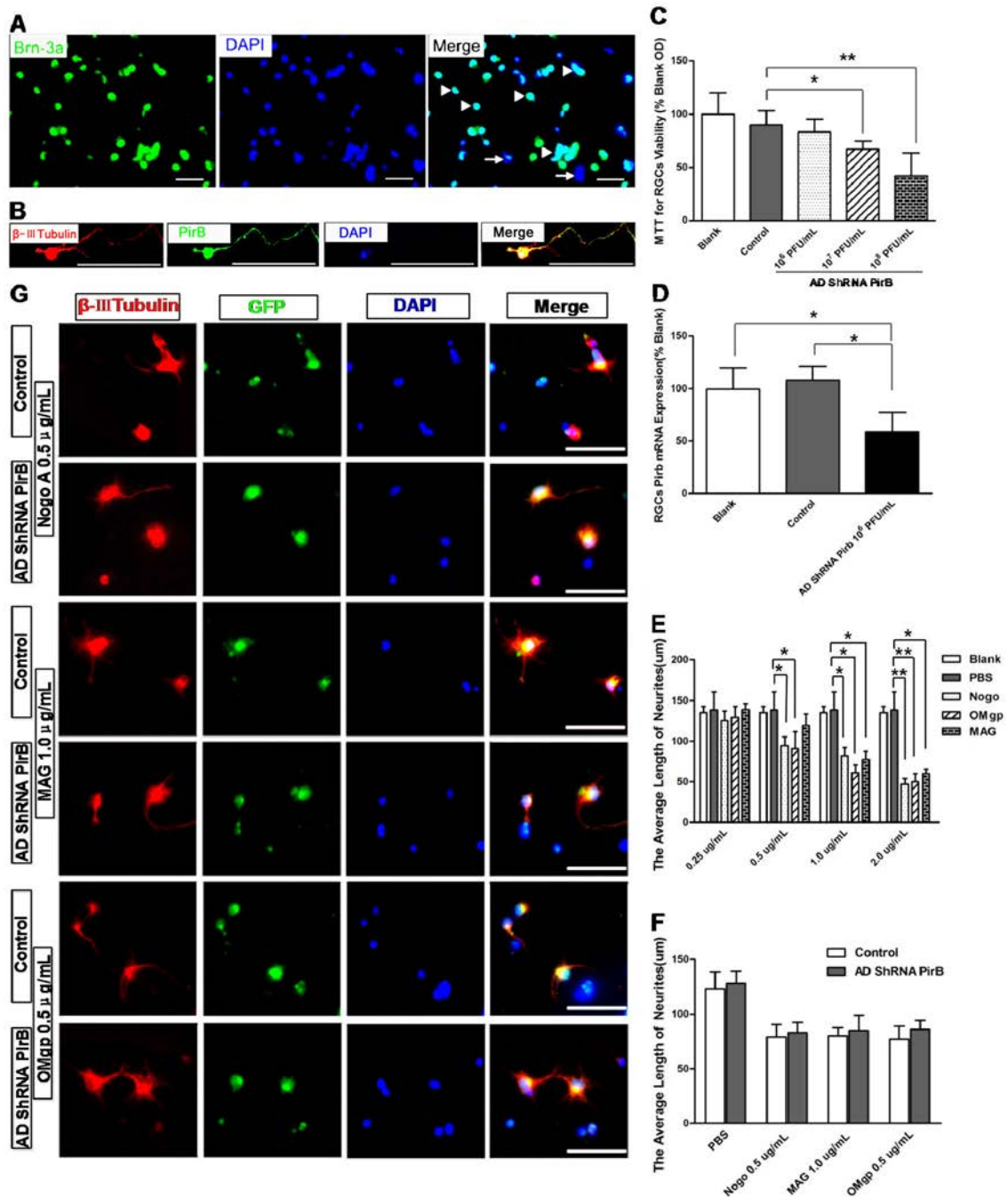


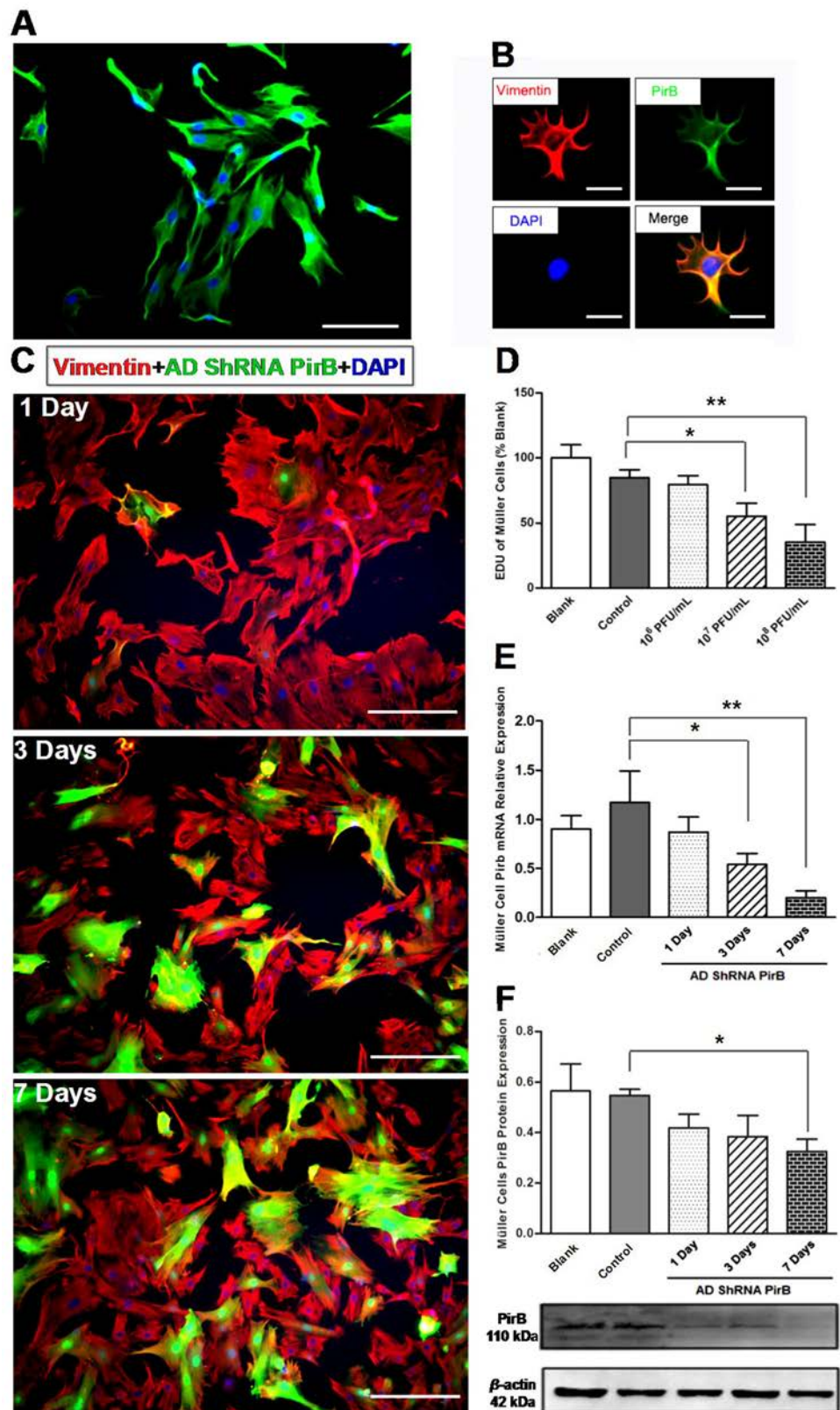
Fig. 1 Effects of RGC PirB knockdown on neurite growth. **A** Representative images of a primary culture of RGCs, where Brn-3a (green, 488 nm) is primarily localized within the nucleus (blue, DAPI nuclear staining; arrows, non-RGC nuclear staining; arrowheads, RGC-positive cells; scale bars, 100 µm). **B** Image of co-localization of RGC PirB (green at 488 nm) with β-III tubulin (red at 594 nm) (blue DAPI nuclear staining; scale bars, 250 µm). **C** MTT assay results showing cytotoxicity of AD PirB shRNA in RGCs. **D** PirB mRNA levels after RGC transfection with AD PirB shRNA as evaluated by real-time PCR. **E** Inhibitory effects of Nogo, MAG, and

OMgp on RGC neurite growth. **F** Effects of AD PirB shRNA on RGC neurite growth after pretreatment with PBS, Nogo (0.5 µg/mL), MAG (1.0 µg/mL), and OMgp (0.5 µg/mL). **G** Representative images of fluorescent staining specific for RGC neurite growth [red (594 nm), β-III tubulin-labeled RGC neurites; green (488 nm), GFP indicating autofluorescence of AD PirB shRNA or empty virus in RGCs; blue, DAPI-labeled nuclei; scale bars, 250 µm]. All data are the mean ± SD. The experiment was repeated three times ($n = 9$). * $P < 0.05$, ** $P < 0.01$, one-way ANOVA or Student's t test.

the lowest value at 7 days after Müller cells were transfected with the virus (0.32 ± 0.05 , $P < 0.05$; Fig. 2F).

Meanwhile, mRNA level detection of the three main nerve growth factors secreted by Müller cells (NGF ,

Fig. 2 Treatment of primary Müller cells with AD PirB shRNA for knockdown. **A** Representative image showing fluorescence-based identification of Müller cells with vimentin (green, 488 nm) located primarily in the cytoplasm (blue, DAPI nuclear staining; scale bar, 250 μ m). **B** Images showing co-localization of vimentin and PirB in a Müller cell. Vimentin (red, 594 nm) was primarily found in the cytoplasm, and PirB (green, 488 nm) was located mostly in the cell membrane (blue, DAPI nuclear staining; scale bars, 250 μ m). **C** GFP expression in Müller cells transfected with AD PirB shRNA over time (red, Müller cells labelled with vimentin; green, GFP fluorescence showing positive expression of AD PirB shRNA; blue, DAPI nuclear staining; scale bars, 250 μ m). **D** Effects of AD PirB shRNA transfection on Müller cell proliferation ($n = 3$). **E** PirB mRNA expression in Müller cells ($n = 3$). **F** PirB protein expression in Müller cells ($n = 3$). * $P < 0.05$, ** $P < 0.01$, one-way ANOVA and Student's t test.



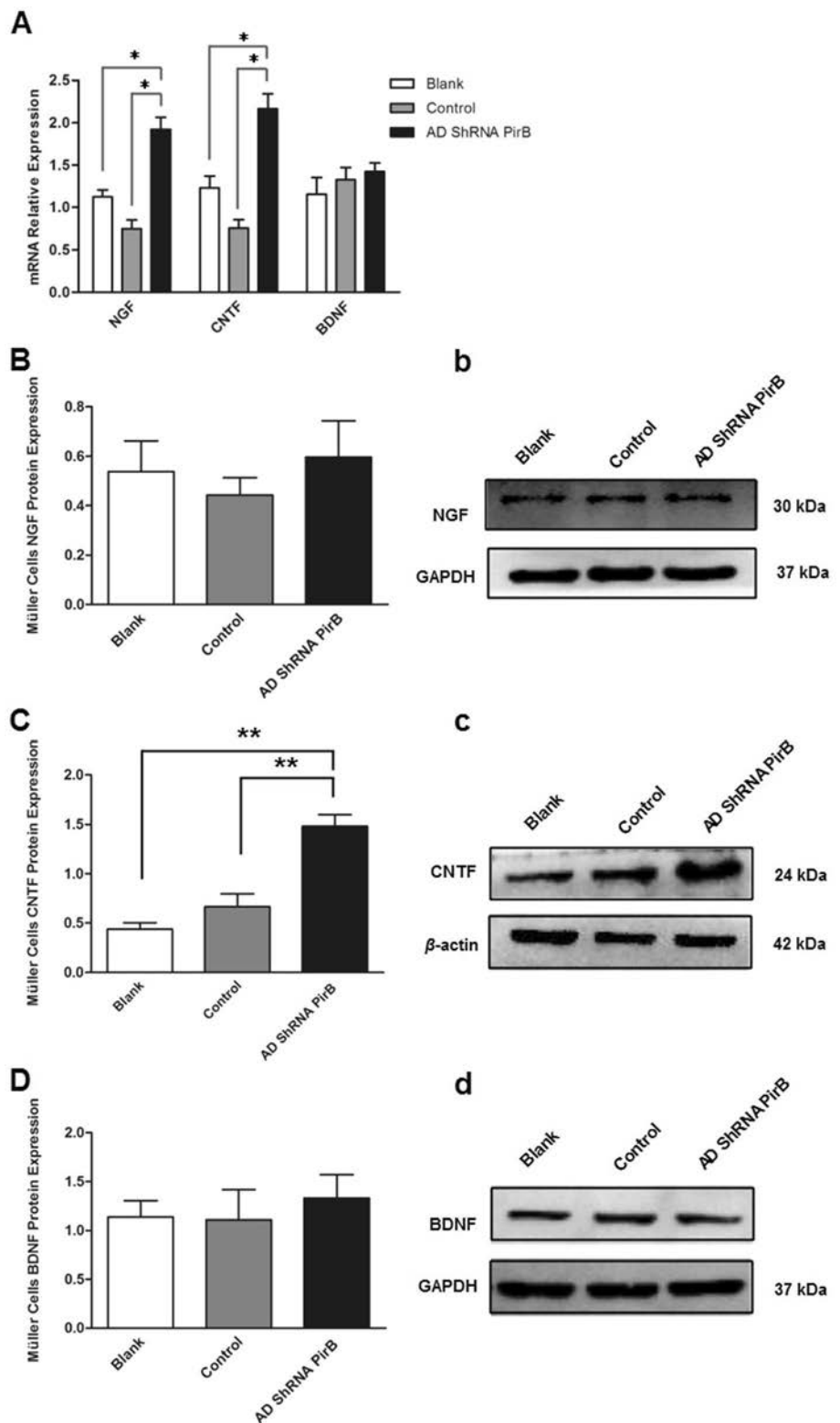
BDNF, and *CNTF*) showed that the *NGF* and *CNTF* mRNA levels were significantly higher in the AD PirB

shRNA group (1.92 ± 0.14 , $P = 0.041$, $P = 0.036$; 2.17 ± 0.18 , $P = 0.298$, $P = 0.018$) than in the blank and control

groups (0.76 ± 0.10 , 1.23 ± 0.14 ; 0.75 ± 0.1 , 1.12 ± 0.09 ; Fig. 3A). The NGF and BDNF protein levels did not significantly differ ($P > 0.05$; Fig. 3B, b and D, d); however, the CNTF protein levels in the AD PirB shRNA

groups (1.48 ± 0.12) were significantly higher than those of the blank and control groups (0.44 ± 0.017 , $P < 0.001$; 0.67 ± 0.13 , $P < 0.001$; Fig. 3C, c). These results

Fig. 3 NGF, CNTF, and BDNF levels in primary Müller cells transfected with AD PirB shRNA. **A** NGF, CNTF, and BDNF mRNA expression in Müller cells ($n = 3$). **B, b** NGF protein expression in Müller cells ($n = 3$). **C, c** CNTF protein expression in Müller cells ($n = 3$). **D, d** BDNF protein expression in Müller cells ($n = 3$). * $P < 0.05$, ** $P < 0.01$, one-way ANOVA and Student's *t* test.

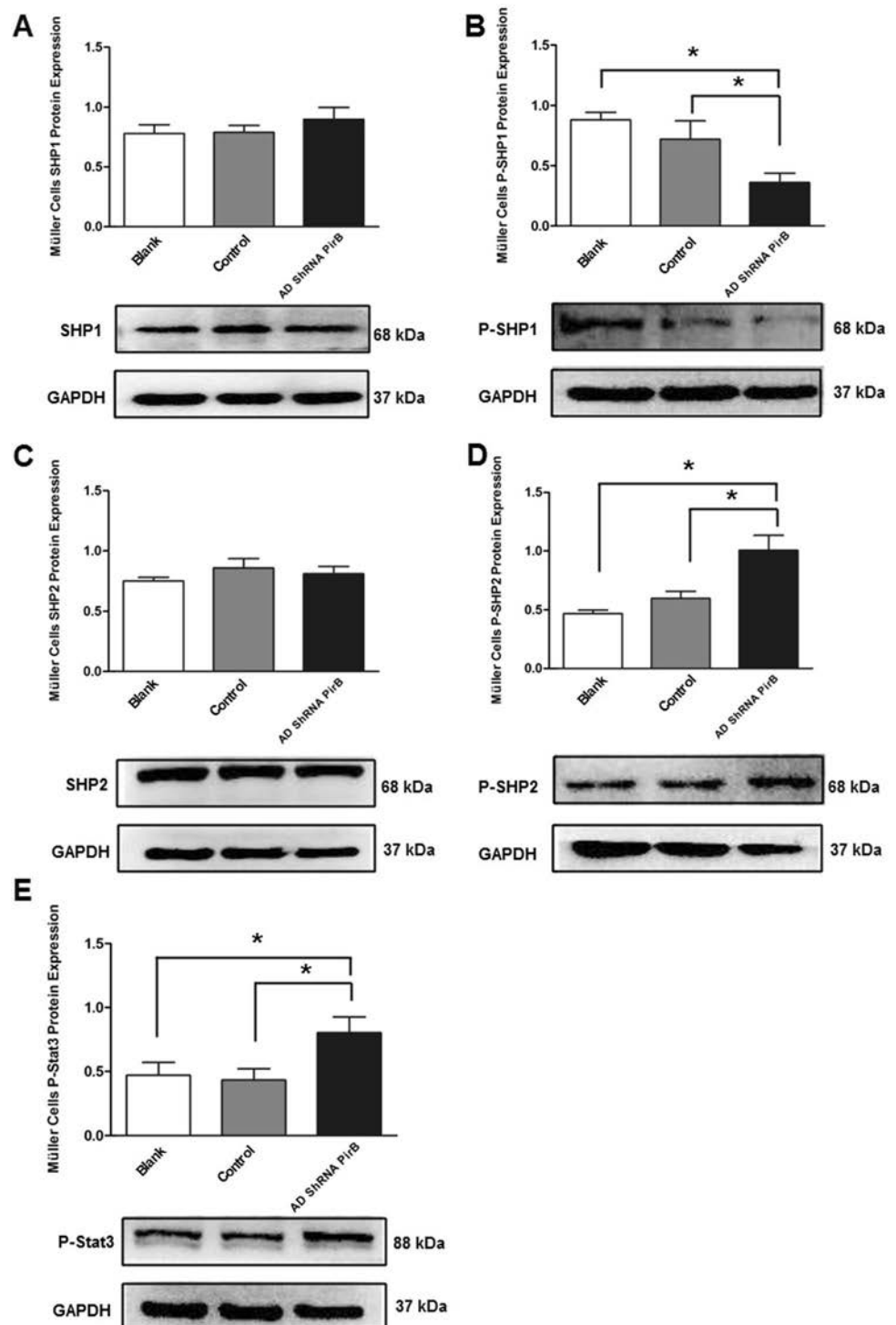


suggested that PirB knockdown in Müller cells mainly results in the increased expression of intracellular CNTF.

To explore the signaling pathways affecting CNTF expression in Müller cells in the context of PirB, we investigated the protein expression levels of signaling molecules downstream of PirB. Western blot analysis showed that the SHP1 and SHP2 protein levels were not

significantly different (Fig. 4A, C) and that the P-SHP1 levels were significantly lower (0.36 ± 0.08) than those of the blank and control groups (0.88 ± 0.06 , $P = 0.031$; 0.72 ± 0.15 , $P = 0.024$, Fig. 4B). The P-SHP2 levels were significantly higher (1.01 ± 0.13) than those of the blank and control groups (0.47 ± 0.03 , $P = 0.038$; 0.59 ± 0.06 , $P = 0.0294$, Fig. 4D). In addition, the P-Stat3 levels were

Fig. 4 Levels of intracellular proteins in primary Müller cells transfected with AD PirB shRNA. GAPDH and β -actin served as internal references. The y-axes show the ratios of gray values of target proteins to those of the respective internal references. Each experiment was repeated three times ($n = 9$). Data are the mean \pm SD; * $P < 0.05$, ** $P < 0.01$, one-way ANOVA and Student's t test.



significantly higher (0.81 ± 0.12) than those of the blank and control groups (0.46 ± 0.10 , $P = 0.0218$; 0.43 ± 0.09 , $P = 0.0189$, Fig. 4E). These findings suggested that the JAK/Stat3 signaling pathway is activated in Müller cells after transfection with AD PirB shRNA.

PirB Knockdown in Müller Cells Promotes Axonal Growth of Co-cultured RGCs

The transwell system (Corning Incorporated, NY, USA, REF No: 3413) allowed cells inside the chamber to be physically separated from those outside so that only the culture medium connected them (Fig. 5C). Primary RGCs were cultured alone for 1 day, then co-cultured with differently-treated Müller cells for 7 days. Neurites in the blank group with RGCs cultured alone were the shortest,

and those of the AD PirB shRNA group were the longest ($202.57 \pm 23.59 \mu\text{m}$, Fig. 5A, B). These differed significantly from the blank (negative control, $166.23 \pm 14.86 \mu\text{m}$, $P = 0.005$), sham ($181.54 \pm 11.13 \mu\text{m}$, $P = 0.041$), and control groups ($173.01 \pm 22.82 \mu\text{m}$, $P = 0.006$). These results suggested that Müller cells promote the growth of co-cultured RGC neurites, and PirB knockdown further enhances this neurite growth-promotion effect.

In Müller Cells with PirB Knockdown, CNTF is a Major Factor That Promotes the Regeneration of RGC Neurites

MTT assays revealed significant cytotoxicity after RGCs were injured for 24 h ($61.33\% \pm 5.03\%$) by exposure to rotenone at 100 nmol/L compared to that of the control

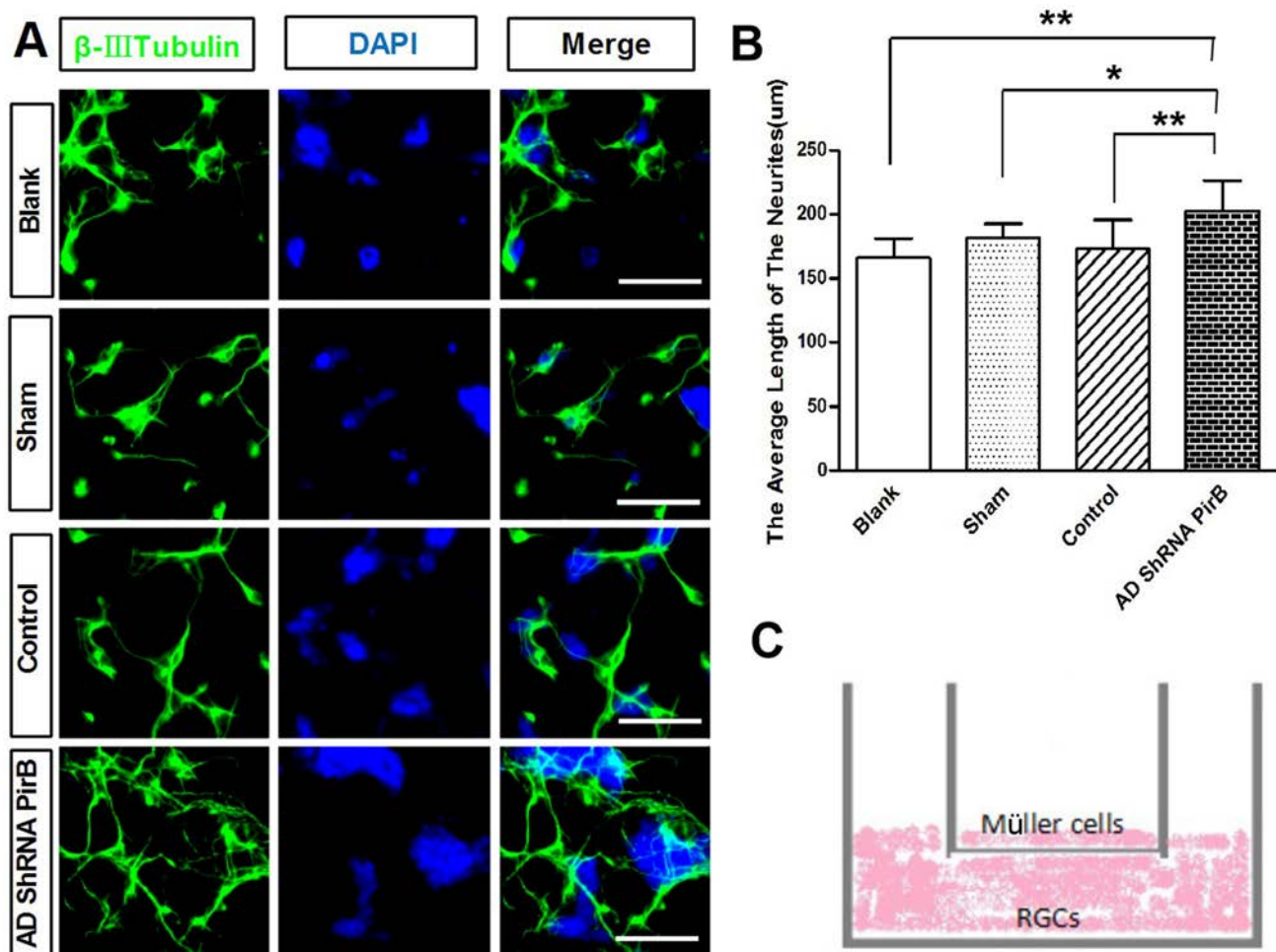


Fig. 5 Effects of Müller cells transfected with AD PirB shRNA on co-cultured RGCs. **A** Representative images of immunofluorescent neurite staining after co-culture of RGCs with differently-treated Müller cells [green (488 nm), β -III tubulin-labeled RGC neurites; blue, DAPI-labeled RGC nuclei; scale bars, 250 μm ; $n = 6$ for each group]. **B** Quantification of RGC neurite lengths. Data are the mean \pm

SD; $*P < 0.05$, $**P < 0.01$, one-way ANOVA and Student's *t* test. **C** Diagram of the co-culture of Müller cells and RGCs. Müller cells in the inner chamber; primary RGCs outside of the chamber; the Müller cells and RGCs were not in contact, but the medium was continuous with both.

group ($100\% \pm 14\%$, $P = 0.001$, Fig. 6A). When injured RGCs were co-cultured with pretreated Müller cells for 4 days, immunofluorescent staining revealed that PirB knockdown in Müller cells promoted the regeneration of neurites in the co-cultured RGCs. In addition, in the siRNA CNTF + AD PirB shRNA group, the regeneration of neurites was significantly inhibited ($55.45 \pm 15.01 \mu\text{m}$) compared with that in the AD PirB shRNA group ($118.39 \pm 13.57 \mu\text{m}$, $P = 0.001$) and the siRNA CNTF + AD shRNA group ($79.86 \pm 8.30 \mu\text{m}$, $P = 0.044$) (Fig. 6B, C).

Discussion

MHC-1 in the CNS is either minimally expressed or not expressed in adulthood, so the effects of PirB in the CNS differ from those in the immune system. A previous study showed that NgR and PirB are co-receptors for Nogo-A,

MAG, and OMgp; however, PirB inhibition is more effective in promoting axonal growth than NgR suppression [8].

In this study, Nogo-A, MAG, and OMgp were used to inhibit primary RGCs, and AD PirB shRNA was used for PirB knockdown. PirB knockdown did not promote the growth of RGC neurites after treatment with Nogo-A, MAG, or OMgp. These results suggested that PirB plays a limited role in the myelin-associated inhibition of RGCs, and inhibition of PirB is not sufficient to significantly promote the regeneration of neurites. There are two likely reasons for these findings. (1) PirB is not the main MAI receptor in inhibiting axonal growth, and other receptors, such as NgR, may play the main inhibitory role; however, previous findings do not support this notion [9, 10]. (2) In RGCs, there are other unidentified inhibitors that may not act through the PirB pathway, so PirB knockdown cannot completely block their effects.

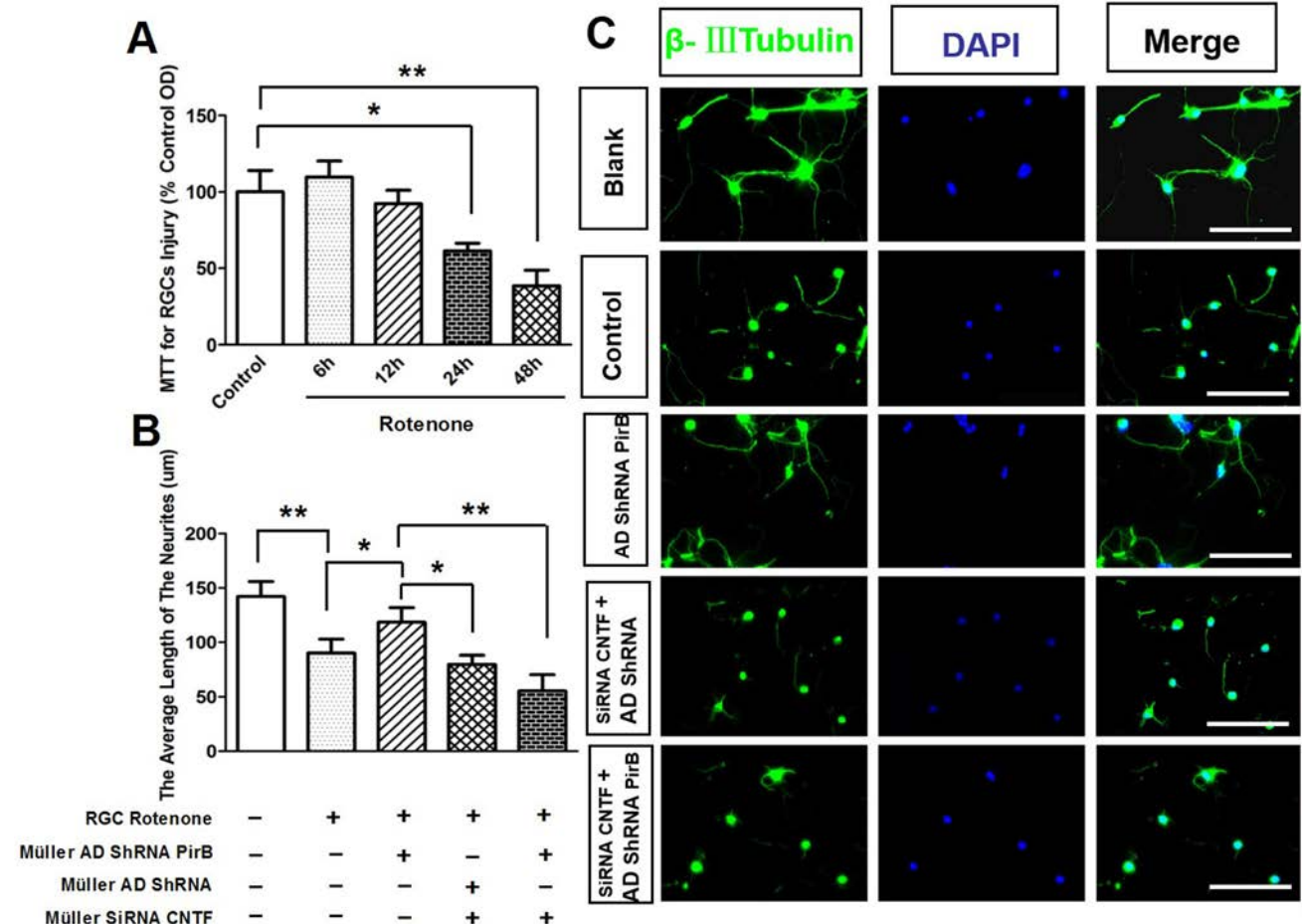


Fig. 6 Effects of Müller cells transfected with AD PirB shRNA on injured RGCs. **A** Toxic effects of rotenone on RGCs (control, untreated RGCs). **B** Neurite growth of injured RGCs co-cultured with Müller cells transfected with AD PirB shRNA (RGCs injured for 24 h by rotenone, Müller cells pretreated with AD PirB shRNA for 72 h, injured RGCs co-cultured with pretreated Müller cells for 4 days, and

Si-r CNTF interference in Müller cells for 4 days, $n = 6$). Data are the mean \pm SD. $*P < 0.05$, $**P < 0.01$, one-way ANOVA. **C** Fluorescent staining of injured RGC neurites [green (488 nm), β -III tubulin-labelled RGC neurites; blue, DAPI-labelled RGC nuclei; scale bars, 250 μm ; $n = 6$ per group].

Although direct PirB knockdown in RGCs did not significantly promote the growth of neurites under MAI inhibition, that does not necessarily mean that PirB does not affect optic nerve regeneration. On the contrary, PirB is very important in optic nerve regeneration. A study by Fujita *et al.* showed that PirB knockout in mice does not directly promote optic nerve regeneration [15], but optic nerve regeneration is stronger in mice with PirB knockdown than in wild-type animals after treatment with exogenous BDNF, suggesting that PirB plays a role in optic nerve regeneration that may not depend on MAI inhibition and is instead caused by other factors that affect neurite growth. Our study demonstrated for the first time that PirB is expressed in retinal Müller cells and that PirB knockdown increases CNTF expression. This suggests that PirB regulates the expression of NGF in Müller cells. Based on this, we infer that PirB also has important physiological functions in non-neuronal cells.

Müller cells are an important component of the microenvironment, as they are neuroprotective and provide nutritional support for RGCs [34]. Here, we revealed that Müller cells with PirB knockdown not only promoted normal RGC neurite growth, but also induced the growth of rotenone-injured RGC neurites when Müller cells and RGCs were co-cultured. There was no significant protective effect on RGCs, however, suggesting that inhibiting PirB in Müller cells primarily promotes the growth of RGC neurites. In addition, treatment of Müller cells with siRNA-CNTF significantly suppressed neurite regeneration, suggesting that this effect is indirectly influenced by the regulation of CNTF expression.

We also revealed that PirB knockdown in Müller cells activated the JAK/Stat3 signaling pathway, and while P-SHP1 levels decreased significantly, P-SHP2 levels markedly increased. Han *et al.* [35] reported that SHP-1 and SHP-2 play negative regulatory roles in the JAK/Stat3 pathway, where their downregulation activates JAK/Stat3 signaling. In this study, the P-SHP1 protein levels were significantly down-regulated and the P-SHP2 protein levels were significantly up-regulated. The expression of these two negative regulatory molecules was inconsistent; however, the JAK/Stat3 signaling pathways were activated. Therefore, we speculate that SHP-1 has a stronger effect than SHP-2 in regulating the signaling pathways. A strategy that incorporates the use of an si-SHP1/2 construct could provide a convincing means of testing this hypothesis; however, further research is required.

We found that PirB is expressed in Müller cells and that its knockdown promotes neurite regeneration in co-cultured RGCs. This regenerative effect may be exerted *via* the PirB-SHP1-JAK/Stat3-CNTF pathway; however, it is unclear if PirB affects the production of other factors in Müller cells. In addition, we used cells from early postnatal

animals in which certain intrinsic factors such as cAMP and NMDA are different from those in adult retinal cells. Thus, age-related differences in the role of PirB require further investigation.

In conclusion, these findings reveal that PirB in Müller cells exerts important effects on RGC neurite regeneration, and our results provide a new basis for the use of PirB as a target molecule to promote nerve regeneration.

Acknowledgements This work was supported by the National Natural Science Foundation of China (81470630).

Conflict of interest The authors declare that they have no conflict of interest.

References

1. Yu-Wai-Man P, Votruba M, Burté F, La Morgia C, Barboni P, Carelli V. A neurodegenerative perspective on mitochondrial optic neuropathies. *Acta Neuropath* 2016, 132: 789–806.
2. Berry M, Ahmed Z, Lorber B, Douglas M, Logan A. Regeneration of axons in the visual system. *Restor Neurol Neurosci* 2008, 26: 147–174.
3. Cafferty WB, Duffy P, Huebner E, Strittmatter SM. MAG and OMgp synergize with Nogo-A to restrict axonal growth and neurological recovery after spinal cord trauma. *J Neurosci* 2010, 30: 6825–6837.
4. Wang KC, Koprivica V, Kim JA, Sivasankaran R, Guo Y, Neve RL, *et al.* Oligodendrocyte-myelin glycoprotein is a Nogo receptor ligand that inhibits neurite outgrowth. *Nature* 2002, 427: 941–944.
5. Fournier AE, Grandpre T, Strittmatter SM. Identification of a receptor mediating Nogo-66 inhibition of axonal regeneration. *Nature* 2001, 409: 341–346.
6. Domeniconi M, Cao Z, Spencer T, Sivasankaran R, Wang K, Nikulina E, *et al.* Myelin-associated glycoprotein interacts with the Nogo66 receptor to inhibit neurite outgrowth. *Neuron* 2002, 35: 283–290.
7. Liu BP, Fournier A, Grandpré T, Strittmatter SM. Myelin-associated glycoprotein as a functional ligand for the Nogo-66 receptor. *Science* 2002, 297: 1190–1193.
8. Atwal JK, Pinkstongosse J, Syken J, Stawicki S, Wu Y, Shatz C, *et al.* PirB is a functional receptor for myelin inhibitors of axonal regeneration. *Science* 2008, 322: 967–970.
9. Zheng B, Atwal J, Ho C, Case L, He XL, Garcia KC, *et al.* Genetic deletion of the Nogo receptor does not reduce neurite inhibition *in vitro* or promote corticospinal tract regeneration *in vivo*. *Proc Natl Acad Sci U S A* 2005, 102: 1205–1210.
10. Kim JE, Liu BP, Park JH, Strittmatter SM. Nogo-66 receptor prevents raphespinal and rubrospinal axon regeneration and limits functional recovery from spinal cord injury. *Neuron* 2004, 44: 439–451.
11. Takai T. Paired immunoglobulin-like receptors and their MHC class I recognition. *Immunology* 2005, 115: 433–440.
12. Masuda A, Nakamura A, Maeda T, Sakamoto Y, Takai T. Cis binding between inhibitory receptors and MHC class I can regulate mast cell activation. *J Exp Med* 2007, 204: 907–920.
13. Syken J, Grandpre T, Kanold PO, Shatz CJ. PirB restricts ocular-dominance plasticity in visual cortex. *Science* 2006, 313: 1795–1800.

14. Cai X, Yuan R, Hu Z, Chen C, Yu J, Zheng Z, *et al.* Expression of PirB protein in intact and injured optic nerve and retina of mice. *Neurochem Res* 2012, 37: 647–654.
15. Fujita Y, Endo S, Takai T, Yamashita T. Myelin suppresses axon regeneration by PIR-B/SHP-mediated inhibition of Trk activity. *EMBO J* 2011, 30: 1389–1401.
16. Dickson HM, Zurawski J, Zhang H, Turner DL, Vojtek AB. POSH is an intracellular signal transducer for the axon outgrowth inhibitor Nogo66. *J Neurosci* 2010, 30: 13319–13325.
17. Ruzafa N, Pereiro X, Lepper MF, Hauck SM, Vecino E. A proteomics approach to identify candidate proteins secreted by Müller glia that protect ganglion cells in the retina. *Proteomics* 2018, 18: e1700321.
18. Bringmann A, Pannicke T, Grosche J, Francke M, Wiedemann P, Skatchkov SN, *et al.* Müller cells in the healthy and diseased retina. *Prog Retin Eye Res* 2006, 25: 397–424.
19. Weber AJ, Viswanathan S, Ramanathan C, Harman CD. Combined application of BDNF to the eye and brain enhances ganglion cell survival and function in the cat after optic nerve injury. *Invest Ophthalmol* 2010, 51: 327–334.
20. Lambiase A, Tirassa PA, Micera A, Aloe L, Bonini S. Pharmacokinetics of conjunctivally applied nerve growth factor in the retina and optic nerve of adult rats. *Invest Ophthalmol Vis Sci* 2005, 46: 3800–3806.
21. Cui ZL, Kang J, Hui YN, Hu D. Effects of CNTF and Ad-BDNF on survival of RGC after optic nerve injury. *Int J Ophthalmol* 2008, 8: 1130–1132.
22. Kobayashi W, Onishi A, Tu HY, Takihara Y, Matsumura M, Tsujimoto K, *et al.* Culture systems of dissociated mouse and human pluripotent stem cell-derived retinal ganglion cells purified by two-step immunopanning. *Invest Ophthalmol Vis Sci* 2018, 59: 776–787.
23. Liu H, Wang W, Li X, Huang C, Zhang Z, Yuan M, *et al.* High hydrostatic pressure induces apoptosis of retinal ganglion cells via regulation of the NGF signalling pathway. *Mol Med Rep* 2019, 19: 5321–5334.
24. Ren Z, Yang M, Guan Z, Yu W. Astrocytic $\alpha 7$ nicotinic receptor activation inhibits amyloid- β aggregation by upregulating endogenous αB -crystallin through the PI3K/Akt signaling pathway. *Curr Alzheimer Res* 2019, 16: 1–9.
25. Navneet S, Zhao J, Wang J, Mysona B, Barwick S, Ammal Kaidery N, *et al.* Hyperhomocysteinemia-induced death of retinal ganglion cells: The role of Müller glial cells and NRF2. *Redox Biol* 2019, 24: 101199.
26. Cen LP, Liang JJ, Chen JH, Harvey AR, Ng TK, Zhang M, *et al.* AAV-mediated transfer of RhoA shRNA and CNTF promotes retinal ganglion cell survival and axon regeneration. *Neuroscience* 2017, 343: 472–482.
27. Guimarães RPM, Landeira BS, Coelho DM, Golbert DCF, Silveira MS, Linden R, *et al.* Evidence of Müller glia conversion into retina ganglion cells using neurogenin2. *Front Cell Neurosci* 2018, 12: 410–425.
28. Lindenau W, Kuhrt H, Ulbricht E, Körner K, Bringmann A, Reichenbach A. Cone-to-Müller cell ratio in the mammalian retina: a survey of seven mammals with different lifestyle. *Exp Eye Res* 2019, 181: 38–48.
29. Xu Z, Fouda AY, Lemtalsi T, Shosha E, Rojas M, Liu F, *et al.* Retinal neuroprotection from optic nerve trauma by deletion of arginase 2. *Front Neurosci* 2018, 12: 970.
30. Kamalden TA, Ji D, Osborne NN. Rotenone-induced death of RGC-5 cells is caspase independent, involves the JNK and p38 pathways and is attenuated by specific green tea flavonoids. *Neurochem Res* 2012, 37: 1091–1101.
31. Zhou JX, Liu YJ, Chen X, Zhang X, Xu J, Yang K, *et al.* Low-intensity pulsed ultrasound protects retinal ganglion cell from optic nerve injury induced apoptosis via yes associated protein. *Front Cell Neurosci* 2018, 12: 160.
32. Jia M, Wang X, Zhang H, Ye C, Ma H, Yang M, *et al.* MicroRNA-132 in the adult dentate gyrus is involved in opioid addiction via modifying the differentiation of neural stem cells. *Neurosci Bull* 2019, 3: 486–496.
33. Zeng Y, Shen Y, Hong L, Chen Y, Shi X, Zeng Q, *et al.* Effects of single and repeated exposure to a 50-Hz 2-mT electromagnetic field on primary cultured hippocampal neurons. *Neurosci Bull* 2017, 33: 299–306.
34. Ohlmann A, Tamm ER. Norrin: molecular and functional properties of an angiogenic and neuroprotective growth factor. *Prog Retin Eye Res* 2012, 31: 243–257.
35. Han Y, Amin HM, Franko B, Frantz C, Shi X, Lai R. Loss of SHP1 enhances JAK3/STAT3 signaling and decreases proteasome degradation of JAK3 and NPM-ALK in ALK+ anaplastic large-cell lymphoma. *Blood* 2006, 108: 2796–2803.



Neuroimage-Based Consciousness Evaluation of Patients with Secondary Doubtful Hydrocephalus Before and After Lumbar Drainage

Jiayu Huo¹ · Zengxin Qi^{2,3,4} · Sen Chen¹ · Qian Wang¹ · Xuehai Wu^{2,3,4} ·
Di Zang^{2,3,4} · Tanikawa Hiromi^{2,3,4} · Jiaxing Tan^{2,3,4} · Lichi Zhang¹ ·
Weijun Tang⁵ · Dinggang Shen^{6,7}

Received: 19 August 2019 / Accepted: 10 March 2020 / Published online: 1 July 2020
© Shanghai Institutes for Biological Sciences, CAS 2020

Abstract Hydrocephalus is often treated with a cerebrospinal fluid shunt (CFS) for excessive amounts of cerebrospinal fluid in the brain. However, it is very difficult to distinguish whether the ventricular enlargement is due to hydrocephalus or other causes, such as brain atrophy after brain damage and surgery. The non-trivial evaluation of the consciousness level, along with a continuous drainage test of the lumbar cistern is thus clinically important before the decision for CFS is made. We studied 32 secondary mild hydrocephalus patients with different consciousness levels, who received T1 and diffusion tensor imaging magnetic resonance scans before and after lumbar cerebrospinal fluid drainage. We applied a novel machine-learning method to find the most discriminative features from the multi-modal neuroimages. Then, we built a regression model to regress the JFK Coma Recovery Scale-Revised (CRS-R) scores to quantify the level of consciousness. The experimental results showed that our method not only approximated the CRS-R scores but also tracked the temporal changes in

individual patients. The regression model has high potential for the evaluation of consciousness in clinical practice.

Keywords Hydrocephalus · Disorder of consciousness · Structural imaging · Feature selection · Regression

Introduction

Hydrocephalus is a condition in which there is abnormal accumulation of cerebrospinal fluid (CSF) in cavities within the brain. It typically alters the structure as well as the function of many regions. In order to prevent serious complications of developmental, physical, and intellectual impairments, a shunt, such as a ventriculoperitoneal (VP) or lumbar peritoneal (LP) shunt, is often adopted to treat patients with hydrocephalus [1]. It has been shown that brain regions may recover both structure and function after draining the CSF and relieving the intracranial pressure by ventriculostomy and shunt insertion [2]. A recent review suggested that 84.2% of patients with normal-pressure

Jiayu Huo and Zengxin Qi have contributed equally to this work.

✉ Lichi Zhang
lichizhang@sjtu.edu.cn

✉ Weijun Tang
tangwj83@gmail.com

¹ Institute for Medical Imaging Technology, Shanghai Jiao Tong University, Shanghai 200030, China

² Department of Neurosurgery, Huashan Hospital, Shanghai Medical College, Fudan University, Shanghai 200030, China

³ Neurosurgical Institute of Fudan University, Shanghai Clinical Medical Center of Neurosurgery, Shanghai Key Laboratory of Brain Function Restoration and Neural Regeneration, Shanghai 200030, China

⁴ State Key Laboratory of Medical Neurobiology and Ministry of Education Frontiers Center for Brain Science, School of Basic Medical Sciences and Institutes of Brain Science, Fudan University, Shanghai 200030, China

⁵ Department of Radiology, Huashan Hospital, Fudan University, Shanghai 200030, China

⁶ Department of Radiology and Biomedical Research Imaging Center, University of North Carolina at Chapel Hill, Chapel Hill, NC 27599, USA

⁷ Department of Brain and Cognitive Engineering, Korea University, Seoul 02841, Republic of Korea

hydrocephalus (NPH) secondary to subarachnoid hemorrhage and 83% of patients with NPH secondary to head trauma show clinical improvement after shunting [3]. But the overall rate of complications, including infection, hemorrhage from inserting the tube into the ventricle, and blockage after shunt placement, reaches 22% [3, 4]. Moreover, in patients who develop mild ventricular enlargement and disorder of consciousness (DOC) after traumatic brain injury or cerebral hemorrhage, it is very difficult to attribute the exact cause of the enlargement to hydrocephalus or brain atrophy, and it is important to predict whether or not the shunt is helpful to the patient before the shunt decision is made. To this end, clinicians have to be cautious when treating patients with a shunt, while the identification of shunt-unresponsive patients in advance is very important.

In order to evaluate the outcome of shunting, external lumbar cerebrospinal fluid drainage (LCFD) is often used as a primary test to monitor the shunt responsiveness of hydrocephalus patients in clinical practice [4]. The LCFD test is conducted by placing a flexible tube in the lumbar spine, and then draining the cerebrospinal fluid for a few days. Meanwhile, recovery from abnormal neural structure/function, as well as improvement of the consciousness level in patients are expected. In general, the LCFD test provides an opportunity to track changes in the brain, which helps to evaluate the need for subsequent shunt management [5]. This also helps researchers to identify factors that may modulate the consciousness level within a short time period, which contributes to understanding the pathogenesis of hydrocephalus and the underlying mechanism of human consciousness, as well as the changes in consciousness associated with neuroanatomical changes.

It is necessary to understand the consciousness status of hydrocephalus patients and accurately evaluate the consciousness level in clinical practice, and there are several quantification schemes. The JFK Coma Recovery Scale-Revised (CRS-R), for example, is among the popular tools that clinicians use to assess patients with severe consciousness disorders [6]. Accordingly, a patient may belong to one of several different categories of DOC, including coma, unresponsive wakefulness state (UWS), and minimally conscious state (MCS). Note that the assessment procedure of CRS-R is inevitably subjective, while high expertise from trained raters is required for reproducibility of evaluation. Moreover, the procedure may have to be repeated several times during a short period, which results in a more reliable overall evaluation of the consciousness level, yet with a high cost in time and workload for clinicians [7].

Magnetic resonance (MR) imaging provides a non-invasive and relatively objective way to observe the human brain, although it is non-trivial to quantify the consciousness level from neuroimaging data. For example, NPH patients are significantly different from healthy controls regarding the fractional anisotropy (FA) values in the corpus callosum and corticospinal tract [8]. The FA values in the posterior limb of the internal capsule (IC) are higher among shunt-responsive INPH patients [9] (“INPH” stands for idiopathic normal pressure hydrocephalus, a subtype of NPH). It often occurs in the elderly, and its main clinical manifestations are gait instability, dementia, and urinary incontinence. However, compared with secondary NPH, it lacks subarachnoid hemorrhage, meningitis, and other causes. Its imaging manifestations are ventricular enlargement but normal intracranial pressure. Moreover, significant reduction of functional connectivity in the default mode network (DMN) has been reported in INPH patients [10], particularly between the posterior cingulate cortex, precuneus, and other neural regions in the network. The above studies mostly focused on cross-sectional views by exploring the imaging data at a single time point. Statistical comparisons are conducted at the group level, while the manual engineering of the measures (or features) may lack accuracy or sensitivity sufficient for the prognosis of individual patients [11].

More recent work has aimed to associate neuroimaging evidence with the consciousness status and its recovery during the treatment of patients. Widespread white matter deficits, including the left uncinate fasciculus, right internal capsule, and right corticospinal tract, are correlated with the consciousness level of DOC patients, suggesting the importance of white matter in the clinical assessment of the recovery of consciousness [12]. In traumatic brain injury patients with DOC, Perri *et al.* [13] found altered diffusion parameters (e.g., FA) in multiple regions including the anterior and posterior corona radiata, corticospinal tracts, cingulum fiber bundles, external capsule, and corpus callosum. Moreover, the alterations also correlated with cognition and clinical outcome. In a study aiming to distinguish UWS from MCS patients, Fernandez-Espejo *et al.* [14] classified patients into these diagnostic categories with an accuracy of 95% based on diffusion tensor imaging (DTI) data.

In this study, we explored the multi-modal structural neuroimaging data of hydrocephalus patients before and after LCFD using an advanced machine-learning tool, and revealed clues that associate neural structural changes with the temporal improvement of the consciousness level of patients.

Materials and Methods

Participants

In this study, 32 secondary mild hydrocephalus patients with different levels of DOCs were recruited from Huashan Hospital, Fudan University. All the patients received MR scans before LCFD, and follow-up scans days after LCFD. The majority of these patients were followed up in the rehabilitation hospital. Some patients were later re-admitted for a VP shunt. The patients were clinically diagnosed with different states of DOCs (including coma, UWS, and MCS) and were assessed with CRS-R before each MR scan. The CRS-R scores were quantified by XW, who is an experienced neurosurgeon. Demographic information and clinical characteristics of all the recruited participants are listed in Table 1. Particularly, we classified them into two categories: “Favorable” for patients whose consciousness levels improved after LCFD (with increasing CRS-R scores), and “Unfavorable” for no improvement. We also obtained the overall CRS-R scores before and after the LCFD surgery; each was also classified as either “Favorable” or “Unfavorable”.

Image Acquisition

All MR images were acquired on a 3T Siemens MR scanner in Huashan Hospital, Fudan University, and two structural modalities, T1 and DTI, were used. For T1 images, the scanning parameters were: 176 slices, 1 mm slice thickness, no inter-slice gap, repetition time (TR) = 2300 ms, echo time (TE) = 2.98 ms, inversion time = 900 ms, non-interpolated voxel size = $1 \times 1 \times 1 \text{ mm}^3$, flip angle = 9° , and field of view = $240 \times 256 \text{ mm}^2$. For DTI, the scanning parameters were: 38 slices, 3.5 mm slice thickness, no inter-slice gap, TR = 8400 ms, TE = 82 ms, non-interpolated voxel size = $1.8 \times 1.8 \times 3.5 \text{ mm}^3$, flip angle = 90° , field of view = $128 \times 128 \text{ mm}^2$, 12 diffusion directions with b-value = 1000 in addition to b_0 . The common diffusion tensor parameters FA (functional anisotropy) and ADC (apparent diffusion coefficient) were further reconstructed from DTI data for subsequent analysis.

Table 1 Demographic and clinical information of all the recruited secondary mild hydrocephalus patients. Scanning interval records the days between the two MR scans for individual patients.

Category	Favorable	Unfavorable	<i>P</i> value
Age (years): mean ± SD	47.50 ± 12.23	49.67 ± 11.91	0.6279
Gender: male/female	17/3	6/6	–
Scanning interval (days): mean ± SD	5.20 ± 2.71	6.17 ± 2.72	0.3370
CRS-R score before LCFD: mean ± SD	12 ± 6.02	17.91 ± 6.92	0.0233
CRS-R score after LCFD: mean ± SD	16.05 ± 4.85	17.91 ± 6.92	0.4054

Image Processing

Preprocessing

Motion artifacts may appear during MR acquisition, so quality control of the acquired data was performed to exclude patients with either motion artifacts (2 participants, #23 and #30) or missing image modalities (8 participants, #24–29, #31, and #32). Finally, 22 participants with both T1 and DTI data before and after LCFD qualified for image processing and quantification.

We first converted all MR images from DICOM format to NIFTI with MRI Convert (<https://lcn.uoregon.edu/downloads/mriconvert/mriconvert-and-mcverter>). Then, for each patient and each time point, we first aligned the b_0 image with the T1 image using rigid registration, and then applied its transform matrix to register the FA/ADC map to T1 space, i.e., FLIRT in FSL [15]. We further normalized the intensity ranges of T1, FA, and ADC to [0, 1] to facilitate subsequent feature extraction from the images.

ROI Labeling

Based on our previous work, 17 consciousness-related ROIs were selected as candidate feature sources [12]. All the ROIs are listed in Table 2, and examples in MNI152 atlas space are presented in Fig. 1. We expected to extract image features from the 17 ROIs for each patient and each time point. Concerning the large deformity of the images caused by hydrocephalus or injury, it was extremely difficult to apply existing automated methods for accurate ROI labeling. To this end, one of the authors (SC) was trained to manually delineate the 17 ROIs on all T1 images. The labeling results were later validated by HZ and XW. The Automated Anatomical Labeling atlas [16] and the Johns Hopkins University White Matter Atlas [17] were used for reference during the manual labeling.

Fiber Tractography

Tractography was later carried out on DTI data using DSI Studio with the deterministic fiber-tracking algorithm described in Yeh *et al.* [18]. We restricted tractography within a brain mask, while the manually-labeled ROIs in

T1 were warped to DTI space to filter the output of tractography. The following criteria were used for the fiber-tracking process: 0.5 mm step size, 60° turning angle, 30 mm–300 mm tract length, 0.1 FA threshold, and a maximum tract number of 50,000 per image. The ROIs were used as filters, since we focused only on the fibers that connected each pair of consciousness-related ROIs.

Feature Extraction

We then extracted neural structural image features from T1 and DTI by referring to the 17 labeled ROIs. The features generally consisted of two parts: the single-ROI feature associated with the intensity of each ROI, and the connectivity feature associated with the structural connectivity of a pair of ROIs.

- (a) **The single-ROI feature.** Specifically, for each ROI, we computed the mean intensity and the variance of T1, FA, and ADC. In this way, we concatenated all measures into a feature vector, the length of which was $17 \times 3 \times 2 = 102$ for each patient and each time point.
- (b) **The connectivity feature.** The connectivity feature was obtained from the tractography results. We derived a 17×17 symmetrical matrix for each DTI image, where each element recorded the tract numbers connecting the two corresponding ROIs. The values in the connectivity matrix were normalized over the total number of tracked fibers. We

Table 2 The 17 consciousness-related ROIs.

ROI	Abbreviation
Brainstem	Brainstem
Anterior Cingulate Cortex-Left	ACC-L
Anterior Cingulate Cortex-Right	ACC-R
Posterior Cingulate Cortex-Left	PCC-L
Posterior Cingulate Cortex-Right	PCC-R
Inferior Parietal Lobule-Left	IPL-L
Inferior Parietal Lobule-Right	IPL-R
Insula-Left	Insula-L
Insula-Right	Insula-R
Anterior Internal Capsule-Left	IC-LA
Anterior Internal Capsule-Right	IC-RA
Posterior Internal Capsule-Left	IC-LP
Posterior Internal Capsule-Right	IC-RP
Median Prefrontal Cortex-Left	MPFC-L
Median Prefrontal Cortex-Right	MPFC-R
Thalamus-Left	Thalamus-L
Thalamus-right	Thalamus-R

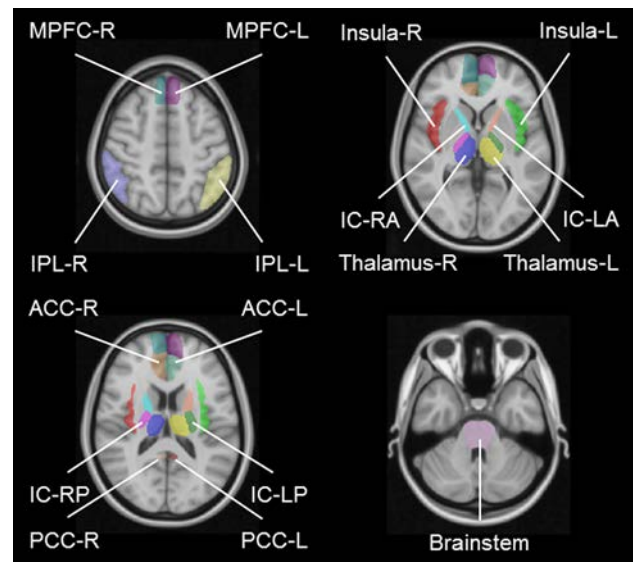


Fig. 1 Examples of the 17 manually-labeled ROIs in the MNI152 atlas space. The ROIs have been reported to be closely associated with consciousness.

further checked the connectivity matrices for all patients, and discarded elements where the structural connectivity was rarely detected by tractography. In the end, there were 107 connectivity features for each patient and each time point.

In summary, we extracted $102 + 107 = 209$ features, while zero-mean-unit-variance normalization was performed for each feature across individual patients and the two time points.

Joint Feature Selection and Regression

Many studies have been devoted to brain regions or networks that are associated with consciousness, including voxel-based analysis [19, 20] and region-based analysis [12]. Most of these have shown that the maintenance of consciousness is mainly associated with a collection of limited regions or networks in the brain. As we extracted a high-dimensional feature vector for each patient and each time point, we aimed to select the most important features and to simultaneously regress out the recovery of consciousness levels in the hydrocephalus patients. In particular, we were inspired by the well-known least absolute shrinkage and selection operator (LASSO) and used the following method for sparse feature selection and regression.

Specifically, we solved the following optimization problem for the joint learning of feature selection and regression:

$$\min_{\mathbf{w}} J(\mathbf{w}) = \frac{1}{2} \sum_{j=1}^2 \|\mathbf{y}_j - \mathbf{X}_j \mathbf{w}_j\|_{j_2}^2 + R_s(\mathbf{w}). \tag{1}$$

The matrix \mathbf{X} records the features of all patients, as each row corresponds to the transposed feature vector of a certain patient; \mathbf{y} is the column vector of the CRS-R scores; \mathbf{w} is the to-be-estimated coefficient vector that gauges the importance/contribution of each feature. The subscript j indicates the first and second time points for each patient. A typical regularization term $R_s(\mathbf{w})$ in the traditional LASSO tends to minimize the L_1 norm of \mathbf{w} , i.e., $R_s(\mathbf{w}) = \sum_{j=1}^2 \|\mathbf{w}_j\|_1$, such that only a sparse set of features is assigned with non-zero coefficients and thus selected.

The same neural regions/features play similar roles in human consciousness, regardless of the time points when the images are acquired. So, we argued that it is necessary to enforce temporal consistency for the coefficient vectors of the features across the two time points. In this way, we devised the regularization term as in Eq. (2).

$$R_s(\mathbf{w}) = \lambda_1 \sum_{j=1}^2 \|\mathbf{w}_j\|_1 + \frac{\lambda_2}{2} \|\mathbf{w}_1 - \mathbf{w}_2\|_2^2 + \frac{\lambda_3}{2} \|(\mathbf{y}_1 - \mathbf{y}_2) - (\mathbf{X}_1 \mathbf{w}_1 - \mathbf{X}_2 \mathbf{w}_2)\|_2^2. \tag{2}$$

There are three parts in the proposed $R_s(\mathbf{w})$, which are controlled by the non-negative scalars λ_1 , λ_2 , and λ_3 . The first part inherits the L_1 norm constraint in LASSO. The second part encourages the two coefficient vectors corresponding to the two time points to be as similar as possible (due to the L_2 norm constraint). Moreover, in the third part, we appended a high-order constraint, and required the difference of the regressed CRS-R scores between the two time points ($\mathbf{X}_1 \mathbf{w}_1 - \mathbf{X}_2 \mathbf{w}_2$) to well approximate the longitudinal difference in real clinical assessment ($\mathbf{y}_1 - \mathbf{y}_2$). In this way, the proposed method is capable of learning the most related ROI features and simultaneously tracking the temporal changes of CRS-R.

Our model resulted in the coefficient vectors \mathbf{w}_1 and \mathbf{w}_2 , which recorded the contributions of individual features to the regression of the CRS-R scores. The coefficients allowed us to predict the CRS-R scores from the features given an unseen test patient. In particular, we computed $\mathbf{X}_j \mathbf{w}_j$, which predicted the CRS-R score at a specific time point for the new patient. Meanwhile, as \mathbf{w}_1 and \mathbf{w}_2 are highly similar, we averaged them to get the mean coefficient vector across the two time points. We then selected the features by finding if the absolute values of the coefficients were neither zero nor near zero, as detailed in Table 5.

Nested Cross-Validation

We adopted nested cross-validation to automatically determine the parameters in our model and to demonstrate its capability of joint feature selection and regression. The data-driven regression model was thus able to map the image features to the CRS-R scores of individual patients. In particular, there were two nested loops in our cross-validation scheme, both of which followed the leave-one-out scheme.

- (a) In the outer cross-validation, each patient was chosen in turn for testing and unseen to training. The rest of the training data was used for modeling/verifying the regression in the inner cross-validation. When the training finished, the coefficient vectors of the features were generated for the regression. By applying the features of the test patient to the regression model, we completed the prediction of the pre-/post-LCFD CRS-R scores, as well as the change, for the test patient.
- (b) In the inner cross-validation to automatically optimize the model parameters, each training patient was isolated in turn from the training data to validate the performance of the regression model, which was trained with the remaining training data. With a grid search of all parameters, the optimal parameters were determined by referring to all validation cases in the inner loop. The parameters were then adopted for feature selection and regression on all training data, while the coefficients and the regression model were used for the test in the outer cross-validation.

The proposed method for consciousness tracking is shown in Fig. 2. In particular, we modified the SLEP toolbox (<https://github.com/divelab/slep/>) to implement our work. While most parameters were determined automatically by nested cross-validation, we empirically adjusted λ_3 for faster convergence of the training and numerical stability. That is, in the very beginning, λ_3 was bound by a relatively small value (i.e., $10e-2$). With the iterative optimization of \mathbf{w} in the proposed model, λ_3 gradually increased and finally reached $10e0$. Our experiment showed that the above strategy yielded satisfactory results when tracking the temporal changes of CRS-R scores.

Results

In this section, we present the experimental results of the proposed method and verification of the method on the data acquired from the hydrocephalus patients. First, we show that our method is capable of regressing out the CRS-R scores before and after LCFD based on the multi-modal

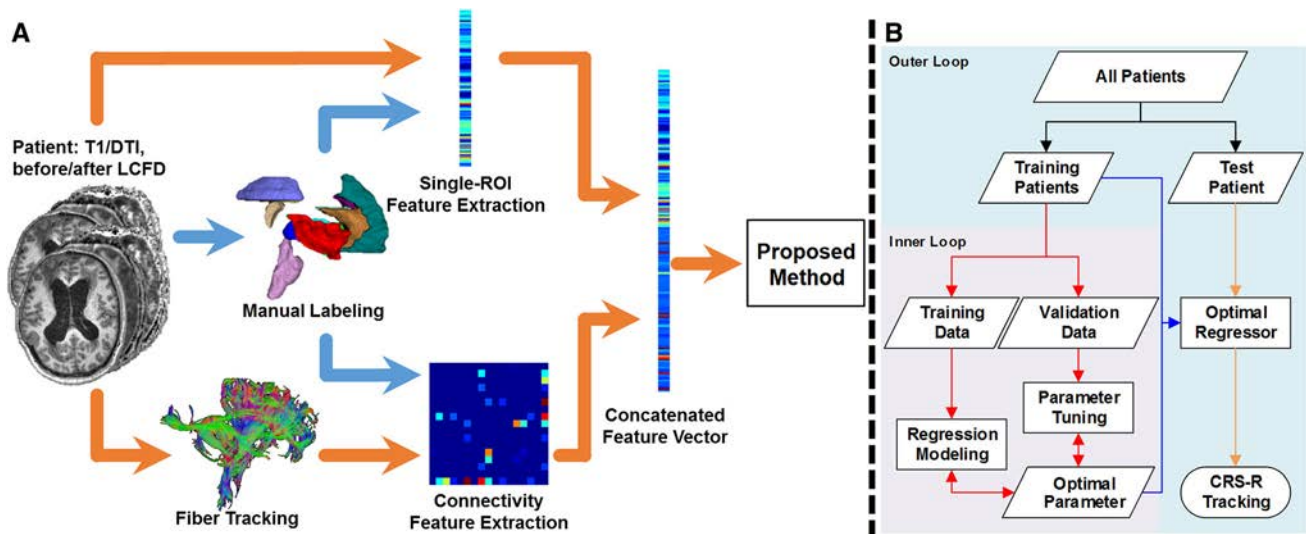


Fig. 2 Our proposed method for consciousness level assessment and tracking for hydrocephalus patients: **A** the pipeline; **B** the flowchart for nested cross-validation.

neuroimaging data. Second, we show that the regression results are helpful in evaluating the effect of LCFD. Finally, we provide the most discriminative features that were jointly selected during the regression task, for the assessment of human consciousness.

Regression for CRS-R Tracking

We demonstrated the performance of our method to track the CRS-R scores, and compared it with several existing methods as follows.

- SVR: We applied linear support vector regression (SVR) to all image features for the direct regression of the CRS-R scores. Note that SVR is a popular machine-learning tool for regression, especially given a small number of participants. In this setting, no feature selection was adopted before the regression, while the optimal parameters of SVR were determined in the same nested cross-validation scheme with our proposed method and all other methods under comparison.
- CFS+SVR: We applied correlation-based feature selection (CFS) before SVR. For each feature in particular, we computed the correlation of the measures from all images and the corresponding CRS-R scores. Then we selected the features with high positive/negative correlation, and only the selected features were used by SVR for regression. The number of selected features was determined automatically in nested cross-validation.
- PCA+SVR: Principal component analysis (PCA) was used to reduce the dimensionality of the feature

vectors. Then, a much shorter feature vector was acquired for each image after PCA, and this was later used for the regression by SVR. The parameter used by PCA for feature selection was determined automatically in nested cross-validation.

- LASSO: Feature selection and regression were jointly conducted in traditional LASSO. Different from our proposed method, the traditional LASSO method adopts a simplified regulation of the computed coefficients of the features, by setting λ_2 and λ_3 to zero in Eq. (2).

To evaluate the outcome of the regression, we computed the Pearson's correlation coefficient (CC) between the predicted and real CRS-R scores. We also computed the mean square errors (MSEs) between our CRS-R predictions and the real scores. The results are summarized in Table 3, which includes the highest CC and lowest mean squared error produced by our method. These results confirmed that our method regressed the CRS-R scores more accurately than any of the other methods under comparison.

In particular, without any feature selection, SVR might be limited by a relatively poor ability to regress the CRS-R scores. Incorporating correlation-based feature selection (CFS) and PCA as independent feature-selection tools may increase the power of the regression model, even though fewer (yet more representative) features were actually used by the subsequent SVR. Finally, with joint feature selection and regression (in LASSO and our method), we concluded that the CRS-R scores can be well approximated with the features extracted from multi-modal neuroimages.

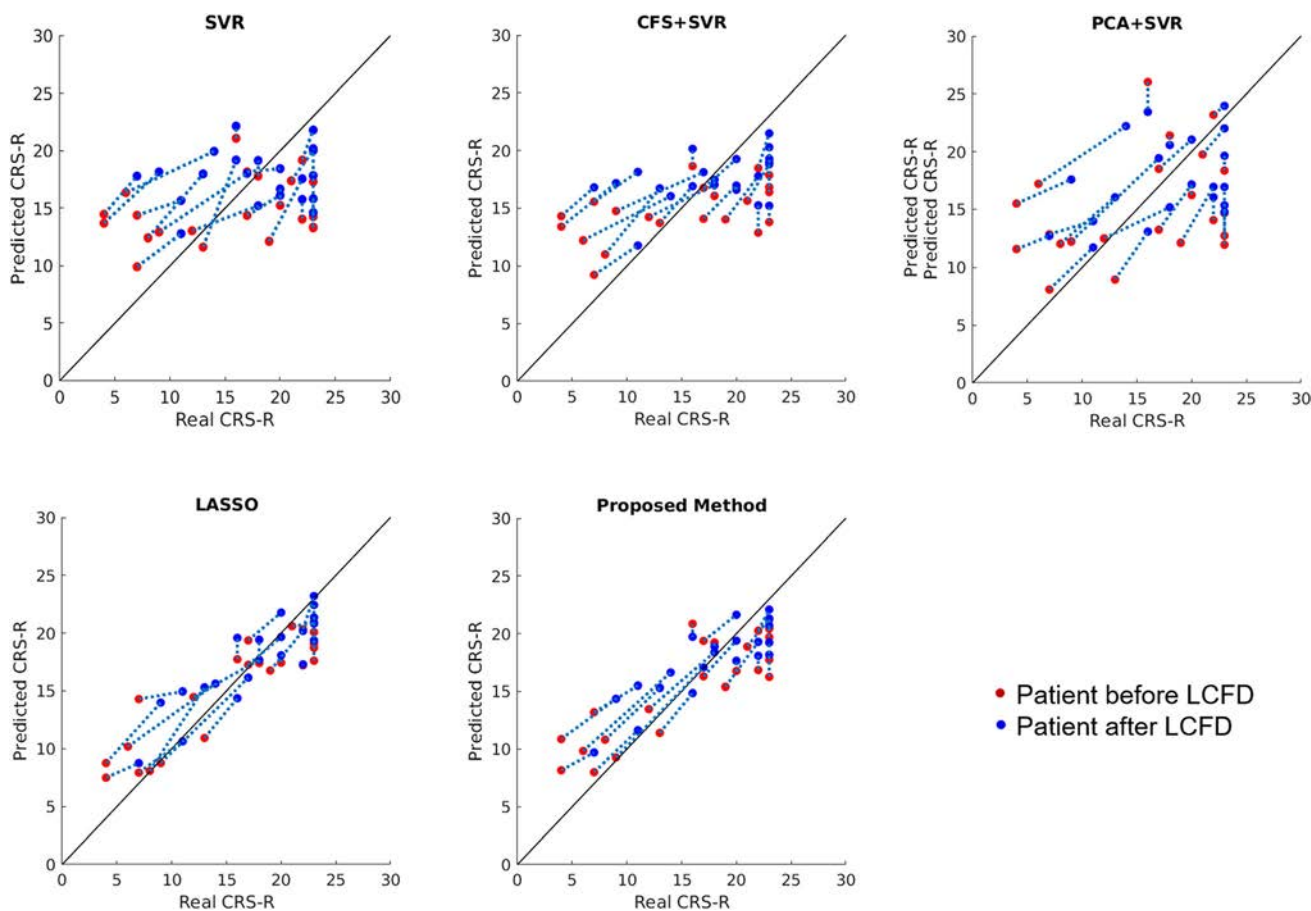


Fig. 3 Scatter plots of the regression results using different methods. Red dots, patients and the corresponding CRS-R score before LCFD; blue dots, scores after LCFD (red and blue dots for the same patient are connected by a dashed line).

The regression performance using our proposed method and the alternative methods are further visualized as scatter plots in Figure 3. Note that the plots for LASSO and our proposed method are closely distributed around the diagonals, indicating their relatively high regression performance for the data acquired at two time points.

It is also notable that the patients with a low baseline showed a significant improvement in their CRS-R score

(Fig. 3), which also demonstrated the validity of LCFD. On the other hand, in some patients with a high CRS-R score before LCFD, the improvement was not as strong as those with a low CRS-R score, since their room for improvement was also limited compared with the latter.

Categorization of Consciousness Recovery

Since each patient was grouped as either “favorable” or “unfavorable” (indicating whether the consciousness level improved after LCFD), we conducted the same categorization based on the CRS-R scores predicted by our method, to determine whether the drainage was beneficial to a specific patient. To evaluate the categorization performance, we further computed the accuracy (ACC), sensitivity (SEN) and specificity (SPE) of the categorization results (Table 4). In particular, the proposed method demonstrated much better ability in terms of consistently higher ACC, SEN, and SPE than LASSO (0.864, 0.857, and 0.875 with our proposed method *versus* 0.818, 0.786, and 0.875 with LASSO). We attribute this gain to the introduction of the sophisticated temporal regularization in

Table 3 Comparison of different methods in regressing the CRS-R scores.

	CRS-R regression	
	CC	MSE
SVR	0.318	33.957
CFS+SVR	0.530	26.955
PCA+SVR	0.396	34.083
LASSO	0.856	10.874
Proposed method	0.895	8.783

CC correlation coefficient, MSE mean squared error

our method. The ROC curves of all models are shown in Fig. 4.

Consciousness-Related Image Features

The coefficient vectors w_1 and w_2 gauged the contributions of individual features to the regression of the CRS-R scores. Due to the L_1 norm regularization in our proposed method, the coefficients of many features were near zero, which implied their negligible roles in the regression. In particular, we set the threshold at 0.1% of the coefficient of the highest absolute value of w , which was averaged over w_1 and w_2 of the two time points. The features with coefficients higher than the threshold were “selected” in each outer cross-validation loop. Since there were 22 loops, each feature could be selected up to 22 times. To this end, a

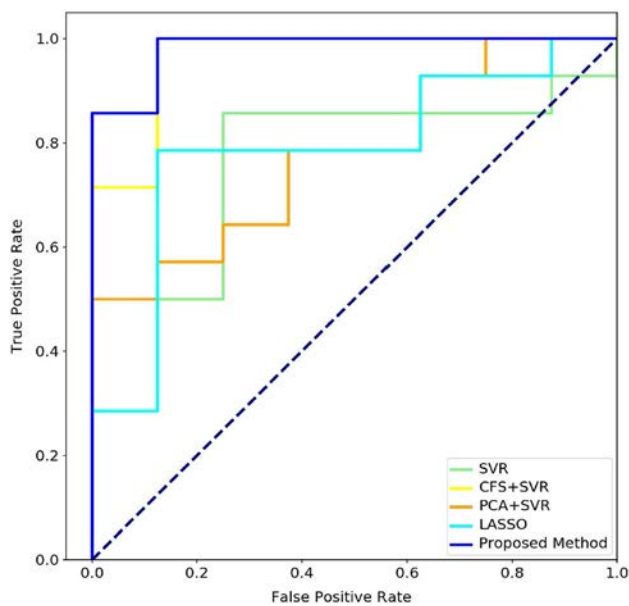


Fig. 4 ROC curves of different methods of categorizing consciousness recovery.

Table 4 Comparisons of different methods of categorizing consciousness recovery.

	Categorization of consciousness recovery		
	ACC	SEN	SPE
SVR	0.818	0.857	0.750
CFS+SVR	0.773	0.714	0.875
PCA+SVR	0.727	0.786	0.625
LASSO	0.818	0.786	0.875
Proposed method	0.864	0.857	0.875

ACC accuracy, SEN sensitivity, SPE specificity

feature was considered to be potentially important to the consciousness assessment if it was always selected in the cross-validation.

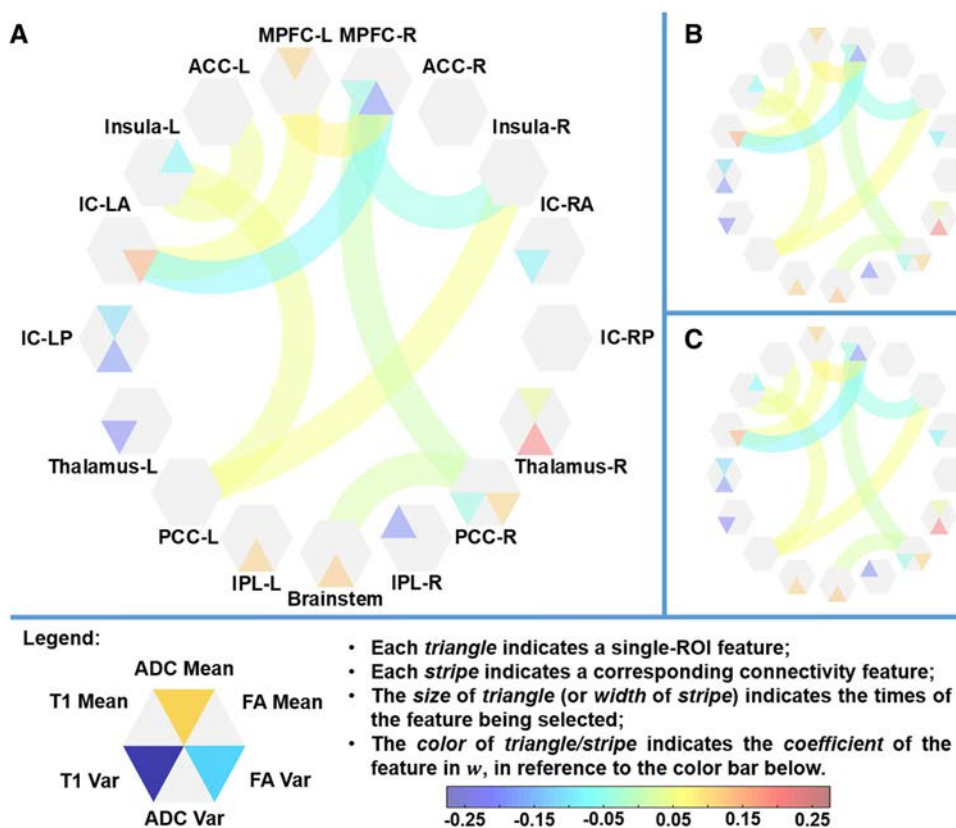
It is also notable that the coefficient w can only demonstrate that this feature is useful or helpful to our regression task when its value is not equal to zero. It does not further indicate that one feature is more important than others if the coefficient’s absolute value is higher. For instance, if the weight of the connection feature between the right posterior cingulate cortex and the right median prefrontal cortex is 0.025 and the correlation coefficient is 0.337, while the weight of the connection feature between IC-LA and MPFC-L is 0.054, much larger than the former, and the correlation coefficient is 0.108, smaller than the former, these non-zero coefficients are not comparable with each other.

All features selected by w are shown in Fig. 5A and detailed in Table 5. In general, 25 features were determined to be potentially critical to CRS-R assessment. Among them, 16 features were associated with single ROIs: 5 from T1, 8 from ADC, and 3 from FA. The remaining 9 features described the connectivity information between pairs of ROIs (Fig. 5). We also show the features selected by w_1 and w_2 , respectively, in Fig. 5B, C. The patterns of the selected features were very consistent across w_1 , w_2 , and w – only slight alterations of the coefficients occur in Table 5 – due to the regularization in Eq. (2).

Discussion

In this work, we present a method for joint feature selection and regression from multi-modal neuroimages to the CRS-R scores. The CRS-R score is the most used and recognized tool that can help clinicians to assess patients with consciousness disorders. In the clinic, some hydrocephalus patients are shunt-unresponsive while others are responsive. It is very important to identify the type of patient so that a therapy plan can be worked out. Usually, LCFD is used to monitor the shunt responsiveness of hydrocephalus patients. The CRS-R score was used to evaluate the consciousness levels of hydrocephalus patients before and after LCFD. Since the assessment procedure of CRS-R is inevitably subjective, it was the main purpose of this paper to provide an automatic algorithm to replace the judgment of the human supervisor. If two-stage CRS-R scores could be regressed out accurately by our proposed model, we could track the changes of the CRS-R scores for each individual patient before and after LCFD, which would provide a computer-assisted solution for quantitative prognosis. Also, the high time cost and workload of clinicians could be substantially reduced. Moreover, the

Fig. 5 The selected features according to **A** w , **B** w_1 , and **C** w_2 . Only the selected features are shown. The color of the triangle/stripe encodes the coefficient value.



factors could be identified that may modulate the consciousness level within a short time period by observing changes in the importance of different features.

Our method is capable of assessing the consciousness level of a patient and tracking the changes over multiple time points. The regression of the CRS-R scores provides an image-based assessment of the consciousness levels of hydrocephalus patients before and after LCFD, to assist relevant clinical decisions. Meanwhile, the method can help identify structural image features as biomarkers that are critical to interpreting and understanding improvement of the consciousness levels of hydrocephalus patients.

There have also been some comprehensive studies on the interpretation of weight vectors in classification and regression models. For example, Haufe *et al.* [21] surveyed linear models and whether their parameters can be interpreted in terms of the brain activity of interest, using simulated data as well as on real functional MRI and electromyographic (EEG) data. Kia *et al.* [22] presented a novel theoretical definition for interpretation, and a heuristic method to approximate the interpretability in multivariate analysis of magnetoencephalography (MEG) responses based on simulated and real MEG data. Weichwald *et al.* [23] focused on causal terminology for the interpretation of encoding/decoding models based on EEG, and provided guidelines for selecting causal statements that are

supported by empirical data. Generally, they found that only encoding models in the stimulus-based setting support unambiguous causal interpretations.

It is notable that our method required MRI images before and after LCFD, which is also true for other methods like SVR and LASSO. Clinically, the LCFD test is often used to evaluate the need for a VP shunt. Besides the change of neurological behavior, MRI before and after LCFD can show differences in the structure and function of the brain. Therefore, it is essential to obtain the MRI data in two stages from each patient. This also means that predicting the consciousness level after LCFD using the MRI data before LCFD is quite challenging. It is quite hard to not only trace the changes of brain ROIs between two stages, but also to identify the features that may modulate the consciousness level using only the MRI data before LCFD.

The sparse learning method has demonstrated a strong ability to select the features that track CRS-R scores. Compared with independent feature selection such as PCA, the traditional feature-reduction method LASSO, and the proposed joint feature reduction method both significantly improved the regression performance by integrating feature selection and regression into a unified framework. We computed the correlation between each selected feature and the CRS-R score over all patients (Table 5). Although the

Table 5 List of the selected features, their selected times, and the coefficients determined by the proposed method, as well as their correlation with the CRS-R scores (* $P < 0.05$).

Feature	#Selected	w	w_1	w_2	Correlation to CRS-R	
					CC	P value
T1-Mean-IPL-R	22	− 0.194	− 0.194	− 0.194	− 0.081	0.300
T1-Var-Thalamus-L	22	− 0.208	− 0.208	− 0.208	− 0.118	0.223
T1-Var-IC-RA	22	− 0.083	− 0.081	− 0.086	− 0.203	0.094
T1-Var-PCC-R	22	− 0.041	− 0.042	− 0.041	− 0.205	0.091
T1-Var-MPFC-R	22	− 0.037	− 0.039	− 0.035	0.0196	0.450
ADC-Mean-Thalamus-R	22	0.045	0.046	0.043	− 0.014	0.464
ADC-Mean-IC-LP	22	− 0.111	− 0.111	− 0.111	0.090	0.281
ADC-Mean-MPFC-L	22	0.110	0.110	0.111	− 0.235	0.062
ADC-Var-Thalamus-R	22	0.205	0.205	0.204	0.009	0.477
ADC-Var-IC-LP	22	− 0.183	− 0.183	− 0.183	− 0.268	0.040*
ADC-Var-MPFC-R	22	− 0.194	− 0.195	− 0.194	0.030	0.424
ADC-Var-IPL-L	22	0.130	0.130	0.129	− 0.190	0.109
ADC-Var-Brainstem	22	0.126	0.126	0.126	0.125	0.210
FA-Mean-Insula-L	22	− 0.068	− 0.067	− 0.069	− 0.112	0.234
FA-Var-IC-LA	22	0.146	0.146	0.147	0.189	0.110
FA-Var-PCC-R	22	0.107	0.106	0.108	− 0.011	0.472
Connect-Insula-R-PCC-L	22	0.064	0.064	0.064	− 0.180	0.122
Connect-Insula-R-MPFC-R	22	− 0.039	− 0.039	− 0.039	− 0.214	0.082
Connect-Insula-L-ACC-L	22	0.049	0.049	0.050	0.079	0.305
Connect-Insula-L-PCC-L	22	0.048	0.048	0.048	0.081	0.302
Connect-IC-LA-MPFC-R	22	− 0.077	− 0.076	− 0.077	− 0.232	0.065
Connect-IC-LA-MPFC-L	22	0.054	0.053	0.055	0.108	0.242
Connect-PCC-R-MPFC-R	22	0.025	0.025	0.025	0.337	0.013*
Connect-PCC-R-Brainstem	22	0.025	0.025	0.026	0.332	0.014*
Connect-MPFC-R-MPFC-L	22	0.070	0.069	0.071	0.033	0.417

proposed method was designed in a very different way with correlation, 3 (out of 25) selected features were eventually correlated with the CRS-R scores. We noted that, due to the L_1 regularization in the proposed method, only a few critical features were selected to contribute to the regression. While many features (even with a high correlation with CRS-R) were ignored for the regression, they are not necessarily trivial to the recovery of human consciousness [24]. The selected features are highly dependent on the design of the regression model and the regularization of the proposed method.

Nevertheless, the selected features draw our attention toward their roles underlying human consciousness, which are mostly in line with the literature. Traditionally, T1 imaging is used to diagnose hydrocephalus and DOC. For example, significant local brain atrophy in subcortical regions of DOC patients was reported by Lutkenhoff *et al.* [25], suggesting that the atrophy is correlated with the CRS-R score. Among them, the thalamocortical system has long been considered to be crucial to human consciousness [26–30]. In those studies, for example, different FA values have been found in the thalamus between hydrocephalus

patients and normal controls, and before and after a VP shunt. In this work, we identified from T1 images that 5 single-ROI features were correlated with the CRS-R scores, including the thalamic region. Our finding provides more evidence to highlight structural changes of thalamus in the clinical assessment of consciousness.

In addition to T1, DTI provides comprehensive scalar measures to help infer the structural integrity of white matter, which has been shown to be important to strengthen the diagnosis of hydrocephalus and DOC [11, 12, 14]. Specifically, the internal capsule (IC) is frequently discussed in the literature related to DOC [9, 20, 31–34]. In Hulkower *et al.* [35], IC is ranked among the most common abnormal ROIs in a literature review, particularly the altered FA and mean diffusivity in the posterior limb. In our work, 3 scalar features of DTI were selected and associated with the IC; its number of features was more than that of the other regions. This suggests the importance of the IC in assessing the CRS-R scores and evaluating the effect of LCFD.

Nine connectivity features were selected, most of which were associated with the insula, posterior cingulate cortex,

and median prefrontal cortex. Note that the coefficients in w for 2 (out of 9) connectivity features were negative, in line with their inverse correlation to the CRS-R scores. In general, we argue that a better consciousness status would be correlated with more abundant connectivity. Here, the connectivity features were extracted as the number of fibers connecting a pair of ROIs, while the overall number of fibers was set to 50,000 per image. Thus, the feature was not an absolute measure of the connectivity between ROIs, but rather a fraction of the connectivity over the entire brain.

Admittedly, our work suffered from a relatively small number of participants. While it was difficult to recruit more patients, the deficits in current neuroimage analysis toolkits made it hard to automatically process images with large abnormal deformity. Therefore, we manually labeled the ROIs, which was very time-consuming and would be difficult to apply to a bigger dataset. So, we will refer from [36, 37] and develop designated image analysis tools in future. Besides, additional studies with more patients are needed to resolve the issues in image labeling, to further validate and confirm the regression model and the statistical analysis conducted in this work. We will also refer from other graph-based methods [38, 39] to further improve our model.

Conclusions

In general, we are among the first to develop a highly sophisticated machine-learning tool that is capable of tracking changes in CRS-R scores based on multi-modal neuroimages before and after LCFD. We have proposed a novel method for this purpose, which can also select some image features that are highly related to the consciousness level. Specifically, abundant features were extracted from T1 and DTI data, and we used our proposed method for the joint learning of feature selection and the regression of CRS-R scores. With this model, we were able to predict the CRS-R scores for an unseen patient before and after LCFD. Therefore, we have devised a promising solution to complete image-based consciousness assessment, which has high potential in clinical practice.

Acknowledgements This work was supported by the National Natural Science Foundation of China (81571025 and 81702461), the National Key Research and Development Program of China (2018YFC0116400), the International Cooperation Project from Shanghai Science Foundation (18410711300), Shanghai Science and Technology Development Funds (16JC1420100), the Shanghai Sailing Program (17YF1426600), STCSM (19QC1400600, 17411953300), the Shanghai Pujiang Program (19PJ1406800), the Shanghai Municipal Science and Technology Major Project (No.2018SHZDZX01) and ZJlab, and the Interdisciplinary Program of Shanghai Jiao Tong University.

Conflicts of interest The authors claim that there are no conflicts of interest.

References

1. Chari A, Czosnyka M, Richards HK, Pickard JD, Czosnyka ZH. Hydrocephalus shunt technology: 20 years of experience from the Cambridge Shunt Evaluation Laboratory. *J Neurosurg* 2014, 120: 697–707.
2. Del Bigio MR. Neuropathology and structural changes in hydrocephalus. *Dev Disabil Res Rev* 2010, 16: 16–22.
3. Daou B, Klinge P, Tjoumakaris S, Rosenwasser RH, Jabbour P. Revisiting secondary normal pressure hydrocephalus: does it exist? A review. *Neurosurg Focus* 2016, 41: E6.
4. Governale LS, Fein N, Logsdon J, Black PM. Techniques and complications of external lumbar drainage for normal pressure hydrocephalus. *Neurosurgery* 2008, 63: 379–384.
5. Marmarou A, Young HF, Aygok GA, Sawauchi S, Tsuji O, Yamamoto T, *et al.* Diagnosis and management of idiopathic normal-pressure hydrocephalus: a prospective study in 151 patients. *J Neurosurg* 2005, 102: 987–997.
6. Giacino JT, Kalmar K, Whyte J. The JFK Coma Recovery Scale-Revised: measurement characteristics and diagnostic utility. *Arch Phys Med Rehabil* 2004, 85: 2020–2029.
7. Noirhomme Q, Brecheisen R, Lesenfants D, Antonopoulos G, Laureys S. “Look at my classifier’s result”: Disentangling unresponsive from (minimally) conscious patients. *Neuroimage* 2017, 145: 288–303.
8. Osuka S, Matsushita A, Yamamoto T, Saotome K, Isobe T, Nagatomo Y, *et al.* Evaluation of ventriculomegaly using diffusion tensor imaging: correlations with chronic hydrocephalus and atrophy. *J Neurosurg* 2010, 112: 832–839.
9. Seo SW, Kim ST, Lee JI, Nam DH. Differential diagnosis of idiopathic normal pressure hydrocephalus from other dementias. *AJNR Am J Neuroradiol* 2011, 32: 1496–1503.
10. Khoo HM, Kishima H, Tani N, Oshino S, Maruo T, Hosomi K, *et al.* Default mode network connectivity in patients with idiopathic normal pressure hydrocephalus. *J Neurosurg* 2016, 124: 350–358.
11. Hoza D, Vlasak A, Horinek D, Sames M, Alfieri A. DTI-MRI biomarkers in the search for normal pressure hydrocephalus aetiology: a review. *Neurosurg Rev* 2015, 38: 239–244; discussion 244.
12. Wu X, Zhang J, Cui Z, Tang W, Shao C, Hu J, *et al.* White matter deficits underlying the impaired consciousness level in patients with disorders of consciousness. *Neurosci Bull* 2018, 34: 668–678.
13. Di Perri C, Thibaut A, Heine L, Soddu A, Demertzi A, Laureys S. Measuring consciousness in coma and related states. *World J Radiol* 2014, 6: 589.
14. Fernández-Espejo D, Bekinschtein T, Monti MM, Pickard JD, Junque C, Coleman MR, *et al.* Diffusion weighted imaging distinguishes the vegetative state from the minimally conscious state. *Neuroimage* 2011, 54: 103–112.
15. Jenkinson M, Bannister P, Brady M, Smith S. Improved optimization for the robust and accurate linear registration and motion correction of brain images. *Neuroimage* 2002, 17: 825–841.
16. Tzourio-Mazoyer N, Landeau B, Papathanassiou D, Crivello F, Etard O, Delcroix N, *et al.* Automated anatomical labeling of activations in SPM using a macroscopic anatomical parcellation of the MNI MRI single-subject brain. *Neuroimage* 2002, 15: 273–289.

17. Wakana S, Jiang H, Nagae-Poetscher LM, Van Zijl PC, Mori S. Fiber tract–based atlas of human white matter anatomy 1. *Radiology* 2004, 230: 77–87.
18. Yeh FC, Verstynen TD, Wang Y, Fernández-Miranda JC, Tseng WY. Deterministic diffusion fiber tracking improved by quantitative anisotropy. *PLoS One* 2013, 8.
19. Messe A, Caplain S, Paradot G, Garrigue D, Mineo JF, Soto Ares G, *et al.* Diffusion tensor imaging and white matter lesions at the subacute stage in mild traumatic brain injury with persistent neurobehavioral impairment. *Hum Brain Mapp* 2011, 32: 999–1011.
20. Perlberg V, Puybasset L, Tollard E, Lehericy S, Benali H, Galanaud D. Relation between brain lesion location and clinical outcome in patients with severe traumatic brain injury: a diffusion tensor imaging study using voxel-based approaches. *Hum Brain Mapp* 2009, 30: 3924–3933.
21. Haufe S, Meinecke F, Görden K, Dähne S, Haynes JD, Blankertz B, *et al.* On the interpretation of weight vectors of linear models in multivariate neuroimaging. *Neuroimage* 2014, 87: 96–110.
22. Kia SM, Vega Pons S, Weisz N, Passerini A. Interpretability of multivariate brain maps in linear brain decoding: Definition, and heuristic quantification in multivariate analysis of MEG time-locked effects. *Front Neurosci* 2017, 10: 619.
23. Weichwald S, Meyer T, Özdenizci O, Schölkopf B, Ball T, Grosse-Wentrup M. Causal interpretation rules for encoding and decoding models in neuroimaging. *Neuroimage* 2015, 110: 48–59.
24. Tolosi L, Lengauer T. Classification with correlated features: unreliability of feature ranking and solutions. *Bioinformatics* 2011, 27: 1986–1994.
25. Lutkenhoff ES, Chiang J, Tshibanda L, Kamau E, Kirsch M, Pickard JD, *et al.* Thalamic and extrathalamic mechanisms of consciousness after severe brain injury. *Ann Neurol* 2015, 78: 68–76.
26. Zeman A. Consciousness. *Brain* 2001, 124: 1263–1289.
27. Wu X, Zou Q, Hu J, Tang W, Mao Y, Gao L, *et al.* Intrinsic functional connectivity patterns predict consciousness level and recovery outcome in acquired brain injury. *J Neurosci* 2015, 35: 12932–12946.
28. Laureys S, Owen AM, Schiff ND. Brain function in coma, vegetative state, and related disorders. *Lancet Neurol* 2004, 3: 537–546.
29. Greitz D. Radiological assessment of hydrocephalus: new theories and implications for therapy. *Neurosurg Rev* 2004, 27: 145–165; discussion 166–147.
30. Qin P, Wu X, Huang Z, Duncan NW, Tang W, Wolff A, *et al.* How are different neural networks related to consciousness? *Ann Neurol* 2015, 78: 594–605.
31. Levin HS, Wilde EA, Chu Z, Yallampalli R, Hanten GR, Li X, *et al.* Diffusion tensor imaging in relation to cognitive and functional outcome of traumatic brain injury in children. *J Head Trauma Rehabil* 2008, 23: 197–208.
32. Zhao C, Li Y, Cao W, Xiang K, Zhang H, Yang J, *et al.* Diffusion tensor imaging detects early brain microstructure changes before and after ventriculoperitoneal shunt in children with high intracranial pressure hydrocephalus. *Medicine (Baltimore)* 2016, 95: e5063.
33. Assaf Y, Ben-Sira L, Constantini S, Chang LC, Beni-Adani L. Diffusion tensor imaging in hydrocephalus: initial experience. *AJNR Am J Neuroradiol* 2006, 27: 1717–1724.
34. Cavaliere C, Aiello M, Di Perri C, Fernandez-Espejo D, Owen AM, Soddu A. Diffusion tensor imaging and white matter abnormalities in patients with disorders of consciousness. *Front Hum Neurosci* 2014, 8: 1028.
35. Hulkower M, Poliak D, Rosenbaum S, Zimmerman M, Lipton ML. A decade of DTI in traumatic brain injury: 10 years and 100 articles later. *AJNR Am J Neuroradiol* 2013, 34: 2064–2074.
36. Zhang L, Wang Q, Gao Y, Li H, Wu G, Shen D. Concatenated spatially-localized random forests for hippocampus labeling in adult and infant MR brain images. *Neurocomputing* 2017, 229: 3–12.
37. Zhang L, Wang Q, Gao Y, Wu G, Shen D. Automatic labeling of MR brain images by hierarchical learning of atlas forests. *Med Phys* 2016, 43: 1175–1186.
38. Bai L, Rossi L, Cui L, Cheng J, Hancock ER. A quantum-inspired similarity measure for the analysis of complete weighted graphs. *IEEE Trans Cybern* 2019.
39. Bai L, Hancock ER. Fast depth-based subgraph kernels for unattributed graphs. *Pattern Recognit* 2016, 50: 233–245.



APPL2 Negatively Regulates Olfactory Functions by Switching Fate Commitments of Neural Stem Cells in Adult Olfactory Bulb *via* Interaction with Notch1 Signaling

Chong Gao¹ · Tingting Yan¹ · Xingmiao Chen¹ · Kenneth K. Y. Cheng^{2,3,4} ·
Aimin Xu^{2,3} · Jiangang Shen¹

Received: 21 October 2019 / Accepted: 8 February 2020 / Published online: 28 May 2020
© Shanghai Institutes for Biological Sciences, CAS 2020

Abstract Adult olfactory neurogenesis plays critical roles in maintaining olfactory functions. Newly-generated neurons in the subventricular zone migrate to the olfactory bulb (OB) and determine olfactory discrimination, but the mechanisms underlying the regulation of olfactory neurogenesis remain unclear. Our previous study indicated the potential of APPL2 (adaptor protein, phosphotyrosine interacting with PH domain and leucine zipper 2) as a modulating factor for neurogenesis in the adult olfactory system. In the present study, we report how APPL2 affects neurogenesis in the OB and thereby mediates olfactory discrimination by using both *in vitro* neural stem cells (NSCs) and an *in vivo* animal model—APPL2 transgenic (Tg) mice. In the *in vitro* study, we found that APPL2 overexpression resulted in NSCs switching from neuronal differentiation to gliogenesis while APPL2 knockdown promoted neurogenesis. In the *in vivo* study, APPL2 Tg

mice had a higher population of glial cells and dampened neuronal production in the olfactory system, including the corpus callosum, OB, and rostral migratory stream. Adult APPL2 Tg mice displayed impaired performance in olfactory discrimination tests compared with wild-type mice. Furthermore, we found that an interaction of APPL2 with Notch1 contributed to the roles of APPL2 in modulating the neurogenic lineage-switching and olfactory behaviors. In conclusion, APPL2 controls olfactory discrimination by switching the fate choice of NSCs *via* interaction with Notch1 signaling.

Keywords APPL2 · Neurogenesis · Olfactory bulb · Notch1 signaling

Introduction

Olfactory functions like olfactory sensitivity and smell memory are important factors affecting cognitive and mental functions [1, 2]. Disrupted olfactory function is considered to be an indicator of multiple neurological disorders including head trauma, depression, and neurodegeneration [3, 4]. Neurogenesis in the olfactory bulb (OB) provides new neurons to facilitate olfactory functions such as odor information processing, learning, and discrimination [5–8]. Neuroblasts committed from adult neural stem cells (NSCs) in the subventricular zone (SVZ), migrate along the rostral migratory stream (RMS), mature into neurons, and integrate into local OB circuits [9]. The balance of lineage commitment between neurogenesis and gliogenesis determines the production of neurons in the olfactory system [10], and thereby regulates the ability of animals to encode odor information [11–13]. The NSCs in the SVZ decline with age and their re-activation can be

Chong Gao and Tingting Yan made equal contributions to the research.

✉ Jiangang Shen
shenjg@hku.hk

- ¹ School of Chinese Medicine, Li Ka Shing Faculty of Medicine, The University of Hong Kong, Pok Fu Lam, Hong Kong SAR, China
- ² State Key Laboratory of Pharmaceutical Biotechnology, The University of Hong Kong, Pok Fu Lam, Hong Kong SAR, China
- ³ Department of Medicine, Li Ka Shing Faculty of Medicine, The University of Hong Kong, Pok Fu Lam, Hong Kong SAR, China
- ⁴ Department of Health Technology and Informatics, The Hong Kong Polytechnic University, Hung Hom, Hong Kong SAR, China

harnessed as regenerative power against neurodegeneration [14, 15]. Olfactory dysfunction with impaired olfactory neurogenesis may be one of the characteristics in neurodegenerative diseases [16, 17]. Thus, elucidating the factors that modulate olfactory neurogenesis may provide new therapeutic targets for drug discovery in the treatment of neurodegenerative disorders.

By affecting adult olfactory neurogenesis, neurogenic mediators may regulate olfactory behaviors. Among multiple neurogenic regulators, Notch signaling may be a key regulator in controlling olfactory behaviors and adult neurogenesis [18, 19]. Notch signaling is responsible for cell fate choice during the development of NSCs [20, 21]. Activation of Notch signaling initiates NSCs switching from neurogenesis to gliogenesis [22]. In *Drosophila* and mice, Notch signaling plays critical roles in regulating olfactory plasticity and turnover of the olfactory epithelium progenitor/stem cells [23, 24]. Loss of Notch1 in mitral cells affects the neuronal response to olfactory stimuli and Notch1cKOKIn mice display reduced olfactory aversion to propionic acid compared to wild-type littermates [25]. Therefore, uncovering the underlying mechanisms regulating Notch signaling would help to identify new therapeutic targets for promoting adult olfactory functions.

APPLs (adaptor protein, phosphotyrosine interacting with PH domain and leucine zipper) are critical signaling molecules in regulating cellular behaviors. APPLs bind to multiple cellular molecules such as membrane receptors, nuclear factors, and signaling proteins linked to cell proliferation, chromatin remodeling, endosomal trafficking, cell survival, cell metabolism, and apoptosis [26]. There are two proteins in the APPL family: APPL1 and APPL2. APPL1 was the first member identified, with the functions of interacting with adiponectin receptors and adiponectin signaling and having crosstalk with insulin signaling pathways for metabolic regulation [26, 27]. As a downstream effector of Adipo-R1 and -R2, APPL1 mediates adiponectin-evoked endothelial nitric oxide production and endothelium-dependent vasodilation [28]. APPL1-deficient mice have impaired glucose-stimulated insulin secretion through inhibition of mitochondrial function in pancreatic beta cells [29]. APPL1 has also been implicated in regulating the Akt and/or MAPK signaling pathways and affects cell growth [30–32]. APPL1 participates in the pathological process of diabetic diseases *via* modulating the insulin, adiponectin, and epidermal growth factor (EGF) signaling pathways [32–35]. However, whether APPL1 modulates the growth of NSCs remains unknown.

APPL2 is an isoform with 54% identity in sequence and co-localizes with APPL1 in cells [32]. By interacting with TBC1D1, APPL2 also regulates insulin signaling for glucose metabolic regulation. It has been reported that the APPL2-inhibited insulin-stimulated glucose uptake is

mediated by the membrane recruitment of GLUT4 in skeletal muscle [36]. Our previous study has identified APPL2 as a key neurogenic regulator contributing to the depression-induced disruption of olfactory sensitivity [37, 38]. By regulating the glucocorticoid receptor, APPL2 acts as a cellular signaling molecule to affect adult neurogenesis and its related symptoms include depressive/anxiety-like behaviors and impaired olfactory sensitivity [37, 38]. However, how APPL2 regulates olfactory functions, particularly olfactory discrimination, at the physiological level remains unknown. Like the functions of Notch signaling, an *in vivo* clone study revealed that overexpressed APPL2 induces hippocampal NSCs to switch from neurogenesis to gliogenesis [38]. Thus, in the present study, we tested the hypothesis that APPL2 regulates olfactory neurogenesis and affects olfactory discrimination, and the underlying mechanisms are associated with affecting the Notch signaling for cell-fate decision in NSCs.

Materials and Methods

Cell Culture

Mouse neural progenitor C17.2 cells were obtained from the American Type Culture Collection and cultured in high-glucose Dulbecco's modified Eagle's medium (DMEM, Hyclone, Omaha, NE, USA) supplemented with 8% fetal bovine serum (FBS; Gibco, Waltham, MA, USA). Primary NSCs were prepared from fetal Sprague–Dawley rats (embryonic days E14–15) as previously described [39]. Briefly, cells were dissociated from the cerebral cortex and suspended (at 2×10^5 cells/mL) in DMEM/F12 medium supplemented with 2% B27, recombinant human basic fibroblast growth factor (20 ng/mL), and EGF (20 ng/mL). Neurospheres formed during culture were dissociated into single-cell suspensions in the culture medium for subculture. NSCs at 2–5 passages were used in the experiments.

Cell Culture for NSC Differentiation

Cultured NSCs at 2–5 passages were mechanically dissociated into single cells and directly plated onto poly-L-lysine-coated coverslips in different culture media. DMEM/F12 supplemented with 2% B27 was used to induce normal differentiation in the dissociated cells. Neurobasal medium supplemented with 2% B27 was applied to induce neuronal differentiation in the dissociated cells, whereas DMEM/F12 with 10% FBS was used to induce astrocytic differentiation.

Western Blot

Cells were harvested in ice-cold RIPA lysis buffer containing protease inhibitor and phosphatase inhibitor cocktail (Sigma, USA). Protein concentrations were determined with a protein assay kit (Bio-Rad, USA). Equal amounts of protein were subjected to SDS-polyacrylamide gel electrophoresis and then transferred to polyvinylidene difluoride membranes (Millipore, Burlington, MA, USA). After blocking, the membranes were probed with the appropriate primary antibodies overnight at 4°C, including β -tubulin III (Tuj-1, 1:1000; Covance), glial fibrillary acidic protein (GFAP, 1:1000; Sigma-Aldrich, St. Louis, MO, USA), Notch1 (1:300; Cell signaling, Danvers, MA, USA), Hes1 (1:200; Santa Cruz, CA, USA), notch intracellular domain (NICD, 1:400; Cell Signaling, Danvers, MA, USA), β -actin (1:2000; Sigma-Aldrich, St. Louis, MO, USA), and glyceraldehyde 3-phosphate dehydrogenase (GAPDH, 1:2000; Millipore, Burlington, MA, USA). The blots were subjected to HRP-conjugated corresponding secondary antibodies. Protein bands were visualized by adding ECL Advance (GE Healthcare Bio-Sciences, Wauwatosa, WI, USA) according to the manufacturer's instructions. Results were analyzed using Quantity One software (Bio-Rad, Hercules, CA, USA).

RNAi Treatment and Adenovirus Infection

We applied short-interfering RNA (siRNA) transfection to knock down APPL2 in cells. Commercial APPL2 siRNA or control siRNA (Life Technologies, Waltham, MA, USA) was transfected into NSCs with Lipofectamine RNAiMAX. To maintain the knockdown efficiency, we transfected the differentiated NSCs on days 1 and 4 post-differentiation and harvested them on day 7. To construct adenoviral vectors for overexpression of APPL2, cDNA encoding the APPL2 gene was cloned into the pAdeasy-1 adenoviral backbone vector (Stratagene, Bellingham, WA, USA) as described previously [33, 36]. Adenovirus encoding 3*flag-tagged APPL2 and luciferase control was generated and titered. NSCs were infected with adenovirus at a multiplicity of infection (MOI) of 10 for 2 h, followed by incubation with fresh medium for 7 days. The MOI was assessed with bioluminescence assays.

Animals, Drug Treatment, and Tissue Processing

APPL2 transgenic (Tg) mice were gifts from Prof. Xu Aimin's group. Mice were mated and genotyped. Wild-type C57BL/6 mice at the same age were obtained from the Laboratory Animal Unit at the University of Hong Kong. We measured the level of APPL2 expression in brain tissue and the genotyping protocol was used as in our previous

report [38]. The experimental protocol was approved by the institutional Animal Care and Ethics Committee at the University of Hong Kong (CULATR No. 2969-13). Every effort was made to minimize the number of animals used and their suffering. DAPT (20 mg/kg; N-[N-(3,5-difluorophenacetyl-L-alanyl)]-S-phenylglycine t-butyl ester, GSI-IX; Sigma-Aldrich, St. Louis, MO, USA) was injected i.p. into APPL2 Tg mice daily for 2 weeks. PBS was daily administered i.p. into mice in the vehicle control group. The mouse brain was perfused with 4% paraformaldehyde for fixation, penetrated with 30% sucrose solution, and frozen-sectioned at 20 μ m. One out of every 6 consecutive sections (at 100- μ m intervals) was selected to avoid repeated counting of cells.

Bromodeoxyuridine (BrdU) Incorporation

To monitor cellular proliferation, we injected BrdU (50 mg/kg per day, i.p.) to mice for 5 days and sacrificed them 2 h after the final injection. To determine newborn neuron maturation and cell survival, we injected BrdU at the same dose and route for 3 days and sacrificed the mice 11 days later. Positive staining with BrdU in sections from the OB and SVZ were identified as actively-proliferating cells.

Immunofluorescence

Cells and frozen brain sections were fixed in 4% paraformaldehyde, blocked in PBS with 5% goat serum and 0.1% Triton X-100, and then incubated with primary antibodies against Tuj1 (1:300; Covance, Beijing, China), glial fibrillary acidic protein (GFAP, 1:500; Millipore, Burlington, MA, USA), microtubule-associated protein 2 (MAP2, 1:500; Millipore, Burlington, MA, USA), APPL1 (1:500; provided by Prof. Aimin Xu), APPL2 (1:500; provided by Prof. Aimin Xu), Doublecortin (DCX, 1:300; Cell Signaling, Danvers, MA, USA), and Notch1 (1:300; Santa Cruz, Santa Cruz, CA, USA) overnight in a cold room and then incubated with the secondary antibodies Alexa 488 or 568 (Life Technologies, Waltham, MA, USA) at room temperature for 2 h. For BrdU staining, tissue was incubated with 2 N HCl for 1 h at room temperature before blocking and primary antibody incubation (BrdU, 1:400; Abcam, Cambridge, UK). DAPI was used to stain nuclei. Ten random fields from each experiment were selected and > 1000 cells were counted.

For *in vitro* tests, cell images were captured with a confocal fluorescence microscope (LSM700, LSM780, Carl Zeiss, Jena, Germany). Tissue images were observed with the 20 \times objective of a confocal fluorescent microscope (LSM800, Carl Zeiss, Jena, Germany). Each image was obtained projection of Z-stack with range of 20 μ m.

The tissue images of whole RMS-OB region were obtained by tiles scanning. dSTORM (direct stochastic optical reconstruction microscopy) images were processed following our previous protocol [37]. Cell counts and fluorescence intensity were recorded with ImageJ. Super-resolution images were obtained by dSTORM microscopy (NBI, Los Angeles, CA, USA) [37]. Molecular distances in dSTORM were obtained with the ‘spot profile’ model and exported with ImageJ (<https://imagej.nih.gov/ij/>).

Olfactory Discrimination Test (ODT)

A 60-min locomotion test was used to assess the differences in total distance covered by the APPL2 transgenic and wild-type mice ($n = 10$ per group). Then, olfactory performance was evaluated by conducting odor discrimination experiments in which 8–12 week-old mice were familiarized with a first odor (habituation odor) in four sessions and exposed once to a novel odor (dishabituation odor). The tests were run during the light phase of the animals’ 12-h dark/light cycle. The odor solutions butanol, pentanol, and limonene were diluted 1×10^{-3} in mineral oil and applied to a cotton stick. The odors were presented by inserting the stick into the animal’s home cage (habituation) in 4 successive sessions for 50 s per session, separated by 2-min intervals. In the fifth presentation, a different odor was delivered (dishabituation). If a mouse spent more time exploring in the fifth dishabituation session than in the fourth habituation session, the mouse was recognized being able to discriminate a novel from a familiar odor.

Statistical Analysis

Data are presented as the mean \pm SEM. For statistical analysis, we used Student’s *t*-test for two independent groups and ANOVA (one-way for single factor and two-way for two factors) followed by Tukey’s *post-hoc* test for multiple group analysis. Statistical significance was defined as $P < 0.05$.

Results

Increased APPL2 Expression is Associated with NSC Differentiation *in vitro*

To assess the correlation between APPL proteins and adult neurogenesis, we measured the dynamic changes in the expression levels of APPL1 during NSC differentiation *in vitro* ($n = 6$ batches of cultures per group). Western blot was used to assess the expression of APPL1 and APPL2 in the cultured NSCs at days 1, 3, 5, and 7. The expression of

Tuj1 and GFAP was used as references for neurogenesis and gliogenesis, respectively. We found that the expression of APPL1 was little changed in the process of neurogenesis or glia formation (Fig. 1A–D). We further used immunofluorescence to check the distributions of APPL1 and APPL2 in the cell types. Dual positive staining of APPL1 and Tuj1 was found in the cultured NSCs at day 7 rather than day 1, indicating that APPL1 is mainly present in differentiated cells committed into neural progenitors (Fig. 1E). Interestingly, APPL2 differed from APPL1 during the process of NSC differentiation. Western blot analysis revealed that the expression of APPL2 gradually increased with culture time (Fig. 1A–D). The increased expression of APPL2 coincided with the enhanced levels of Tuj1 and GFAP expression. Importantly, the expression of APPL2 was co-localized with GFAP⁺ rather than Tuj1⁺ cells in both the cultured NSCs *in vitro* and the wild-type mice *in vivo* (Fig. 1F, G). Taken together, these results indicated that APPL1 is not associated with the process of neurogenesis whereas APPL2 is a potential modulating factor to promote gliogenesis and affects the cell-fate decision of NSCs.

APPL2 Regulates Cell-Fate Choice During NSC Differentiation

To elucidate the roles of APPL2 in regulating the lineage commitments of NSCs, we manipulated the APPL2 levels in cultured NSCs using adenovirus-mediated overexpression and siRNA-induced knockdown. Western blots showed that the transfection approach successfully resulted in overexpression and knockdown of APPL2 (Fig. 2D, I). The overexpressed APPL2 reduced the percentages of Tuj1⁺ and MAP2⁺ neuronal cells but increased the GFAP⁺ astrocytic cells (Fig. 2A–C, H). To exclude the possibility of artificial effects of APPL2 siRNA on NSC differentiation, we applied two APPL2 siRNAs targeting different domains. Knockdown of APPL2 remarkably increased Tuj1⁺ and MAP2⁺ cells along with decreased GFAP⁺ cells (Fig. 2E–G, J). These results provided evidence supporting the role of APPL2 in regulating the fate choice of NSCs towards the glial direction.

APPL2 Overexpression Suppresses Neurogenesis but Elevates Gliogenesis in the Olfactory Bulb

To further confirm the roles of APPL2 in regulating neurogenesis and gliogenesis in the olfactory system, we conducted an immunofluorescence study of APPL2 Tg mice. The fluorescence intensity of doublecortin (DCX) was lower in the granule cell layer of the OB in the APPL2 Tg mice (Fig. 3A), suggesting a negative role of APPL2 in neuronal differentiation. We then injected BrdU daily for

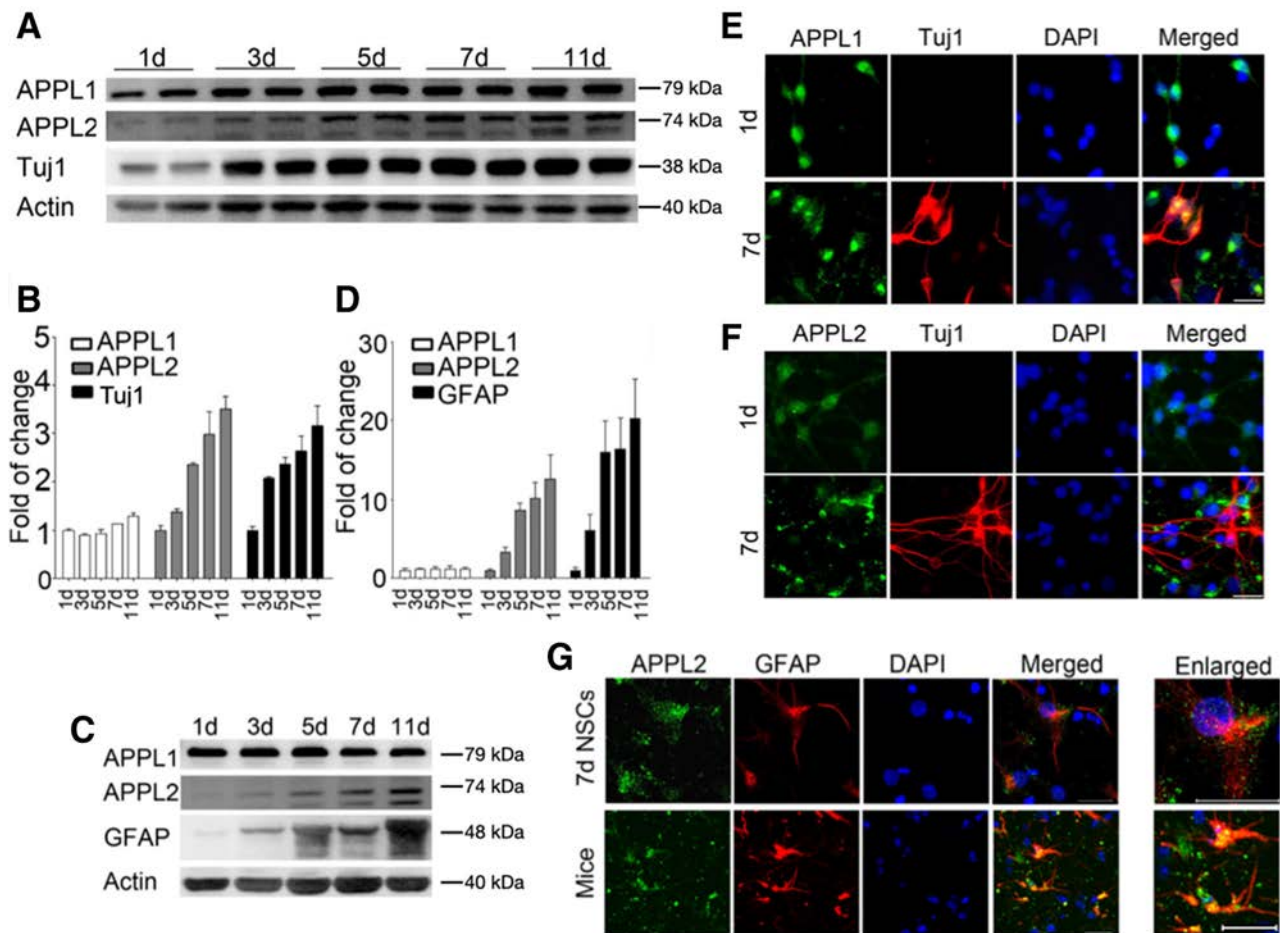


Fig. 1 APPL2 increases during NSC differentiation *in vitro*. **A** Representative western blots for APPL1, APPL2, and Tuj1 when NSCs are cultured for neuronal differentiation. **B** Quantitative analysis of the expression of APPL1, APPL2, and Tuj1. Data are presented as the mean \pm SEM, $n = 6$ per group. **C** Western blots of APPL1, APPL2, and GFAP when NSCs are cultured to induce astrocytic differentiation. **D** Quantitative analysis of the expression of APPL1, APPL2 and GFAP. Data are presented as the mean \pm SEM, $n = 6$ per group.

5 days to label actively proliferating cells. The APPL2 Tg mice displayed fewer BrdU⁺/DCX⁺ cells than WT mice, indicating reduced neural differentiation (Fig. 3B). BrdU was then injected daily for 3 days to examine the effects of APPL2 on the survival of newborn neurons, and the mice were sacrificed 11 days later. APPL2 Tg mice showed fewer BrdU⁺/NeuN⁺ cells than WT mice (Fig. 3C). Meanwhile, APPL2 Tg mice had a lower DCX fluorescence intensity and higher GFAP/Iba1 fluorescence in the OB region than WT mice, indicating reduced neurogenesis but enhanced gliogenesis in the APPL2 Tg mice (Fig. 3D). Consistent with this, APPL2 Tg mice showed fewer BrdU⁺/DCX⁺ co-stained cells in the SVZ (Fig. 3G). Western blot analysis also showed the APPL2 Tg mice established the increased expression of astrocytic and microglial markers GFAP and Iba1, indicating the

enhanced gliogenesis (Fig. 3E, F). Notably, APPL2 Tg mice had more GFAP⁺-staining cells around the SVZ, especially in the CC (Fig. 3H). Collectively, these results suggested that APPL2 participates in modulating fate choice to induce gliogenesis but inhibits neurogenesis in the olfactory system.

enhanced gliogenesis (Fig. 3E, F). Notably, APPL2 Tg mice had more GFAP⁺-staining cells around the SVZ, especially in the CC (Fig. 3H). Collectively, these results suggested that APPL2 participates in modulating fate choice to induce gliogenesis but inhibits neurogenesis in the olfactory system.

APPL2 Overexpression Decreases Neurogenesis but Elevates Gliogenesis along the Rostral Migratory Stream

To clarify the effects of APPL2 on the migration of NPCs along the RMS, we injected BrdU daily for 3 days and sacrificed the mice 11 days later. BrdU⁺-staining cells were labelled in the SVZ and distributed along the RMS (Fig. 4A–C). In APPL2 Tg mice, the BrdU⁺ staining was

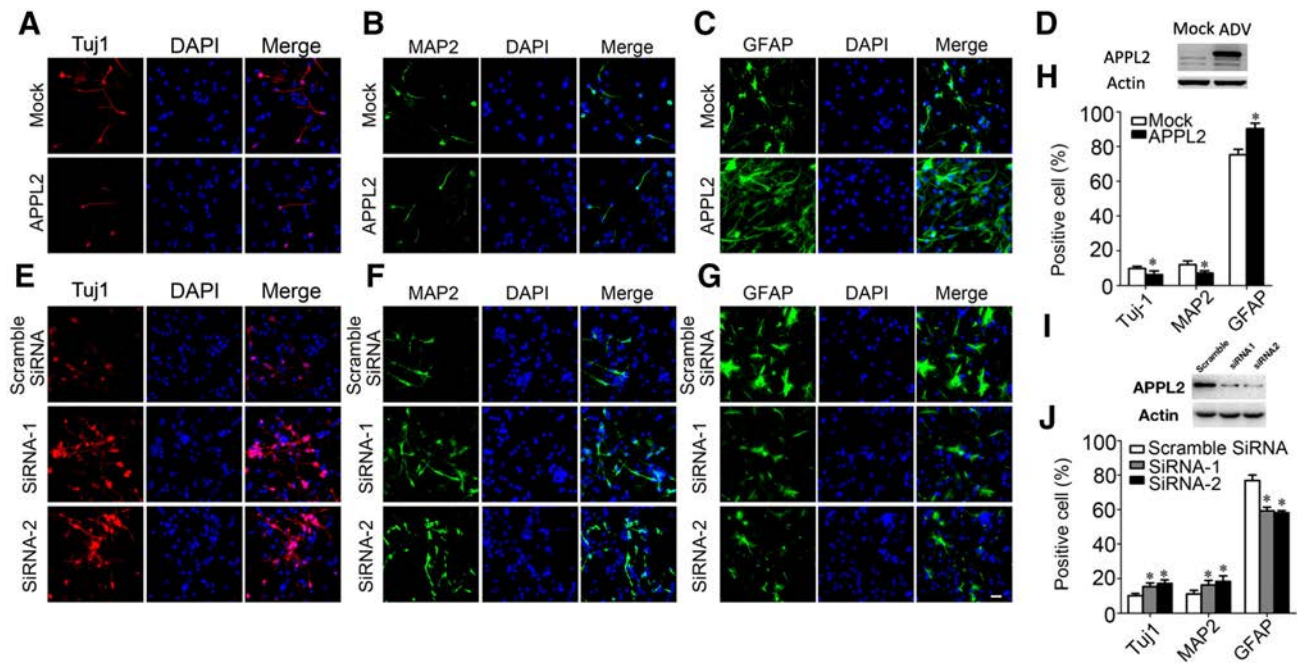


Fig. 2 APPL2 regulates cell-fate decision in NSC differentiation. **A–C** Images of immunofluorescence staining for Tuj1, MAP2, and GFAP in cells treated with adenovirus overexpressing luciferase (Mock) or APPL2 adenovirus. **D, I** Western blots showing the APPL2 levels in adenovirus- and siRNA-induced overexpression or

downregulation. **H** Statistics for experiments as in **A–C** ($*P < 0.05$ vs Mock). **E–G** Images as in **A–C**, but in cells treated with scrambled siRNA or two APPL2 siRNAs (scale bar, 20 μ m). **J** Statistics for experiments as in **E–G** ($*P < 0.05$, vs scrambled siRNA; $n = 6$ batches of culture per group).

decreased along the RMS and became sparse at its OB end (Fig. 4A, D). Quantitative analysis revealed a decreased distribution of BrdU⁺/DCX⁺ cells from the SVZ to the anterior RMS in the APPL2 Tg mice (Fig. 4E). We also detected GFAP⁺ signaling at the CC and RMS regions from the start and end points, respectively. Elevated gliogenesis was found along the RMS in the APPL2 Tg mice (Fig. 4B, E, F). Collectively, these results suggested that the overexpression of APPL2 reduces neuronal survival but promotes gliogenesis along the RMS.

APPL2 Tg Mice Display Impaired Odor Discrimination

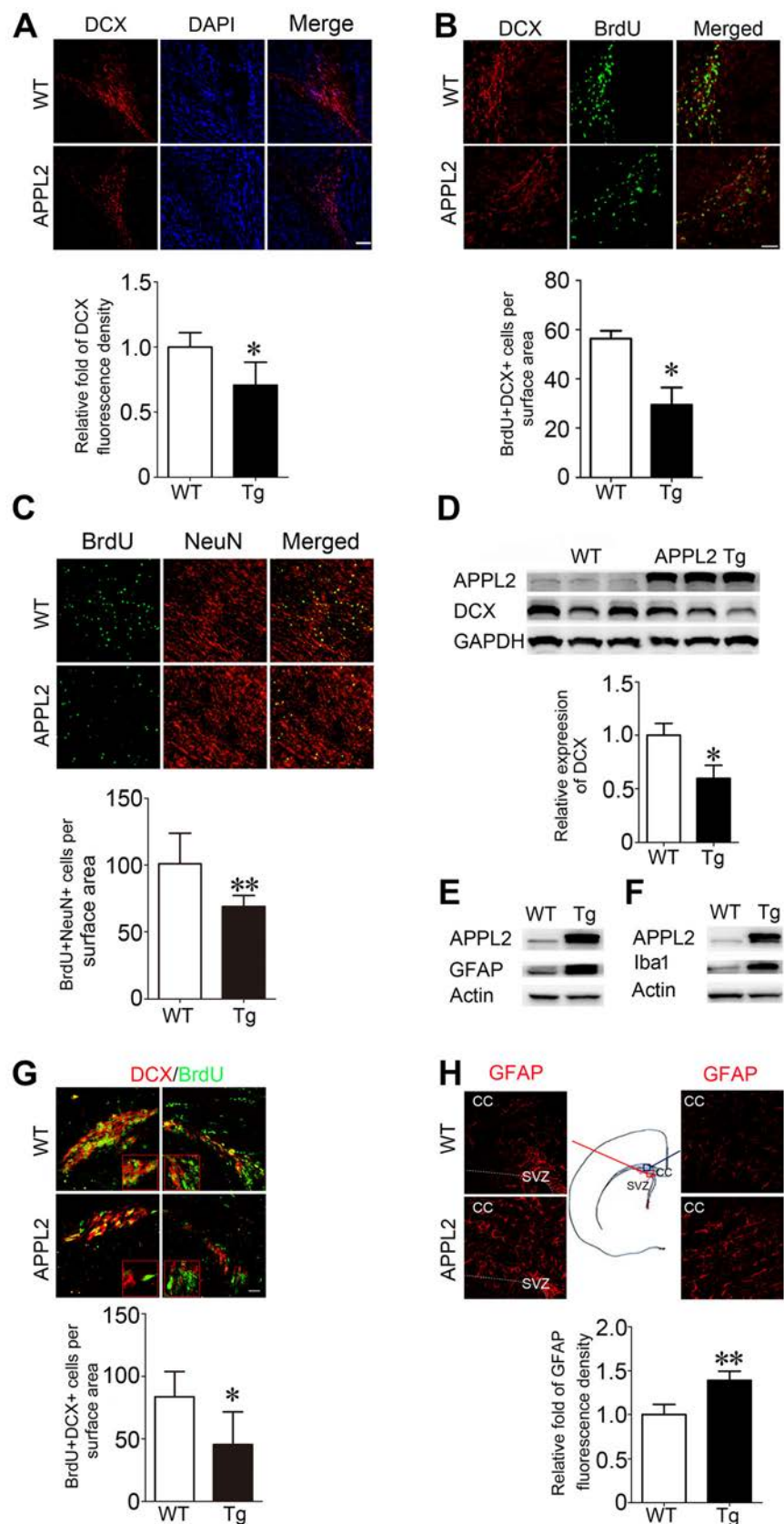
The renewal of integrated interneurons is important for maintaining normal olfactory functions. With decreased newborn neurons in the OB of APPL2 Tg mice (Figs. 3, 4), we conjectured that they might have impaired olfactory functions. To test this hypothesis, we compared performance in the ODT in APPL2 Tg mice and WT littermates. When presented with pentanol after 4 sessions of butanol exposure, the WT mice spent much more time sniffing the stick, indicating normal olfactory discrimination (Fig. 5). Interestingly, APPL2 Tg mice showed unchanged time sniffing the stick when butanol was replaced with pentanol, indicating impaired olfactory discrimination (Fig. 5A). The same results were obtained in the limonene + vs

limonene– tests (Fig. 5B). To exclude the potential influence of preferences for different odors on sniffing behavior, all odors were presented separately for a 2-min session, and the sniffing durations were similar in the APPL2 and WT mice (Fig. 5C, D). These results suggested that APPL2 overexpression remarkably impairs olfactory discrimination.

APPL2 Mediates Neurogenesis/gliogenesis by Interacting with Notch1

The Notch1 signaling pathway is important in regulating the fate choice of NSCs [40]; activated Notch signaling leads NSCs to differentiate to a glial fate commitment [41]. We then addressed the question whether Notch1 signaling contributes to the switching of neurogenesis to gliogenesis in the olfactory system of APPL2 Tg mice. To test this, we investigated the spatial correlation between APPL2 and Notch1 using the dSTORM super-resolution system. The results showed an apparent co-localization of APPL2 and Notch1 in cultured C17.2 NSCs (Fig. 6A, B). In addition, APPL2 Tg mice had significantly increased expression of Notch1 and its downstream NICD and Hes1 in the OB (Fig. 6C). Consistent with this, the knockdown of APPL2 suppressed NICD expression and reduced GFAP expression in the cultured NSCs (Fig. 6D). Suppression of APPL2 subsequently down-regulated the expression of

Fig. 3 APPL2 overexpression attenuates neurogenesis in the olfactory bulb. **A, B** Immunofluorescence images and statistics of DCX⁺/DAPI⁺ and DCX⁺/BrdU⁺ identifying newborn neurons in the granule cell layers of the OB in WT and APPL2 Tg mice. DAPI staining identifies nuclei and overall structure (scale bar, 20 μ m; * P < 0.05 vs WT). **C** Immunofluorescent images and statistics of BrdU⁺/NeuN⁺ identifying mature newborn neurons in the granule cell layers of the OB in WT mice and APPL2 Tg mice (data are presented as the mean \pm SEM; ** P < 0.01 vs WT group). **D** Western blots and analysis for protein expression of APPL2 and DCX in the OB of WT and APPL2 Tg mice (data are presented as the mean \pm SEM; * P < 0.05 vs WT group). **E, F** Western blots of protein expression of APPL2/GFAP and APPL2/Iba1 in the OB of WT and APPL2 Tg mice. **G** Immunofluorescence images and statistics of DCX⁺/BrdU⁺ identifying immature newborn neurons in the SVZ of WT and APPL2 Tg mice (data are presented as the mean \pm SEM; * P < 0.05 vs WT group; scale bar, 20 μ m). **H** Immunofluorescent images and statistics of GFAP⁺ staining in the SVZ and CC of WT and APPL2 Tg mice (dashed line, CC border; scale bar, 20 μ m; data are presented as the mean \pm SEM; ** P < 0.01 vs WT group; n = 6 animals per group).



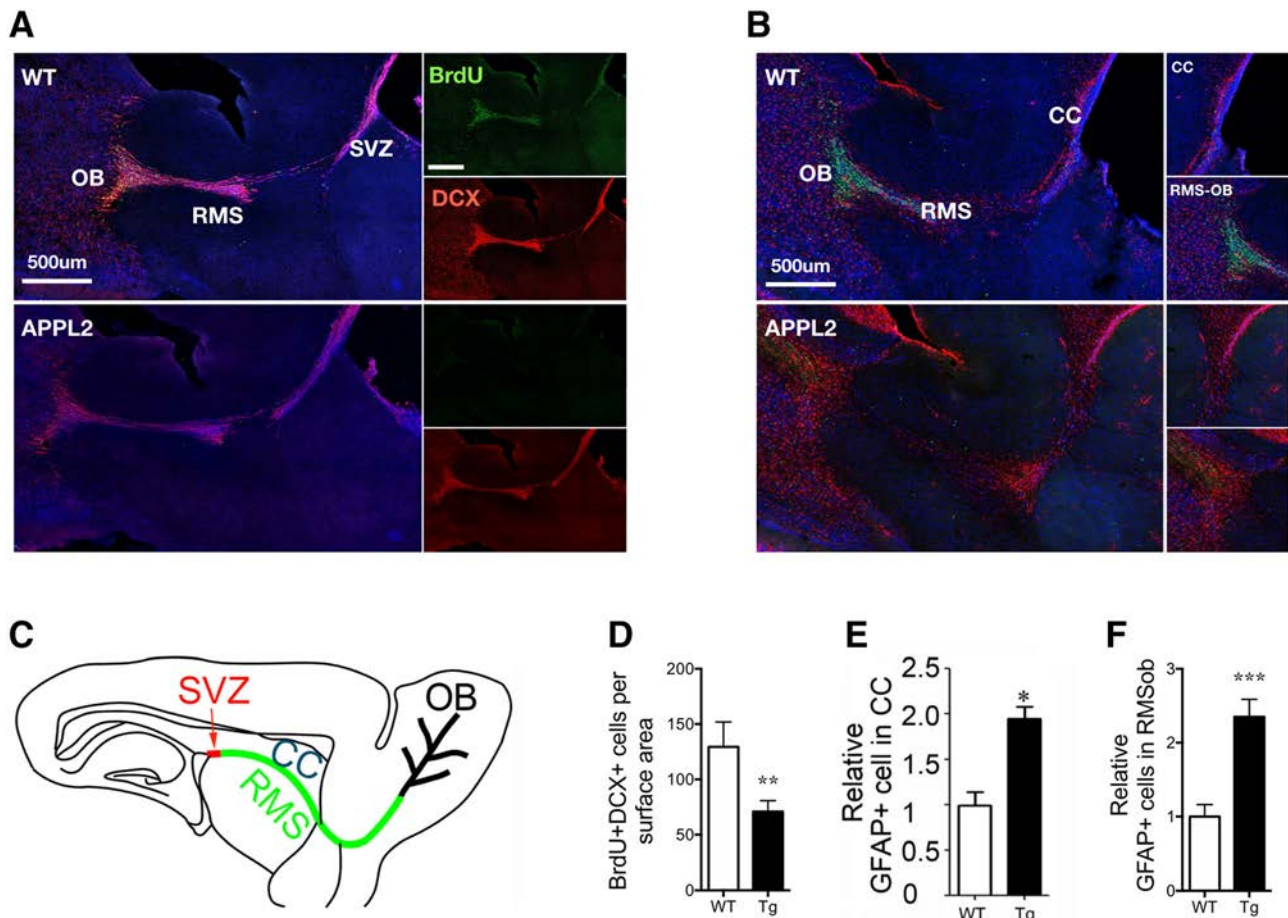


Fig. 4 APPL2 overexpression attenuates survival of progenitor cells in the rostral migratory stream. **A, B** Immunofluorescence images of DCX⁺/BrdU⁺ and GFAP⁺/BrdU⁺ identifying the lineage choice of newborn NSCs in the RMS of WT and APPL2 Tg mice. **C** Diagram of the anterior SVZ–RMS. **D** Cell density of BrdU⁺/DCX⁺ cells in the

APPL2 RMS (***P* < 0.01 vs WT group). **E, F** GFAP intensity in the CC and RMS-olfactory bulb (RMSob) regions of WT and APPL2 Tg mice (**P* < 0.05, ****P* < 0.001 vs WT group; *n* = 6 animals per group).

NICD and Hes1, downstream from Notch (Fig. 6E). To further confirm the causal relationship between APPL2 and Notch signaling, we treated APPL2 Tg mice with the Notch inhibitor DAPT and found that this significantly improved their olfactory discrimination (Fig. 6F). Taken together, Notch1 is a critical cellular signal linking the impaired APPL2-mediated olfactory neurogenesis and olfactory discrimination behavior.

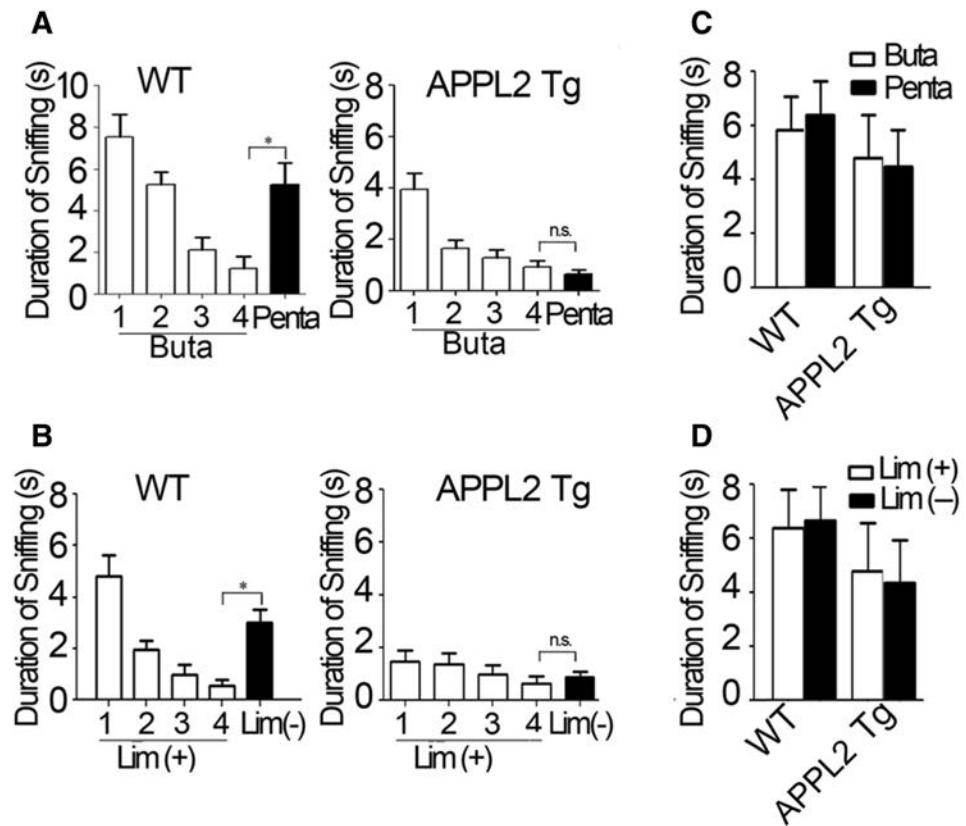
Discussion

The continuous generation of neurons provides structural plasticity in the olfactory system, and olfactory neurogenesis is rigorously modulated by multiple signaling systems [42–44]. Our previous studies showed that APPL2 serves as a negative regulator of adult neurogenesis in the hippocampus and olfactory system, contributing to depressive behaviors [38, 45]. In the current study, we found that

APPL2 regulates the cell-fate choice of NSCs with reduced neurogenic and increased glial formation in the OB, leading to impaired olfactory discrimination. By interacting with Notch1, APPL2 mediates the gliogenic switching of olfactory NSCs and olfactory behaviors.

APPL2 is an isoform with 54% identity in sequence and co-localizes with APPL1 [32]. APPL1 participates in metabolic regulation [33–35] and mediates cell survival in vertebrate development [46]. Our previous study revealed that APPL2 is expressed in nestin⁺ NSCs in the hippocampus [38]. In the current study, we found unchanged APPL1 expression in NSC differentiation but a gradual increase in APPL2 with culture time, accompanied by increased Tuj1⁺ and GFAP⁺ populations (Fig. 1). Although APPL2 and Tuj1 simultaneously increased in cultured NSCs (Fig. 1A), only the GFAP⁺ astrocytic population occurred with APPL2⁺ staining in both NSCs at day 7 and brain tissue of WT mice (Fig. 1F, G). Given its ubiquitous expression in GFAP⁺ cells rather than Tuj1⁺

Fig. 5 APPL2 Tg mice are deficient in the discrimination of odor in a cotton stick presentation-based task. **A** Duration of sniffing in 10-week-old mice exposed to 4 sessions of butanol (Buta) followed by pentanol (Penta) ($*P < 0.05$). **B** Duration of sniffing in mice exposed to 4 sessions of limonene [Lim(+)] followed by mineral oil [Lim(-)] (data presented as the mean \pm SEM; $*P < 0.05$). **C**, **D** Durations of sniffing showing no preference for the odors presented in the experiments. $n = 10$ animals per group.



cells, APPL2 may be a player in gliogenesis. The presence of APPL2 in differentiated NSCs or progenitor cells could specifically promote gliogenesis.

We then conducted the siRNA and adenovirus transfer experiments to overexpress and knock down APPL2, respectively, and used WT and APPL Tg mice to further confirm the roles of APPL2 in the modulation of gliogenesis and the cell-fate decision for lineage commitment. In the cultured NSCs, APPL2 overexpression decreased the Tuj1⁺ and MAP2⁺ neuronal cells but increased the GFAP⁺ astrocytes (Fig. 2A–D). In contrast, APPL2 knockdown remarkably increased the Tuj1⁺ and MAP2⁺ cells but decreased the GFAP⁺ cells (Fig. 2E–H). Consistent with this, APPL2 Tg mice had fewer BrdU⁺/DCX⁺ and BrdU⁺/NeuN⁺ cells but more GFAP⁺ cells in both the OB and SVZ than WT mice. The BrdU⁺/DCX⁺ and BrdU⁺/NeuN⁺ staining marked newly-generated immature and mature neurons, respectively. With these *in vitro* and *in vivo* experiments, we demonstrated that APPL2 functions to modulate fate choice by inducing gliogenesis but inhibiting neurogenesis in the olfactory system (Figs. 3, 4). Similarly, our recent study revealed that APPL2 Tg mice have elevated gliogenesis and suppressed neurogenesis in the hippocampus [38]. Normally, neuronal stem/progenitor cells migrating along the lateral ventricle give rise to different lineages [19, 47]. These NSCs enter into rapid

proliferation to generate neuroblasts (type-A cells) that migrate along the RMS towards the OB and differentiate into interneurons [19, 47]. Here, we found that APPL2 Tg mice had decreased neurogenesis in the OB and SVZ (Fig. 3). Along the RMS, overexpressed APPL2 suppressed neuronal generation but elevated astrocyte production (Fig. 4). Individual neuroblasts in the OB migrate radially to the outer layer and differentiate into olfactory interneurons, granule cells, or periglomerular cells that integrate into the olfactory neuronal network [48]. These newly-generated neurons determine the capacity for olfactory discrimination [49]. As expected, the APPL2 Tg mice showed impaired olfactory discrimination under normal conditions (Fig. 5). Our previous study suggested roles of APPL2 in impaired olfactory sensitivity in an animal model of depression [37]. Here, we further addressed how APPL2 regulated olfactory neurogenesis and olfactory functions at the physiological level. Thus, we can draw the conclusion that APPL2 is an important factor in inhibiting olfactory functions and determines olfactory memory and discrimination.

The strength of neurogenesis is orchestrated by a combination of intrinsic genetic programs and environmental niches [47, 50, 51]. The Notch signaling pathway is now widely recognized as a critical mechanism that determines the fate choice of NSCs at an early stage

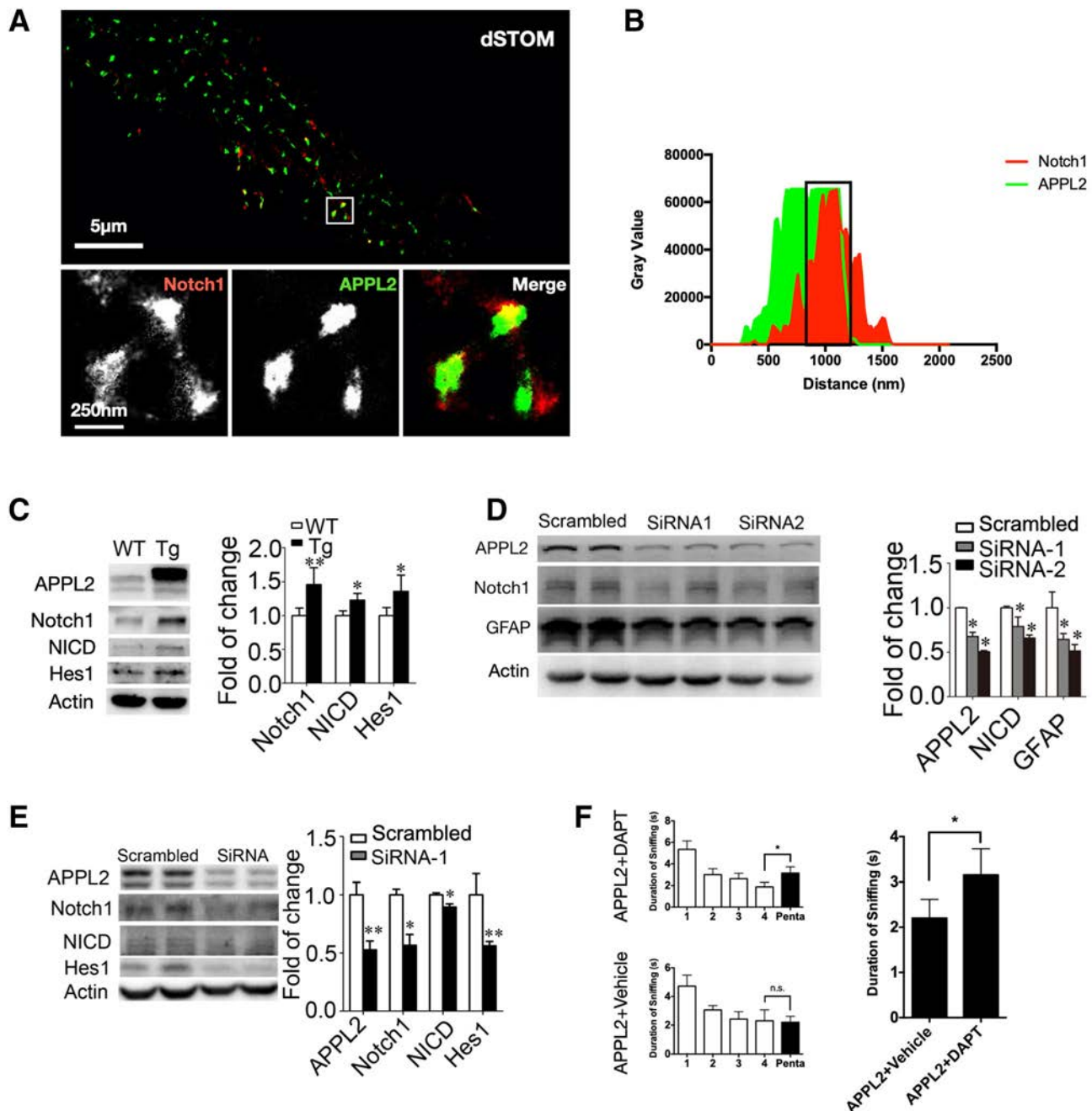


Fig. 6 APPL2 modulates the Notch signaling pathway. **A** Reconstructed dSTORM images showing co-localization of Notch1 and APPL2 in C17.2 cells (100 × oil immersion lens). **B** Spot intensity analysis of the selected region (intensity of the two channels show the same distribution with distance and intensity). **C** Western blots and analysis of targeted proteins Notch1, NICD, and Hes1 in the OB of APPL2 Tg and WT mice ($*P < 0.05$ vs WT group). **D** APPL2 siRNA

decreases NICD and GFAP expression in primary cultured NSCs ($*P < 0.05$ vs scrambled siRNA group). **E** Decreased Notch1, NICD, and Hes1 induced by down-regulated APPL2 ($**P < 0.01$, $*P < 0.05$ vs scrambled siRNA group). **F** Effects of Notch inhibitor DAPT on olfactory function in APPL2 Tg mice ($*P < 0.05$ vs APPL2 Tg vehicle; $n = 6$ animals or batches of culture per group).

[19, 52–55]. This pathway promotes the switching of NSCs to gliogenic differentiation [56]. Notch1 cKOKIn mice display reduced olfactory aversion to propionic acid and Notch1 is involved in olfactory processing and affects olfactory behavior [25]. These lines of evidence indicate

critical roles of Notch signaling in regulating olfactory neurogenesis and olfactory behaviors. By regulating downstream Hes1/5, molecules like Tis21 act as essential regulators of olfactory neurogenesis and olfactory behaviors [57]. Consistent with this finding, our study suggests

that APPL2 performs as a regulator of the fate choice of NSCs by inducing gliogenesis but inhibiting neurogenesis *via* interaction with Notch1, subsequently affecting olfactory functions and olfactory discrimination.

In conclusion, we uncover APPL2 as a novel cell lineage regulator for adult neurogenesis. By interacting with Notch1, APPL2 can affect neurogenesis in the adult SVZ-OB system and subsequently regulate olfactory behaviors, and APPL2 may be a new therapeutic target to regulate olfactory behaviors and promote neural regeneration.

Acknowledgements This work was supported by Areas of Excellence (AoE/P-705/16) and the General Research Fund, Hong Kong SAR (GRF No. 777313 M). We greatly appreciate the support of the Faculty Core Facility, LKS Faculty of Medicine in The University of Hong Kong for providing technological help with confocal microscopy, dSTORM, and image data analysis.

Conflict of interest The authors have no conflict interest.

References

- Devanand DP, Michaels-Marston KS, Liu X, Pelton GH, Padilla M, Marder K, *et al.* Olfactory deficits in patients with mild cognitive impairment predict alzheimer's disease at follow-up. *Am J Psychiatry* 2000, 157: 1399–1405.
- Chen B, Zhong X, Mai N, Peng Q, Zhang M, Chen X, *et al.* Interactive effect of depression and cognitive impairment on olfactory identification in elderly people. *J Alzheimers Dis* 2018, 66: 1645–1655.
- Doty RL, Yousef DM, Pham LT, Kreshak AA, Geckle R, Lee WW. Olfactory dysfunction in patients with head trauma. *Arch Neurol* 1997, 54: 1131–1140.
- Yuan TF, Slotnick BM. Roles of olfactory system dysfunction in depression. *Prog Neuropsychopharmacol Biol Psychiatry* 2014, 54: 26–30.
- Ming GL, Song H. Adult neurogenesis in the mammalian central nervous system. *Annu Rev Neurosci* 2005, 28: 223–250.
- Taupin P. Adult neurogenesis in the mammalian central nervous system: functionality and potential clinical interest. *Med Sci Monit* 2005, 11: RA247–252.
- Breton-Provencher V, Lemasson M, Peralta MR, 3rd, Saghatel-yan A. Interneurons produced in adulthood are required for the normal functioning of the olfactory bulb network and for the execution of selected olfactory behaviors. *J Neurosci* 2009, 29: 15245–15257.
- Sultan S, Mandairon N, Kermen F, Garcia S, Sacquet J, Didier A. Learning-dependent neurogenesis in the olfactory bulb determines long-term olfactory memory. *FASEB J* 2010, 24: 2355–2363.
- Gheusi G, Lledo PM. Adult neurogenesis in the olfactory system shapes odor memory and perception. *Prog Brain Res* 2014, 208: 157–175.
- Young KM, Fogarty M, Kessar N, Richardson WD. Subventricular zone stem cells are heterogeneous with respect to their embryonic origins and neurogenic fates in the adult olfactory bulb. *J Neurosci* 2007, 27: 8286–8296.
- Crews L, Mizuno H, Desplats P, Rockenstein E, Adame A, Patrick C, *et al.* Alpha-synuclein alters notch-1 expression and neurogenesis in mouse embryonic stem cells and in the hippocampus of transgenic mice. *J Neurosci* 2008, 28: 4250–4260.
- Siopi E, Denizet M, Gabellec MM, de Chaumont F, Olivo-Marín JC, Guilloux JP, *et al.* Anxiety- and depression-like states lead to pronounced olfactory deficits and impaired adult neurogenesis in mice. *J Neurosci* 2016, 36: 518–531.
- Horgusluoglu E, Nudelman K, Nho K, Saykin AJ. Adult neurogenesis and neurodegenerative diseases: a systems biology perspective. *Am J Med Genet B Neuropsychiatr Genet* 2017, 174: 93–112.
- Engler A, Rolando C, Giachino C, Saotome I, Erni A, Brien C, *et al.* Notch2 signaling maintains nsc quiescence in the murine ventricular-subventricular zone. *Cell Rep* 2018, 22: 992–1002.
- Fricke IB, Viel T, Worlitzer MM, Collmann FM, Vrachimis A, Faust A, *et al.* 6-hydroxydopamine-induced parkinson's disease-like degeneration generates acute microgliosis and astrogliosis in the nigrostriatal system but no bioluminescence imaging-detectable alteration in adult neurogenesis. *Eur J Neurosci* 2016, 43: 1352–1365.
- Marin C, Vilas D, Langdon C, Alobid I, Lopez-Chacon M, Haehner A, *et al.* Olfactory dysfunction in neurodegenerative diseases. *Curr Allergy Asthma Rep* 2018, 18: 42.
- De la Rosa-Prieto C, Saiz-Sanchez D, Ubeda-Banon I, Flores-Cuadrado A, Martinez-Marcos A. Neurogenesis, neurodegeneration, interneuron vulnerability, and amyloid-beta in the olfactory bulb of app/ps1 mouse model of alzheimer's disease. *Front Neurosci* 2016, 10: 227.
- Hsieh YW, Alqadah A, Chuang CF. Mechanisms controlling diversification of olfactory sensory neuron classes. *Cell Mol Life Sci* 2017, 74: 3263–3274.
- Imayoshi I, Kageyama R. The role of notch signaling in adult neurogenesis. *Mol Neurobiol* 2011, 44: 7–12.
- Lewis J. Notch signalling and the control of cell fate choices in vertebrates. *Semin Cell Dev Biol* 1998, 9: 583–589.
- Muskavitch MA. Delta-notch signaling and drosophila cell fate choice. *Dev Biol* 1994, 166: 415–430.
- Morrison SJ, Perez SE, Qiao Z, Verdi JM, Hicks C, Weinmaster G, *et al.* Transient notch activation initiates an irreversible switch from neurogenesis to gliogenesis by neural crest stem cells. *Cell* 2000, 101: 499–510.
- Dai Q, Duan C, Ren W, Li F, Zheng Q, Wang L, *et al.* Notch signaling regulates lgr5(+) olfactory epithelium progenitor/stem cell turnover and mediates recovery of lesioned olfactory epithelium in mouse model. *Stem Cells* 2018, 36: 1259–1272.
- Kidd S, Struhl G, Lieber T. Notch is required in adult drosophila sensory neurons for morphological and functional plasticity of the olfactory circuit. *PLoS Genet* 2015, 11: e1005244.
- Brai E, Marathe S, Zentilin L, Giacca M, Nimpf J, Kretz R, *et al.* Notch1 activity in the olfactory bulb is odour-dependent and contributes to olfactory behaviour. *Eur J Neurosci* 2014, 40: 3436–3449.
- Liu Z, Xiao T, Peng X, Li G, Hu F. App1s: More than just adiponectin receptor binding proteins. *Cell Signal* 2017, 32: 76–84.
- Mao X, Kikani CK, Riojas RA, Langlais P, Wang L, Ramos FJ, *et al.* App1 binds to adiponectin receptors and mediates adiponectin signalling and function. *Nat Cell Biol* 2006, 8: 516–523.
- Cheng KK, Lam KS, Wang Y, Huang Y, Carling D, Wu D, *et al.* Adiponectin-induced endothelial nitric oxide synthase activation and nitric oxide production are mediated by app1 in endothelial cells. *Diabetes* 2007, 56: 1387–1394.
- Wang C, Li X, Mu K, Li L, Wang S, Zhu Y, *et al.* Deficiency of app1 in mice impairs glucose-stimulated insulin secretion through inhibition of pancreatic beta cell mitochondrial function. *Diabetologia* 2013, 56: 1999–2009.
- Tan Y, Xin X, Coffey FJ, Wiest DL, Dong LQ, Testa JR. App1 and app2 are expendable for mouse development but are

- essential for hgf-induced akt activation and migration in mouse embryonic fibroblasts. *J Cell Physiol* 2016, 231: 1142–1150.
31. Hennig J, McShane MP, Cordes N, Eke I. Appl proteins modulate DNA repair and radiation survival of pancreatic carcinoma cells by regulating atm. *Cell Death Dis* 2014, 5: e1199.
 32. Miaczynska M, Christoforidis S, Giner A, Shevchenko A, Uttenweiler-Joseph S, Habermann B, *et al.* Appl proteins link rab5 to nuclear signal transduction *via* an endosomal compartment. *Cell* 2004, 116: 445–456.
 33. Cheng KK, Iglesias MA, Lam KS, Wang Y, Sweeney G, Zhu W, *et al.* Appl1 potentiates insulin-mediated inhibition of hepatic glucose production and alleviates diabetes *via* akt activation in mice. *Cell Metab* 2009, 9: 417–427.
 34. Cheng KK, Lam KS, Wu D, Wang Y, Sweeney G, Hoo RL, *et al.* Appl1 potentiates insulin secretion in pancreatic beta cells by enhancing protein kinase akt-dependent expression of snare proteins in mice. *Proc Natl Acad Sci U S A* 2012, 109: 8919–8924.
 35. Deepa SS, Dong LQ. Appl1: Role in adiponectin signaling and beyond. *Am J Physiol Endocrinol Metab* 2009, 296: E22–36.
 36. Cheng KK, Zhu W, Chen B, Wang Y, Wu D, Sweeney G, *et al.* The adaptor protein appl2 inhibits insulin-stimulated glucose uptake by interacting with tbc1d1 in skeletal muscle. *Diabetes* 2014, 63: 3748–3758.
 37. Gao C, Du Q, Li W, Deng R, Wang Q, Xu A, *et al.* Baicalin modulates appl2/glucocorticoid receptor signaling cascade, promotes neurogenesis, and attenuates emotional and olfactory dysfunctions in chronic corticosterone-induced depression. *Mol Neurobiol* 2018, 55: 9334–9348.
 38. Gao C, Chen X, Xu A, Cheng K, Shen J. Adaptor protein appl2 affects adult antidepressant behaviors and hippocampal neurogenesis *via* regulating the sensitivity of glucocorticoid receptor. *Mol Neurobiol* 2018, 55: 5537–5547.
 39. Rietze RL, Reynolds BA. Neural stem cell isolation and characterization. *Methods Enzymol* 2006, 419: 3–23.
 40. Zhang R, Engler A, Taylor V. Notch: an interactive player in neurogenesis and disease. *Cell Tissue Res* 2018, 371: 73–89.
 41. Pierfelice T, Alberi L, Gaiano N. Notch in the vertebrate nervous system: an old dog with new tricks. *Neuron* 2011, 69: 840–855.
 42. Suh H, Deng W, Gage FH. Signaling in adult neurogenesis. *Annu Rev Cell Dev Biol* 2009, 25: 253–275.
 43. Zhao C, Deng W, Gage FH. Mechanisms and functional implications of adult neurogenesis. *Cell* 2008, 132: 645–660.
 44. Canastar A, Maxson SC, Bishop CE. Aggressive and mating behaviors in two types of sex reversed mice: xy females and xx males. *Arch Sex Behav* 2008, 37: 2–8.
 45. Gao C, Du Q, Li W, Deng R, Wang Q, Xu A, *et al.* Baicalin modulates appl2/glucocorticoid receptor signaling cascade, promotes neurogenesis, and attenuates emotional and olfactory dysfunctions in chronic corticosterone-induced depression. *Mol Neurobiol* 2018, 55: 9334–9348.
 46. Schenck A, Goto-Silva L, Collinet C, Rhinn M, Giner A, Habermann B, *et al.* The endosomal protein appl1 mediates akt substrate specificity and cell survival in vertebrate development. *Cell* 2008, 133: 486–497.
 47. Hsieh J. Orchestrating transcriptional control of adult neurogenesis. *Genes Dev* 2012, 26: 1010–1021.
 48. Kaneko N, Sawada M, Sawamoto K. Mechanisms of neuronal migration in the adult brain. *J Neurochem* 2017, 141: 835–847.
 49. Liu YH, Lai WS, Tsay HJ, Wang TW, Yu JY. Effects of maternal immune activation on adult neurogenesis in the subventricular zone-olfactory bulb pathway and olfactory discrimination. *Schizophr Res* 2013, 151: 1–11.
 50. Gage FH. Neurogenesis in the adult brain. *J Neurosci* 2002, 22: 612–613.
 51. Goritz C, Frisen J. Neural stem cells and neurogenesis in the adult. *Cell Stem Cell* 2012, 10: 657–659.
 52. Kageyama R, Ohtsuka T, Shimojo H, Imayoshi I. Dynamic notch signaling in neural progenitor cells and a revised view of lateral inhibition. *Nat Neurosci* 2008, 11: 1247–1251.
 53. Kuhn HG, Cooper-Kuhn C, Eriksson P, Nilsson M. Signals regulating neurogenesis in the adult olfactory bulb. *Chem Senses* 2005, 30 Suppl 1: i109–110.
 54. Imayoshi I, Sakamoto M, Yamaguchi M, Mori K, Kageyama R. Essential roles of notch signaling in maintenance of neural stem cells in developing and adult brains. *J Neurosci* 2010, 30: 3489–3498.
 55. Aguirre A, Rubio ME, Gallo V. Notch and egfr pathway interaction regulates neural stem cell number and self-renewal. *Nature* 2010, 467: 323–327.
 56. Li Y, Lau WM, So KF, Tong Y, Shen J. Caveolin-1 promote astroglial differentiation of neural stem/progenitor cells through modulating notch1/nicd and hes1 expressions. *Biochem Biophys Res Commun* 2011, 407: 517–524.
 57. Farioli-Vecchioli S, Ceccarelli M, Saraulli D, Micheli L, Cannas S, D'Alessandro F, *et al.* Tis21 is required for adult neurogenesis in the subventricular zone and for olfactory behavior regulating cyclins, bmp4, hes1/5 and ids. *Front Cell Neurosci* 2014, 8: 98.



Changes of Effective Connectivity in the Alpha Band Characterize Differential Processing of Audiovisual Information in Cross-Modal Selective Attention

Weikun Niu^{1,2,4} · Yuying Jiang^{1,2,4} · Xin Zhang^{1,2} · Tianzi Jiang^{1,2,3,4} · Yujin Zhang^{1,2} · Shan Yu^{1,2,3,4}

Received: 30 October 2019 / Accepted: 6 January 2020 / Published online: 26 July 2020
© Shanghai Institutes for Biological Sciences, CAS 2020

Abstract Cross-modal selective attention enhances the processing of sensory inputs that are most relevant to the task at hand. Such differential processing could be mediated by a swift network reconfiguration on the macroscopic level, but this remains a poorly understood process. To tackle this issue, we used a behavioral paradigm to introduce a shift of selective attention between the visual and auditory domains, and recorded scalp electroencephalographic signals from eight healthy participants. The changes in effective connectivity caused by the cross-modal attentional shift were delineated by analyzing spectral Granger Causality (GC), a metric of frequency-specific effective connectivity. Using data-driven methods of pattern-classification and feature-analysis, we found that a change in the α band (12 Hz–15 Hz) of GC is a stable feature across different individuals that can be used to decode the attentional shift. Specifically, auditory attention induces more pronounced information flow in the α band, especially

from the parietal–occipital areas to the temporal–parietal areas, compared to the case of visual attention, reflecting a reconfiguration of interaction in the macroscopic brain network accompanying different processing. Our results support the role of α oscillation in organizing the information flow across spatially-separated brain areas and, thereby, mediating cross-modal selective attention.

Keywords Human EEG · Audiovisual selective attention · Granger Causality · Pattern classification

Introduction

Humans are endowed with the ability to selectively attend to specific visual or auditory stimuli when faced with audiovisual information [1, 2]. This is a reflection of the more general ability of cross-modal attention, which is vital to flexibly choose the information that is most relevant to the task at hand. Understanding the neural mechanisms underlying such cross-modal attention is an active field in systems neuroscience. On one side, functional imaging studies have elucidated the specific roles of certain brain areas by recording the activation variance reflected in the blood oxygen level-dependent signals during a cross-modal attentional shift. For instance, the posterior parietal and prefrontal cortices serve as essential areas in controlling audiovisual selective attention, accompanying the interaction between the visual and auditory cortices [3–6]. On the other side, at the electrophysiological level, plentiful research has agreed on the entrainment mechanism as the underpinning of an audiovisual attentional transition [7–10]. That is, oscillations at certain frequencies are evoked in the brain corresponding to the temporal structure of the rhythmic stimulus to which the participant is

Weikun Niu and Yuying Jiang contributed equally to this work.

✉ Yujin Zhang
yujin.zhang@nlpr.ia.ac.cn

✉ Shan Yu
shan.yu@nlpr.ia.ac.cn

¹ Brainnetome Center, Institute of Automation, Chinese Academy of Sciences, Beijing 100190, China

² National Laboratory of Pattern Recognition, Institute of Automation, Chinese Academy of Sciences, Beijing 100190, China

³ Center for Excellence in Brain Science and Intelligence Technology, Chinese Academy of Sciences, Beijing 100190, China

⁴ University of Chinese Academy of Sciences, Beijing 100049, China

attending. Specifically, the frequency and phase of ongoing oscillations in primary sensory cortices are entrained by the corresponding external rhythmic stimuli, reflected in phase-reset [9, 11, 12] and cross-frequency interactions [13–15].

The above studies have provided insights into both the key brain areas involved in audiovisual selective attention and the mechanisms by which the attended stimuli modulate the activity of specific areas more effectively. However, high-level cognitive tasks such as attention often require sophisticated interactions among spatially-separated brain areas to perform collective information processing [16, 17]. Thus, an important aspect of understanding cross-modal selective attention is to reveal how the interactions among different brain areas are flexibly reconfigured during a shift of attention to support different information processing. Unfortunately, so far little is known regarding such an attention-dependent reorganization of area–area interactions.

To address this issue, here we recorded EEG signals in participants during the execution of an audiovisual selective attention (ASA) task. Spectral Granger Causality (GC) analysis was applied to delineate the frequency-specific interaction structure of the macroscopic network. With pattern classification techniques including feature-rating and feature-selection, we applied a data-driven approach to unravel the changes in network interaction structure accompanying a cross-modal attentional transition.

Materials and Methods

Participants and Recording

Four male and four female graduate students aged 21 years–30 years (mean, 25 years) at the Institute of Automation, Chinese Academy of Sciences (CASIA) participated in this experiment. They all had normal or corrected-to-normal vision and normal audition. Each participant provided informed written consent after the experimental paradigm was explained. The study was approved by the Ethics Committee of CASIA.

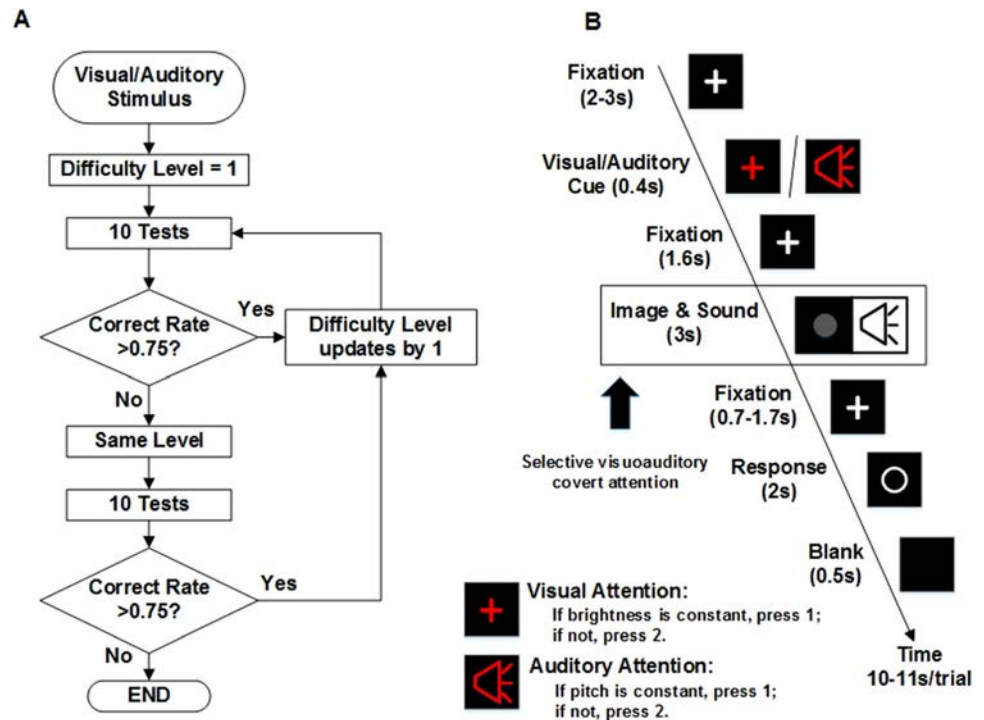
EEG signals were recorded by the Brain Vision system (Brain Products Ltd., Munich, Germany) with a 64-electrode cap (Easycap GmbH, Herrsching, Germany) at a sampling rate of 1024 Hz. An electro-oculographic (EOG) electrode was placed ~ 2 cm below the left eye to record blink artifacts. In addition, eye movements were monitored by an eye tracker (ETL-200, Iscan Inc., Woburn, MA, USA) at a 240 Hz sampling rate to ensure that during the presentation of visual stimuli, the participants' eyes were open and looking at the stimulus. The visual stimuli were presented on a 21.7-inch LED monitor (resolution

1920 \times 1080), placed 60 cm away from the participant's eyes. The auditory stimuli were delivered by headphones. Stimulus presentation was coordinated by E-Prime 2.0 software (Psychology Software Tools, Inc., Sharpsburg, PA, USA).

Experimental Design

Our experiments consisted of a pre-experiment phase (Fig. 1A) and a formal testing phase (Fig. 1B). Since each participant had different sensitivity to visual and auditory stimuli, we conducted a pre-experiment with each participant before the formal test to select the appropriate visual/auditory stimulation for him/her, making the difficulty of the behavioral task comparable across participants by controlling the response accuracy at $\sim 75\%$. Specifically, the pre-experiment contained two parts, one visual and one auditory. In the visual pre-experiment, following a fixation period of 2 s–3 s (with a white “+” at the center of the black screen), a 3-s video clip was displayed at the center of the screen, showing a disc with a radius of 3 cm and its brightness could change (increase or decrease) or remain constant with the same probability during the presentation. Following the clip, the fixation marker “+” re-appeared for 0.7 s–1.7 s, and then a small white ring appeared on the screen for 2 s. During this 2-s period, participants were asked to press the “1” or “2” button on the keyboard to signal whether or not the brightness of the disc changed during the 3-s video clip. There were several progressive sessions. As shown in Fig. 1A, at the beginning, individuals participated in a session with 10 trials at the easiest level: the range of brightness change was 5%, which was readily detectable by all participants. After this session, if the correct rate was >0.75 , the difficulty of the next session was increased by reducing the range of brightness change (from 5% to 4%, 3%, 2%, 1.2%, 0.6%, and 0.3% in sequence). If not, a session at the current difficulty level was repeated once. If the averaged correct rate of two successive sessions was >0.75 , the difficulty of the next session was increased. These procedures were repeated iteratively until the eventual correct rate was just below 0.75. The highest level of difficulty with a correct rate >0.75 was then set as the participant-specific level of the visual stimuli in the subsequent formal experiment. The initial brightness of the disc was randomly set to 43%–60%. In the auditory pre-experiment, participants looked at the fixation marker “+” at the center of the screen and paid attention to a tone clip presented through headphones. The duration of the tone clip was 3 s with a random initial frequency between 400 Hz and 600 Hz, with an equal probability of changing (increase or decrease) or staying at the same frequency. Similar to the visual pre-experiment, after a blank period of 0.7 s–1.7 s, a small white ring

Fig. 1 Experimental paradigm. **A** Pre-experiment. **B** Formal test.



appeared on the screen for 2 s and the participants were asked to press the “1” or “2” button to signal whether or not the pitch of the presented tone clip changed (rising or falling). Following the same procedure as in the visual pre-experiment, several progressive sessions (the range of frequency change started from 60 Hz to 40 Hz, 20 Hz, and 10 Hz in sequence) were conducted to identify the participant-specific level of auditory stimuli (i.e. the highest difficulty tested with a correct rate >0.75) for the subsequent formal experiment.

In the formal test (Fig. 1B), the participants were first asked to fixate on the white “+” at the center of the black screen for 2 s–3 s. Then with equal probability, the “+” changed to color to indicate a visual trial or remained white but was accompanied by a brief tone to indicate an auditory trial, dictating which modality of stimuli should be attended to later. Then a 3-s video clip (a gray disc with changing or constant brightness) was displayed and concurrently a 3-s audio clip (a tone with changing or constant pitch) was delivered *via* headphones. After a blank period (a fixation “+” appeared on the screen) of 0.7 s–1.7 s, a small white ring appeared on the screen for 2 s and the participants were asked to press the “1” or “2” button to signal whether or not the stimulus in the attended domain (according to the cue at the beginning of the trial) changed brightness or pitch. In the formal experiment, there were three sessions, with a 5-min break between, and each session consisted of 100 trials. The number of correct trials for each subject (S) was as follows (V, visual trials; A, auditory trials): S1 (V 120, A 139); S2 (V 115, A 85); S3

(V 115, A 125); S4 (V 112, A 132); S5 (V 142, A 113); S6 (V 123, A 124); S7 (V 110, A 105); S8 (V 145, A 113). In total, we obtained 982 visual trials and 936 auditory trials. The overall correct rate of all participants was ~ 0.81 .

Data Pre-processing

The raw EEG data were pre-processed using BrainVision Analyzer 2.0 (Brain Products Ltd). The steps included re-referencing by the average of all electrodes, down-sampling the raw data to 1000 Hz, band-pass filtering at 1 Hz–100 Hz, notch-filtering at ~ 50 Hz, and independent component analysis to exclude artifacts from eye-movements and heartbeats. To focus on the transition of ASA states, we extracted all the trials with a correct response from the pre-processed EEG data of 63 channels (excluding the EOG electrode) and concentrated on the data from 1 to 3 s following the stimulus onset to exclude the stimulus-evoked potentials (Fig. 2A).

Granger Causality

The data processing pipeline is depicted in Fig. 2B. The first step was to calculate the GC. For the GC analysis, we further down-sampled the data to 200 Hz, removed the line drift of each channel, and removed the temporal mean to provide a zero-mean situation for each resultant trial [18, 19]. The GC was then computed using a well-established method [20]. Specifically, the temporal dynamics of two time series of

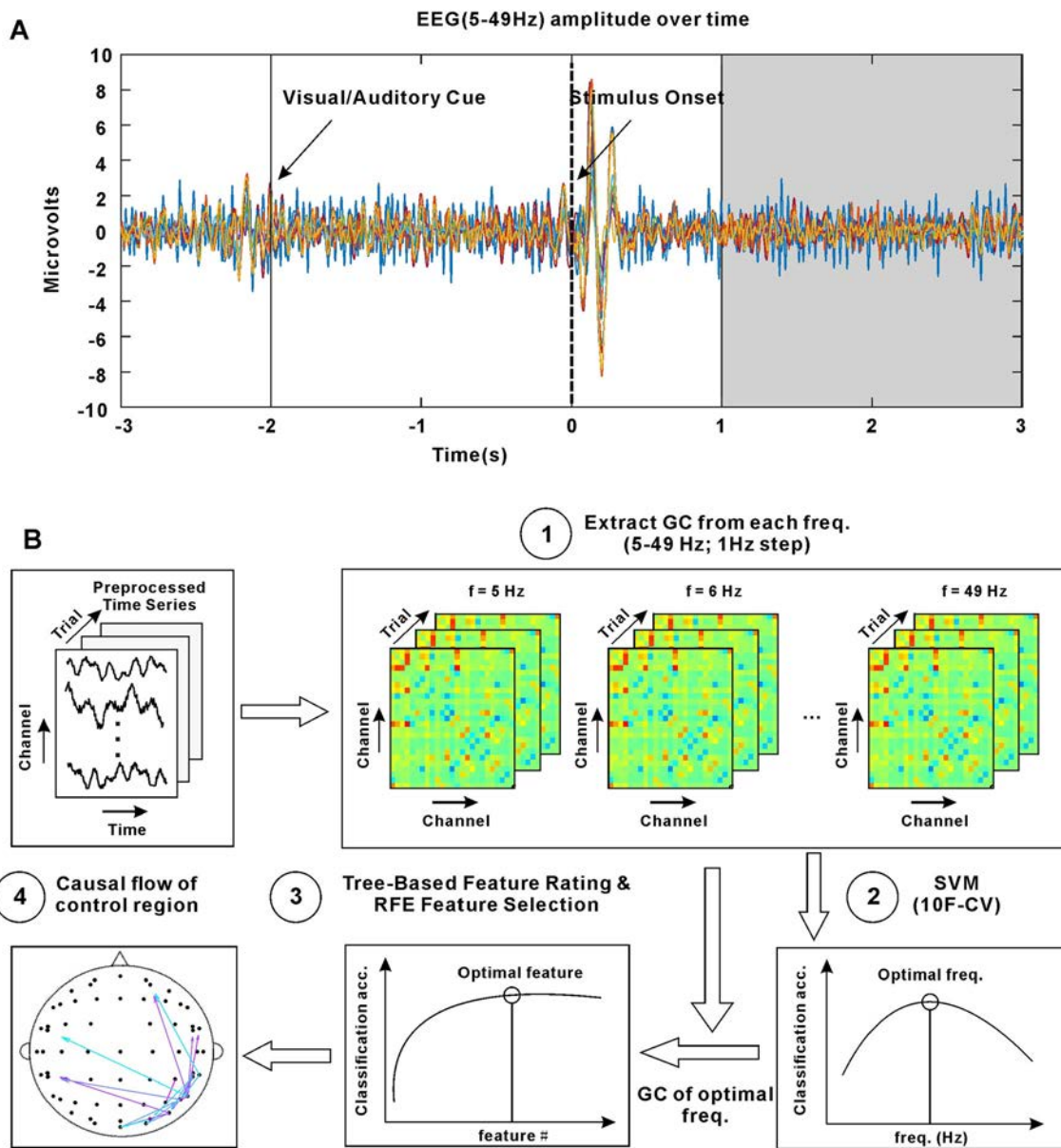


Fig. 2 Example EEG traces and data analysis pipeline. **A** Band-pass filtered EEG from Subject 1 during a typical trial. Different colors represent different electrodes. The vertical solid line at -2 s indicates the onset of the visual or auditory cue; the vertical dashed line at 0 s indicates the onset of an audiovisual stimulus; and the shaded area at -1 – 3 s indicates the period we analyzed. **B** The data analysis pipeline.

The GCs at each frequency (5 Hz–49 Hz at 1-Hz step) were calculated and used as features for binary classification with a support vector machine (SVM). The optimal frequency was then identified to select the optimal features. The causal flows of the nodes related to the optimal features were then calculated for further analysis (10F-CV, 10-fold cross-validation).

$X_1(t)$ and $X_2(t)$ (both of length T) can be described by a bivariate autoregressive (AR) model:

$$X_1(t) = \sum_{j=1}^p A_{11,j}X_1(t-j) + \sum_{j=1}^p A_{12,j}X_2(t-j) + \xi_1(t) \quad (1)$$

$$X_2(t) = \sum_{j=1}^p A_{21,j}X_1(t-j) + \sum_{j=1}^p A_{22,j}X_2(t-j) + \xi_2(t) \quad (2)$$

where A contains the GC coefficients and P is the order of the model, i.e. the maximum number of lagged observations ($P < T$); the optimal order of AR was estimated by the Akaike Information Criterion and was chosen between 5 and 12 accordingly [21]; ξ_1 and ξ_2 are the residuals of X_1 and X_2 , respectively, which are also a functions of t . If the variance of ξ_1 is reduced by inclusion of the X_2 term, then it is said that X_2 Granger-Causes X_1 . Specifically, the

degree of GC at each frequency was then evaluated according to the following equation:

$$F_{2 \rightarrow 1}(\omega) = \ln \frac{S_{11}(\omega)}{\tilde{H}_{11}(\omega) \text{var}(\xi_1(t)) \tilde{H}_{11}^*(\omega)} \quad (3)$$

where $S_{11}(\omega)$ is the auto-spectrum of X_I at the frequency ω ; $\tilde{H}_{11}(\omega)$ is the diagonal element of the normalized form of the transfer matrix $\tilde{H}(\omega)$; and $\tilde{H}_{11}^*(\omega)$ is the complex conjugate of $\tilde{H}_{11}(\omega)$ [19, 22, 23]. The calculation of GC in the frequency domain was carried out using a customized MatLab toolbox provided by [20]. Since the AR model might be unstable at very low frequencies and near the Nyquist frequency [21], we confined our analysis to frequencies between 5 Hz and 49 Hz. Therefore, in this frequency range, the spectral GCs for each resultant trial were calculated across all pairs of electrodes in 1-Hz steps.

Causal Flow

Based on the spectral GC, the causal flow [24] of a node at a specific frequency is defined as the difference between the out-degree (the summed GC value of all outgoing connections) and its in-degree (the summed GC value of all incoming connections). Thus, the causal flow can identify nodes that have distinctive causal effects on network dynamics: a node with a positive flow is a causal ‘source’ and a node with a negative flow is a causal ‘sink’ [20].

Common Spatial Pattern

The Common Spatial Pattern (CSP) is a supervised machine-learning method that aims to extract spatial filters that make the trials discriminable by the power of spatially-filtered signals [25]. The input data to the CSP were the pre-processed signals at 1 Hz–100 Hz (50 Hz excluded) (see [26, 27] for details of computations).

Pattern Classification

A Support Vector Machine (SVM) was used for binary classification between the auditory/visual ASA states. The SVM works by constructing an optimal hyperplane as a decision surface such that the margin of separation between the two classes in the data is maximized [28]. In this study, the SVM was implemented using the MatLab in-built function ‘`fitsvm`’ with the kernel of radial basis function.

The classification results were obtained by either 10 times of 10-fold cross-validation or the one-left classification test. The one-left test refers to using one participant’s data as the test data-set and all the other participants’ data as the training data-set.

Feature Analysis

A tree-based method was used to rate the feature importance and the Recursive Feature Elimination (RFE) method was applied to select the optimal number of features. Both methods were implemented by scikit-learn, an open-source machine-learning toolbox (<https://scikit-learn.org>). The tree-based feature importance analysis was implemented by an extra-trees classifier, which fitted a number of randomized decision trees on various sub-samples of the dataset and used averaging to control overfitting [29].

The RFE was performed by recursively considering smaller and smaller sets of features [30]. First, the initial features were trained on the estimator (a linear-kernel SVM) and the importance of each feature was obtained. Then the least important features were excluded. This procedure was recursively repeated on the remaining features until the desired number of features was finally reached.

Statistical Analysis

The Wilcoxon rank-sum test was used to determine significant differences between the median values of two groups of data. The *t*-test was applied to test whether the mean value of one group of data was significantly different from one specific value. The false discovery rate (FDR) method was used for correction. $P < 0.05$ was considered significant.

Results

The Optimal Frequency Band that Decodes the ASA Shift Lies between 12 Hz and 15 Hz

To search for the optimal frequency bands that are mostly informative about the ASA shift, we first computed the GCs across all pairs of electrodes from 5 to 49 Hz (at 1-Hz step) for each participant, and used the GCs as feature vectors for binary classification between the auditory/visual ASA states with an SVM-based classifier. Then we derived a classification accuracy curve with varying frequencies and identified the optimal frequency point for each participant, i.e., the frequency with the highest mean accuracy across 10 times – 10-fold cross-validation. For all 8 participants, the decoder based on GC patterns reliably discriminated the ASA state (Fig. 3A). However, each participant exhibited a distinct accuracy curve. The optimal frequency point varied from 5 Hz to 38 Hz, in which most participants (7 out of 8) showed a frequency < 20 Hz. To gain a general profile across all participants, we concatenated all their GC trials at each frequency point, then used

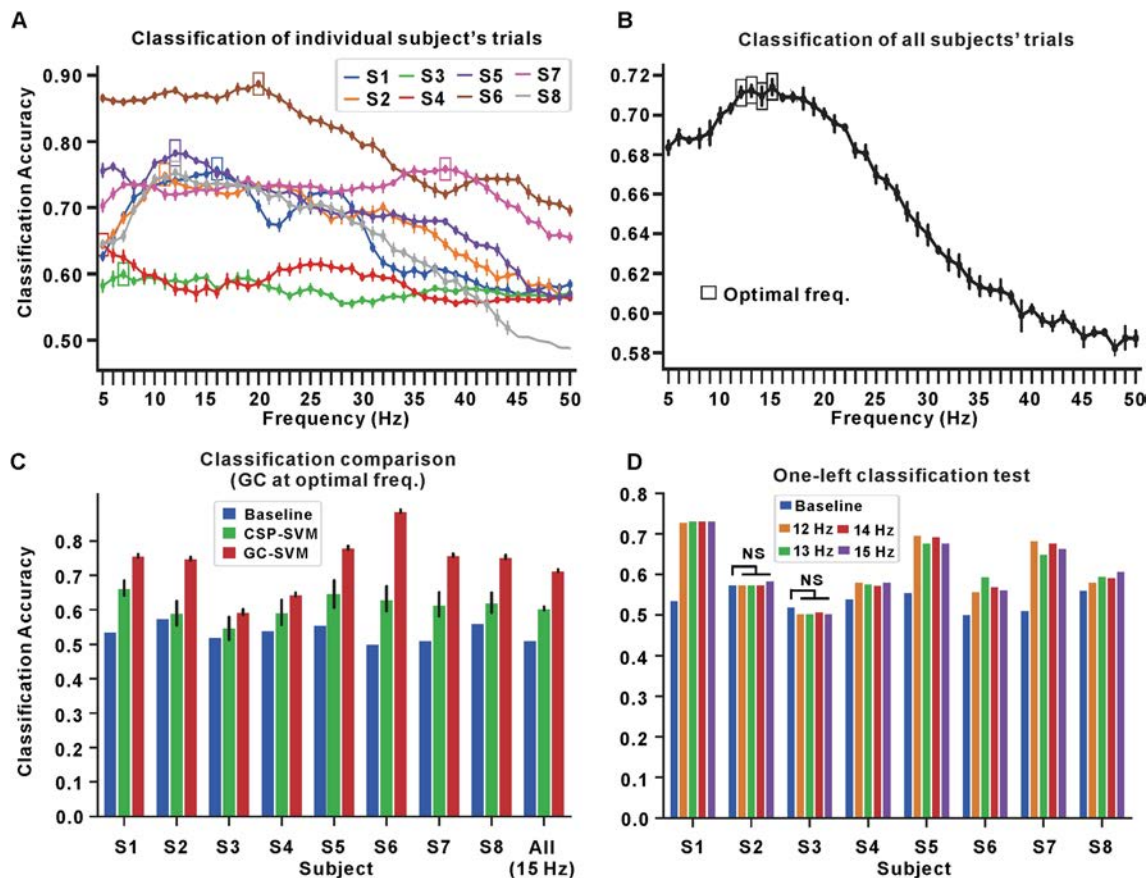


Fig. 3 Classification performance of GC-SVM. **A, B** Classification accuracy for individual participants (**A**, color-coded) and for the group analysis (**B**) (boxes mark the optimal frequency/frequencies with the highest mean accuracy). **C** Classification comparisons with

baseline (chance level; blue) and CSP (green) (accuracy estimated by 10 times of 10-fold cross validation, shown as the mean \pm SD). **D** One-left classification test for each participant.

the same SVM-based classifier to decode the ASA states, and finally obtained a group-level accuracy curve (Fig. 3B). At the group level, the peak accuracy was achieved at 12 Hz–15 Hz, in the range of the α band [31]. Next, we compared the classification accuracy provided by GC-SVM (at the optimal frequency), CSP-SVM based on features of the time domain, and the chance level defined as $\max(V, A)/(V + A)$ (Fig. 3C). For both individual and group conditions, GC-SVM achieved higher accuracy than CSP-SVM ($P < 0.01$, Wilcoxon rank sum test, FDR-corrected), which was also significantly above chance ($P < 0.05$, one-sided one-sample t -test, FDR-corrected). These results indicate primarily that the ASA shift is reflected by the activity at the macroscopic network level in terms of both the temporal and frequency domains, supporting the notion that network reconfiguration underpins the cross-modal attentional shift. Furthermore, specific frequency band(s) may play critical roles in mediating such shifts, reflected by the results that GCs in certain frequency bands serve as better discriminative features than the broad-band temporal signals.

More importantly, despite the substantial individual differences (Fig. 3A), there were general principles at the group level concerning the GCs at 12 Hz–15 Hz that were associated with the ASA shift. To further test the generality of this principle, we applied the one-left classification test to each participant. Specifically, we used one participant's trials as the test dataset and those of all the others as the training dataset, with the same SVM-based classifier. The attentive states of the majority of participants (6 out of 8) were predicted by the data of the others, given the features of GC at 12–15 Hz ($P < 0.05$, one-sided one-sample t -test, FDR-corrected). Thus, in the subsequent analyses, we focused on the GC at 12 Hz–15 Hz to explore the patterns linked with the ASA transition.

Searching for the Optimal Features at 12 Hz–15 Hz that Decode the ASA Shift

To determine the optimal features characterizing the ASA transition, we applied feature analysis to the group-level GCs at 12 Hz–15 Hz, including tree-based feature-rating

and RFE (see “Materials and Methods” section for details). Taking GCs at 15 Hz as an example (similar results were obtained for the other frequencies), a tree-based feature-rating method was applied and the results were sorted in a descending order (Fig. 4A). The importance of each feature varied greatly, having different functional implications for all the pairwise GCs among electrodes for the ASA shift. Next, we used RFE to select the most informative GC features based on the decoding performance. Surprisingly, only a very small proportion of GCs (<5%) contributed most to the classification accuracy. The peak decoding performance was achieved with <160 (among ~4,000) GC features (Fig. 4B). We distilled the optimal features that achieved the highest classification score (measured by 10-fold cross-validation) and mapped them onto the spatial locations (Fig. 4C). A wide range of brain areas were involved, including the prefrontal, temporal, and parietal areas, while the dominant regions

(connected by more reddish edges in the figure) mainly clustered in the parietal–occipital areas. Then, these optimal features were tested in individual trials. We showed that, in the majority of cases, these optimal features also decoded the ASA states for each participant with accuracy significantly above chance ($P < 0.05$, one-sided one-sample t -test; FDR-corrected), although with dramatically reduced dimensionality of the feature space (Fig. 4D).

In the above analyses, we derived optimal GC features associated with the ASA shift. As GCs serve as pairwise interactions among electrodes, even the optimal GC features still had a feature space with very high dimension, we wondered whether it was possible to further reduce the feature dimension while maintaining the decoding performance. To this end, we computed the optimal CFs (see “Materials and Methods” section for details) from the derived optimal GCs. In comparison, we also computed

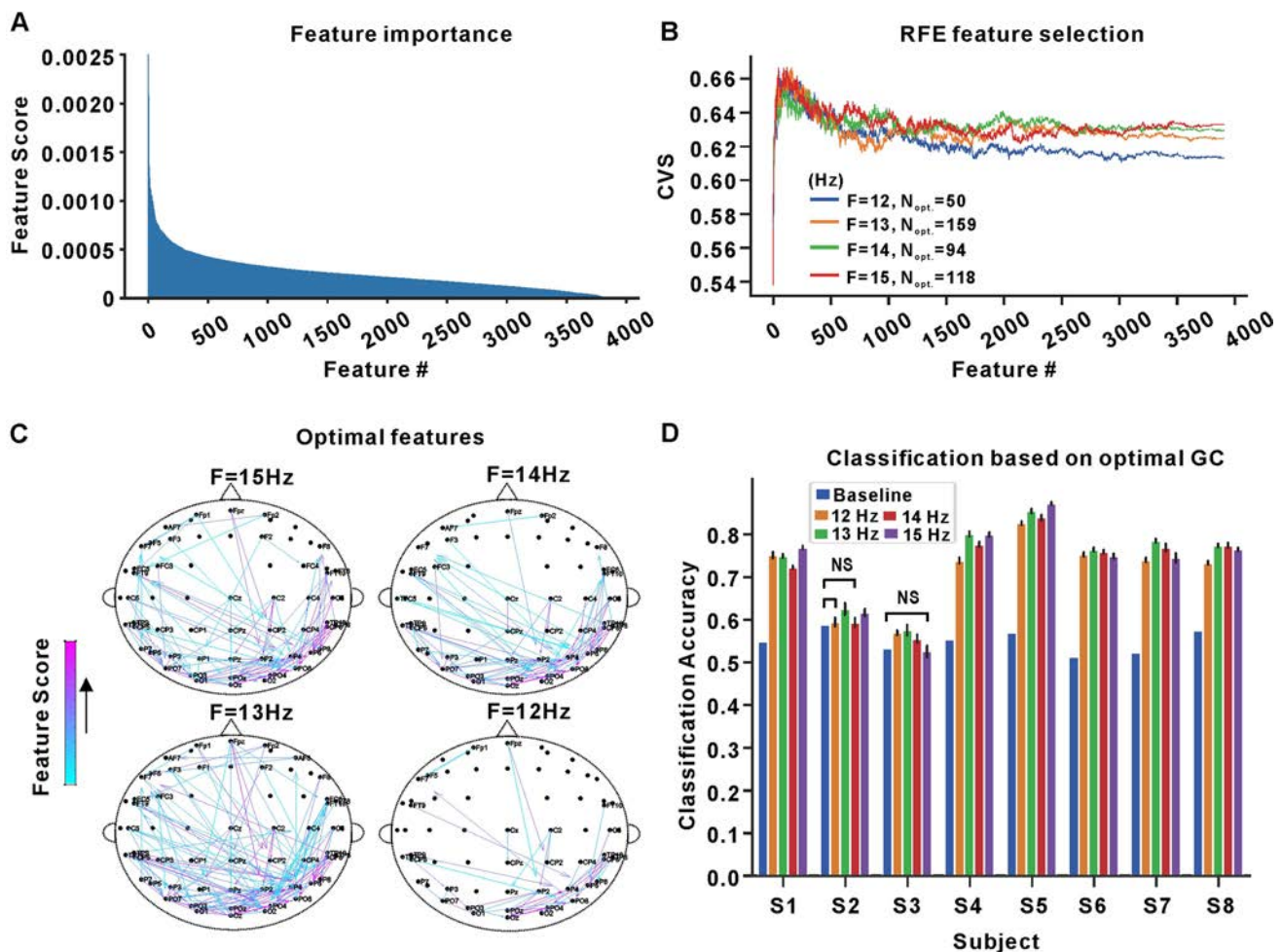


Fig. 4 Feature selection of GCs based on group-level analysis. **A** Feature scores of GCs at 15 Hz. **B** Feature selections by RFE for GCs at 12–15 Hz (CVS, cross-validation score). **C** Spatial maps of optimal features derived by RFE. **D** Classification accuracy achieved

by the optimal features tested in individual participants (accuracy measured by 10 times of 10-fold cross validation, shown as the mean \pm SD; NS, not significant).

CFs from all pairwise GCs without feature selection (i.e., all CFs). The CF in one node is a metric that describes the node's net causal effect on the network [20]. Then we used both the optimal and all CFs as features for binary classification with the same SVM-based classifier. The classification accuracy by the optimal CFs and all CFs (0.65–0.7) at the group level was very close to the classification accuracy achieved by using all GC features (0.7 at the group-level and 0.55–0.8 at the individual level) (Fig. 5A), demonstrating the feasibility of using CFs to decode ASA states. Moreover, we found that the optimal CFs with lower feature dimension (<63) but improved accuracy ($P < 0.05$, Wilcoxon rank sum test, FDR-corrected) were superior to all CFs, demonstrating the necessity of feature selection with GCs in the earlier steps. Next, we tested the optimal CFs in individual trials (10-fold cross-validation; Fig. 5B) and in the one-left test (Fig. 5C). In both tests, the optimal CFs also decoded the ASA states with accuracy significantly above chance in the

majority of cases ($P < 0.05$, one-sample t -test, FDR-corrected), which validated the effectiveness of derived optimal CFs with much lower feature dimension than GCs in decoding the ASA transition. The results of the one-left test also revealed that the optimal CFs derived from the group-level can be used to decode for individual participants, suggesting its robustness across participants.

The Parietal–Occipital Region Typically Characterizes the Transition of ASA States

In light of the effectiveness and simplicity of CFs, we next explored the patterns reflected by the optimal CFs that decode the ASA states. The mean CF patterns derived from the group-level samples for 12 Hz–15 Hz are presented in Fig. 6A–D. Each frequency had highly-correlated CF patterns between the two ASA states (Pearson correlation, 0.9875 ± 0.0079), revealing that the overall pattern of information flow in the network is similar in the two ASA

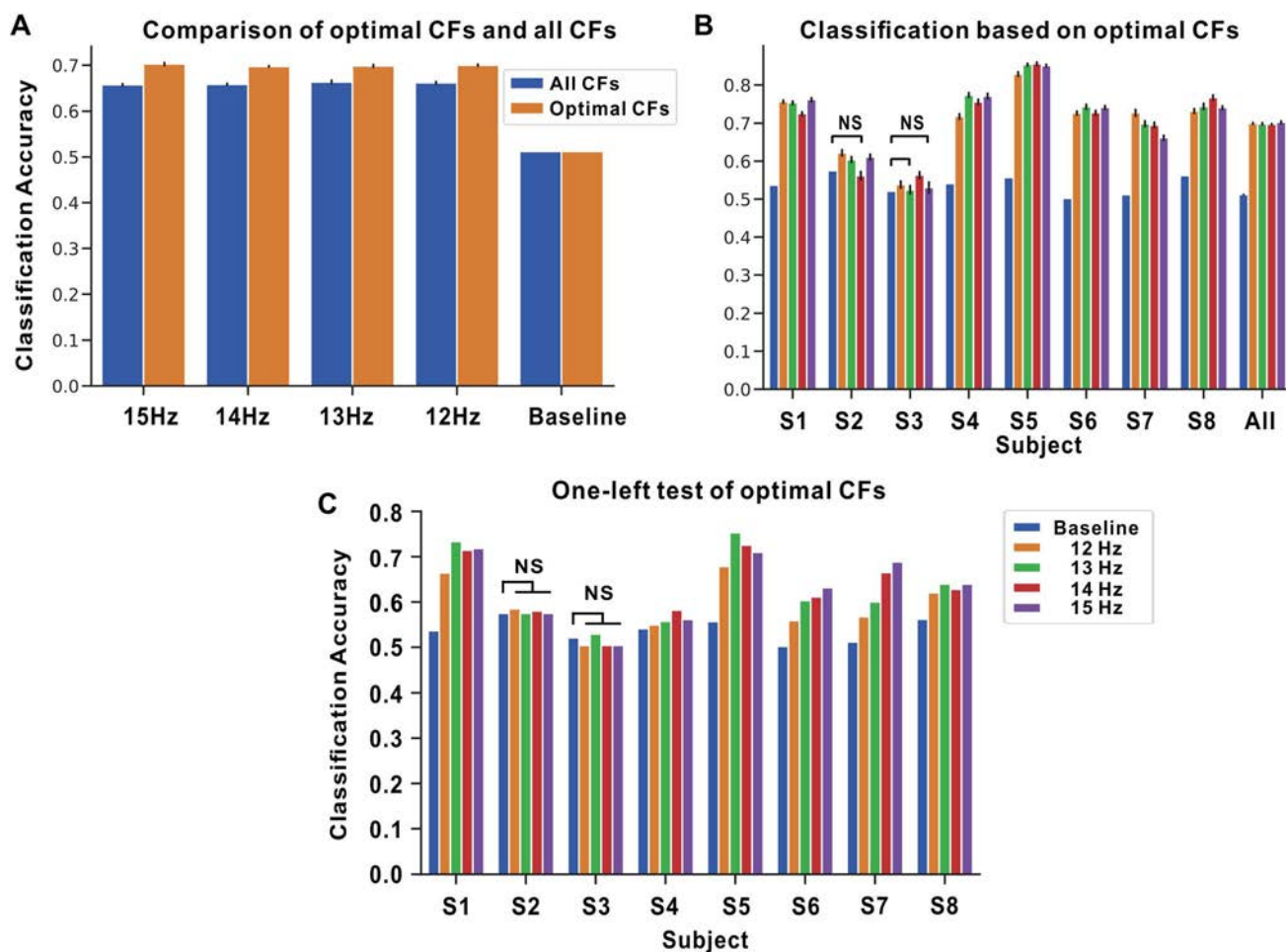


Fig. 5 Classification based on CFs derived from the optimal GCs. **A** Comparisons with CFs of all electrodes without GC feature selection. **B** Classification results for individual participant and group

analysis (accuracy measured by 10 times of 10-fold cross validation, shown as the mean \pm SD). **C** One-left classification test for each participant (NS, not significant).

Fig. 6 Distribution of optimal CFs for group analysis at 12–15 Hz (A–D, respectively). In each panel: left, CF distribution across electrodes (mean \pm SD; blue, visual trials; yellow, auditory trials); upper right, map of the causal source nodes (CF >0 for visual trials); lower right, map of the causal sink nodes (CF <0 for visual trials). CFa, CF for auditory trial; CFv, CF for visual trial; Corr., Pearson correlation coefficient; N_node, number of electrodes.

states. This was further demonstrated in the results for individual participants (Fig. 7). These results suggested that ASA states are associated with subtle but consistent changes in the pattern of information flow across the network.

To pinpoint the brain areas associated with such changes, we calculated the difference of CFs between the two ASA states for various electrodes. We found that the most notable differences (more reddish nodes in the spatial maps) lay in the parieto-occipital (PO) area as well as the temporo-parietal (TP) area. Moreover, the PO and TP assumed different causal roles in the network, with PO as a causal source and TP as a causal sink.

Next, to quantify the importance of CF features in decoding the ASA states, we again applied tree-based feature-rating to the optimal CFs and all CFs. The scores for electrodes were then presented according to their names in the international standard 10–20 system (e.g., PO7 and PO8 were both taken as PO; for the abbreviations of brain regions please refer to Table 1). The results are presented in Fig. 8. Consistent with the analyses shown in Fig. 6, the PO area was demonstrated to be the most important region in decoding the ASA transition ($P < 0.05$, Wilcoxon rank-sum test, FDR-corrected).

Discussion

In this study, based on an ASA experimental paradigm, we first applied spectral GC to depict the frequency-specific network dynamics during cross-modal attentional shifts. Then, with pattern classification techniques, we used a data-driven method to unravel the network characteristics for the ASA transition. We revealed that GC patterns in the α band characterize the ASA transition most reliably. Furthermore, distinct patterns of CF derived from GC revealed subtle differences in the information flow for different attentive states, and identified the key brain regions associated with ASA.

Methodological Considerations

EEG signals are susceptible to volume conduction, which causes spurious increases of neural synchrony such as

coherence and phase-locking values [32, 33]. Thus, the interpretation of EEG-based measures of functional connectivity, which is usually measured by correlation among signals, should be made with caution. It has been suggested that the effective connectivity, mainly based on the consistent time-lag between signals, is less affected by volume conduction under certain assumptions [34, 35]. Thus, in the present study, we analyzed the effective connectivity based on the GC at the sensor level. Both the areas that we found to be more importantly involved in the network reconfigurations – the parietal-occipital areas – and the directed interaction from the visual to the auditory areas, are consistent with the results of previous fMRI studies [3, 6, 36], indicating the validity of the current methods. However, it has also been argued that the effective connectivity is not intrinsically immune to the effects of volume conduction [35]. Although it has been suggested that electromagnetic source imaging targeting the source-level connectivity might be more effective in extracting the underlying interactions [37, 38], this methodological issue has not been settled, awaiting further studies for a more comprehensive understanding.

Another issue for consideration is the relatively small number of participants involved in our study ($n = 8$). However, we showed that in most cases (6 out of 8), the attentional states of individuals were predicted by the classifier trained entirely with the datasets of others (Figs. 3D and 5C). This strongly supports the conclusion that the main effect we found here, namely the pattern of network reconfiguration in the α band, is a stable feature across individuals. Nevertheless, future studies to examine individual differences in both the ability of cross-modal attention and the neural underpinnings would be very informative.

PO Alpha Activity Characterizes the Network Reconfiguration During ASA Transition

Using feature analysis, we found the changes in α activity in the PO area to be most pronounced at the ASA transition, which is consistent with a previous study using functional imaging [6]. Moreover, previous findings on visuospatial selective attention have reported that α power in the PO area robustly decodes the attended spatial location [39–41]. Similarly, α modulation in the auditory cortex has been revealed in an audio-spatial selective attention task [42]. Recently, it has been demonstrated that the changes in α power in the parietal area are causally associated with the ability to attend [43]. All these findings point to the important role of α power in unimodal as well as cross-modal selective attention. Indeed, it has been reported that α power participates in the allocation of attentional resources by an inhibitory mechanism, i.e.

CF distribution of individual subjects

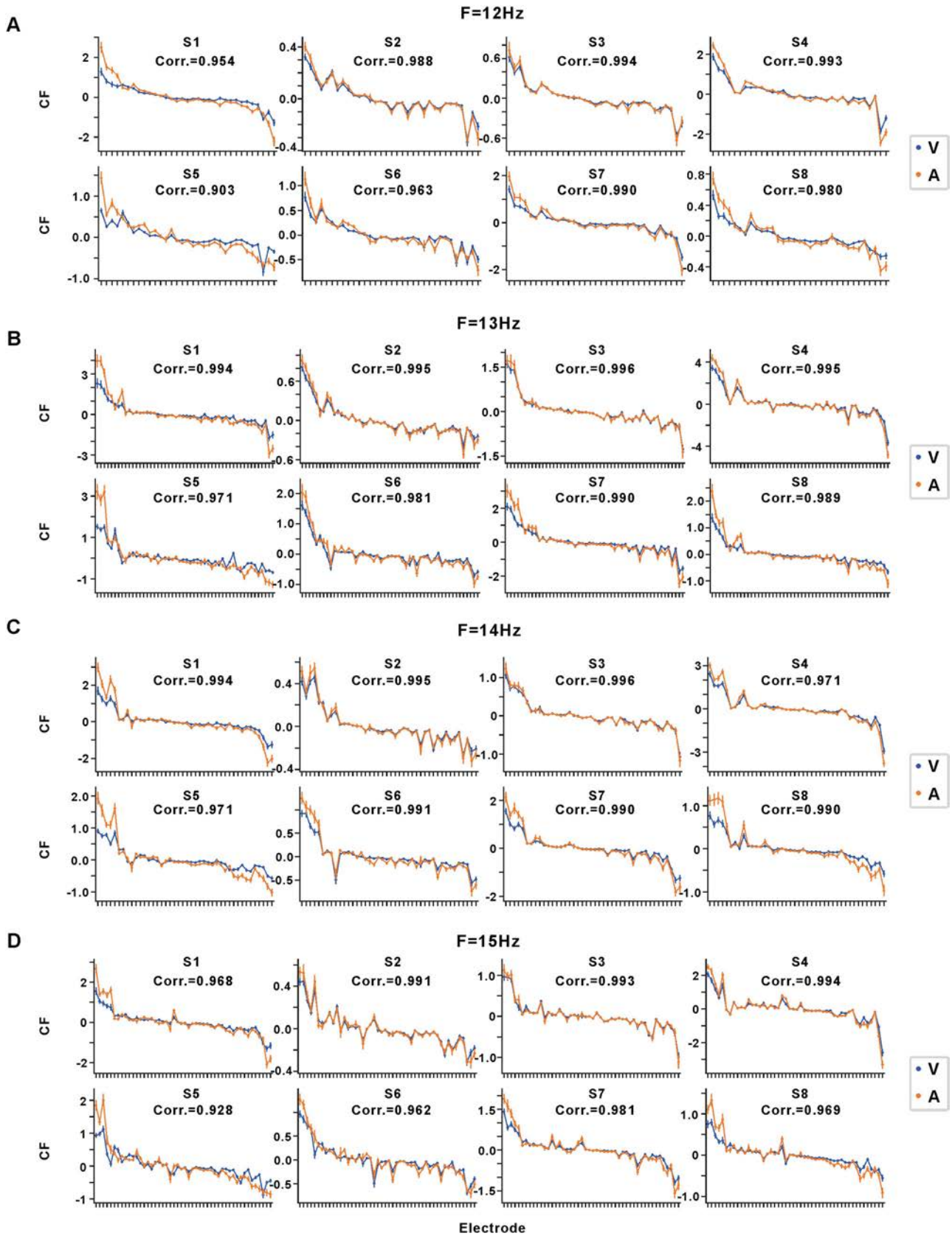


Fig. 7 Distribution of the optimal CFs for individual participants at 12–15 Hz (A–D, respectively). The horizontal axes (from left to right) correspond to the electrode list in Fig. 6 (from upper to lower) for each frequency. Results are presented as the mean \pm SD. V, visual trials; A, auditory trials.

Table 1 Abbreviations for brain regions.

Brain region	Abbreviation
Anterior-Frontal	AF
Central	C
Central-Parietal	CP
Frontal	F
Frontal-Central	FC
Frontal-Temporal	FT
Occipital	O
Parietal	P
Parietal-Occipital	PO
Prefrontal	Fp
Temporal	T
Temporal-Parietal	TP

suppressing distractors and irrelevant information [8, 44–47]. Consistent with this, we found enhanced α activity at PO in the auditory compared to the visual attentive state in cross-modal selective attention.

Importantly, our results indicate that α oscillation not only plays a role in modulating the activity of individual areas, but is also vital to modulate the information flow among areas to achieve a flexible network reconfiguration. This provides new insights into the network mechanisms underlying cross-modal selective attention.

It is noteworthy that previous studies of cross-modal selective attention also revealed suppressive effects of PO

α evoked by cues preceding the stimulus onset [45, 48]. But these effects can be interleaved with exogenous cues and endogenous attentional deployment. Here, we focused on the endogenous process by selecting the period 1 s after stimulus onset for analysis. Thus, our results demonstrate that the suppressive effect of PO α can not only be evoked by specific sensory cues, but is an important aspect during attentional deployment with the ongoing processing of sensory information.

GC and CF Provide a Specific Network Property that Can Detect the ASA Transition

One previous study reported no significant differences in terms of network topology parameters (clustering coefficient, average path length, and small-world index) when attention is deployed to different sensory modalities [49]. This is consistent with our current findings with similar CF patterns at 12 Hz–15 Hz across sensory modalities. Nevertheless, subtle differences can be detected using GC and CF, which measure more detailed network properties than those coarse-grained graph-theoretical metrics.

In addition, the CF illustrated the causal relations among areas. Specifically, we found significant causal sinks in PO and causal sources in TP, revealing the directional influences from visual to auditory areas. This is consistent with previous fMRI studies reporting modulation of the auditory cortex by the visual cortex [36, 50, 51].

It has also been reported that the cross-modal interactions in sensory areas are controlled by top-down attentional effects of the dorsolateral prefrontal cortex [6, 52–54]. In long-range functional couplings among brain areas, high-frequency bands such as β (15 Hz–30 Hz) and γ (>30 Hz) have also been reported to subservise high-level cognitive functions [55–58]. This is consistent with the current results that the classification accuracy in β – γ

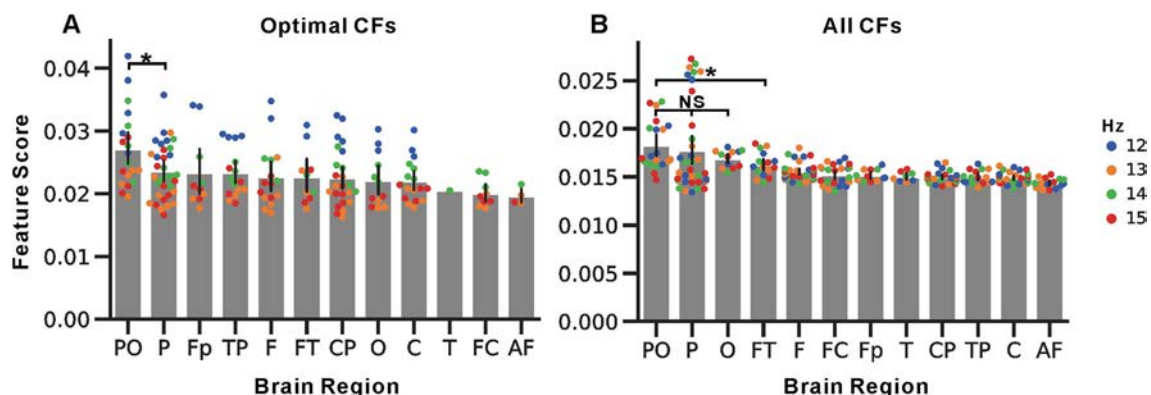


Fig. 8 Regional importance in decoding the transition of ASA states (sorted by the mean value in descending order). **A** Feature importance of optimal CFs. **B** Feature importance of all CFs. Results are presented as the mean \pm SD; * $P < 0.05$; NS, not significant.

remained above chance, although inferior to α (Fig. 3A, B), which can be explored by future studies.

In conclusion, our results demonstrated the role of α activity in mediating the network configuration supporting cross-modal selective attention. This is not only informative to understanding the neural mechanism underlying attentional modulation at the network level, but also opens new possibilities of EEG-based brain-computer interfaces. For instance, cross-modal brain-computer interfaces might be applied for state detection in patients with locked-in syndrome or neural-feedback training in patients with attention deficit hyperactivity disorder [59, 60].

Acknowledgments This work was supported by the National Key Research and Development Program of China (2017YFA0105203), the Strategic Priority Research Program of the Chinese Academy of Sciences (CAS) (XDB32040200 and XDB32030200), the Key Research Program of Frontier Sciences, CAS (QYZDJ-SSW-SMC019), and the National Natural Science Foundation of China (81871398, U1636121, and 31571003).

Conflict of interest None.

References

- Driver J, Spence C. Cross-modal links in spatial attention. *Philos Trans R Soc Lond B Biol Sci* 1998, 353: 1319–1331.
- Lavie N. Distracted and confused?: Selective attention under load. *Trends Cogn Sci* 2005, 9: 75–82.
- Laurienti PJ, Burdette JH, Wallace MT, Yen YF, Field AS, Stein BE. Deactivation of sensory-specific cortex by cross-modal stimuli. *J Cogn Neurosci* 2002, 14: 420–429.
- Rahne T, Bochmann M, von Specht H, Sussman ES. Visual cues can modulate integration and segregation of objects in auditory scene analysis. *Brain Res* 2007, 1144: 127–135.
- Johnson JA, Zatorre RJ. Neural substrates for dividing and focusing attention between simultaneous auditory and visual events. *Neuroimage* 2006, 31: 1673–1681.
- Shomstein S, Yantis S. Control of attention shifts between vision and audition in human cortex. *J Neurosci* 2004, 24: 10702–10706.
- Calderone DJ, Lakatos P, Butler PD, Castellanos FX. Entrainment of neural oscillations as a modifiable substrate of attention. *Trends Cogn Sci* 2014, 18: 300–309.
- Gomez-Ramirez M, Kelly SP, Molholm S, Sehatpour P, Schwartz TH, Foxe JJ. Oscillatory sensory selection mechanisms during intersensory attention to rhythmic auditory and visual inputs: a human electrocorticographic investigation. *J Neurosci* 2011, 31: 18556–18567.
- Lakatos P, Karmos G, Mehta AD, Ulbert I, Schroeder CE. Entrainment of neuronal oscillations as a mechanism of attentional selection. *Science* 2008, 320: 110–113.
- Fiebelkorn IC, Kastner S. A rhythmic theory of attention. *Trends Cogn Sci* 2018.
- Fiebelkorn IC, Foxe JJ, Butler JS, Mercier MR, Snyder AC, Molholm S. Ready, set, reset: stimulus-locked periodicity in behavioral performance demonstrates the consequences of cross-sensory phase reset. *J Neurosci* 2011, 31: 9971–9981.
- Romei V, Gross J, Thut G. Sounds reset rhythms of visual cortex and corresponding human visual perception. *Curr Biol* 2012, 22: 807–813.
- Schroeder CE, Lakatos P. Low-frequency neuronal oscillations as instruments of sensory selection. *Trends Neurosci* 2009, 32: 9–18.
- Canolty RT, Knight RT. The functional role of cross-frequency coupling. *Trends Cogn Sci* 2010, 14: 506–515.
- Buzsaki G, Watson BO. Brain rhythms and neural syntax: implications for efficient coding of cognitive content and neuropsychiatric disease. *Dialogues Clin Neurosci* 2012, 14: 345–367.
- Allport A, Wylie G. Task switching, stimulus-response bindings, and negative priming. Cambridge: MIT Press, 2000.
- Koechlin E, Ody C, Kouneiher F. The architecture of cognitive control in the human prefrontal cortex. *Science* 2003, 302: 1181–1185.
- Ding MZ, Bressler SL, Yang WM, Liang HL. Short-window spectral analysis of cortical event-related potentials by adaptive multivariate autoregressive modeling: data preprocessing, model validation, and variability assessment. *Biol Cybern* 2000, 83: 35–45.
- Ding M, Chen Y, Bressler SL. Granger causality: basic theory and application to neuroscience. *Handbook of time series analysis: recent theoretical developments and applications* 2006: 437–460.
- Seth AK. A MATLAB toolbox for Granger causal connectivity analysis. *J Neurosci Methods* 2010, 186: 262–273.
- Richter CG, Coppola R, Bressler SL. Top-down beta oscillatory signaling conveys behavioral context in early visual cortex. *Sci Rep* 2018, 8: 12.
- Geweke J. Measurement of linear-dependence and feedback between multiple time-series. *J Am Stat Assoc* 1982, 77: 304–313.
- Bressler SL, Seth AK. Wiener-Granger Causality: A well established methodology. *Neuroimage* 2011, 58: 323–329.
- Wolpaw JR, Birbaumer N, McFarland DJ, Pfurtscheller G, Vaughan TM. Brain-computer interfaces for communication and control. *Clin Neurophysiol* 2002, 113: 767–791.
- Schirmeister RT, Springenberg JT, Fiederer LDJ, Glasstetter M, Eggenberger K, Tangermann M, *et al.* Deep learning with convolutional neural networks for EEG decoding and visualization. *Hum Brain Mapp* 2017, 38: 5391–5420.
- Muller KR, Tangermann M, Dornhege G, Krauledat M, Curio G, Blankertz B. Machine learning for real-time single-trial EEG-analysis: From brain-computer interfacing to mental state monitoring. *J Neurosci Methods* 2008, 167: 82–90.
- Ramoser H, Muller-Gerking J, Pfurtscheller G. Optimal spatial filtering of single trial EEG during imagined hand movement. *IEEE Trans Rehabil Eng* 2000, 8: 441–446.
- Chang C-C, Lin C-J. LIBSVM: A library for support vector machines. *ACM transactions on intelligent systems and technology* (TIST) 2011, 2: 27.
- Breiman L. Arcing classifiers. *Ann Stat* 1998, 26: 801–824.
- Guyon I, Weston J, Barnhill S, Vapnik V. Gene selection for cancer classification using support vector machines. *Mach Learn* 2002, 46: 389–422.
- Siegel M, Donner TH, Oostenveld R, Fries P, Engel AK. Neuronal synchronization along the dorsal visual pathway reflects the focus of spatial attention. *Neuron* 2008, 60: 709–719.
- van den Broek SP, Reinders F, Donderwinkel M, Peters M. Volume conduction effects in EEG and MEG. *Electroencephalogr Clin Neurophysiol* 1998, 106: 522–534.
- Nunez PL, Srinivasan R, Westdorp AF, Wijesinghe RS, Tucker DM, Silberstein RB, *et al.* EEG coherency. 1. Statistics, reference electrode, volume conduction, Laplacians, cortical imaging, and interpretation at multiple scales. *Electroencephalogr Clin Neurophysiol* 1997, 103: 499–515.

34. Kaminski M, Blinowska KJ. Directed transfer function is not influenced by volume conduction-inexpedient pre-processing should be avoided. *Front Comput Neurosci* 2014, 8: 3.
35. Brunner C, Billinger M, Seeber M, Mullen TR, Makeig S. Volume conduction influences scalp-based connectivity estimates. *Front Comput Neurosci* 2016, 10: 4.
36. Kayser C, Petkov CI, Augath M, Logothetis NK. Functional imaging reveals visual modulation of specific fields in auditory cortex. *J Neurosci* 2007, 27: 1824–1835.
37. Sohrabpour A, Ye S, Worrell GA, Zhang WB, He B. Noninvasive electromagnetic source imaging and granger causality analysis: an electrophysiological connectome (econnectome) approach. *IEEE Trans Biomed Eng* 2016, 63: 2474–2487.
38. Michel CM, Murray MM, Lantz G, Gonzalez S, Spinelli L, de Peralta RG. EEG source imaging. *Clin Neurophysiol* 2004, 115: 2195–2222.
39. Tonin L, Leeb R, Millan JD. Time-dependent approach for single trial classification of covert visuospatial attention. *J Neural Eng* 2012, 9: 9.
40. Trachel RE, Clerc M, Brochier TG. Decoding covert shifts of attention induced by ambiguous visuospatial cues. *Front Hum Neurosci* 2015, 9: 9.
41. Treder MS, Bahramisharif A, Schmidt NM, van Gerven MAJ, Blankertz B. Brain-computer interfacing using modulations of alpha activity induced by covert shifts of attention. *J NeuroEng Rehabil* 2011, 8: 9.
42. Frey JN, Mainy N, Lachaux JP, Muller N, Bertrand O, Weisz N. Selective modulation of auditory cortical alpha activity in an audiovisual spatial attention task. *J Neurosci*. 2014, 34: 6634–6639.
43. Bagherzadeh Y, Baldauf D, Pantazis D, Desimone RJN. Alpha synchrony and the neurofeedback control of spatial attention. *Neuron* 2020, 105: 577–587.e5.
44. Foxe JJ, Snyder AC. The role of alpha-band brain oscillations as a sensory suppression mechanism during selective attention. *Front Psychol* 2011, 2: 154.
45. Fu KMG, Foxe JJ, Murray MM, Higgins BA, Javitt DC, Schroeder CE. Attention-dependent suppression of distracter visual input can be cross-modally cued as indexed by anticipatory parieto-occipital alpha-band oscillations. *Cognit Brain Res* 2001, 12: 145–152.
46. Gould IC, Rushworth MF, Nobre AC. Indexing the graded allocation of visuospatial attention using anticipatory alpha oscillations. *J Neurophysiol* 2011, 105: 1318–1326.
47. Rohenkohl G, Nobre AC. Alpha oscillations related to anticipatory attention follow temporal expectations. *J Neurosci* 2011, 31: 14076–14084.
48. Foxe JJ, Simpson GV, Ahlfors SP. Parieto-occipital similar to 10 Hz activity reflects anticipatory state of visual attention mechanisms. *Neuroreport* 1998, 9: 3929–3933.
49. Hong XF, Sun JF, Tong SB. Functional brain networks for sensory maintenance in top-down selective attention to audiovisual inputs. *IEEE Trans. Neural Syst Rehabil Eng* 2013, 21: 734–743.
50. Busse L, Roberts KC, Crist RE, Weissman DH, Woldorff MG. The spread of attention across modalities and space in a multisensory object. *Proc Natl Acad Sci U S A* 2005, 102: 18751–18756.
51. Degerman A, Rinne T, Pekkola J, Autti T, Jaaskelainen IP, Sams M, *et al.* Human brain activity associated with audiovisual perception and attention. *Neuroimage* 2007, 34: 1683–1691.
52. Johnson JA, Zatorre RJ. Attention to simultaneous unrelated auditory and visual events: Behavioral and neural correlates. *Cereb Cortex* 2005, 15: 1609–1620.
53. Sauseng P, Klimesch W, Stadler W, Schabus M, Doppelmayr M, Hanslmayr S, *et al.* A shift of visual spatial attention is selectively associated with human EEG alpha activity. *Eur J Neurosci* 2005, 22: 2917–2926.
54. Johnson JA, Strafella AP, Zatorre RJ. The role of the dorsolateral prefrontal cortex in bimodal divided attention: Two transcranial magnetic stimulation studies. *J Cogn Neurosci* 2007, 19: 907–920.
55. Fries P. Neuronal gamma-band synchronization as a fundamental process in cortical computation. *Annu Rev Neurosci* 2009, 32: 209–224.
56. Gregoriou GG, Gotts SJ, Zhou H, Desimone R. High-frequency, long-range coupling between prefrontal and visual cortex during attention. *Science* 2009, 324: 1207–1210.
57. Roberts MJ, Lowet E, Brunet NM, Ter Wal M, Tiesinga P, Fries P, *et al.* Robust gamma coherence between macaque V1 and V2 by dynamic frequency matching. *Neuron* 2013, 78: 523–536.
58. Vinck M, Lima B, Womelsdorf T, Oostenveld R, Singer W, Neunschwander S, *et al.* Gamma-phase shifting in awake monkey visual cortex. *J Neurosci* 2010, 30: 1250–1257.
59. Laureys S, Owen AM, Schiff ND. Brain function in coma, vegetative state, and related disorders. *Lancet Neurol* 2004, 3: 537–546.
60. Zhu YC, Jiang XX, Ji WD. The mechanism of cortico-striato-thalamo-cortical neurocircuitry in response inhibition and emotional responding in attention deficit hyperactivity disorder with comorbid disruptive behavior disorder. *Neurosci Bull* 2018, 34: 566–572.



The Joubert Syndrome Gene *arll3b* is Critical for Early Cerebellar Development in Zebrafish

Jian Zhu^{1,2,5} · Han-Tsing Wang^{1,2} · Yu-Rong Chen^{1,2} · Ling-Ya Yan^{1,2} · Ying-Ying Han^{1,2} · Ling-Yan Liu^{1,2,3} · Ying Cao⁴ · Zhi-Zhi Liu^{1,2,3} · Hong A. Xu^{1,2,3}

Received: 16 October 2019 / Accepted: 5 March 2020 / Published online: 18 August 2020
© The Author(s) 2020

Abstract Joubert syndrome is characterized by unique malformation of the cerebellar vermis. More than thirty Joubert syndrome genes have been identified, including *ARL13B*. However, its role in cerebellar development remains unexplored. We found that knockdown or knockout of *arll3b* impaired balance and locomotion in zebrafish larvae. Granule cells were selectively reduced in the corpus cerebelli, a structure homologous to the mammalian vermis. Purkinje cell progenitors were also selectively disturbed dorsomedially. The expression of *atoh1* and *ptf1*, proneural genes of granule and Purkinje cells, respectively, were selectively down-regulated along the dorsal midline of the cerebellum. Moreover, *wnt1*, which is transiently expressed early in cerebellar development, was selectively

reduced. Intriguingly, activating Wnt signaling partially rescued the granule cell defects in *arll3b* mutants. These findings suggested that *Arl13b* is necessary for the early development of cerebellar granule and Purkinje cells. The *arll3b*-deficient zebrafish can serve as a model organism for studying Joubert syndrome.

Keywords Joubert syndrome · *arll3b* · Cerebellum · Development · Granule cell · Purkinje cell · Wnt

Introduction

Joubert syndrome (JS) is an autosomal-recessive neurodevelopmental disorder, which is characterized morphologically by the unique molar tooth sign, a complex malformation of the cerebellar vermis and brainstem, with abnormalities of axonal decussation affecting the corticospinal tract and superior cerebellar peduncles [1]. JS is clinically characterized by impaired motor functions and intellectual disability. Most cases of JS are variably associated with impairments of additional organs, including the retina, kidney, skeleton, and liver. More than 30 genes have been identified to cause JS (213300, Online Mendelian Inheritance in Man). Most of the proteins encoded by these genes are located in or near the primary cilium, an organelle found in eukaryotic cells, and this makes JS a typical ciliopathy [1]. Although malformation of the cerebellar vermis is common in JS, the role and mechanisms of the causative genes in cerebellar development have only been reported recently [2, 3].

Mutations of *ARL13B* (HGNC ID 25419) lead to the classical form of JS [4]. The *ARL13B* gene encodes an enzyme belonging to the small GTPase superfamily and this makes it unique among the known causative genes of

Jian Zhu and Han-Tsing Wang have contributed equally to this work.

Electronic supplementary material The online version of this article (<https://doi.org/10.1007/s12264-020-00554-y>) contains supplementary material, which is available to authorized users.

✉ Hong A. Xu
xuhong@ncu.edu.cn

- ¹ Institute of Life Science, Nanchang University, Nanchang 330031, China
- ² School of Life Sciences, Nanchang University, Nanchang 330031, China
- ³ Jiangxi Provincial Collaborative Innovation Center for Cardiovascular, Digestive and Neuropsychiatric Diseases, Nanchang 330031, China
- ⁴ Department of Molecular and Cell Biology, Tongji University School of Life Sciences and Technology, Shanghai 200092, China
- ⁵ Precise Genome Engineering Center, School of Life Sciences, Guangzhou University, Guangzhou 510006, China

JS. It has been demonstrated that *Arl13b* is critical for processes of neural development, such as interneuron migration and placement [5], polarized radial glial scaffold formation [6], and neural tube patterning [7]. *Arl13b* might also be involved in photoreceptor degeneration and kidney cysts [8, 9]. However, the role of *Arl13b* in cerebellar development remains a mystery.

The zebrafish has been established as a model organism in studying JS [9, 10]. Here, we explored the role of *arl13b* in early development of the cerebellum and we hope use this powerful model to investigate the pathological mechanisms of JS and help to screen for therapeutic targets.

Materials and Methods

Zebrafish Maintenance and Embryo Collection

All zebrafish lines were raised and maintained under a photoperiod of 14 h/10 h (light/dark) at 28.5°C in our facility supplied with filtered fresh circulating water. Wild-type zebrafish of the AB strain and the *arl13b* mutants were kindly provided by Dr. Ying Cao (Tongji University, Shanghai, China) and the *Tg(neurod1:EGFP)* transgenic zebrafish were a gift from Dr. Jing-Wei Xiong (Peking University, Beijing, China). *arl13b* homozygous mutants only survive up to 10 days, so heterozygous mutants were mated to produce homozygous embryos. The homozygous embryos were picked according to the curved tail since this phenotype is almost fully penetrant. The developmental stages of zebrafish were characterized following previously-described morphological criteria [11]. Fish embryos and larvae for *in situ* hybridization and immunostaining were raised in E3 supplemented with 0.003% phenylthiourea from 24 hpf onward to prevent pigment formation. All handling procedures were approved by the Ethics Review Committee at Nanchang University.

Morpholino Oligonucleotide Microinjection

The morpholino (MO) antisense oligonucleotide blocking the translation of *arl13b* (5'-TTTCCCCCTAAATGCTT TCACTGG-3') described previously [9] was purchased from Gene Tools LLC (Philomath, OR, USA). The MO was microinjected into zebrafish embryonic yolk at the one- to two-cell stage.

Imaging of Zebrafish and Behavior

The morphology of the zebrafish larvae (otolith and body curvature) was imaged at 4 dpf using a Nikon AZ100 microscope (Nikon, Tokyo, Japan). The larvae were raised in Petri dishes and transferred to a new dish at 5 dpf for

behavioral analysis. After allowing adaptation to the new environment for 5 min, locomotion was video-recorded for 3 min using a Nikon DS-Fi1 digital camera and processed with NIS-Elements F3.0 (Nikon).

Whole-Mount *In Situ* Hybridization

We made RNA probes from different templates: PCR products and linearized plasmid DNA. For PCR-based *in situ* templates, we designed PCR primers (listed in Supplemental Table 1) to amplify gene-specific products that contained the T3 promoter sequence, and RNA probes were transcribed *in vitro* using T3-RNA-polymerase. For the linearized plasmid DNA-based *in situ* templates, *shh* (HindIII/T7), *atoh1a* (Nco I /SP6), *ptf1a* (Nco I/SP6), *reelin* (NcoI/SP6), and *rora* (ApaI/SP6), the last four plasmids were kindly provided by Dr. Sheng-Ping L. Hwang (Institute of Cellular and Organismic Biology, Academia Sinica, Taipei, China). The antisense RNA probes were synthesized with T7 or SP6 RNA polymerase after plasmid DNA linearization. Whole-mount *in situ* hybridization was performed using digoxigenin-labeled antisense RNA probes and alkaline phosphatase-conjugated anti-digoxigenin antibodies (Roche, Mannheim, Germany), as described previously [12]. Embryos were mounted in glycerol, and images were captured using a Nikon AZ100 microscope.

RNA Isolation and Quantitative Real-Time PCR (qPCR)

Total RNA was extracted from the embryos using RNAiso Plus following the manufacturer's protocol (Takara, Shiga, Japan). Reverse-transcription reactions were carried out with M-MLV reverse transcriptase (Takara). qPCR assays were performed with SYBR Premix Ex Taq II (Takara) on the Abi-Step-One plus Real-Time PCR system (Applied Biosystems, Foster City, CA, USA). All the primer sequences used for qPCR are listed in Supplemental Table 2. All experiments were conducted at least three times. Student's *t*-test was applied to analyze the data and $P < 0.05$ was indicated a statistically significant difference.

Immunostaining

For tubulin antibody staining, we fixed larvae with 2% trichloroacetic acid in PBS for 3 h at room temperature. For other antibodies, we fixed larvae overnight at 4°C in 4% paraformaldehyde (PFA) in PBS supplemented with sucrose (4% w/v) [13]. The larvae were rinsed 3 times in 1×PBST (1×PBS and 0.8% Triton) for 10 min each. Afterward, larvae were dehydrated and rehydrated through graded methanols (50% MeOH once, 100% twice, and 50%

once, 10 min each), and then rinsed 3 times in 1×PBST for 5 min each. The larvae were immersed in ice-cold acetone for 20 min at −20 °C, rinsed 3 times in 1×PBST for 5 min each and digested with proteinase K for permeabilization. The concentration and treatment time of proteinase K was determined by the developmental stages of the larvae. After digestion, the larvae were re-fixed with fresh 4% PFA in 1×PBS for 20 min at room temperature (RT), and then rinsed 3 times in 1×PBST for 10 min each. The larvae were blocked with buffer containing 10% serum and 1% dimethylsulfoxide in 1×PBST for 3 h at RT and incubated with primary antibody overnight at 4°C. After rinsing 4 times in 1×PBST for 30 min each, the larvae were incubated with secondary antibody for 4 h at RT. The larvae were rinsed and counterstained with Hoechst 33342 (10 µg/mL) for nuclear staining. The following primary antibodies were used: mouse anti-tubulin (1:1000, T6793, Sigma), mouse anti-parvalbumin (1:1000, MAB1572, Chemicon), goat 3A10 (1:1000, DSHB), and goat anti-GFP (1:500, 600-101-215, Rockland). For fluorescence detection, we used Alexa Fluor 488 donkey anti-goat IgG (H+L) (1:500, A11055, Invitrogen) and Alexa Fluor 488 donkey anti-mouse IgG (H+L) (1:500, A21202, Invitrogen). Fluorescence images of larvae were acquired using an Olympus FV1000 confocal microscope, and Z-series stacks were shown as two-dimensional projections.

Lithium Treatment

Embryos at 30–37 hpf were incubated in E3 containing LiCl (A100416-0025, Sangon) at a final concentration of 50 mmol/L. Age-matched untreated embryos served as controls.

Results

Depletion of *arll3b* Impairs Posture and Locomotion in Zebrafish Larvae

In order to explore the function of ARL13B *in vivo*, we started to investigate whether the neurological features of JS are mimicked in *arll3b* mutant zebrafish, an established model organism [4, 9]. The null mutation of *arll3b* (*arll3b*^{−/−}), identified in a retroviral insertion screen, led to body axis curvature (Fig. S1) [4, 14]. The curved tail phenotype is almost fully penetrant in homozygous embryos while it is rarely found in wild-type and heterozygous embryos [4]. We took advantage of this readily-recognizable morphological phenotype to pick homozygous mutants for further experiments. The picked embryos were genotyped by PCR which confirmed retroviral insertion into the first exon of the *arll3b* gene.

Furthermore, qPCR results demonstrated that the expression of *arll3b* mRNA was almost undetectable in the picked embryos, while it was normally-expressed in wild-type embryos (Fig. S3). The *arll3b*^{−/−} mutant larvae [5 days post-fertilization (dpf)] were usually motionless and occasionally moved by trembling and circling. These abnormal movements were not found in wild-type larvae, which swam around freely and elegantly (Movie 1).

To assess the phenotype specificity and confirm the locomotor defects, we performed transient knockdown experiments with an antisense morpholino oligonucleotide (MO) designed to specifically block the translation of Arll3b [9]. After injecting 9.7 ng *arll3b* MO into embryos, we observed body curvature and abnormal locomotion like that in *arll3b*^{−/−} mutants (Movie 1). Considering that the curvature might interfere with locomotion, we injected a subthreshold dose of MO (7.3 ng) and found that the larvae showed no apparent body axis defects while they still exhibited impairments in posture and locomotion (Movie 1). Wild-type larvae maintained a normal posture (Fig. 1A). In contrast, the subthreshold-dose morphants usually laid on their sides, i.e., lost posture (Fig. 1B, C). As for the swimming patterns, wild-type larvae often exhibited spontaneous swimming characterized by small bending angles (Fig. 1D). However, the subthreshold-dose morphants swam with trembling and exhibited large bending angles (Fig. 1E). The subthreshold-dose results suggested that the posture and locomotion defects in *arll3b* mutants and morphants are due to the depletion of *arll3b* rather than body curvature.

In addition, the sensation of *arll3b* mutants and morphants was compromised; they were not sensitive to a needle poke, while wild-type embryos were sensitive and swam away quickly (Movie 1).

Taken together, the above results suggested that zebrafish deficient in *arll3b* exhibit impairments in posture and swimming pattern, reminiscent of the signs of JS.

Depletion of *arll3b* Results in Morphological Defects of the Cerebellum

The above behavioral defects suggested the *arll3b*-deficient zebrafish might serve as a good model for studying JS. We first investigated the development of the cerebellum since it is the main cause of the characteristic molar tooth sign in JS. The outline of the cerebellum can easily be distinguished by immunostaining with an anti-tubulin antibody (Fig. 1F). Obvious morphological defects were found in the cerebella of both *arll3b* mutants and morphants, and the antibody-labeled fibers were globally reduced (Fig. 1G, H). The posterior outline of the cerebellum was thinner than that of the wild-type and invaginated anteriorly at the midline, while the anterior outline was

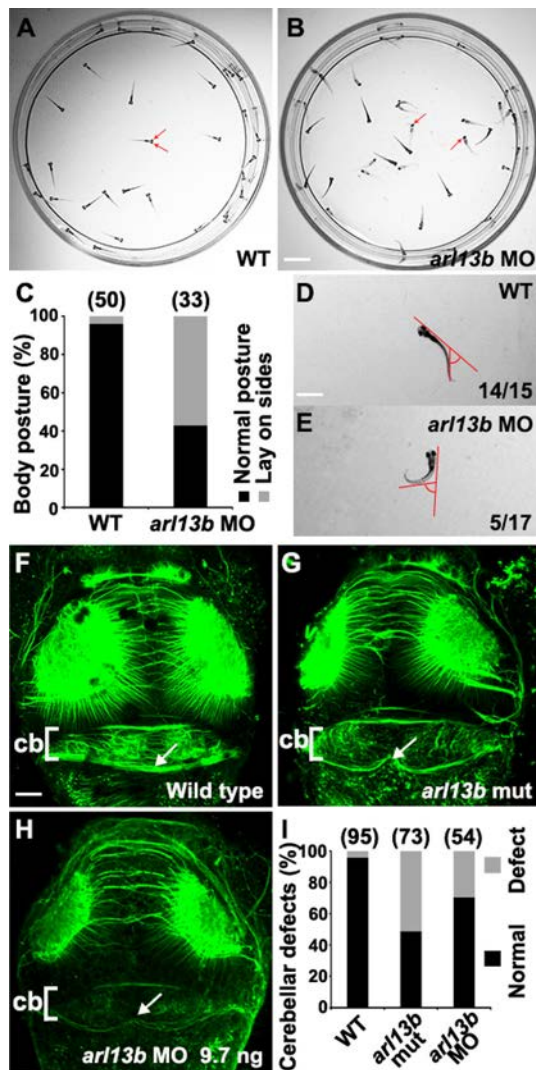


Fig. 1 Knockdown of *arl13b* impairs posture, locomotion, and cerebellar morphology in zebrafish larvae. **A** Wild-type sibling larvae remain vertically oriented at 5 days post-fertilization (dpf), with both eyes visible from a top view (arrows). **B** In contrast, larvae injected with *arl13b* MO (subthreshold dose, 7.3 ng) often lie on their side at the bottom of the dish, with only one eye visible (arrows). Note that the body of the subthreshold-dose *arl13b* morphants are relatively straight and only slightly curved. **C** Statistics of the posture of zebrafish larvae at 5 dpf. **D** Wild-type larvae perform stereotyped spontaneous swimming with small bending angles. **E** The *arl13b* morphants (subthreshold dose, 7.3 ng) swim slower and exhibit greater bending angles. **F–H** Immunostaining with acetylated tubulin antibody outlines the cerebellum of larvae at 3 dpf. Comparing the dorsal view of wild-type embryos (**F**) with *arl13b* mutants (**G**) reveals morphological defects of the cerebellum (arrows). The cerebellar defects were also present in embryos injected with *arl13b* MO (**H**) (cb, cerebellum). **I** Statistics of the embryos with morphological defects of the cerebellum. The number of embryos examined in each condition is indicated above each column. **A–E**, Scale bar 1 cm. **F–H**, Scale bar 100 μ m.

relatively normal (Fig. 1F–I). Moreover, the acetyl-tubulin-positive parallel fibers connecting the cerebellar hemispheres were disturbed in *arl13b*-deficient larvae while the

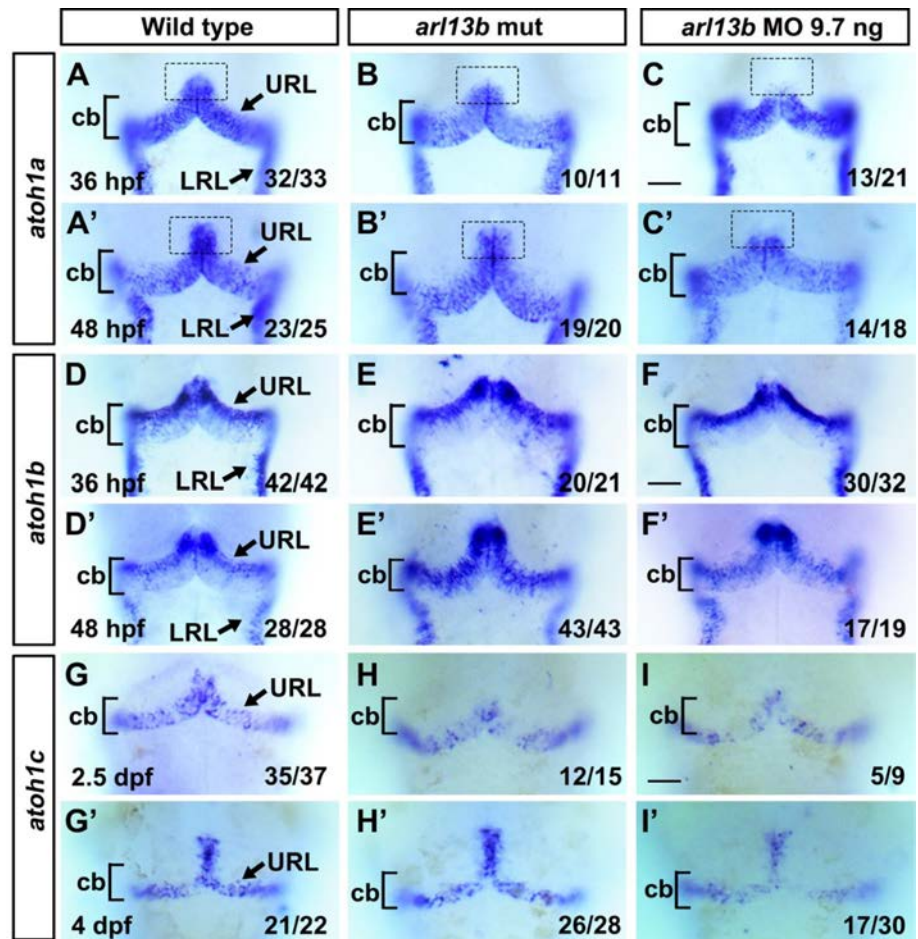
commissural axons between the optic tecta remained largely unaffected (Fig. 1F–H). The midline cerebellar defects in *arl13b* mutants and morphants are reminiscent of the midline cerebellar defects in JS patients [2].

Besides the cerebellum, we also checked other neural tissues. *arl13b* is highly expressed in the ventricle and otic vesicle at early developmental stages [9]; the ciliated cells in the inner ear are important for the formation of otoliths [15]. Usually, there are two otoliths in zebrafish (Fig. S1). The otoliths are critical for proper balance and hearing, and their impairment might contribute to the postural and locomotor defects in *arl13b*-depleted larvae. We also checked motor axons and Mauthner axons, which are involved in locomotion. No morphological defect was observed in either acetylated tubulin-positive motor axons or 3A10-positive Mauthner axons (Fig. S2). We focused on the cerebellum in the subsequent experiments since cerebellar malformation is a major hallmark of JS.

Depletion of *arl13b* Impairs Granule Cell Progenitors in the Developing Cerebellum

The morphological defects in *arl13b*-deficient embryos prompted us to further investigate the role of *arl13b* in the development of cerebellar neural circuits. Like mammals, the zebrafish cerebellum is derived from the dorsal part of the anterior hindbrain [16]. The cerebellum is composed of several types of neurons, which are categorized according to their major neurotransmitter, glutamate or GABA. The glutamatergic granule neurons are derived from granule cell progenitors located in the upper rhombic lip (URL). Granule cells are the most abundant type of neuron in the cerebellum. We first examined the expression of the granule progenitor cell marker *atoh1* using whole-mount *in situ* hybridization. In zebrafish, there are three paralogues of *atoh1* – *1a*, *1b*, and *1c* – which are expressed sequentially in overlapping but distinct granule cell progenitors within the rhombic lip [17, 18]. In wild-type embryos, *atoh1a* was strongly expressed in the URL and the lateral rhombic lip (Fig. 2A). In some *arl13b* morphants, *atoh1a* was absent from the anterior dorsomedial URL along the midline (Fig. 2C). The specific absence of *atoh1a* was maintained at 48 hours post-fertilization (hpf) (Fig. 2A'–C'), suggesting that the phenotype could not be due to developmental delay. No detectable change of *atoh1b* was found (Fig. 2D–F'), indicating that the absence of *atoh1a* dorsomedially was specific and not due to defects in cerebellar structure. The expression level of *atoh1c* was decreased in *arl13b* morphants at 2.5 dpf and 4 dpf (Fig. 2G–I'). In *arl13b* mutants, *atoh1c* was decreased slightly at 2.5 dpf (Fig. 2H). The expression defects of

Fig. 2 The expression of markers of cerebellar granule cell progenitors is impaired in *ar13b*-deficient embryos. **A–I'** Representative images of *in situ* hybridization illustrate that the three paralogues of *atoh1* (*atoh1a*, *1b* and *1c*) are expressed in distinct populations of cerebellar granule cell progenitors. *atoh1a* is expressed in the URL and LRL. Similar expression patterns of *atoh1a* occur in wild-type embryos (**A**) and *ar13b* mutants (**B**) while its expression is absent from the oral dorsomedial URL (dashed box) in *ar13b* morphants (**C**) at 36 hpf and 48 hpf (**A'–C'**). The expression patterns of *atoh1b* remained unaffected in *ar13b* mutants and morphants (**D–F'**). The expression level of *atoh1c* was decreased in the URL in *ar13b* morphants (**I** and **I'**) (cb, cerebellum; URL, upper rhombic lip; LRL, lower rhombic lip). **A–I'**, Scale bar 100 μ m.



atoh1a and *atoh1c* were more apparent in *ar13b* morphants than in mutants. This could be due to the maternally-deposited *ar13b* mRNA in null mutants which might mask the early defects caused by Arl13b deficiency [9]. The MO blocks the translation of *ar13b* mRNA, including the maternally-derived mRNA, so the phenotypes in morphants are more penetrant than in mutants [9]. However, potential off-target effects of the MO could not be excluded although it seems unlikely since most phenotypes have been reported in *ar13b* mutants [9] (and our data).

We performed quantitative PCR (qPCR) using whole body tissues to verify the above results. *atoh1c* was consistently down-regulated in *ar13b* mutants from 36 hpf to 4 dpf (Fig. S3). However, *atoh1a* and *1b* were up-regulated at 36 hpf but down-regulated at later stages, when comparing *ar13b* mutants with the wild-type (Fig. S3). It should be noted that we used the whole zebrafish body and the qPCR results represented the mixed expression of all tissues. According to our *in situ* hybridization results and those of others [17, 18], *atoh1c* is mainly expressed in the URL (Fig. 2). The decrease of

atoh1c in *ar13b* mutants revealed by qPCR indicated that *atoh1c* is reduced mainly in the URL and confirmed our *in situ* hybridization results.

atoh1c and *1a* are critical for the full complement of granule cells in the corpus cerebelli (CCe), a structure homologous to the mammalian cerebellar vermis [17, 19]. The decrease of *atoh1a* and particularly *atoh1c* revealed by *in situ* hybridization and qPCR in *ar13b*-deficient embryos might interfere with the development of granule cells in the CCe.

Zic1 has been shown to be involved in mouse granule cell proliferation [20]. We found that *zic1* was expressed in the URL cells in wild-type zebrafish at 48 hpf while it was dramatically down-regulated in *ar13b* morphants and mutants (Fig. 3A–C).

These results suggested that Arl13b participates in cerebellar development by regulating the development of granule cell progenitors.

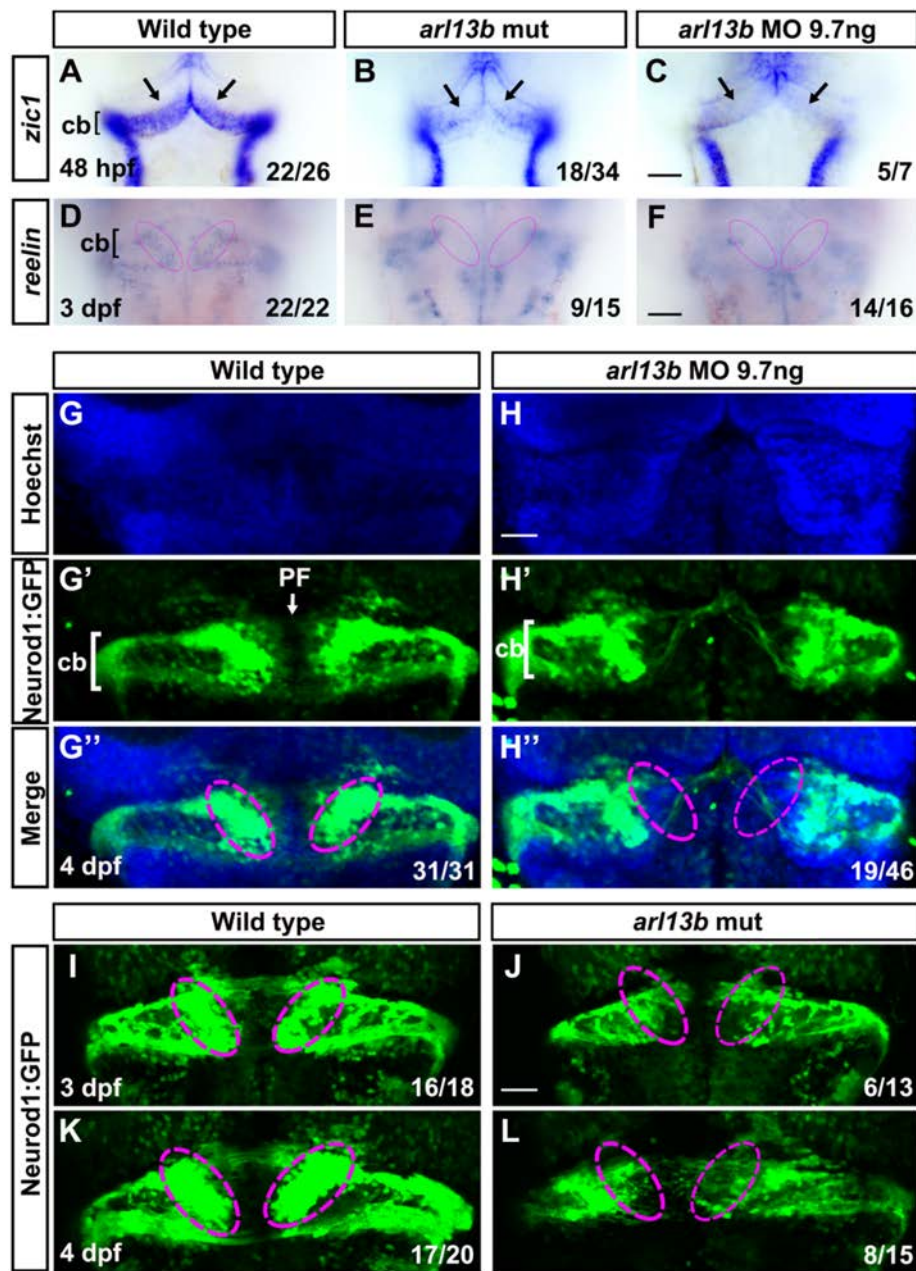


Fig. 3 Disruption of *arl13b* impairs the development of cerebellar granule cells. **A** Expression of the granule cell progenitor marker, *zic1*, in the cerebellum of wild-type embryos at 48 hpf revealed by *in situ* hybridization. **B, C** Expression of *zic1* is reduced in the URL of both *arl13b* mutant and morphant embryos compared with wild-type embryos. Note that *zic1* expression is severely reduced in the dorsomedial subregions of the URL (arrows). **D** The expression of the differentiated granule cell marker, *reelin*, in the cerebellum of wild-type embryos at 3 dpf. **E, F** Expression of *reelin* is reduced in the cerebellum of both *arl13b* mutant and morphant embryos. Note that in some embryos *reelin* expression is almost absent in the dorsal medial subregions of the cerebellum (colored ovals). **G–G''** In

Tg(neurod1:eGFP) transgenic embryos, GFP+ granule cells are grouped into three clusters, the dorsomedial (dashed ovals), dorso-posterior, and ventrolateral subdivisions. **H–H''** The pattern of GFP+ granule cells is dramatically altered in the cerebellum, and particularly in the dorsomedial cerebellar subdivisions (dashed ovals) are severely affected in *arl13b* morphants. The parallel fibers connecting the two hemispheres are disrupted in *arl13b* morphants. Dorsal views of the embryos are shown. **I–L** Malformations of the dorsomedial cerebellar subdivisions (dashed ovals) and parallel fibers are also present in *arl13b* mutants both at 3 dpf and 4 dpf. cb, cerebellum; PF, parallel fiber. **A–F**, Scale bar 100 μ m. **G–L**, Scale bar 50 μ m.

Depletion of *ar13b* Impairs Granule Neurons Specifically in the Corpus Cerebelli

The impairment of granule cell progenitors might interfere with the subsequent development of granule neurons, so we next examined the differentiation of granule neurons. We found that *reelin*, a marker of differentiated granule cells [21], was markedly decreased in the cerebellum of *ar13b*-deficient embryos, particularly in the dorsomedial subregions (Fig. 3D–F). It has been demonstrated that *NEUROD1* is expressed in immature and mature cerebellar granule neurons in both mammals and zebrafish [18, 22]. We found that *neurod1* was absent from the dorsomedial cerebella of *ar13b* morphants (Fig. S4) while the dorsolateral neurons were not affected, similar to the expression of *reelin*. We further examined the development of cerebellar granule cells using the transgenic line *Tg(neurod1:EGFP)* [23]. In these embryos, GFP was expressed in three main clusters: two close to the midline, the dorsomedial and dorsoposterior granule cells, and one distant from the midline, the ventrolateral granule cells (Fig. 3G–G’). The patterns of the *Tg(neurod1:EGFP)* GFP+ granule cells resembled the granule cells labeled by *Tg(gatal:GFP)* [19]. Knocking down *ar13b* in *Tg(neurod1:EGFP)* embryos caused a global reduction of GFP+ granule neurons compared to the control transgenic embryos. Particularly, the dorsomedial clusters were severely affected and, in some embryos, these clusters were totally absent (Fig. 3H–H’). The ventrolateral and dorsoposterior clusters were still present though with reduced numbers of GFP+ neurons (Fig. 3H–H’). These results were consistent with the expression pattern of *neurod1* detected by *in situ* hybridization (Fig. S4). The dorsomedial subdivision of granule neurons populate the CCE [17, 19]. The defects of CCE granule cells in *ar13b*-deficient zebrafish resembled the defects in the cerebellar vermis found in JS patients. *Tg(neurod1:EGFP)* labeled some parallel fibers at the midline of cerebellum (Fig. 3G’). Upon *ar13b* knockdown, the parallel fibers were dramatically disrupted (Fig. 3H’), similar to those found by anti-tubulin immunostaining (Fig. 1F–I). These phenotypes were also found in *ar13b* mutants (Fig. 3I–L). The *ar13b* mutants were crossed with *Tg(neurod1:EGFP)* fish and transgenic labeled *ar13b* homozygotes were picked. The selective malformation of CCE granule cells and disruption of parallel fibers were frequently observed in *ar13b* mutants both at 3 dpf (Fig. 3I, J) and 4 dpf (Fig. 3K, L).

The qPCR results revealed that the markers of differentiated granule cells *calbindin 2a* (*calretinin*, *calb2a*) and GABA receptor alpha 6a (*gabrab6a*) were dramatically reduced in *ar13b* mutants (Fig. S3). These results suggested that not only the proliferation and migration but also

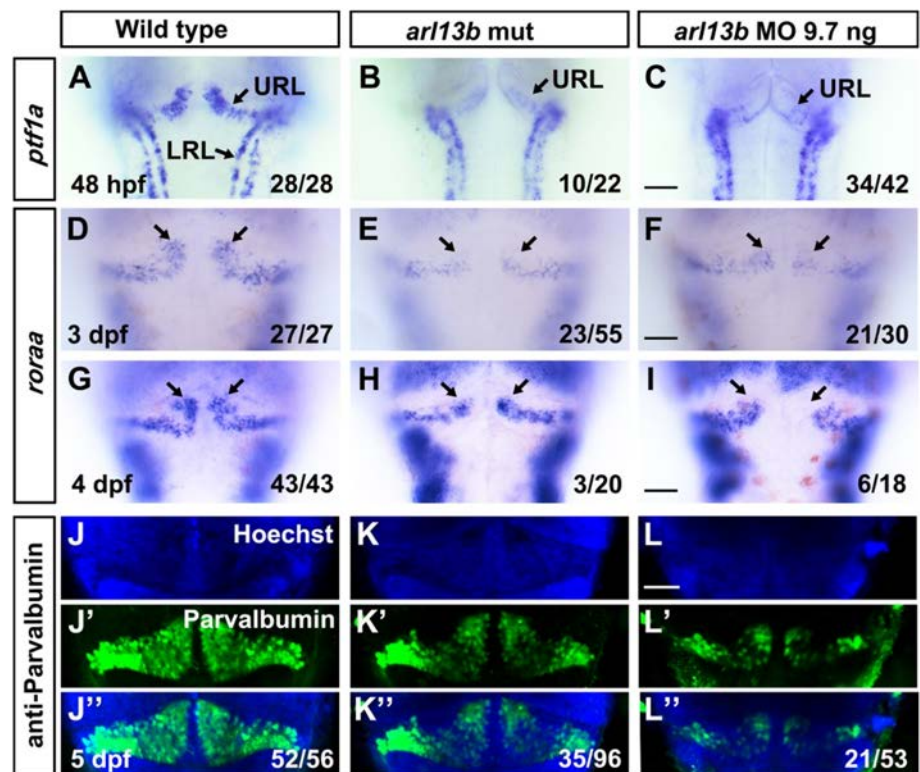
the differentiation of granule cells is impaired in *ar13b*-deficient embryos.

Depletion of *ar13b* Impairs the Development of Cerebellar Purkinje Cells

Both the function and development of the cerebellum are dependent on the cooperation between granule neurons and Purkinje cells, two major neuronal types in the cerebellum, so we further investigated the role of *ar13b* in the development of Purkinje cells. *ptfla* was used as a marker to label the precursors of Purkinje cells by *in situ* hybridization and it was found to be expressed in the ventricular zone of wild-type embryos at 48 hpf (Fig. 4A). In *ar13b* mutant and morphant embryos, the expression level of *ptfla* was dramatically and selectively reduced in the dorsomedial ventricular zone, while it was relatively normal in the ventrolateral regions (Fig. 4B, C). The phenotype of morphants was more penetrating than that of mutants, as found in granule cells. These results demonstrated that the progenitors of Purkinje cells are selectively reduced dorsomedially in *ar13b*-deficient embryos. We further examined differentiating Purkinje cells using *roraa* as a marker [24]. This revealed that the dorsomedial clusters of differentiating Purkinje cells were dramatically reduced, while the ventrolateral clusters were only mildly reduced in *ar13b*-deficient embryos at 3 dpf (Fig. 4D–F). This is reminiscent of the selective reduction of dorsomedial granule cell clusters (Fig. 3). A similar decrease of dorsomedial clusters was observed at 4 dpf (Fig. 4G–I). As Purkinje cells differentiate and mature, early distinct clusters of Purkinje cells merge together, become unified, and form a continuous layer spanning the mediolateral width of the cerebellum [25]. Immunostaining with an antibody against parvalbumin was used to label differentiated Purkinje cells and demonstrated that they were dramatically reduced globally in the cerebellum at 5 dpf, including both the dorsomedial and ventrolateral clusters (Fig. 4K–L’). qPCR results revealed that the markers of immature and mature Purkinje cells *roraa*, *aldoca*, and *pvalb7* were reduced (Fig. S3D), consistent with the immunostaining results.

The global reduction of mature Purkinje cells differed from the specific reduction of dorsomedial clusters of granule cells at the late larval stage. The early specific dorsomedial defects of both Purkinje progenitors and granule progenitors are likely due to unknown common defects in the mechanisms required and partly shared by the two types of neural progenitor.

Fig. 4 Disruption of *arl13b* reduces both precursor and differentiated cerebellar Purkinje cells. **A–I** Representative images of *in situ* hybridization using anti-sense probes against *ptfla* and *roraa* to label Purkinje precursors and differentiated cells, respectively. The dorsomedial clusters of precursor of Purkinje cells and differentiated Purkinje neurons are selectively reduced (arrows). **J–L''** Immunostaining of mature Purkinje neurons using anti-parvalbumin antibody reveals that the dorsomedial Purkinje neurons are reduced in *arl13b*-deficient embryos. **A–I**, Scale bar 100 μ m. **J–L''** Scale bar 50 μ m.



Depletion of *arl13b* Reduces *wnt1* Expression in the Developing Cerebellum

Arl13b has been demonstrated to be associated with Hedgehog signaling pathways [7, 26, 27], so we examined the expression of Hedgehog signaling components by *in situ* hybridization and qPCR. *shh* was not detected in the cerebellar anlage at 24 hpf although it was ventrally expressed along the neural tube (Fig. S5). No detectable change of *shh* expression in the cerebellum was observed in *arl13b* morphants, although its expression in the zona limitans intrathalamica was reduced dorsally (Fig. S5). The expression level of the hedgehog receptor *patched1* was relatively low (Fig. S5). It was hard to tell whether it was expressed in the cerebellum in wild-type embryos at 30 hpf as well as whether its expression level or pattern changed. We then used qPCR to assess the expression levels of Shh signaling components. The expression of the receptors *smoothen* (*smo*) and *patched1* (*pch1*), and the Hedgehog signaling components *gli2a*, *gli2b*, and *gli3* were dynamically regulated in the early stages of cerebellar development (Fig. S5). These results suggested that Hedgehog signaling components are altered globally in *arl13b* mutants while no detectable change occurs early in cerebellar development.

Wnt signaling is also critical for cerebellar development [28] and cooperates with Hedgehog signaling to regulate cerebellar olig2+ cell development [29]. Intriguingly,

recessive mutations of human *WNT1* result in hypoplasia of the cerebellum, particularly of the vermis, suggesting a conserved role of WNT1 in vermis development [30]. Besides being mainly expressed at the midbrain–hindbrain boundary, in mice *wnt1* is also transiently expressed in the URL [31], from which many cerebellar neurons are derived. The transient expression of *wnt1* in the URL is conserved in zebrafish [29]. We found that *wnt1* was transiently expressed in the dorsal cerebellum at 30 hpf in wild-type embryos (Fig. 5A). Its expression was strikingly reduced and almost absent from the cerebellum of some *arl13b* mutants (Fig. 5B), indicating that Wnt signaling is disrupted early in cerebellar development.

Activating Wnt Signaling Partially Rescues Cerebellar Defects in *arl13b* Mutants

We started to explore whether activating Wnt signaling with lithium, an agonist of Wnt signaling, can mitigate the cerebellar defects in *arl13b*-deficient embryos. The dose of lithium chloride (LiCl) was optimized for different developmental stages. We found that treating the embryos with 50 mmol/L LiCl at 30–37 hpf reduced the cerebellar structural defects in *arl13b* mutants. The wild-type embryos treated with LiCl at the same time showed no detectable cerebellar defects (Fig. 6A–E). We further examined the rescue effects of LiCl with *Tg(neurod1:EGFP)* embryos and found that the dorsomedial

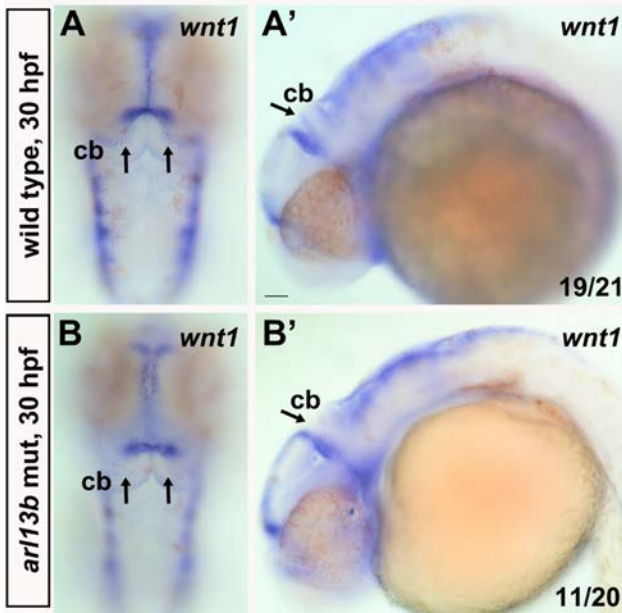


Fig. 5 Wnt1 is selectively down-regulated in the cerebellum of *ar13b* mutants. *wnt1* is transiently expressed in the cerebellum of WT embryos (A, A') (arrows) while it is dramatically reduced in *ar13b* mutants (B, B'). A and B, dorsal view; A' and B', lateral view. Note that the expression of *wnt1* is selectively decreased in the cerebellum while its expression at the midbrain–hindbrain boundary is intact. A–B', Scale bar 100 μ m.

reduction of granule cells caused by *ar13b* knockdown was mitigated by LiCl treatment (Fig. 6F–J).

Discussion

Most published papers study the role of JS genes during late embryonic or postnatal development of the cerebellum, though the molar tooth sign can be detected early in the first trimester [32]. Moreover, these studies mainly focus on cerebellar granule cells. In this study, we found that the disruption of *ar13b* in zebrafish larvae leads to early cerebellar malformations and defects in both granule and Purkinje cell progenitors. The early developmental patterning of cerebellar granule neurons is compromised particularly in the dorsomedial subregions of the CCE, a structure homologous to the mammalian cerebellar vermis. This phenotype is reminiscent of hypoplasia of the cerebellar vermis in JS. Molecular and cellular studies revealed that the early development of the progenitors of both granule cells and Purkinje cells are selectively altered in *ar13b*-deficient embryos. Ar13b may be involved in regulating a network of signaling pathways, including Wnt and Atoh1. Treating the *ar13b* mutants with Li⁺, an agonist of Wnt signaling, partially rescued the cerebellar defects.

Our finding that granule neurons are reduced specifically in the dorsomedial subregions of the CCE in *ar13b*-deficient zebrafish larvae is consistent with the enrichment of *ar13b* expression in the ventricle at early stages, from 25 hpf to 40 hpf and later [9, 33]. This finding is also consistent with reports that granule neurons are reduced

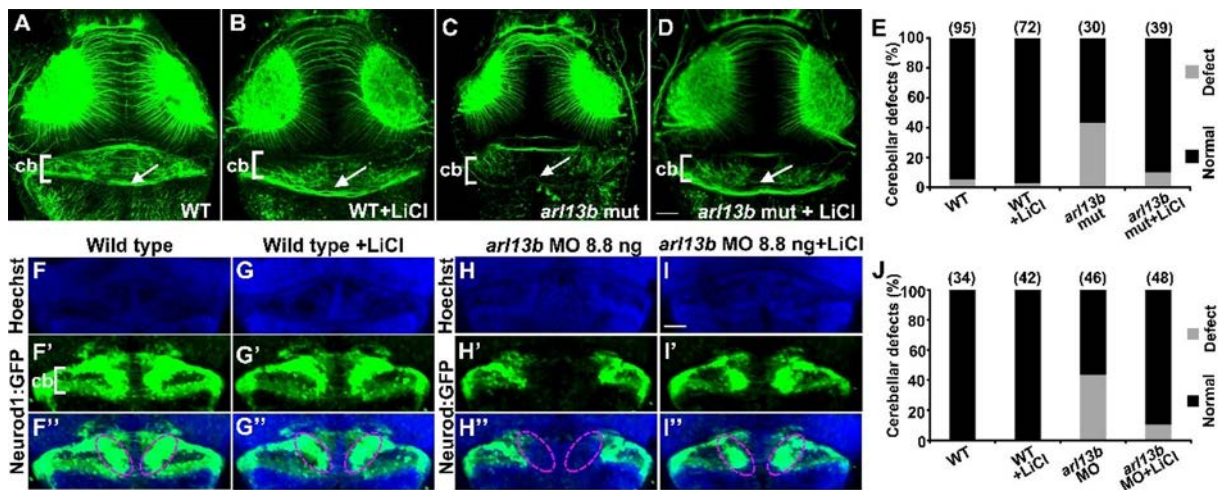


Fig. 6 Treating the *ar13b* mutants with lithium mitigates the morphological defects in the cerebellum. A–D Representative images of embryos treated with 50 mmol/L LiCl at 30–37 hpf, fixed at 3 dpf, and immunostained with anti-tubulin antibody to reveal cerebellar morphology. Treatment of wild-type embryos with Li⁺ does not affect the cerebellar morphology (A, B) (arrows). The morphological defects of the cerebellum in *ar13b* mutants treated with Li⁺ are partially rescued (C, D) (arrow). A–D, Scale bar 100 μ m. E Statistics revealing that the proportion of *ar13b* mutant embryos with

cerebellar defects is dramatically decreased by LiCl treatment. F–I' Representative images of *Tg(neurod1:EGFP)* transgenic embryos used to label granule cells. Treating wild-type transgenic embryos with Li⁺ causes no defect (F–G'') (dashed ovals). Treating *ar13b* morphant transgenic embryos restores the dorsomedial cluster of granule cells (H–I'') (dashed ovals). F–I'', Scale bar 100 μ m. J The proportion of *ar13b* morphant embryos with cerebellar defects in the dorsomedial clusters is dramatically reduced by LiCl treatment.

along the anteroposterior but not the mediolateral axis in mouse mutants of the cilia genes *Kif3a*, *Ift8*, or *Rpgrip11* [34, 35]. The reduction of granule neurons in these mutants could be caused by proliferation defects in granule progenitors [34, 35]. Although the cerebellar granule neurons in *Ahi1*- or *Cep290*- knockout mice are only slightly affected, there are significant proliferation defects of granule cells at an early developmental stage (E16.5) [2]. Proliferation defects of granule progenitors seem to be common in these cilia gene mutants [3, 34, 35]. The reduction of granule neurons in *ar13b*-deficient zebrafish was likely caused by proliferation defects in granule progenitors since the expression pattern of *atoh1a* was altered and *atoh1c* was dramatically down-regulated (Fig. 2 and S3). Atoh1 is known to be critical for cerebellar granule neurogenesis in the mouse [36] and for the proliferation of granule cells in zebrafish [18]. *atoh1c*-derived cells contribute to the majority of granule neurons in the CCe, while a minority is derived from *atoh1a* progenitors [17, 18]. The dramatic down-regulation of *atoh1c* and the selective hypoplasia of the CCe in *ar13b*-deficient embryos are consistent with the critical role of *atoh1c* in populating granule neurons in the CCe [17]. The dramatically decreased expression of *zic1* and *neurod1* specifically in the dorsomedial subregions of the cerebellum (Figs. 2 and S4) is also consistent with the proliferation defects of granule progenitors since both genes are implicated in granule cell proliferation [18, 20]. We immunostained the embryos using anti-pH3 antibody, a marker of cell proliferation, and found reduced fluorescence intensity of pH3-positive cells in the cerebellum of *ar13b* mutants (Fig. S6). These results are consistent with potential proliferation defects of granule cells in the cerebellum.

It has been shown that Arl13b regulates the migration and location of interneurons [5]. The specific hypoplasia of the dorsomedial subregions of the CCe in *ar13b*-deficient zebrafish could also be due to migration defects in granule cell precursors. It has been demonstrated that the URL generates different populations of granule cell precursors along its mediolateral axis. These precursors migrate along different routes and form different functional compartments of the mature cerebellum: the eminentia granularis and the CCe [19]. Atoh1 has been shown to be critical for the migration of granule cell precursors out of the URL in mice and particularly Atoh1c in zebrafish [17, 36]. The reduction of *atoh1c* expression in *ar13b*-deficient zebrafish could lead to migration defects of the granule cell precursors. The migration defects might impair the differentiation of granule neurons since several markers of granule neurons are altered, particularly *neurod1*. The absence of *Tg(neurod1:EGFP)*+ cells in the dorsomedial domain of the cerebellum in *ar13b* mutants differs from

that seen in *atoh1c* mutants [17], in which *neurod1* is expressed in most of the *Tg(atoh1c:kaede)*+ granule cell progenitors, including the dorsomedial cells along the midline. These results suggest that depletion of *ar13b* also disrupts other signaling pathways besides Atoh1.

Wnt1 is transiently expressed in the cerebellum of zebrafish [29] (Fig. 5) and mouse [31] and its mutations in humans result in hypoplasia of the cerebellar vermis [30], indicating that Wnt signaling is a potential mechanism underlying the pathology of *ar13b* mutant zebrafish and humans. Besides *wnt1*, other *wnt* genes have also been detected in the cerebellum, such as *wnt3*, *wnt7a* and *wnt10b* [37], which might be involved in early cerebellar development [3, 38, 39]. Further study is required to investigate whether they are also regulated by Arl13b. The Wnt downstream signaling components β -catenin and Gsk3 β regulate the transcription and protein stability of Atoh1 [40, 41]. Wnt1 has been proposed to regulate Atoh1 expression in the developing cerebellum [31]. These reports are consistent with our findings that *atoh1c* and *1a* expression is reduced in *ar13b*-deficient embryos (Figs. 2 and S3). Moreover, *wnt1* is also expressed at the midbrain–hindbrain boundary and it has been speculated to contribute to the development of the cerebellum. Whether the boundary Wnt1 also contributes to the cerebellar defects in *ar13b*-deficient embryos needs further experiments. Lithium treatment partially rescues the cerebellar defects in both zebrafish *ar13b* (Fig. 6) and mouse *Ahi1* mutants [2], suggesting that Wnt signaling is a conserved key pathway regulating early cerebellar development and could serve as a common potential therapy target in JS. Atoh1 and Wnt signaling might only partially contribute to the mechanisms of Arl13b signaling since Arl13b has been found to be distributed subcellularly in the cilium and cytoplasm and is expressed in many tissues and cells.

Most JS research has focused on granule cells and has seldom dealt with Purkinje cells. In human JS samples, the migration of cerebellar Purkinje cells is faulty, with heterotopic and locally-interrupted Purkinje cell layers [42]. The malformation of the Purkinje cell monolayer has also been found in JS gene mutant mice [3, 43]. These late Purkinje cell defects could be due to an early developmental deficiency. It has been demonstrated that mutations of the JS gene *Zfp423/ZNF423* in the mouse impair the early development of Purkinje cell progenitors [44]. Our results also demonstrated that the progenitors of Purkinje cells were selectively disrupted in the dorsomedial cluster in *ar13b*-deficient embryos (Fig. 4), like the early defects in granule cell progenitors. The coincident selective defects of Purkinje and granule cell progenitors suggest that these two populations interact or share common mechanisms. Radial glia and the Bergmann glial cells derived from them provide a scaffold for the migration of both Purkinje cells

and granule cells early in cerebellar development [45, 46]. Ciliary *Arl13b* has been shown to be critical for the polarization of the radial glial scaffold and the laminar organization of neurons in mouse cerebral cortex [6]. The available evidence and our current results suggest that the role of *Arl13b* in neural development is conserved between species and *Arl13b* participates in the polarization of the radial glial scaffold as well as coordinating the proliferation and migration of both Purkinje cells and granule cells early in cerebellar development. The migration of Purkinje cells and granule cells also shares molecular mechanisms, such as Reelin signaling [45], the expression level of which was also selectively reduced in the dorsomedial cerebellum in *arll3b*-deficient embryos (Fig. 3).

Conclusions

We have established a JS model using *arll3b*-deficient zebrafish, which recapitulate some of the signs of JS, such as locomotor and cerebellar developmental defects. The disruption of *arll3b* resulted in a dramatic reduction of granule cells specifically in the CCE, a structure homologous to the human cerebellar vermis. The expression of the proneural gene *atoh1* in a subpopulation of granule cells was down-regulated in the cerebellum. The early development of Purkinje cells was also selectively disrupted in the dorsomedial cerebellum. *wnt1*, a gene transiently expressed early in cerebellar development, was dramatically down-regulated. Furthermore, activating Wnt signaling mitigated the granule cell defects caused by *arll3b*-disruption. Our results reveal the critical role of *arll3b* in the early development of cerebellar granule and Purkinje cells. We propose that the *arll3b*-deficient zebrafish can serve as a powerful tool to investigate the pathological mechanisms underlying JS.

Acknowledgements This work was supported by grants from the National Natural Science Foundation of China (31171044, 81160144, and 81760216) and the Young Scientist Project of Jiangxi Province, China (20122BCB23007). We thank Dr. Zhao-Xia Sun (Yale University) for kindly providing the *arll3b* mutants, Dr. Jing-Wei Xiong (Peking University) for the *Tg(neurod1:EGFP)* transgenic fish, and Dr. Sheng-Ping L. Hwang (Institute of Cellular and Organismic Biology, Academia Sinica, Taipei, China) for kindly providing plasmids. We specially thank Professor Shi-Wen Luo (Nanchang University) for critical discussion and valuable advice.

Conflict of interest The authors declare that they have no conflicts of interest.

Open Access This article is licensed under a Creative Commons Attribution 4.0 International License, which permits use, sharing, adaptation, distribution and reproduction in any medium or format, as long as you give appropriate credit to the original author(s) and the source, provide a link to the Creative Commons licence, and indicate

if changes were made. The images or other third party material in this article are included in the article's Creative Commons licence, unless indicated otherwise in a credit line to the material. If material is not included in the article's Creative Commons licence and your intended use is not permitted by statutory regulation or exceeds the permitted use, you will need to obtain permission directly from the copyright holder. To view a copy of this licence, visit <http://creativecommons.org/licenses/by/4.0/>.

References

- Romani M, Micalizzi A, Valente EM. Joubert syndrome: congenital cerebellar ataxia with the molar tooth. *Lancet Neurol* 2013, 12: 894–905.
- Lancaster MA, Gopal DJ, Kim J, Saleem SN, Silhavy JL, Louie CM, *et al.* Defective Wnt-dependent cerebellar midline fusion in a mouse model of Joubert syndrome. *Nat Med* 2011, 17: 726–731.
- Bashford AL, Subramanian V. Mice with a conditional deletion of *Talpid3* (KIAA0586)—a model for Joubert syndrome. *J Pathol* 2019, 248: 396–408.
- Cantagrel V, Silhavy JL, Bielas SL, Swistun D, Marsh SE, Bertrand JY, *et al.* Mutations in the cilia gene *ARL13B* lead to the classical form of Joubert syndrome. *Am J Hum Genet* 2008, 83: 170–179.
- Higginbotham H, Eom TY, Mariani LE, Bachleda A, Hirt J, Gukassyan V, *et al.* *Arl13b* in primary cilia regulates the migration and placement of interneurons in the developing cerebral cortex. *Dev Cell* 2012, 23: 925–938.
- Higginbotham H, Guo J, Yokota Y, Umberger NL, Su CY, Li J, *et al.* *Arl13b*-regulated cilia activities are essential for polarized radial glial scaffold formation. *Nat Neurosci* 2013, 16: 1000–1007.
- Caspary T, Larkins CE, Anderson KV. The graded response to sonic Hedgehog depends on cilia architecture. *Dev Cell* 2007, 12: 767–778.
- Song P, Dudinsky L, Fogerty J, Gaivin R, Perkins BD. *Arl13b* interacts with *Vangl2* to regulate cilia and photoreceptor outer segment length in zebrafish. *Invest Ophthalmol Vis Sci* 2016, 57: 4517–4526.
- Duldulao NA, Lee S, Sun Z. Cilia localization is essential for in vivo functions of the Joubert syndrome protein *Arl13b/Scorpion*. *Development* 2009, 136: 4033–4042.
- Zhu L, Chen L, Yan L, Perkins BD, Li S, Li B, *et al.* Mutant *Ahl1* affects retinal axon projection in zebrafish via toxic gain of function. *Front Cell Neurosci* 2019, 13: 81.
- Kimmel CB, Ballard WW, Kimmel SR, Ullmann B, Schilling TF. Stages of embryonic development of the zebrafish. *Dev Dyn* 1995, 203: 253–310.
- Liu ZZ, Zhu J, Wang CL, Wang X, Han YY, Liu LY, *et al.* *CRMP2* and *CRMP4* are differentially required for axon guidance and growth in zebrafish retinal neurons. *Neural Plast* 2018, 2018: 8791304.
- Mu Z, Zhang S, He C, Hou H, Liu D, Hu N, *et al.* Expression of *SoxC* transcription factors during zebrafish retinal and optic nerve regeneration. *Neurosci Bull* 2017, 33: 53–61.
- Sun Z, Amsterdam A, Pazour GJ, Cole DG, Miller MS, Hopkins N. A genetic screen in zebrafish identifies cilia genes as a principal cause of cystic kidney. *Development* 2004, 131: 4085–4093.
- Riley BB, Zhu C, Janetopoulos C, Aufderheide KJ. A critical period of ear development controlled by distinct populations of ciliated cells in the zebrafish. *Dev Biol* 1997, 191: 191–201.

16. Hibi M, Shimizu T. Development of the cerebellum and cerebellar neural circuits. *Dev Neurobiol* 2012, 72: 282–301.
17. Kidwell CU, Su CY, Hibi M, Moens CB. Multiple zebrafish *atoh1* genes specify a diversity of neuronal types in the zebrafish cerebellum. *Dev Biol* 2018, 438: 44–56.
18. Kani S, Bae YK, Shimizu T, Tanabe K, Satou C, Parsons MJ, *et al.* Proneural gene-linked neurogenesis in zebrafish cerebellum. *Dev Biol* 2010, 343: 1–17.
19. Volkmann K, Rieger S, Babaryka A, Koster RW. The zebrafish cerebellar rhombic lip is spatially patterned in producing granule cell populations of different functional compartments. *Dev Biol* 2008, 313: 167–180.
20. Aruga J, Minowa O, Yaginuma H, Kuno J, Nagai T, Noda T, *et al.* Mouse *Zic1* is involved in cerebellar development. *J Neurosci* 1998, 18: 284–293.
21. Costagli A, Kapsimali M, Wilson SW, Mione M. Conserved and divergent patterns of Reelin expression in the zebrafish central nervous system. *J Comp Neurol* 2002, 450: 73–93.
22. Miyata T, Maeda T, Lee JE. *NeuroD* is required for differentiation of the granule cells in the cerebellum and hippocampus. *Genes Dev* 1999, 13: 1647–1652.
23. Gao H, Bu Y, Wu Q, Wang X, Chang N, Lei L, *et al.* *Mecp2* regulates neural cell differentiation by suppressing the *Id1* to *Her2* axis in zebrafish. *J Cell Sci* 2015, 128: 2340–2350.
24. Katsuyama Y, Oomiya Y, Dekimoto H, Motooka E, Takano A, Kikkawa S, *et al.* Expression of zebrafish ROR alpha gene in cerebellar-like structures. *Dev Dyn* 2007, 236: 2694–2701.
25. Hamling KR, Tobias ZJ, Weissman TA. Mapping the development of cerebellar Purkinje cells in zebrafish. *Dev Neurobiol* 2015, 75: 1174–1188.
26. Horner VL, Caspary T. Disrupted dorsal neural tube BMP signaling in the cilia mutant *Arl13b hnn* stems from abnormal *Shh* signaling. *Dev Biol* 2011, 355: 43–54.
27. Shao J, Xu L, Chen L, Lu Q, Xie X, Shi W, *et al.* *Arl13b* promotes gastric tumorigenesis by regulating *smo* trafficking and activation of the Hedgehog signaling pathway. *Cancer Res* 2017, 77: 4000–4013.
28. Hibi M, Matsuda K, Takeuchi M, Shimizu T, Murakami Y. Evolutionary mechanisms that generate morphology and neural-circuit diversity of the cerebellum. *Dev Growth Differ* 2017, 59: 228–243.
29. McFarland KA, Topczewska JM, Weidinger G, Dorsky RI, Appel B. *Hh* and *Wnt* signaling regulate formation of olig2+ neurons in the zebrafish cerebellum. *Dev Biol* 2008, 318: 162–171.
30. Aldinger KA, Mendelsohn NJ, Chung BH, Zhang W, Cohn DH, Fernandez B, *et al.* Variable brain phenotype primarily affects the brainstem and cerebellum in patients with osteogenesis imperfecta caused by recessive *WNT1* mutations. *J Med Genet* 2016, 53: 427–430.
31. Hagan N, Zervas M. *Wnt1* expression temporally allocates upper rhombic lip progenitors and defines their terminal cell fate in the cerebellum. *Mol Cell Neurosci* 2012, 49: 217–229.
32. Quarello E. Enlarged intracranial translucency and molar tooth sign in the first trimester as features of Joubert syndrome and related disorders. *Ultrasound Obstet Gynecol* 2016, 48: 532–534.
33. Song P, Perkins BD. Developmental expression of the zebrafish *Arf*-like small GTPase paralogs *arl13a* and *arl13b*. *Gene Expr Patterns* 2018, 29: 82–87.
34. Spassky N, Han YG, Aguilar A, Strehl L, Besse L, Laclef C, *et al.* Primary cilia are required for cerebellar development and *Shh*-dependent expansion of progenitor pool. *Dev Biol* 2008, 317: 246–259.
35. Chizhikov VV, Davenport J, Zhang Q, Shih EK, Cabello OA, Fuchs JL, *et al.* Cilia proteins control cerebellar morphogenesis by promoting expansion of the granule progenitor pool. *J Neurosci* 2007, 27: 9780–9789.
36. Ben-Arie N, Bellen HJ, Armstrong DL, McCall AE, Gordadze PR, Guo Q, *et al.* *Math1* is essential for genesis of cerebellar granule neurons. *Nature* 1997, 390: 169–172.
37. Duncan RN, Panahi S, Piotrowski T, Dorsky RI. Identification of *Wnt* genes expressed in neural progenitor zones during zebrafish brain development. *PLoS One* 2015, 10: e0145810.
38. Lucas FR, Salinas PC. *WNT-7a* induces axonal remodeling and increases synapsin I levels in cerebellar neurons. *Dev Biol* 1997, 192: 31–44.
39. Salinas PC, Fletcher C, Copeland NG, Jenkins NA, Nusse R. Maintenance of *Wnt-3* expression in Purkinje cells of the mouse cerebellum depends on interactions with granule cells. *Development* 1994, 120: 1277–1286.
40. Shi F, Cheng YF, Wang XL, Edge AS. *Beta-catenin* up-regulates *Atoh1* expression in neural progenitor cells by interaction with an *Atoh1* 3' enhancer. *J Biol Chem* 2010, 285: 392–400.
41. Tsuchiya K, Nakamura T, Okamoto R, Kanai T, Watanabe M. Reciprocal targeting of *Hath1* and *beta-catenin* by *Wnt* glycogen synthase kinase 3beta in human colon cancer. *Gastroenterology* 2007, 132: 208–220.
42. Aguilar A, Meunier A, Strehl L, Martinovic J, Bonniere M, Attie-Bitach T, *et al.* Analysis of human samples reveals impaired *SHH*-dependent cerebellar development in Joubert syndrome/Meckel syndrome. *Proc Natl Acad Sci U S A* 2012, 109: 16951–16956.
43. Abdelhamed ZA, Abdelmottaleb DI, El-Asrag ME, Natarajan S, Wheway G, Inglehearn CF, *et al.* The ciliary Frizzled-like receptor *Tmem67* regulates canonical *Wnt/beta-catenin* signalling in the developing cerebellum via *Hoxb5*. *Sci Rep* 2019, 9: 5446.
44. Casoni F, Croci L, Bosone C, D'Ambrosio R, Badaloni A, Gadesi D, *et al.* *Zfp423/ZNF423* regulates cell cycle progression, the mode of cell division and the DNA-damage response in Purkinje neuron progenitors. *Development* 2017, 144: 3686–3697.
45. Schilling K. Moving into shape: cell migration during the development and histogenesis of the cerebellum. *Histochem Cell Biol* 2018, 150: 13–36.
46. Xu H, Yang Y, Tang X, Zhao M, Liang F, Xu P, *et al.* Bergmann glia function in granule cell migration during cerebellum development. *Mol Neurobiol* 2013, 47: 833–844.



Macrophage–NLRP3 Inflammasome Activation Exacerbates Cardiac Dysfunction after Ischemic Stroke in a Mouse Model of Diabetes

Hong-Bin Lin^{1,2,3} · Guan-Shan Wei¹ · Feng-Xian Li¹ · Wen-Jing Guo¹ ·
Pu Hong¹ · Ya-Qian Weng¹ · Qian-Qian Zhang¹ · Shi-Yuan Xu¹ · Wen-Bin Liang⁴ ·
Zhi-Jian You² · Hong-Fei Zhang¹

Received: 6 October 2019 / Accepted: 17 March 2020 / Published online: 18 July 2020
© Shanghai Institutes for Biological Sciences, CAS 2020

Abstract Ischemic stroke is one of the leading causes of death worldwide. In the post-stroke stage, cardiac dysfunction is common and is known as the brain–heart interaction. Diabetes mellitus worsens the post-stroke outcome. Stroke-induced systemic inflammation is the major causative factor for the sequential complications, but the mechanism underlying the brain–heart interaction in diabetes has not been clarified. The NLRP3 (NLR pyrin domain-containing 3) inflammasome, an important component of the inflammation after stroke, is mainly activated in M1-polarized macrophages. In this study, we found that the cardiac dysfunction induced by ischemic stroke is more

severe in a mouse model of type 2 diabetes. Meanwhile, M1-polarized macrophage infiltration and NLRP3 inflammasome activation increased in the cardiac ventricle after diabetic stroke. Importantly, the NLRP3 inflammasome inhibitor CY-09 restored cardiac function, indicating that the M1-polarized macrophage–NLRP3 inflammasome activation is a pathway underlying the brain–heart interaction after diabetic stroke.

Keywords Ischemic stroke · Diabetes mellitus · Cardiac dysfunction · NLRP3 inflammasome · Macrophage

Hong-Bin Lin and Guan-Shan Wei have contributed equally to this work.

Electronic supplementary material The online version of this article (<https://doi.org/10.1007/s12264-020-00544-0>) contains supplementary material, which is available to authorized users.

✉ Hong-Fei Zhang
zhanghongfei@smu.edu.cn

Shi-Yuan Xu
xsy998@smu.edu.cn

Zhi-Jian You
13928460320@163.com

¹ Department of Anesthesiology, Zhujiang Hospital of Southern Medical University, Guangzhou 510220, China

² Department of Anesthesiology, Shenzhen SAMII Medical Center, Shenzhen 518118, China

³ Department of Anesthesiology, The Second Affiliated Hospital, Shantou University Medical College, Shantou 515041, China

⁴ University of Ottawa Heart Institute and Department of Cellular and Molecular Medicine, University of Ottawa, Ontario, K1N, Canada

Introduction

Stroke is the leading cause of disability and death, affecting nearly 30 million people worldwide each year, most of which are ischemic strokes [1]. Stroke can not only cause immediate death but also induce various complications such as cardiac dysfunction, which is common and is known as the brain–heart interaction [2]. The main symptoms are myocardial injury and arrhythmias [3–5], often accompanied by increased serum cardiac enzymes such as N-terminal pro-brain natriuretic peptide (NT-proBNP) [6, 7]. Importantly, patients without primary heart disease may also develop cardiac dysfunctions, indicating that stroke is the primary cause [8, 9].

Systemic inflammation is the major causative factor for the sequential complications after stroke, especially for the brain–heart interaction [2], but the underlying molecular pathway has not been clarified. Many stroke patients have diabetes, which is a major risk factor for a poor outcome [10]. It is unclear whether and how diabetes affects the brain–heart interaction. Animal studies have shown that middle cerebral artery occlusion (MCAO) increases

catecholamine levels [11] and impairs cardioprotective signaling pathways [12], thus inducing cardiac dysfunction and cardiomyocyte injury. Other studies have suggested that ischemic stroke induces arrhythmia by impairing calcium and other ionic currents in ventricular cardiomyocytes [13–15]. Pro-inflammatory factors [16] and chronic inflammation [17] might also be involved in the cardiac dysfunction induced after ischemic stroke. An important component of inflammation, the NLR family pyrin domain-containing 3 (NLRP3) inflammasome, has been attested to participate in many inflammatory diseases including type 2 diabetes mellitus, atherosclerosis, cardiovascular diseases, and neurodegenerative diseases [18–22]. Our previous study has shown that inhibition of the NLRP3 inflammasome ameliorates ischemic stroke injury in diabetic mice [23]. However, the role of the NLRP3 inflammasome in the brain–heart interaction and the corresponding mechanisms have not been studied in diabetes.

NLRP3 inflammasomes are mainly activated in macrophages, especially in M1-polarized macrophages [24]. M1-polarized macrophages are classified as showing pro-inflammatory status, while M2-polarized macrophages are alternatively activated macrophages associated with anti-inflammatory activity [25, 26]. We hypothesized that the polarization status of macrophages may play a dominant role in the brain–heart interaction in diabetes. To investigate whether ischemic stroke induce cardiac dysfunction, we used an ischemic stroke mouse model by applying the MCAO procedure. Afterwards, we investigated whether diabetic status aggravates cardiac dysfunction after stroke using a type 2 diabetes mouse model. Furthermore, we studied the role of NLRP3 and the polarized macrophages responsible in the brain–heart interaction. The sequential questions we have addressed provide a causative pathway for the brain–heart interaction, and shed light on therapeutic targets for diabetic patients after ischemic stroke.

Materials and Methods

Animals

This study was approved by the Medical Faculty Ethics Committee of Southern Medical University. Male C57BL/6 J mice (4–6 weeks old, 14–18 g) were purchased from the Animal Experimental Center of Southern Medical University. All experimental animals were maintained under a 12-h light and 12-h dark cycle and were supplied with adequate food and water before experiments.

Type 2 Diabetes Mellitus Mouse Model

This followed the protocol of our previous study [23]. Briefly, to establish a diabetic mouse model, we initially fed each mouse on a high-fat diet (Guangdong Medical Laboratory Animal Center, Guangzhou, China) for 3 weeks, then gave an intraperitoneal injection of 0.1 g/kg streptozotocin (STZ, Sigma, St. Louis, MO, USA). After that, mice were fed with the high-fat diet for another 4 weeks. The blood glucose concentration was measured after fasting for 8 h on days 1, 22, 36, and 50. The criterion for a type 2 diabetes mellitus mouse was a fasting glucose > 10.0 mmol. Non-diabetic mice were housed in the same environment, fed with a normal diet, and given an intraperitoneal injection of vehicle (saline).

Focal Cerebral Ischemia Mouse Model

The ischemic stroke mouse model was generated by MCAO following the protocol of our previous study [23]. In brief, mice were anesthetized with 2% isoflurane (RWD Life Science Co., Ltd, Shenzhen, China). After a midline neck incision, a 4–0 nylon monofilament (Yushun Bio Technology Co. Ltd., Pingdingshan, China) was inserted into the right MCA to block the blood flow. The monofilament was withdrawn after blocking the flow for 60 min. Sham-operated mice underwent the same procedure without inserting the monofilament. A heating pad was used to keep the rectal temperature at 37 ± 0.5 °C during the whole procedure. Cerebral blood flow (CBF) was evaluated using the 2-dimensional laser speckle imaging system and laser Doppler flowmetry (Fig. 1B). Mice were considered to be ischemic stroke models when the blood flow in the ischemic core decreased by > 70%, and were included in further analyses.

Cardiac Function Measurements

Echocardiography was used to evaluate cardiac function before stroke and 4 weeks later. The procedure followed that described by Ay *et al.* [9]. In brief, the thoracic hair was shaved and ultrasound transmission gel applied. Serial cardiac ultrasound analyses used the Vevo 2100 ultrasound imaging system (VisualSonics Inc., Toronto, Canada) with a 30-MHz probe. Ejection fraction (EF) and fractional shortening (FS) were calculated from 2-dimensionally targeted M-mode tracings. All primary measurement data were processed and analyzed using the Vevo 2100 analysis system and repeated three times.

Neurological Scoring

The neurological deficit, based on the motor behavior and level of consciousness of each mouse [23], was scored on days 1, 7, 14, 21, and 28 after MCAO. Scoring was done by a researcher who was blinded to the experimental grouping.

Survival Analysis

The vital signs of each mouse were checked every 24 h after MCAO. Times of death were recorded, and data from survivors were collected for 28 days.

Histological and Immunohistochemical Assessment

The whole brain was removed immediately after euthanasia by isoflurane overdose on day 28 after MCAO. The right hemispheric atrophy volume (right hemispheric volume/left hemispheric volume) after stroke was assessed using ImageJ (version 1.49, National Institutes of Health, Bethesda, MD, USA), then sectioned for staining in 2% 2,3,5-triphenyltetrazolium chloride (TTC). The heart was isolated and weighed after expressing the blood, then fixed in 4% paraformaldehyde before being embedded in paraffin and coronal sections of the ventricle were cut at 6 μm . PicroSirius Red staining was used to assess the interstitial collagen fraction. For immunostaining, the following primary antibodies were used: mouse anti-IBA1 (1:1000, Thermo Fisher, Waltham, MA, USA), rabbit anti-NLRP3 (1:1000, Thermo Fisher, Waltham, MA, USA), mouse anti-caspase-1 (1:250; Santa Cruz Biotechnology, Santa Cruz, CA, USA), and rabbit anti- α -smooth muscle actin (1:1000; Cell Signaling Technology, Danvers, MA, USA). All heart sections for analysis were processed at the same time in a single round of the immunohistochemical experiment.

Real-Time Quantitative RT-PCR

RT-PCR was used to measure mRNA expression (primer sequences are listed in Table 1). RNA was extracted from the apex myocardial tissue using the RNAiso Plus kit (9109, Takara Bio Inc., Shiga, Japan). cDNA was generated using the Veriti PCR System (Applied Biosystems Inc., Beverly, MA, USA). RT-PCR was applied using the SYBR Green kit (RR820A, Takara Bio Inc.) using 10 μL cDNA. The mRNA expression was normalized to the housekeeping gene β -actin.

Western Blot Assay

Apex myocardial tissue from each heart was ground with a Tissue grinder (JXFSTPRP-32, Shanghai Jingxin, Co., Ltd,

China) and total protein was isolated. The primary antibodies were: anti-NLRP3 (1:3000; 15101, Cell Signaling Technology), anti-caspase-1 (1:3000; sc-56036, Santa Cruz Biotechnology), and anti- α -tubulin (1:10000; RM2007, Beijing Ray Antibody Biotech, China).

ELISA for NT-proBNP Analysis

Blood plasma was collected on day 28 after MCAO or sham operation. Samples were analyzed for the concentrations of NT-proBNP using an ELISA kit according to the manufacturer's protocol (E-EL-M0834c, Elabscience Biotechnology Co. Ltd., Wuhan, China).

Statistical Analysis

All data are expressed as the mean \pm SD. Differences between groups were compared using Student's *t* test for single comparisons or one-way variance (ANOVA) for continuous variables with a normal distribution. The means across groups with repeated measurements over time were analyzed using repeated-measures ANOVA. Survival comparisons were analyzed using Prism7 software (GraphPad7, San Diego, CA, USA). Statistical significance was defined as $P < 0.05$.

Results

Ischemic Stroke Induces Cardiac Dysfunction in the MCAO Mouse Model

To study the brain–heart interaction after ischemic stroke, we used the MCAO mouse model [23] and tested cardiac functions before and afterwards. MCAO for 60 min induced ischemic stroke by blocking the major cerebral blood flow (Fig. 1A, B); this was further confirmed by the decreased right hemispheric volume on day 28 after surgery (Fig. 1C). Compared to the sham-operated mice, although there was no difference in the echocardiography before MCAO (Fig. S1A), it showed reduced EF and FS on day 28 in the MCAO mice (Fig. 1D), demonstrating impaired cardiac function after ischemic stroke. We also found that the plasma level of NT-proBNP (a major biomarker of cardiac dysfunction) was significantly elevated in MCAO (Fig. 1G). When checking the morphological changes in the heart, enlargement was revealed by the heart/body weight ratio (Fig. 1H). Furthermore, a higher cardiac interstitial collagen fraction was seen in ventricular sections from MCAO mice than in those from the sham group (Fig. 1E). Consistent with the morphological changes, the fibrotic protein α -SMA was also higher in the ventricles from stroke mice than in sham mice

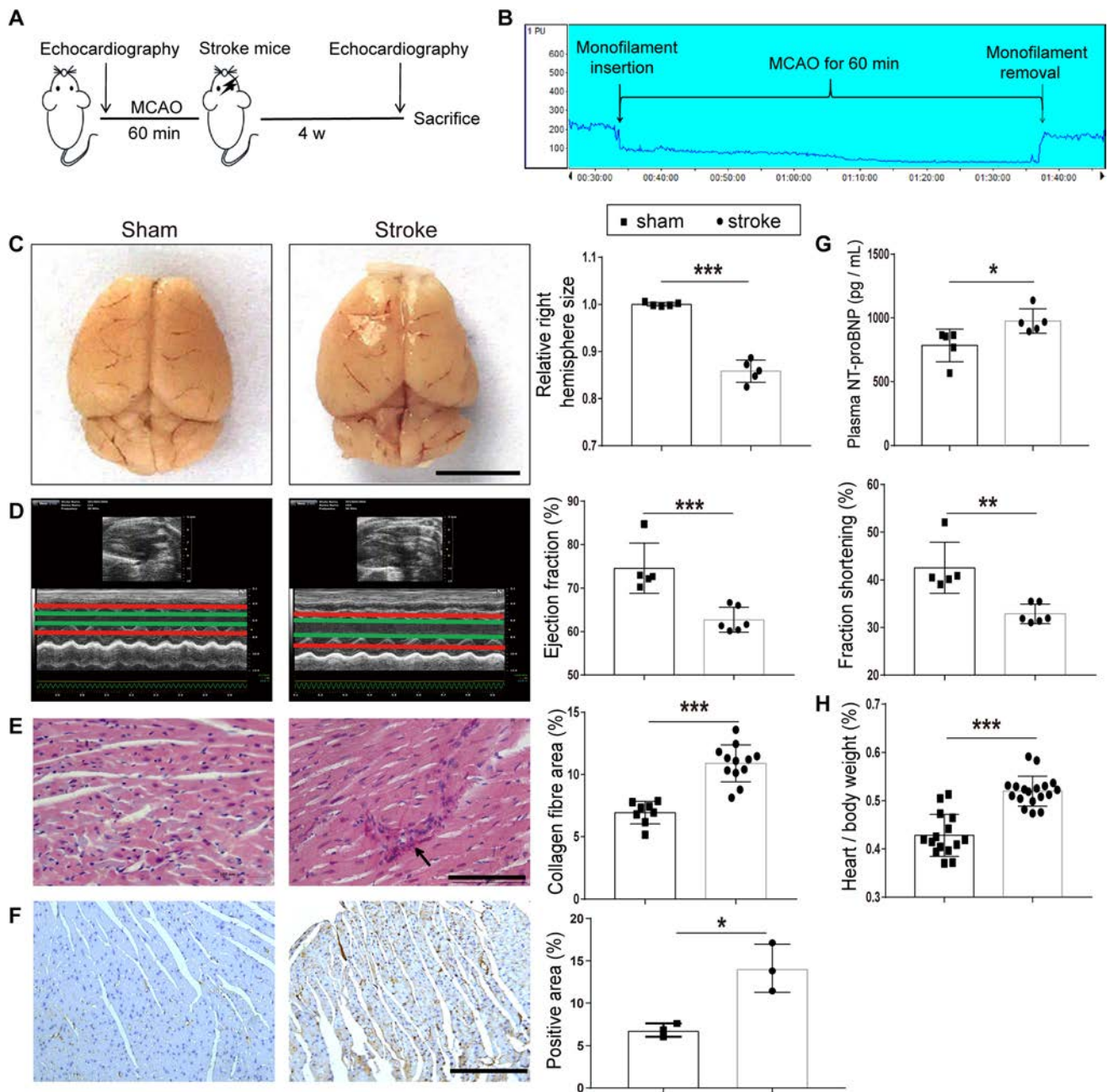


Fig. 1 Cardiac dysfunction in MCAO mice. **A** Diagram of the MCAO model echocardiography protocol. **B** Example of laser Doppler measurement showing that MCAO sharply reduces cerebral blood flow (CBF) when the monofilament is inserted. CBF is restored after the monofilament is removed. **C** Changes in brain morphology and right hemispheric atrophy in the sham and stroke groups ($n = 5$ per group). **D** Left, examples of echocardiography in mice at day 28 after MCAO. Right, bar graphs show the ejection fraction and fractional shortening in the sham ($n = 5$) and stroke groups ($n = 6$). **E** Left, PicroSirius Red staining for interstitial collagen (arrow) in

cardiac ventricular tissue. Right, interstitial collagen fraction in sham ($n = 8$) and stroke groups ($n = 12$). **F** Left, immunohistochemical staining for α -SMA in cardiac ventricular tissue. Right, α -SMA-positive area in the sham and stroke groups ($n = 3$ per group). **G** Plasma levels of NT-proBNP in the sham and stroke groups ($n = 5$ per group). **H** Heart/body weight ratio in the sham ($n = 15$) and stroke groups ($n = 18$). Data are expressed as the mean \pm SD. * $P < 0.05$; ** $P < 0.01$; *** $P < 0.001$ (Student's t -test). Magnification, 400 \times in **E** and 200 \times in **F**; scale bars, 5 mm in **C**, 100 μ m in **E**, and 50 μ m in **F**.

Table 1 Primer list.

Gene	Forward primer: 5′-3′	Reverse primer: 5′-3′
NLRP3	ATTACCCGCCGAGAAAGG	TCGCAGCAAAGATCCACACAG
Caspase-1	AATACAACCACTCGTACACGTC	AGCTCCAACCTCGGAGAAA
IL-1 β	GAAATGCCACCTTTTGACAGTG	TGGATGCTCTCATCAGGACAG
β -actin	GTGCTATGTTGCTCTAGACTTCG	ATGCCACAGGATTCCATACC
M1 markers		
CD16	TTTGACACCCAGATGTTTCAG	GTCTTCCTTGAGCACCTGGATC
INOS	CAAGCACCTTGGAAGAGGAG	AAGGCCAAACACAGCATACC
TNF- α	CGTCGTAGCAAACCACCAAG	GAGATAGCAAATCGGCTGACG
M2 markers		
Ym1/2	CAGGGTAATGAGTGGGTTGG	CACGGCACCTCCTAAATTGT
IL-10	TGGACAACATACTGCTAACCGAC	CCACTGCCTTGCTCTTATTTTC
TGF- β	TGCGCTTGACAGATTAATAA	CGTCAAAGACAGCCACTCA

NLRP3, NLR pyrin domain containing 3; IL, interleukin; INOS, inducible nitric oxide synthase; TNF- α , tumor necrosis factor alpha; TGF- β , transforming growth factor beta.

(Fig. 1F). These results demonstrated a brain–heart interaction in the MCAO mouse model.

Cardiac Dysfunction is More Severe in Diabetic Stroke

To address whether diabetic status affects cardiac dysfunction after ischemic stroke, we established a type 2 diabetes mouse model by a high-fat diet and intraperitoneal STZ injection, which showed a sustained high glucose level until day 50 (Fig. 2B). The MCAO procedure was done 4 weeks after STZ injection and cardiac functions were measured accordingly (Fig. 2A). Comparable infarcted regions and right hemisphere size were induced after MCAO in both diabetic and non-diabetic mice (Fig. 2C). Surprisingly, although there was no difference in the echocardiography before MCAO (Fig. S1B), diabetic mice exhibited a robust reduction of EF and FS by day 28 post-stroke (Fig. 2D), indicating a susceptibility to post-stroke cardiac dysfunction in diabetes. Furthermore, a higher level of plasma NT-proBNP (Fig. 2D) and heart/body weight ratio (Fig. 2H) were detected in diabetic stroke mice compared to the non-diabetic stroke mice. Correlated with the echocardiography and NT-proBNP changes, the cardiac interstitial collagen fraction and fibrotic protein α -SMA also increased significantly in the diabetic stroke myocardium compared to the non-diabetic stroke mice (Fig. 2E–F). Our data indicated that diabetic status worsens cardiac dysfunction, the cardiac interstitial collagen fraction, and hypertrophy in mice with ischemic stroke.

Diabetic Status Worsens the Overall Outcome of Stroke

As cardiac dysfunction was more severe in diabetic stroke mice, we set out to determine how diabetes affects the neurological deficits and the overall outcome in our MCAO model. Consistent with other reports [27], our diabetic stroke mice showed higher neurological deficit scores at days 1, 7, and 28 after MCAO (Fig. 3A). Referring to the overall mortality rate, fewer diabetic stroke mice survived at the end of day 28 compared to the non-diabetic group (Fig. 3B). These data suggested that not only the cardiac dysfunction but also the overall outcome was affected by diabetic status in the MCAO mouse model.

NLRP3 Activation is Indispensable for Brain–Heart Interaction in Diabetic Stroke

The results of cardiac dysfunction and worse neurologic outcomes indicated that a stronger brain–heart interaction exists in diabetic stroke mice. Taking into account that both stroke and diabetes exhibit NLRP3 activation and worsen the respective outcomes, we tested the corresponding mRNA and protein levels. As anticipated, the NLRP3 mRNA and protein levels, as well as caspase-1 and IL-1 β levels showed more robust elevation in the myocardium from diabetic stroke mice than those from non-diabetic mice (Fig. 4A–C). Surprisingly, the NLRP3 inhibitor CY-09 (HY-103666; MedChem Express, Monmouth Junction, NJ, USA) sufficiently restored the cardiac function, showing improved EF and FS compared with the vehicle group (Fig. 4D). Morphological studies also revealed a reduction in the heart/body weight ratio (Fig. 4G), the cardiac interstitial collagen fraction (Fig. 4E), and fibrotic protein α -SMA expression after CY-09 administration

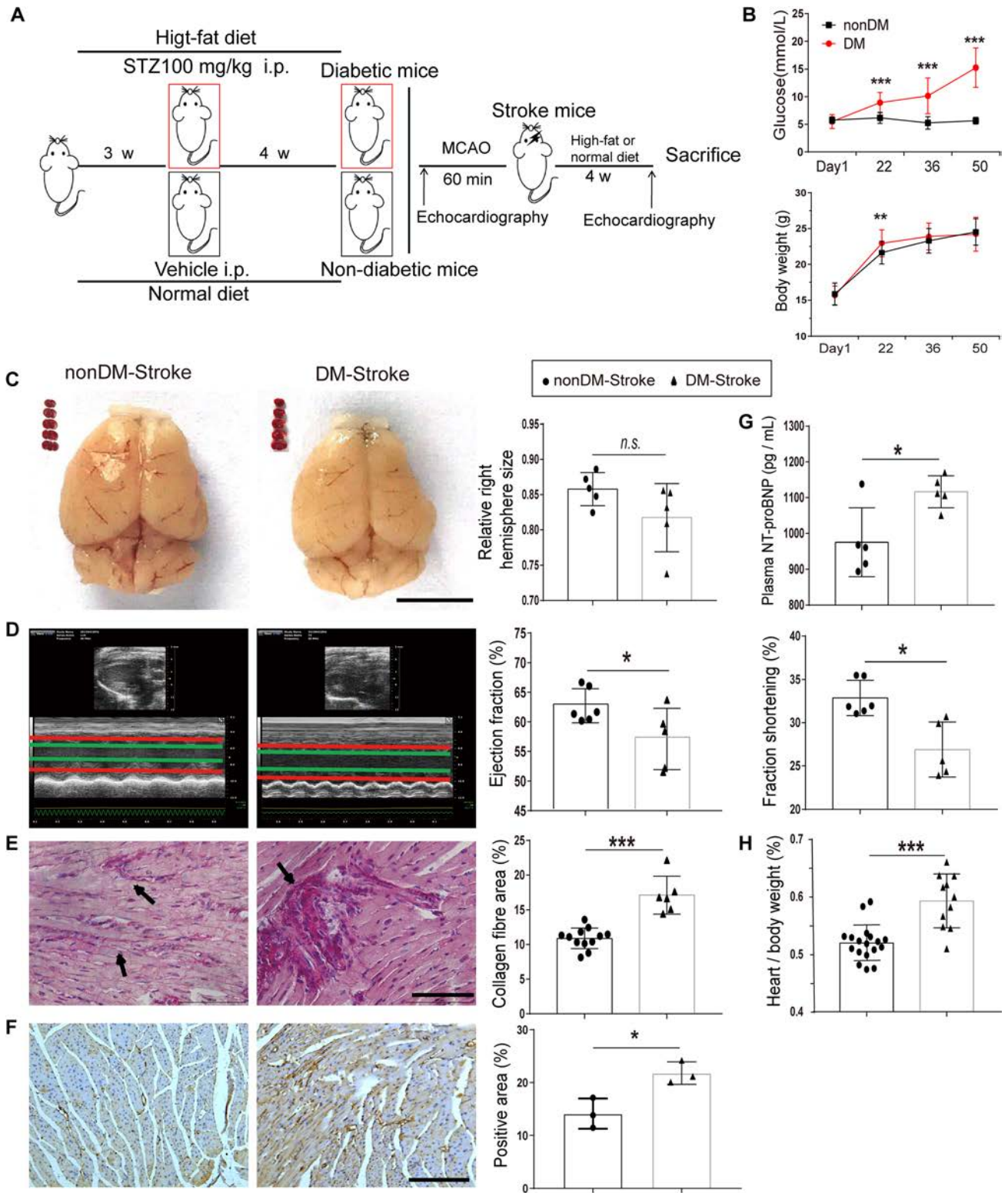


Fig. 2 Ischemic stroke induces severe cardiac dysfunction in diabetic mice. **A** Diagram of protocols for establishing the type 2 diabetes mellitus and MCAO mouse models. **B** Time courses of blood glucose and body weight showing significant increases from day 22 in diabetic mice ($n = 22$) compared with non-diabetic mice ($n = 33$). **C** Brain morphology and TTC staining in coronal brain sections from non-diabetic stroke (nonDM-Stroke) and diabetic stroke (DM-Stroke) mice ($n = 5$ per group). **D** Echocardiographic traces (left) and ejection fraction and fractional shortening (right) in nonDM-Stroke ($n = 6$) and DM-Stroke ($n = 5$) mice. **E** Left, PicroSirius red staining for interstitial collagen (arrows) in cardiac ventricular tissue. Right, interstitial collagen fraction in nonDM-Stroke ($n = 12$) and DM-Stroke ($n = 6$) mice. **F** Left, immunohistochemical staining for α -SMA in cardiac ventricular tissue. Right, α -SMA-positive area in nonDM-Stroke and DM-Stroke ($n = 3$ per group) mice. **G** Plasma levels of NT-proBNP in nonDM-Stroke and DM-Stroke ($n = 5$ per group) mice. **H** Heart/body weight in nonDM-Stroke ($n = 18$) and DM-Stroke ($n = 11$) mice. DM, diabetes mellitus; STZ, streptozotocin; i.p. intraperitoneal. Data are expressed as the mean \pm SD. * $P < 0.05$; ** $P < 0.01$; *** $P < 0.001$, *n.s.* not significant (Student's *t*-test). Magnification, 400 \times in **E** and 200 \times in **F**; scale bars, 5 mm in **C**, 100 μ m in **E**, and 50 μ m in **F**.

(Fig. 4F). The inhibitory effect of CY-09 on NLRP3 activation was further confirmed in myocardial tissue as reduced expression of NLRP3, caspase-1, and IL-1 β compared to the vehicle group (Fig. 4H–I). These results identified a role of NLRP3 in the brain–heart interaction in the diabetic mouse.

M1 Macrophages are Responsible for NLRP3-Mediated Brain–Heart Interaction

NLRP3 inflammasomes are mainly from M1- rather than M2-polarized macrophages [24]. To dissect the source of the NLRP3 inflammasomes, we confirmed the expression of the macrophage marker IBA1 in the myocardium from diabetic stroke mice (Fig. 5A). Furthermore, polarized markers were measured and indicated that M1- (revealed by CD16, iNOS, and TNF- α), but not M2- (revealed by Ym1/2, IL-10, and TGF- β) polarized macrophages were the dominant type infiltrating the myocardium in post-diabetic stroke (Fig. 5B). The expression levels of these markers implied that M1-polarized macrophage–NLRP3 inflammasome activation is an indispensable molecular pathway. Considering the restorative effects of the NLRP3 inhibitor CY-09 on the brain–heart interaction, we tested whether it affects the macrophage polarization status. Surprisingly, CY-09 significantly elevated the mRNA expression levels of Ym1/2, IL-10, and TGF- β , while decreasing the levels of CD16, iNOS, and TNF- α in diabetic stroke mice compared to the vehicle group (Fig. 5C). The results indicated that the infiltrating macrophages switched to M2 after CY-09 administration,

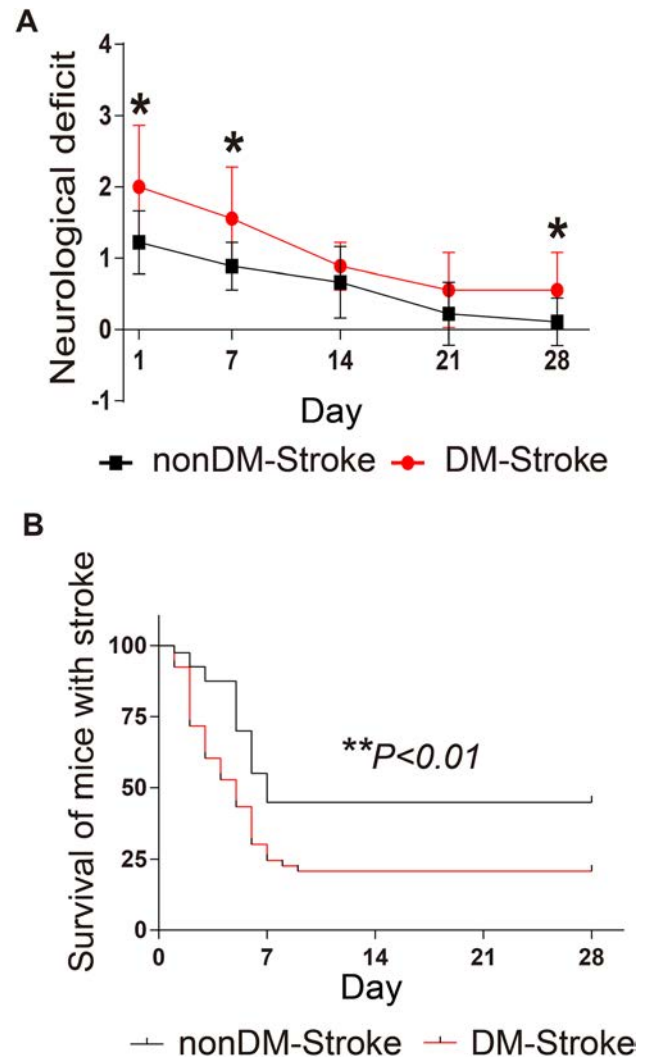


Fig. 3 Diabetes leads to a worse prognosis after ischemic stroke. **A** Neurological deficit scores in nonDM-Stroke and DM-Stroke mice at 24 h and 7, 14, 21, and 28 days ($n = 9$ per group). **B** Mortality until day 28 in nonDM-Stroke ($n = 40$) and DM-Stroke ($n = 53$) mice. nonDM-Stroke, non-diabetic stroke group; DM-Stroke, diabetic stroke group. Data are expressed as the mean \pm SD. * $P < 0.05$; ** $P < 0.01$ (Student's *t*-test in **A** and log-rank test in **B**).

strongly supporting the specific role of NLRP3 in the brain–heart interaction.

The overall results demonstrated that the brain–heart interaction is due to the infiltration of M1-polarized macrophages into the myocardium after diabetic stroke. This infiltration sequentially induces NLRP3 inflammasome activation and impairs cardiac function, which is responsible for the poor outcome in diabetic stroke (Fig. 6).

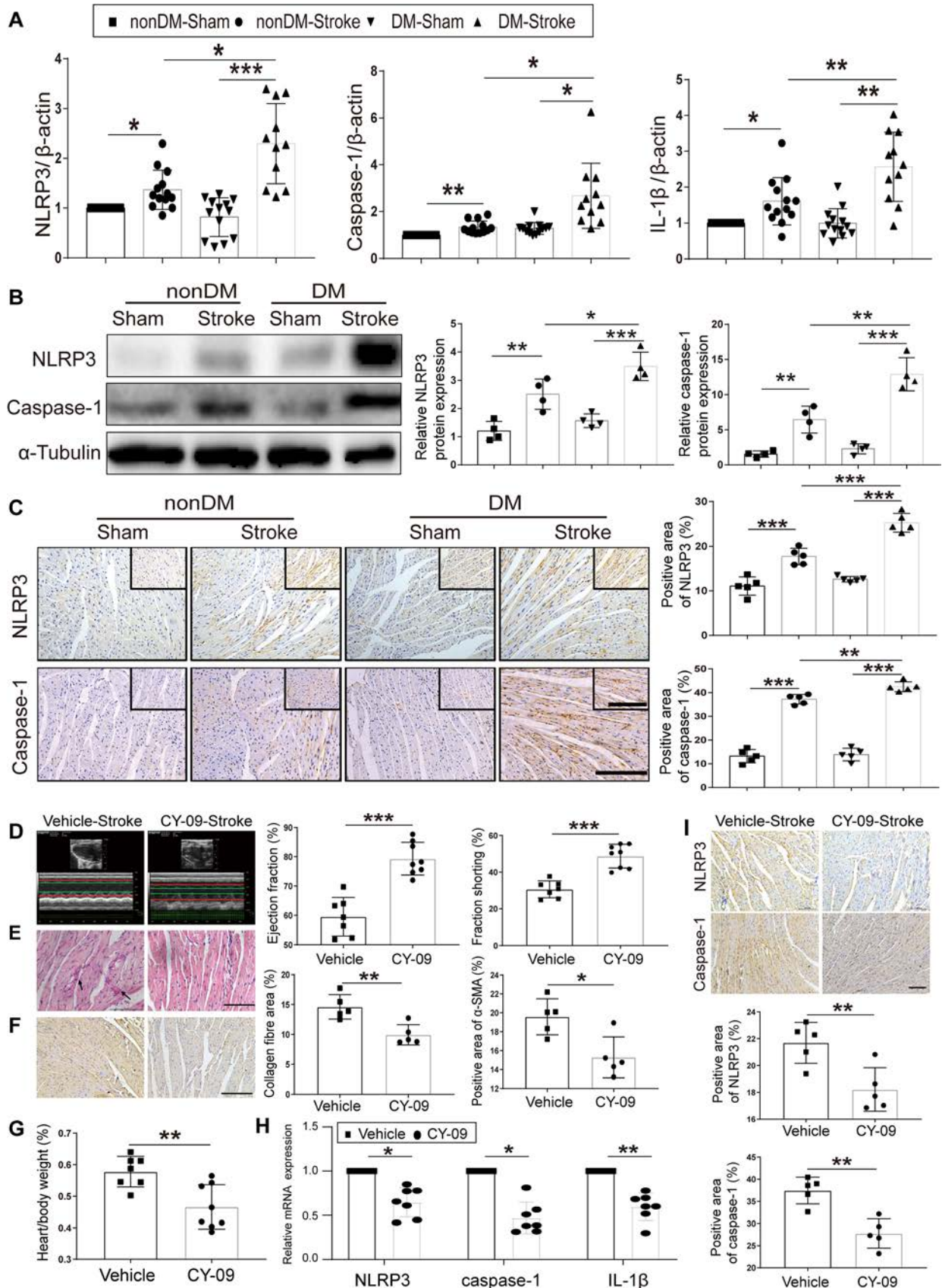


Fig. 4 NLRP3 activation plays an important role in the brain–heart interaction in diabetic stroke. **A** Relative gene expression of NLRP3, caspase-1, and IL-1 β in apex myocardial tissue. β -Actin served as an endogenous reference gene ($n = 13$ in nonDM-Sham, nonDM-stroke, and DM-Sham; $n = 11$ in DM-Stroke). **B** Left, NLRP3 and caspase-1 in apex myocardial tissue indicated by western blot. Right, integrated density value of relative protein expression of NLRP3 and caspase-1 ($n = 4$ per group). **C** Left, protein expression of NLRP3 and caspase-1 in cardiac ventricular tissue by immunocytochemistry. Right, NLRP3, caspase-1-positive area in different group mice ($n = 5$ per group). **D** Echocardiographic measurement of ejection fraction and fractional shortening in Vehicle-Stroke ($n = 7$) and CY-09-Stroke ($n = 8$) mice. **E** Left, PicroSirius red staining for interstitial collagen (arrows) in ventricular tissue. Middle, interstitial collagen fraction in Vehicle-Stroke and CY-09-Stroke mice ($n = 5$ per group). **F α -SMA immunohistochemical staining (left) of ventricular tissue and α -SMA area (right) in Vehicle-Stroke and CY-09-Stroke mice ($n = 5$ per group). **G** Heart/body weight in Vehicle-Stroke ($n = 7$) and CY-09-Stroke ($n = 8$) mice. **H** Relative gene expression of NLRP3, caspase-1, and IL-1 β in apex myocardial tissue ($n = 7$ per group). **I** Top, immunohistochemical staining for NLRP3 and caspase-1 in cardiac ventricular tissue. Bottom, NLRP3 and caspase-1-positive area in Vehicle-Stroke and CY-09-Stroke mice ($n = 5$ per group). nonDM-Sham, non-diabetic sham group; nonDM-Stroke, non-diabetic stroke group; DM-Sham, diabetic sham group; DM-Stroke, diabetic stroke group; Vehicle, Vehicle-Stroke group; CY-09, CY-09-Stroke group. Data are expressed as the mean \pm SD. * $P < 0.05$; ** $P < 0.01$; *** $P < 0.001$ (Student's *t*-test or one-way ANOVA). Magnification, 400 \times in C (upper right) and E; 200 \times in C, F, and I; scale bars, 100 μ m in E; 50 μ m in C, F, and I.**

Discussion

Our results revealed that severe cardiac dysfunction occurs in diabetic ischemic stroke, shown as the brain–heart interaction, due to NLRP3 inflammasome activation in M1-polarized macrophages. We first provided evidence that diabetic status worsened the cardiac dysfunction, as well as increasing the interstitial collagen fraction and cardiac hypertrophy after stroke in a type 2 diabetes MCAO mouse model. Second, M1-polarized macrophage infiltration and NLRP3 inflammasome activation were enhanced in the post-stroke myocardium, and were more severe in diabetic mice. Moreover, inhibiting the NLRP3 inflammasome with CY-09 restored the cardiac function and reversed the myocardial morphological changes after ischemic stroke.

Clinical evidence has implied that the brain–heart interaction occurs in the post-stroke stage. Nearly 19% of patients suffer at least one major detrimental cardiac complication within the first 3 months following an acute ischemic stroke [28]. The cardiac dysfunctions include, but are not limited to, impaired pumping action, fibrosis, and hypertrophy. It has been reported that > 50% of stroke patients have left ventricular diastolic dysfunction and 13%–29% have systolic dysfunction [29, 30]. Furthermore, 75%–92% of stroke patients present a new ECG abnormality [31]. By measuring the cardiac function using

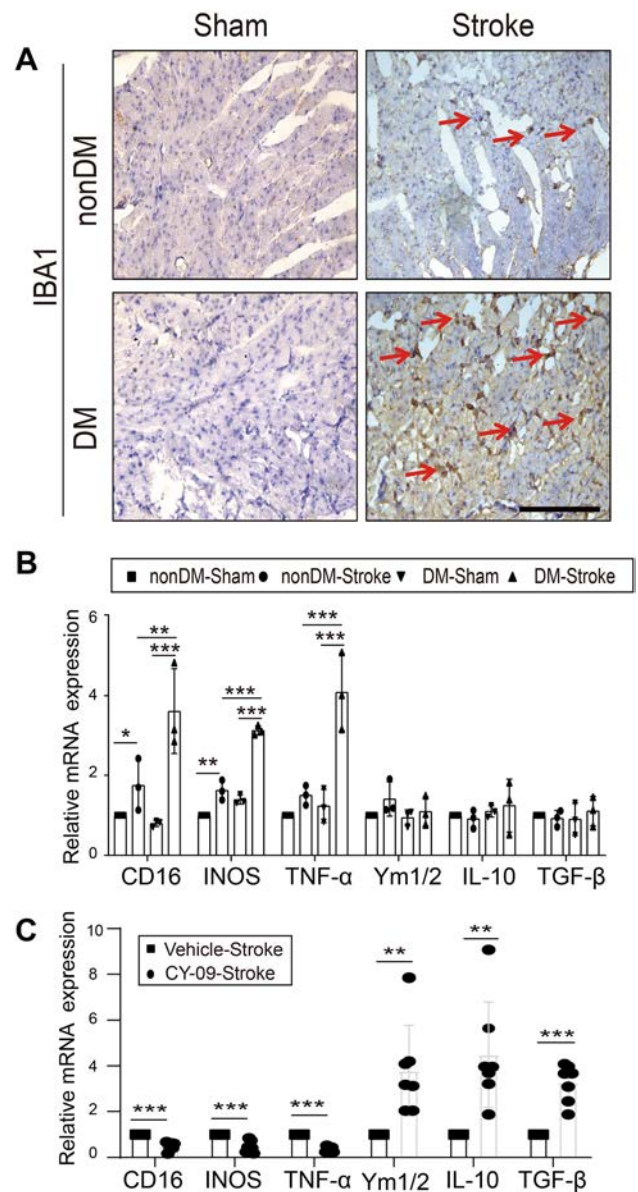


Fig. 5 Macrophages increase and polarize in the brain–heart interaction. **A** Representative immunocytochemical staining for the macrophage marker IBA1 in cardiac tissue (magnification, 400 \times ; scale bar, 100 μ m). **B**, **C** Relative mRNA expression of macrophage-polarization markers in apex myocardial tissue (M1 markers: CD16, INOS, and TNF- α ; M2 markers: Ym1/2, IL-10, and TGF- β) ($n = 3$ in nonDM-Sham, non-DM stroke, DM-Sham and DM-Stroke; $n = 7$ in Vehicle-Stroke and CY-09-Stroke). IL, interleukin; INOS, inducible nitric oxide synthase; TNF- α , tumor necrosis factor alpha; TGF- β , transforming growth factor beta. Data are expressed as the mean \pm SD. * $P < 0.05$; ** $P < 0.01$; *** $P < 0.001$ (Student's *t*-test or one-way ANOVA).

echocardiography, we also found remarkable changes after the MCAO procedure in diabetic and non-diabetic mice, indicating the clinical relevance of our methodology.

Many studies have suggested various mechanisms of the brain–heart interaction induced by ischemic stroke,

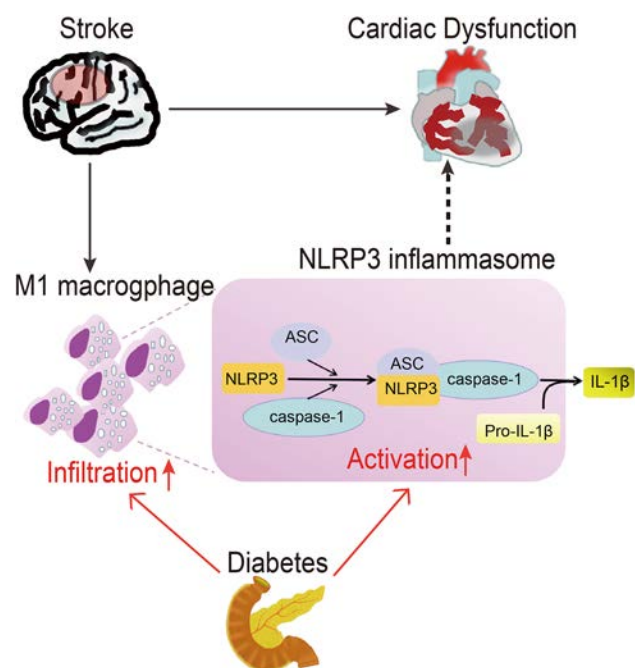


Fig. 6 Schematic of the underlying mechanism for ischemic stroke-induced cardiac dysfunction in the diabetic mouse. M1-polarized macrophage infiltration and NLRP3 inflammasome activation in the heart after ischemic stroke induce cardiac dysfunction. Diabetes mellitus exacerbates the cardiac dysfunction after ischemic stroke through increased M1-polarized macrophage infiltration and NLRP3 inflammasome activation in the heart. NLRP3, NLR pyrin domain containing 3; ASC, apoptosis-associated speck-like protein containing a CARD.

including cardiac autonomic dysfunction after ischemic injury of the insular cortex [32], systemic inflammation, the hypothalamic–pituitary–adrenal axis, blood–brain barrier disruption, and gut microbiome dysbiosis [2, 11]. However, the underlying molecular mechanisms are still far from precisely dissected, especially in diabetic patients. Diabetic status not only exacerbates ischemic brain injury, but also increases post-stroke complications [33, 34]. A clinical study reported that diabetes is an independent predictor of unfavorable outcomes, and mortality increases while the cardiac pumping function decreases after stroke [35]. Another study showed that pioglitazone, a classic hypoglycemic drug, improves the cardiovascular functions of patients after ischemic stroke or transient ischemic attack [36]. These studies point to a role of inflammation in the brain–heart interaction. Chronic inflammation plays an important role in cardiac fibrosis [37] as well as ischemic stroke [38, 39]. Microglial infiltration induced by ischemic stroke increases inflammation by releasing pro-inflammatory cytokines and chemokines such as TNF- α , IL-1 β , and vascular cell adhesion protein 1 [40, 41]. As a result, brain tissue releases glial fibrillar acidic protein, S100 and myelin basic protein and sheds extracellular microvesicles, then activates the peripheral immune system [34]. The

extracellular microvesicles and pro-inflammatory molecules can recruit macrophages and switch them to M1 polarization [42] and hence activate NLRP3 inflammasomes [43]. Notably, M1-polarized macrophages are closely associated with fibrosis [25]. In our study, the process of M1-polarized macrophage–NLRP3 inflammasome activation was shown to be the molecular pathway for inducing cardiac dysfunction and myocardial fibrosis. CY-09, a specific inhibitor of NLRP3, binds to the ATP-binding motif of the NLRP3 NACHT domain and inhibits NLRP3 ATPase activity, hence inhibiting NLRP3 inflammasome assembly and activation in macrophages [44]. As shown in our study, the anti-inflammatory effect of CY-09 also benefits cardiac functions after diabetic ischemic stroke, providing strong evidence for its clinical relevance.

In summary, our study suggested that diabetic status decreases cardiac function after ischemic stroke by increasing infiltration by M1-polarized macrophages and NLRP3 inflammasome activation. A compensatory mechanism would partially rescue the neurological deficit after stroke [45]. This explains why the neurological deficit gradually recovered although the cardiac morphological changes lasted for at least 28 days. Further study should focus on how to manipulate M1-polarized macrophages to reverse the pathological myocardial changes before they form scar-like tissue after stroke.

Acknowledgements This work was supported by grants from the National Natural Science Foundation of China (81771232 and 81974192) and the Natural Science Foundation of Guangdong Province, China (2019A1515010654).

Conflict of interest The authors claim that there are no conflicts of interest.

References

1. Wang W, Jiang B, Sun H, Ru X, Sun D, Wang L, *et al.* Prevalence, incidence, and mortality of stroke in China: results from a nationwide population-based survey of 480 687 adults. *Circulation* 2017, 135:759–771.
2. Chen Z, Venkat P, Seyfried D, Chopp M, Yan T, Chen J. Brain–heart interaction: cardiac complications after stroke. *Circ Res* 2017, 121: 451–468.
3. Yoshimura S, Toyoda K, Ohara T, Nagasawa H, Ohtani N, Kuwashiro T, *et al.* Takotsubo cardiomyopathy in acute ischemic stroke. *Ann Neurol* 2008, 64: 547–554.
4. Samuels MA. The brain–heart connection. *Circulation* 2007, 116: 77–84.
5. Kumar S, Selim MH, Caplan LR. Medical complications after stroke. *Lancet Neurol* 2010, 9: 105–118.
6. Bugnicourt JM, Rogez V, Guillaumont MP, Rogez JC, Canaple S, Godefroy O. Troponin levels help predict new-onset atrial fibrillation in ischaemic stroke patients: a retrospective study. *Eur Neurol* 2010, 63: 24–28.

7. Cushman M, Judd SE, Howard VJ, Kissela B, Gutierrez OM, Jenny NS, *et al.* N-terminal pro-B-type natriuretic peptide and stroke risk: the reasons for geographic and racial differences in stroke cohort. *Stroke* 2014, 45: 1646–1650.
8. Cheshire WJ, Saper CB. The insular cortex and cardiac response to stroke. *Neurology* 2006, 66: 1296–1297.
9. Ay H, Koroshetz WJ, Benner T, Vangel MG, Melnosky C, Arsava EM, *et al.* Neuroanatomic correlates of stroke-related myocardial injury. *Neurology* 2006, 66: 1325–1329.
10. Ergul A, Abdelsaid M, Fouda AY, Fagan SC. Cerebral neovascularization in diabetes: implications for stroke recovery and beyond. *J Cereb Blood Flow Metab* 2014, 34: 553–563.
11. Bieber M, Werner RA, Tanai E, Hofmann U, Higuchi T, Schuh K, *et al.* Stroke-induced chronic systolic dysfunction driven by sympathetic overactivity. *Ann Neurol* 2017, 82: 729–743.
12. Meloux A, Rochette ERL, Cottin Y, Bejot Y, Vergely C. Ischemic stroke increases heart vulnerability to ischemia-reperfusion and alters myocardial cardioprotective pathways. *Stroke* 2018, 49: 2752–2760.
13. Wang L, Sun L, Zhang Y, Wu H, Li C, Pan Z, *et al.* Ionic mechanisms underlying action potential prolongation by focal cerebral ischemia in rat ventricular myocytes. *Cell Physiol Biochem* 2009, 23: 305–316.
14. Sun L, Ai J, Wang N, Zhang R, Li J, Zhang T, *et al.* Cerebral ischemia elicits aberration in myocardium contractile function and intracellular calcium handling. *Cell Physiol Biochem* 2010, 26: 421–430.
15. Sun L, Du J, Zhang G, Zhang Y, Pan G, Wang L, *et al.* Aberration of L-type calcium channel in cardiac myocytes is one of the mechanisms of arrhythmia induced by cerebral ischemia. *Cell Physiol Biochem* 2008, 22: 147–156.
16. Ishikawa H, Tajiri N, Vasconcellos J, Kaneko Y, Mimura O, Dezawa M, *et al.* Ischemic stroke brain sends indirect cell death signals to the heart. *Stroke* 2013, 44: 3175.
17. Acosta SA, Mashkouri S, Nwokoye D, Lee JY, Borlongan CV, Ishikawa H, *et al.* Chronic inflammation and apoptosis propagate in ischemic cerebellum and heart of non-human primates. *Oncotarget* 2017, 8: 102820–102834.
18. Vandanmagsar B, Youm YH, Ravussin A, Galgani JE, Stadler K, Mynatt RL, *et al.* The NLRP3 inflammasome instigates obesity-induced inflammation and insulin resistance. *Nat Med* 2011, 17: 179–188.
19. Liu D, Zeng X, Li X, Mehta JL, Wang X. Role of NLRP3 inflammasome in the pathogenesis of cardiovascular diseases. *Basic Res Cardiol* 2017, 113: 5.
20. Zeng J, Chen Y, Ding R, Feng L, Fu Z, Yang S, *et al.* Isoliquiritigenin alleviates early brain injury after experimental intracerebral hemorrhage via suppressing ROS- and/or NF-kappaB-mediated NLRP3 inflammasome activation by promoting Nrf2 antioxidant pathway. *J Neuroinflammation* 2017, 14: 119.
21. Peng Y, Liu B, Pei S, Zheng D, Wang Z, Ji T, *et al.* Higher CSF levels of NLRP3 inflammasome is associated with poor prognosis of anti-N-methyl-D-aspartate receptor encephalitis. *Front Immunol* 2019, 10: 905.
22. Xu L, Qiu X, Wang S, Wang Q, Zhao XL. NMDA receptor antagonist MK801 protects against 1-bromopropane-induced cognitive dysfunction. *Neurosci Bull* 2019, 35: 347–361.
23. Hong P, Li FX, Gu RN, Fang YY, Lai LY, Wang YW, *et al.* Inhibition of NLRP3 inflammasome ameliorates cerebral ischemia-reperfusion injury in diabetic mice. *Neural Plast* 2018, 2018: 1–8.
24. Liu W, Zhang X, Zhao M, Zhang X, Chi J, Liu Y, *et al.* Activation in M1 but not M2 macrophages contributes to cardiac remodeling after myocardial infarction in rats: a critical role of the calcium sensing receptor/NLRP3 inflammasome. *Cell Physiol Biochem* 2015, 35: 2483–2500.
25. Ploeger DT, Houser NA, Schipper M, Koerts JA, de Rond S, Bank RA. Cell plasticity in wound healing: paracrine factors of M1/M2 polarized macrophages influence the phenotypical state of dermal fibroblasts. *Cell Commun Signal*. 2013, 11: 29.
26. Kanazawa M, Ninomiya I, Hatakeyama M, Takahashi T, Shimohata T. Microglia and monocytes/macrophages polarization reveal novel therapeutic mechanism against stroke. *Int J Mol Sci* 2017, 18: 2135.
27. Ma S, Wang J, Wang Y, Dai X, Xu F, Gao X, *et al.* Diabetes mellitus impairs white matter repair and long-term functional deficits after cerebral ischemia. *Stroke* 2018, 49: 2453–2463.
28. Marto JP, Kauppila LA, Jorge C, Calado S, Viana-Baptista M, Pinho-E-Melo T, *et al.* Intravenous thrombolysis for acute ischemic stroke after recent myocardial infarction: case series and systematic review. *Stroke* 2019, 50: 2813–2818.
29. Park HK, Kim BJ, Yoon CH, Yang MH, Han MK, Bae HJ. Left ventricular diastolic dysfunction in ischemic stroke: functional and vascular outcomes. *J Stroke* 2016, 18: 195–202.
30. Prosser J, MacGregor L, Lees KR, Diener HC, Hacke W, Davis S. Predictors of early cardiac morbidity and mortality after ischemic stroke. *Stroke* 2007, 38: 2295–2302.
31. Khechinashvili G, Asplund K. Electrocardiographic changes in patients with acute stroke: a systematic review. *Cerebrovasc Dis* 2002, 14: 67–76.
32. Krause T, Werner K, Fiebich JB, Villringer K, Piper SK, Haeusler KG, *et al.* Stroke in right dorsal anterior insular cortex is related to myocardial injury. *Ann Neurol* 2017, 81: 502–511.
33. Jia Q, Zhao X, Wang C, Wang Y, Yan Y, Li H, *et al.* Diabetes and poor outcomes within 6 months after acute ischemic stroke: the China national stroke registry. *Stroke* 2011, 42: 2758–2762.
34. Scheitz JF, Nolte CH, Doehner W, Hachinski V, Endres M. Stroke heart syndrome: clinical presentation and underlying mechanisms. *Lancet Neurol* 2018, 17: 1109–1120.
35. Siedler G, Sommer K, Macha K, Marsch A, Breuer L, Stoll S, *et al.* Heart failure in ischemic stroke: relevance for acute care and outcome. *Stroke* 2019, 50: 3051–3056.
36. Young LH, Viscoli CM, Schwartz GG, Inzucchi SE, Curtis JP, Gorman MJ, *et al.* Heart failure after ischemic stroke or transient ischemic attack in insulin-resistant patients without diabetes mellitus treated with pioglitazone. *Circulation* 2018, 138: 1210–1220.
37. Zhao Q, Yan T, Li L, Chopp M, Venkat P, Qian Y, *et al.* Immune response mediates cardiac dysfunction after traumatic brain injury. *J Neurotrauma* 2018, 36: 619–629.
38. Chen J, Cui C, Yang X, Xu J, Venkat P, Zacharek A, *et al.* MiR-126 affects brain-heart interaction after cerebral ischemic stroke. *Transl Stroke Res* 2017, 8: 374–385.
39. Doll DN, Barr TL, Simpkins JW. Cytokines: their role in stroke and potential use as biomarkers and therapeutic targets. *Aging Dis* 2014, 5: 294–306.
40. Iadecola C, Anrather J. The immunology of stroke: from mechanisms to translation. *Nat Med* 2011, 17: 796–808.
41. Yilmaz G, Granger DN. Leukocyte recruitment and ischemic brain injury. *Neuromolecular Med* 2010, 12: 193–204.
42. Singla DK, Johnson TA, Tavakoli Dargani Z. Exosome treatment enhances anti-inflammatory M2 macrophages and reduces inflammation-induced pyroptosis in doxorubicin-induced cardiomyopathy. *Cells* 2019, 8:1224.
43. Tschopp J, Schroder K. NLRP3 inflammasome activation: the convergence of multiple signalling pathways on ROS production? *Nat Rev Immunol* 2010, 10: 210–215.
44. Jiang H, He H, Chen Y, Huang W, Cheng J, Ye J, *et al.* Identification of a selective and direct NLRP3 inhibitor to treat inflammatory disorders. *J Exp Med* 2017, 214: 3219–3238.
45. Cassidy JM, Cramer SC. Spontaneous and therapeutic-induced mechanisms of functional recovery after stroke. *Transl Stroke Res* 2017, 8: 33–46.



Comparing GWAS and Brain Structure-Specific Gene Expression Profiles Identifies Psychiatric Disorder-Related Brain Structures at Different Developmental Stages

Xin Qi¹ · Cuiyan Wu¹ · Yanan Du¹ · Shiqiang Cheng¹ · Yan Wen¹ · Mei Ma¹ · Chujun Liang¹ · Li Liu¹ · Bolun Cheng¹ · Lu Zhang¹ · Ping Li¹ · Feng Zhang¹

Received: 18 August 2019 / Accepted: 14 March 2020 / Published online: 30 May 2020
© Shanghai Institutes for Biological Sciences, CAS 2020

Dear Editor,

Psychiatric disorders are a group of mental disorders characterized by psychological or behavioral disabilities. Losing of the ability to work and assuming the extensive cost of long-term treatment, patients with psychiatric disorders are forced to support a heavy financial and medical burden. The growth and development of brain structures are dynamic, and different brain structures have major and specific functions to control behavior and performance. It has been demonstrated that the dysfunction of different brain structures involved in different psychiatric disorders is due to widespread alterations in the functional connectivity in the brain. Because of the dynamic alterations during brain growth and development, it is reasonable to infer that different psychiatric disorders are involved in the dysfunction of different brain structures at different life stages.

Genetic factors display a strong component in the etiology of psychiatric disorders. Gene expression is regulated by heredity, and the integration of genome-wide association studies (GWASs) and gene expression profile datasets has become a hot topic in recent studies, providing

new insights into the mechanism underlying complex diseases. Based on these, it is feasible to further investigate the mechanisms of complex diseases through integrating GWASs and expression profile datasets. However, there are few studies comparing GWASs and gene expression profile datasets with the consideration of different brain structures and developmental stages for psychiatric disorders.

In this study, we explored the abnormal brain structures associated with different psychiatric disorders at different life stages, through a comparative analysis of brain structure-specific and age-specific gene expression profiles and GWAS datasets for psychiatric disorders (Supplementary materials). The mRNA expression profiles of 16 brain structures at 13 developmental stages were derived from BrainSpan (Atlas of the Developing Human Brain, <http://www.brainspan.org>). To ensure the sample sizes of gene expression profile analysis, the brain transcriptomes were divided into five age groups: < 37 post-conceptual weeks (pcw), 0–3 years, 4–13 years, 14–25 years, and > 25 years. Each age group had at least three samples for different brain structures analyzed in this study. For each brain structure, the limma package was used to compare the gene expression profiles of each age group with that of all remaining samples in the same brain structure. The brain-specific differentially-expressed gene sets can be viewed as the gene expression biomarkers of the corresponding brain structure at a certain stage. Specifically in this study, the top 10% of identified differentially-expressed genes were used to generate representative gene sets specific to a certain brain structure at a certain development stage. The latest GWAS datasets of five common psychiatric disorders were downloaded from the Psychiatric Genomics Consortium website (<http://www.med.unc.edu/pgc/>). Briefly, these GWAS datasets included 7,387 cases and 8,567 controls

Xin Qi and Cuiyan Wu have contributed equally to this work.

Electronic supplementary material The online version of this article (<https://doi.org/10.1007/s12264-020-00521-7>) contains supplementary material, which is available to authorized users.

✉ Feng Zhang
fzhxjtu@mail.xjtu.edu.cn

¹ Key Laboratory of Trace Elements and Endemic Diseases of National Health and Family Planning Commission, School of Public Health, Health Science Center, Xi'an Jiaotong University, Xi'an 710061, China

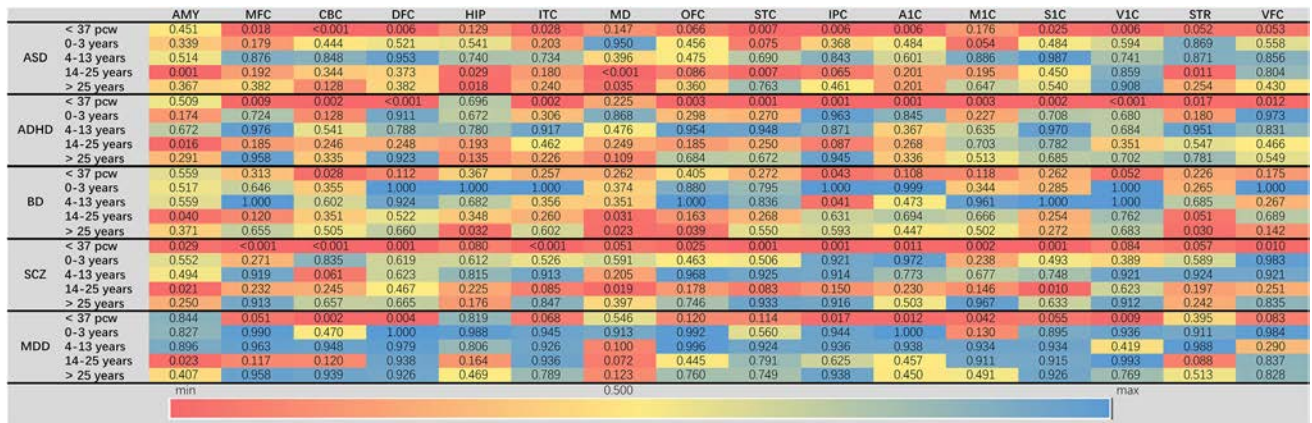


Fig. 1 Heat map of gene set enrichment analysis for the five psychiatric disorders annotating GWAS SNPs to nearby genes. *ADHD* attention-deficit hyperactivity disorder, *ASD* autism spectrum disorder, *MDD* major depressive disorder, *BD* bipolar disorder, *SCZ* schizophrenia, *AMY* amygdaloid complex, *MFC* anterior (rostral) cingulate (medial prefrontal) cortex, *CBC* cerebellar cortex, *DFC* dorsolateral prefrontal cortex, *HIP* hippocampus, *ITC* inferolateral

temporal cortex, *MD* mediodorsal nucleus of thalamus, *OFC* orbital frontal cortex, *STC* posterior superior temporal cortex, *IPC* posteroventral parietal cortex, *A1C* primary auditory cortex, *M1C* primary motor cortex, *S1C* primary somatosensory cortex, *V1C* primary visual cortex, *STR* striatum, *VFC* ventrolateral prefrontal cortex.

for autism spectrum disorder (ASD), 20,183 cases and 35,191 controls for attention-deficit hyperactivity disorder (ADHD), 20,129 cases and 54,065 controls for bipolar disorder (BD), 33,426 cases and 54,065 controls for schizophrenia (SCZ), and 135,458 cases and 344,901 controls for major depressive disorder (MDD). The significant single-nucleotide polymorphisms (SNPs) identified by the GWASs of psychiatric disorders were mapped to genes according to their physical distances to nearby genes and methylation quantitative trait loci (meQTLs) annotation information [1, 2]. SNPs were mapped into nearby genes, which means they have an effect on the genes due to the short distance. SNPs were aligned with the SNP-target gene annotation data of meQTLs, which means that SNPs influence the genes due to the regulation of DNA methylation status at CpG sites. With the brain structure-specific gene sets at different stages (identified by gene expression profiles) and genes associated with psychiatric disorders (identified by GWASs), the gene set enrichment analysis (GSEA) approach was implemented to evaluate the functional relevance of 16 brain structures to psychiatric disorders at a certain development stage [3]. Significant enrichment was detected at a false discovery rate (FDR) < 0.05.

For annotating GWAS SNPs to nearby genes, the GSEA results of the five psychiatric disorders are summarized in Fig. 1. We identified 16, 14, 9, 15, and 7 enrichment signals related to brain structure for ASD, ADHD, BD, SCZ, and MDD, respectively, such as primary auditory cortex before 37 pcw ($FDR_{nearby} = 6.30 \times 10^{-3}$ for ASD, $FDR_{nearby} = 5.00 \times 10^{-4}$ for ADHD).

For annotating GWAS SNPs to meQTL-related target genes, GSEA results of the five psychiatric disorders are summarized in Fig. 2. We found 15, 12, 22, 27, and 10 enrichment signals related to brain structure for ASD, ADHD, BD, SCZ and MDD, respectively, such as posteroventral parietal cortex before 37 pcw ($FDR_{meQTLs} = 8.32 \times 10^{-3}$ for BD, $FDR_{meQTLs} = 5.83 \times 10^{-4}$ for SCZ, $FDR_{meQTLs} = 1.97 \times 10^{-2}$ for MDD).

Besides, several overlapped brain structure-related enrichment signals shared by annotating GWAS SNPs to nearby genes and meQTL-related target genes were found. Specific to ASD, ADHD, BD, SCZ, and MDD, 11, 10, 7, 14, and 6 overlapped brain structure-related enrichment signals were discovered, respectively, such as amygdaloid complex at 14–25 years ($FDR_{nearby} = 1.33 \times 10^{-3}$, $FDR_{meQTLs} = 7.27 \times 10^{-3}$ for ASD), cerebellar cortex before 37 pcw ($FDR_{nearby} < 0.001$, $FDR_{meQTLs} = 2.00 \times 10^{-3}$ for SCZ), and orbital frontal cortex after 25 years ($FDR_{nearby} = 3.94 \times 10^{-2}$, $FDR_{meQTLs} = 2.50 \times 10^{-4}$ for BD) (Table 1).

It has been demonstrated that different psychiatric disorders involve the dysfunction of different brain structures, due to widespread alterations in functional connectivity. For instance, Moberget *et al.* reported that cerebellar cortical volume is significantly reduced in patients with SCZ compared with healthy controls [4]. Ishida *et al.* detected abnormalities in the cerebellum of BD patients [5]. ADHD has been found to be associated with volumetric reductions of the frontal regions [6]. Besides, there is growing evidence supporting the hypothesis that the age of onset of brain dysfunction ranges from early childhood for

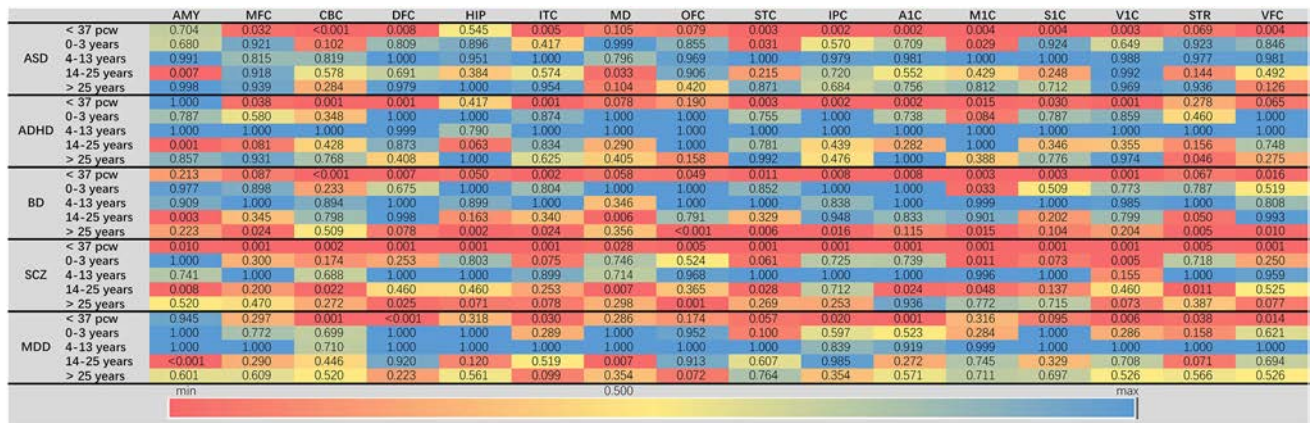


Fig. 2 Heat map of gene set enrichment analysis for the five psychiatric disorders annotating GWAS SNPs to the meQTL-related target genes (abbreviations as in Fig. 1).

ASD to late adolescence and early adulthood for SCZ [7]. Psychiatric disorders usually begin at certain stages of life with specific gene expression patterns that contribute to brain dysfunction during the development of psychiatric disorders [8]. Therefore, we combined the brain structures and developmental stages to explore the genetic mechanisms of psychiatric diseases.

For SCZ, after comparing the GSEA results of nearby and meQTL-related genes, the significant developmental stages were < 37 pcw and 14–25 years, consistent with previous studies showing that the age of onset for SCZ typically begins at late adolescence or early adulthood [9]. Our results also suggested that dysfunction of the cerebellar cortex and dorsolateral prefrontal cortex contributed to the development of SCZ. One study that found a significant difference in cerebellar volume between SCZ patients and healthy controls implied that this abnormality is specific to SCZ [10]. Moreover, a previous study found that long-interval cortical inhibition of dorsolateral prefrontal cortex in SCZ patients is significantly lower than in healthy cases ($P = 0.004$) [11].

For BD, two stages (14–25 and > 25 years) were both significant in the GSEA results of nearby and meQTL-related genes. A previous study found that the typical age of onset for BD is young adulthood, consistent with our results [12]. Moreover, we discovered that the abnormal development of orbital frontal cortex and the striatum greatly contributed to the etiology of BD. Of note, there is supporting evidence that dysfunctional orbital prefrontal cortex is associated with mania, which is included in BD, using high-sensitivity positron emission tomography [13]. By comparing the transcriptomic sequencing between 18 BD patients and 17 controls and co-expression network analysis, the module with the highest genetic association signal for BD was also enriched in the gene expression of

dorsal striatum medium spiny neurons, implying that the etiology of BD is associated with striatal function at the gene level [14]. In addition, novel isoforms of the PDE10A gene, usually expressed in the striatum, have been associated with BD [15].

Psychiatric disorders usually begin at certain stages of life with specific gene expression patterns, contributing to brain dysfunction during the development of psychiatric disorders. A comparative analysis of the genetic loci associated with psychiatric disorders and gene expression patterns specific to brain structures can be used to evaluate the functional relevance of different brain structures to psychiatric disorders. Our research supplies a method that can realize the localization of brain structures related to the different developmental stages of psychiatric disorders. This study also provides a new approach to studying the pathogenic mechanisms underlying complex mental diseases.

Nevertheless, there were three limitations in our study. First, we analyzed the differently-expressed genes in the differential developmental stages of 16 brain areas. However, due to the limitation of cases, other brain structures were not analyzed. Second, the data used in this study were obtained from Europeans. There are differences among ethnic groups in the mechanisms of psychiatric disorders. For this reason, careful interpretation is needed while applying our results to other groups. Third, although in the GSEA results we used $FDR < 0.05$ to control the false-positive rate, we did not control the false-positive rate when calculating the differently expressed genes specific to a brain structure at a certain developmental stage. In further research, this issue requires attention.

In this study, we aimed to evaluate the functional relevance of different brain structures in five common psychiatric disorders at different developmental stages. Our

Table 1 List of the common brain structure-related enrichment signals for the five psychiatric disorders by annotating GWAS SNPs to nearby genes and meQTL-related target genes.

Brain Structures	Stages	ASD		ADHD		BD		SCZ		MDD	
		FDR _{nearby}	FDR _{meQTLs}								
CBC	< 37 pcw	< 0.001	< 0.001	1.75 × 10 ⁻³	5.00 × 10 ⁻⁴	2.75 × 10 ⁻²	< 0.001	&< 0.001	2.00 × 10 ⁻³	2.25 × 10 ⁻³	1.25 × 10 ⁻³
MD	14–25 years	< 0.001	3.31 × 10 ⁻²			3.10 × 10 ⁻²	5.75 × 10 ⁻³	1.89 × 10 ⁻²	6.71 × 10 ⁻³		
AMY	14–25 years	1.33 × 10 ⁻³	7.27 × 10 ⁻³	1.60 × 10 ⁻²	1.25 × 10 ⁻³	4.00 × 10 ⁻²	3.31 × 10 ⁻³	2.08 × 10 ⁻²	8.08 × 10 ⁻³		
IPC	< 37 pcw	5.58 × 10 ⁻³	1.50 × 10 ⁻³	5.00 × 10 ⁻⁴	2.00 × 10 ⁻³	4.32 × 10 ⁻²	8.32 × 10 ⁻³	6.00 × 10 ⁻⁴	5.83 × 10 ⁻⁴	1.67 × 10 ⁻²	1.97 × 10 ⁻²
VIC	< 37 pcw	6.07 × 10 ⁻³	3.43 × 10 ⁻³							8.88 × 10 ⁻³	6.17 × 10 ⁻³
DFC	< 37 pcw	6.19 × 10 ⁻³	7.80 × 10 ⁻³	< 0.001	1.40 × 10 ⁻³			6.25 × 10 ⁻⁴	1.00 × 10 ⁻³	4.00 × 10 ⁻³	< 0.001
AIC	< 37 pcw	6.30 × 10 ⁻³	1.67 × 10 ⁻³	5.00 × 10 ⁻⁴	1.63 × 10 ⁻³			1.06 × 10 ⁻²	7.86 × 10 ⁻⁴	1.17 × 10 ⁻²	6.67 × 10 ⁻⁴
STC	< 37 pcw	7.25 × 10 ⁻³	3.00 × 10 ⁻³	9.00 × 10 ⁻⁴	2.69 × 10 ⁻³			1.38 × 10 ⁻³	6.67 × 10 ⁻⁴		
SIC	< 37 pcw	2.48 × 10 ⁻²	4.00 × 10 ⁻³	1.67 × 10 ⁻³	2.99 × 10 ⁻²			5.00 × 10 ⁻⁴	6.25 × 10 ⁻⁴		
ITC	< 37 pcw	2.82 × 10 ⁻²	4.80 × 10 ⁻³	1.50 × 10 ⁻³	1.42 × 10 ⁻³			< 0.001	7.50 × 10 ⁻⁴		
MFC	< 37 pcw	1.81 × 10 ⁻²	3.20 × 10 ⁻²	9.32 × 10 ⁻³	3.77 × 10 ⁻²			< 0.001	6.11 × 10 ⁻⁴		
MIC	< 37 pcw			3.17 × 10 ⁻³	1.53 × 10 ⁻²			1.5 × 10 ⁻³	1.09 × 10 ⁻²		
STR	> 25 years					2.96 × 10 ⁻²	4.56 × 10 ⁻³				
HIP	> 25 years					3.20 × 10 ⁻²	1.88 × 10 ⁻³				
OFC	> 25 years					3.94 × 10 ⁻²	2.50 × 10 ⁻⁴				
VFC	< 37 pcw							9.59 × 10 ⁻³	9.09 × 10 ⁻⁴		
OFC	< 37 pcw							2.46 × 10 ⁻²	5.30 × 10 ⁻³		
AMY	< 37 pcw							2.86 × 10 ⁻²	1.04 × 10 ⁻²	2.27 × 10 ⁻²	< 0.001

ADHD attention-deficit hyperactivity disorder, *ASD* autism spectrum disorder, *MDD* major depressive disorder, *BD* bipolar disorder, *SCZ* schizophrenia, *AMY* amygdaloid complex, *MFC* anterior (rostral) cingulate (medial prefrontal) cortex, *CBC* cerebellar cortex, *DFC* dorsolateral prefrontal cortex, *ITC* inferolateral temporal cortex, *MD* mediodorsal nucleus of thalamus, *OFC* orbital frontal cortex, *STC* posterior superior temporal cortex, *IPC* posteroventral parietal cortex, *AIC* primary auditory cortex, *MIC* primary motor cortex, *STR* striatum, *SIC* primary somatosensory cortex, *VFC* ventrolateral prefrontal cortex, *VIC* primary visual cortex, *HIP* hippocampus.

results provide novel clues for understanding the biological mechanisms of these disorders considering different brain structures at different ages.

Acknowledgements This work was supported by the National Natural Scientific Foundation of China (81673112), the Key Projects of International Cooperation among Governments in Scientific and Technological Innovation (2016YFE0119100), the Natural Science Basic Research Plan in Shaanxi Province of China (2017JZ024), and the Fundamental Research Funds for the Central Universities.

Conflict of interest The authors claim that there are no conflicts of interest.

References

1. Wang K, Li M, Bucan M. Pathway-based approaches for analysis of genome-wide association studies. *Am J Hum Genetics* 2007, 81: 1278–1283.
2. McClay JL, Shabalina AA, Dozmorov MG, Adkins DE, Kumar G, Nerella S, *et al.* High density methylation QTL analysis in human blood via next-generation sequencing of the methylated genomic DNA fraction. *Genome Biol* 2015, 16: 291.
3. Subramanian A, Tamayo P, Mootha VK, Mukherjee S, Ebert BL, Gillette MA, *et al.* Gene set enrichment analysis: A knowledge-based approach for interpreting genome-wide expression profiles. *Proc Natl Acad Sci U S A* 2005, 102: 15545–15550.
4. Moberget T, Doan NT, Alnæs D, Kaufmann T, Córdova-Palomera A, Lagerberg TV, *et al.* Cerebellar volume and cerebellocerebral structural covariance in schizophrenia: a multisite mega-analysis of 983 patients and 1349 healthy controls. *Mol Psychiatry* 2017, 23: 1512.
5. Ishida T, Donishi T, Iwatani J, Yamada S, Takahashi S, Ukai S, *et al.* Elucidating the aberrant brain regions in bipolar disorder using T1-weighted/T2-weighted magnetic resonance ratio images. *Psychiatry Res* 2017, 263: 76–84.
6. Noordermeer SDS, Luman M, Greven CU, Veroude K, Faraone SV, Hartman CA, *et al.* Structural brain abnormalities of attention-deficit/hyperactivity disorder with oppositional defiant disorder. *Biol Psychiatry* 2017, 82: 642–650.
7. Marín O. Developmental timing and critical windows for the treatment of psychiatric disorders. *Nat Med* 2016, 22: 1229.
8. Johnson MB, Kawasawa YI, Mason CE, Krsnik Z, Coppola G, Bogdanović D, *et al.* Functional and evolutionary insights into human brain development through global transcriptome analysis. *Neuron* 2009, 62: 494–509.
9. Gomes FV, Rincón-Cortés M, Grace AA. Adolescence as a period of vulnerability and intervention in schizophrenia: Insights from the MAM model. *Neurosci Biobehav Rev* 2016, 70: 260–270.
10. Laidi C, d'Albis MA, Wessa M, Linke J, Phillips ML, Delavest M, *et al.* Cerebellar volume in schizophrenia and bipolar I disorder with and without psychotic features. *Acta Psychiatrica Scand* 2015, 131: 223–233.
11. Farzan F, Garcia Dominguez L, Semeralul MO, Radhu N, Daskalakis ZJ, Richter MA, *et al.* Evidence for inhibitory deficits in the prefrontal cortex in schizophrenia. *Brain* 2014, 138: 483–497.
12. Nowrouzi B, McIntyre RS, MacQueen G, Kennedy SH, Kennedy JL, Ravindran A, *et al.* Admixture analysis of age at onset in first episode bipolar disorder. *J Affect Disord* 2016, 201: 88–94.
13. Blumberg HP, Stern E, Ricketts S, Martinez D, de Asis J, White T, *et al.* Rostral and orbital prefrontal cortex dysfunction in the manic state of bipolar disorder. *Am J Psychiatry* 1999, 156: 1986–1988.
14. Pacifico R, Davis RL. Transcriptome sequencing implicates dorsal striatum-specific gene network, immune response and energy metabolism pathways in bipolar disorder. *Mol Psychiatry* 2016, 22: 441.
15. MacMullen CM, Vick K, Pacifico R, Fallahi-Sichani M, Davis RL. Novel, primate-specific PDE10A isoform highlights gene expression complexity in human striatum with implications on the molecular pathology of bipolar disorder. *Transl Psychiatry* 2016, 6: e742.



Molecular Basis for Cephalic Mechanosensitivity of *Drosophila* Larvae

Zhenyu Zhang¹ · Zhiyuan Li¹ · Ting Liu¹ · Wei Zhang¹

Received: 9 December 2019 / Accepted: 3 June 2020 / Published online: 6 August 2020
© Shanghai Institutes for Biological Sciences, CAS 2020

Dear Editor,

For an animal to explore its environment, the mechanosensors on its head are of particular importance. For example, in *Drosophila* larvae that constantly explore the surrounding substrate during foraging and wandering, the cephalic segments host highly specialized organs with extraordinary mechanical sensitivity [1]. While mechanosensation on the thoracic and abdominal segments has been studied extensively [2], the functions and molecular features of cephalic mechanosensation have not yet been characterized, despite the unambiguous presence of mechanosensors [3].

In *Drosophila*, there are mainly two types of mechanosensory neuron (Types I and II) in the peripheral nervous system [4]. Type I neurons include external sensory (es) organ neurons and internal chordotonal neurons [5]. In contrast, Type II neurons are characterized by elaborate arborizations and are involved in mechanosensation and proprioception [2]. Moreover, the functions of several genes in the transient receptor potential (TRP) family have been demonstrated in larval abdominal gentle touch, sound, and locomotion [2, 6]. It is still an open question whether these genes function in cephalic mechanosensation [7]. Considering the anatomical differences between larval cephalic, thoracic, and abdominal segmental sensory organs, it is critical to determine the

expression and function of these genes in larval cephalic sensory organs as well as their functions in mechanotransduction.

Fly larvae show stereotyped responses to gentle touch and the behavior pattern depends on the touch location. Previous studies have used a human eyelash to stroke the thoracic segments from posterior to anterior and quantified the touch sensitivity by scoring each response [8]. Given that such stimulation might be too strong for the larval head, we fabricated a U-shaped polypropylene probe to deliver reliable and mild touch stimuli (Fig. 1A). We found that the score in response to head touch was ~ 10 (summation of 5 trials) in wild-type larvae (Fig. 1B). As a first step to investigate the molecular mechanism underlying the head-touch response, we tested the head touch sensitivity of the mutants from a pool of mechanotransduction channel genes with the above assay (Fig. 1B). Among these genes, *nompC* and *nanchung* (*nan*) mutant larvae showed a significant defect in the head-touch response (Fig. 1B), while *piezo* and *pickpocket*, channels involved in nociception, were dispensable for cephalic touch sensation (Fig. 1B).

The phenotype of the *nompC* mutant paralleled the previous findings on the role of *nompC* in gentle touch [2]. To gain mechanistic insights onto how *nompC* senses head touch, we first explored its expression in the cephalic segment with *nompC* driver lines. There are four types of external sensory organ in the larval head: the terminal organ (TO), dorsal organ (DO), ventral organ (VO), and labial organ [9]. In the DO, *nompC*-QF labels neurons in a non-overlapping pattern with Gr21a- and Or83b- positive olfactory neurons (Fig. 1F), suggesting that these neurons are tubular body-containing neurons in the cylindrical portion of the DO [10, 11]. In the TO, *nompC*^{GFP} knock-in exhibited regular sensilla distribution and sub-cellular

Electronic supplementary material The online version of this article (<https://doi.org/10.1007/s12264-020-00555-x>) contains supplementary material, which is available to authorized users.

✉ Wei Zhang
wei_zhang@mail.tsinghua.edu.cn

¹ School of Life Sciences, Tsinghua-Peking Joint Center for Life Sciences, IDG/McGovern Institute for Brain Research, Tsinghua University, Beijing 100084, China

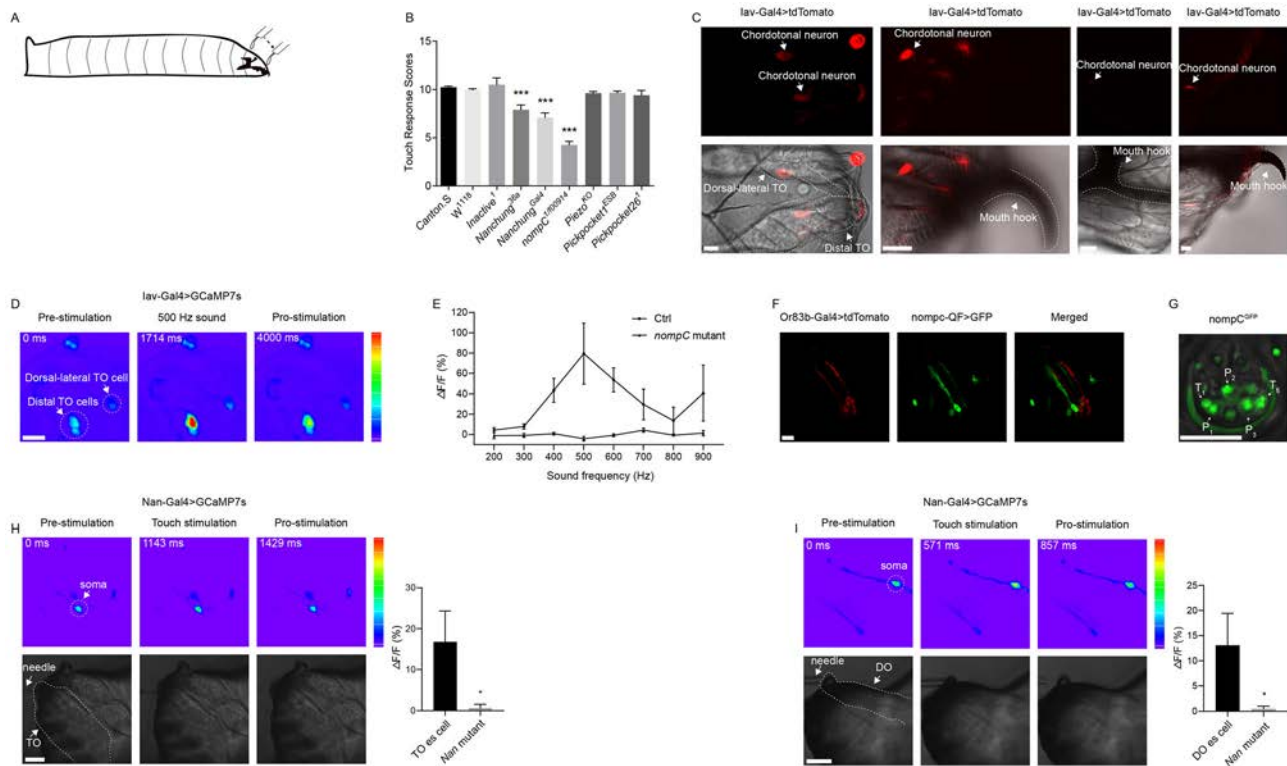


Fig. 1 TRP channel genes are required for larval cephalic mechanosensation. **A** Schematic of the larval head-touch assay. Gentle touch stimuli were applied to the head from posterior to anterior. **B** Screen for the head-touch response in mutants of candidate mechanotransduction channel genes. Mutants of the TRPV gene *nanchung* show a defective response. **C** *Iav-Gal4* marks chordotonal neurons in the larval head. From left to right: two cells (white arrowheads) in the TO with cell bodies located in the TOG; one cell (white arrowhead) in the dorso-distal part of the TO with the cell body located in the “bridge” between DO and TO; one cell located under mouthhook (white arrowhead); one cell may belong to the thoracic internal organ (white arrowhead); and one cell located around the mouth (white arrowhead) (scale bars, 10 μ m). **D** Cephalic chordotonal neurons (labelled by both *iav* and *nan*) respond to 500 Hz sound

stimuli. Genotype is *iav-Gal4*; *UAS-GCaMP7s* (color range, 0–255; scale bar, 10 μ m). **E** Chordotonal neurons in the terminal organ have a frequency selectivity similar to abdominal chordotonal neurons. The response to sound disappears in the *nompC* mutant. Ctrl: *w*; *iav-Gal4/+*; *UAS-GCaMP7s/+*. *nompC* mutant: *nompC¹/nompC³*. **F** *nompC-QF* (green) labels neurons in the dorsal organ. Olfactory neurons are labelled with the *Or83b-Gal4*. Green: *w*; *nompC-QF*, *QUAS-GFP*. Red: *or83b-Gal4*, *UAS-tdTomato* (scale bar, 10 μ m). **G** *nompC* is enriched in the tip of the TO sensilla (anterior view; scale bar, 10 μ m). **H, I** Cephalic es neurons in the TO (**H**) and DO (**I**) from wild-type and *Nan^{Gal4}* flies respond to external mechanical stimuli (color range, 0–255; scale bars, 10 μ m). **P* < 0.05, ***P* < 0.005, ****P* < 0.0005

localization. We saw strong GFP signals from the dendrite tips, indicating a highly specialized subcellular enrichment of the *nompC* protein (Fig. 1G).

Since the *nan* mutant also exhibited a significantly reduced head-touch response (Fig. 1B), we next asked how *nan* functions in touch sensation. We first checked the expression of *nan-Gal4* in the larval head sensory organs. Nine neurons were labeled in each hemi-segment and 6 of them were co-labelled with *iav-Gal4*. *Nan* and *iav* are usually co-expressed in chordotonal neurons that sense stretch and vibration [6, 12]. Among these 6 neurons, one was located in thoracic internal organs, one under the mouth hook, one in the mouth that may belong to the labial organ, two in the TO, and one in the dorsolateral part of the TO (Fig. 1C). The larval Cho neurons are vibration sensors that trigger an avoidance response [6]. All 6 of these

neurons showed a significant response to 500 Hz sound stimuli (data not shown). We also checked the frequency-dependence of the Cho neurons in the TO. These two neurons showed a frequency dependence similar to abdominal Cho neurons (Fig. 1E). We thus speculated that the cephalic Cho neurons play a role in vibration detection in the cephalic segment, although we were not able to test their functional involvement as there is no specific marker for these neurons.

In contrast, the 3 *nan⁺iav⁻* neurons were separately located in the TO, DO, and VO. The neuron in TO may belong to the T₁ sensilla that contained a tubular body-positive neuron (data not shown). We then checked the co-expression of *nan* and *nompC* in the TO and DO, and found that, compared to *nompC-QF* larvae, the average number of neurons expressing GFP did not change when combining

nan-Gal4 and *nompC*-QF, indicating that the nan-Gal4-labeled neurons in the TO and DO also express *nompC*. Based on their morphology, these $\text{nan}^+ \text{nompC}^+ \text{iav}^-$ neurons were likely es organ neurons. As described above, *nan* mutant larvae showed a reduced touch response while *iav* mutants did not, suggesting that the es organ neurons in the TO and DO are essential for touch sensation. To test this hypothesis, we monitored the activity of the nan^+ es organ neurons with the Ca^{2+} indicator GCaMP [6]. These neurons responded to touch on the cephalic end and the response was largely absent from the *nan* mutant larvae (Fig. 1H, I). The Nan-Gal4 used here did not label other external organ or md neurons in the body segments [12], indicating that the cephalic es organs may be enriched in specific mechanoreceptors.

Mechanosensation in the cephalic segments exhibits features remarkably different from that in the other body segments. To gain more insight into how the spatial pattern of gene expression contributes to this inter-segmental heterogeneity, we used RNA-seq to identify genes enriched in the larval head. We collected mRNA from the cephalic segment and analyzed the differential gene expression relative to the A4–A6 abdominal segments.

To verify that our RNA-seq faithfully identified genes with higher expression in the head, we used the Berkeley *Drosophila* Genome Project *in situ* database (<https://insitu.fruitfly.org/cgi-bin/ex/insitu.pl>), Flymine (<http://www.flymine.org/flymine/begin.do>), and Flybase (<http://flybase.org/>) to annotate the expression patterns and molecular functions of the top 40 genes from our RNA-seq results (Table S1), some of which were reported to be expressed in the chemosensory and visual organs located on the head. Most of the rest were expressed in the embryonic head epidermis, embryonic antennal sensory organs, and other organs in the head. These results validated the reliability of our RNA-seq data.

To begin discerning the molecular basis of the heterogeneity of mechanosensation in the larval cephalic segments, we first examined the genes with trans-membrane domains that are most likely involved in mechanotransduction. We selected those with at least two predicted trans-membrane domains from the cephalically-enriched genes in our RNA-seq, resulting in a pool of 146 genes as candidates for our initial behavioral screening (Fig. 2A). We obtained RNAi and/or mutant stocks for most of these genes and tested the head-touch response. Among the 17 genes that showed reduced touch sensitivity (Fig. 2B, C), some have been reported to be important for the development of *Drosophila* md neurons [13], so it thus was surprising that interference with their function disrupted the touch response. For example, *starry night* (*stan*) is one of the two adhesion G-protein-coupled receptors in fly because its extracellular domain has cell-cell adhesion

motifs [14]. In *stan* mutant embryos, md neurons show overextended dendrites [13], which may account for the reduced gentle touch response found here. Another example is *Otk* (Fig. 2B), a gene required for the projection of motoneuron axon tracts [15, 16]. Both motor and sensory problems could contribute to the touch defect of the *otk* mutant.

Among all these hits, a previously uncharacterized gene, CG43778, was of particular interest because its mutant had the most severe touch defect among all the genes tested and its molecular/cellular function had not yet been studied (Fig. 2B). We named this gene *headbutt* (*hbt*). The MIMIC (Minos-mediated integration cassette) insertion of HBT showed only half of the touch response score of the wild-type w^{1118} (Fig. 2C). To confirm this touch response phenotype, we generated a full knockout of HBT using the CRISPR/Cas9 method. The back-crossed homozygous knockout of HBT and the trans-heterozygotes of MIMIC and knockout showed a touch response defect as severe as the MIMIC line (Fig. 2D), indicating that this gene is critical for mediating the head-touch response.

To further investigate how HBT is involved in touch sensation, we knocked-in a superfolder GFP at the C-terminal of the HBT coding sequence (HBT^{GFP}). The GFP fluorescence then served as an indicator for the distribution HBT protein. We found strong GFP signals in the TO and DO (Fig. 2E, F). In the TO, the expression of HBT was divided into dorsolateral and distal parts (Fig. 2E). Interestingly, HBT protein was notably enriched in the TO but not the TOG (terminal organ ganglion) (Fig. 2E), forming a tubule-like structure in the dorsolateral part that hosts the cell bodies of the sensory neurons (Fig. 2F). We also observed that HBT protein forms a sheath-like layer surrounding the brain and the ventral nerve cord, a structure resembling glial ensheathment [17]. In the DO, HBT^{GFP} formed a tube-like structure (Fig. 2F). We checked the co-localization of HBT^{GFP} cells and Or83b chemosensory neurons and found that, like the Cho neurons in the TO, Or83b-labeled sensory neurons were enwrapped by HBT^{GFP} cells (Fig. 2G).

The MIMIC line for *hbt* used here was generated by inserting a MiMIC transposon in the first intron after a non-coding exon in the HBT genome region. The MiMIC transposon contains an enhanced GFP after the three stop codons but before the ATG of the HBT coding sequence, thus resulting in the production of GFP under the control of the regulatory regions of HBT and reflecting the expression pattern of HBT (we named this line *hbt*-GFP as it used a mechanism similar to enhancer-trap). Indeed, the GFP expression driven by this *hbt*-GFP largely recapitulated the pattern of the HBT^{GFP} larvae (Fig. 2J–L).

We next asked how HBT regulates mechanosensation as an extrinsic protein. During the development of each type I

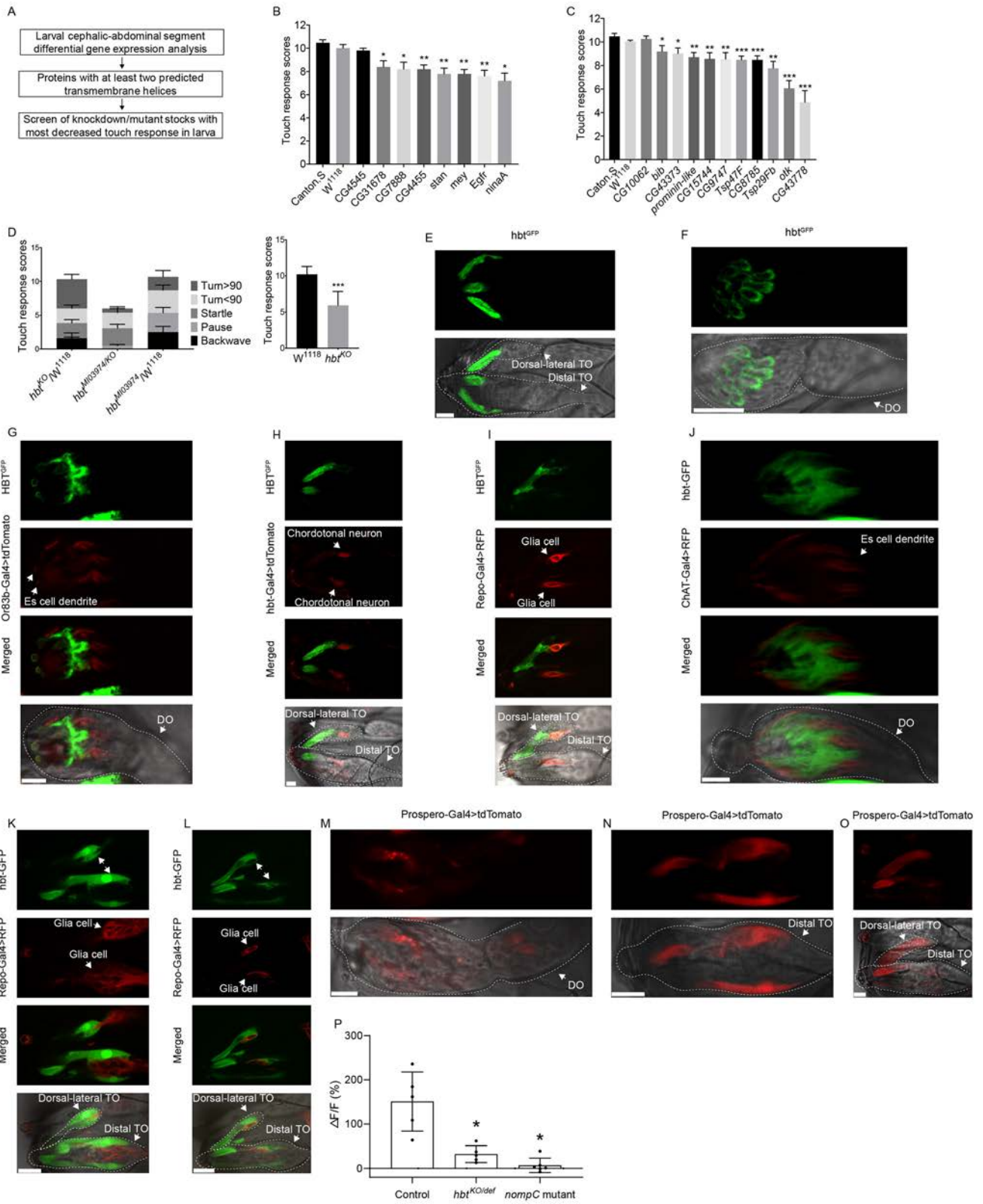


Fig. 2 HBT functions in sheath cells for cephalic sensory organs to sense touch. **A** Flowchart of the screen for genes involved in the larval head-touch response. **B** Hits from the screen for genes with gene-specific RNAi. UAS-RNAi lines were crossed to Cha-Gal4 ($n \geq 5$); CG4545 is the positive control. **C** Hits from the screen using mutant alleles ($n \geq 10$); CG10062 is the positive control. **D** Gentle touch response of *hbt* mutant larvae ($hbt^{M103974}$, HBT MiMIC insertion; hbt^{KO} , HBT full knockout). **E** HBT is enriched in the anterior region of both the dorsolateral and distal parts of the TO (scale bar, 10 μ m). **F** HBT proteins bundle to form a tube-like structure in the DO (scale bar, 10 μ m). **G** In the DO, HBT proteins wrap the dendrites of es cells (green, HBT^{GFP}; red, Or83b > tdTomato; scale bar, 10 μ m). **H** In the TO, HBT proteins wrap the cell bodies of chordotonal neurons (green, HBT^{GFP}; red, chordotonal neurons, HBT-Gal4 > tdTomato; scale bar, 10 μ m). **I** In the TO, HBT proteins wrap glial cells of chordotonal neurons (green, HBT^{GFP}; red, glial cells, Repo-Gal4 > RFP; scale bar, 10 μ m). **J–L** HBT MiMIC labels cells in a pattern similar to HBT^{GFP} in the DO (**J**), TO (**K**), and glial cells ensheathing chordotonal neurons (**L**) (green, HBT MiMIC insertion line; red, Repo-Gal4 > RFP (**J**), ChAT-Gal4 > RFP (**K**, **L**); scale bars, 10 μ m). **M–O** prospero-Gal4 labels sheath cells in the DO, distal TO, and dorsolateral TO (red, prospero-Gal4 > UAS-tdTomato; scale bars, 10 μ m). **P** HBT is required for larval TO mechanosensation. *hbt* mutant larval chordotonal neurons in the TO show a significantly reduced Ca²⁺ response (*nompC* mutant is the positive control). * $P < 0.05$, ** $P < 0.005$, *** $P < 0.0005$

sensilla, four asymmetric mitotic divisions produce one or more sensory neurons, three surrounding support cells, and a glial cell [18]. The thecogen cell forms the sheath cell of neurons, may secrete the extracellular matrix surrounding the neural dendrites [18], and can be labeled by the transcription factor prospero. The remaining glial cells accumulate the common glia marker Repo. We first checked whether the *hbt*-expressing cells are indeed glial cells. We used Repo-Gal4 to express RFP in glial cells in larval TOs and DOs. A glial cell was found in the dorsal-distal part of the TO where one chordotonal neuron soma is located, and a ring-like structure surrounds this soma (Fig. 2H, I). The cells labeled in the *hbt*-GFP line also formed a large ring-like structure that exactly surrounded the glial cell (Fig. 2L). The other part of this cell extended to the distal part of the TO like HBT^{GFP}. The distal part of the TO contained two chordotonal neurons whose cell bodies were located more distal in the TOG (Fig. 2L), although the glial cell was larger.

In the DO, however, the situation was slightly different. The DO does not contain any chordotonal neurons and all cell bodies are located in the DOG (dorsal organ ganglion). Glial cells were only found in the proximal part of the DO and they did not entirely ensheath the dendrites of the DO sensory neurons. Instead, the HBT-GFP cells were not located in the DOG, but they formed a tube-like structure in the DO similar to HBT^{GFP} (Fig. 2J). This was reminiscent of the prospero-positive sheath cells of the DO [19]. Previous work has suggested that the DO is composed of

14 sensilla, each containing a sheath cell [19]. Considering the very similar structure, we reasoned that HBT is expressed in sheath cells in the type I sensilla of the DO and TO. We used the enhancer-trap line of prospero to drive expression of tdTomato. Importantly, the expression patterns in the TO and DO were similar to those of HBT protein (Fig. 2M–O). These results support the hypothesis that HBT is expressed in sheath cells of the TO and DO.

The larval TO and DO both contain mechanosensory type I cells. As *hbt* mutant larvae show a much-reduced touch response and HBT is enriched in the distal part of the sheath cells, we next asked whether *hbt* mutation influences the mechanosensitivity of type I neurons in the TO and DO. We tested whether *hbt* is required for the Ca²⁺ response of the TO chordotonal neurons and found that, compared to the control group, TO Cho neurons in HBT mutant larvae had a reduced Ca²⁺ response to touch (Fig. 2P). As a positive control, we found that in the *nompC* mutant larvae the Cho neurons lost their normal response to external mechanical stimuli (Fig. 2P), similar to the abdominal Cho neurons [6].

HBT does not have known conserved orthologues in vertebrates. Although this gene appears to play a very specific role in sheath cells in the TO and DO, its molecular function is still an open question. HBT protein is enriched in the anterior parts of both the TO and DO. Given that it has four transmembrane domains and forms a thin tubular structure in the DO, it is possible that HBT is a transmembrane protein and is required for the normal connections between *hbt*-expressing cells and other parts of the DO and TO; it is also conceivable that *hbt* protein is important for maintaining a stable lumen micro-environment in the TO and DO. However, due to the lack of molecular motif prediction, the molecular roles of HBT protein remains to be investigated.

In summary, we characterized the mechanosensory neurons in the larval cephalic segments and found that a triad of TRP channels mediate their mechanosensitivity. Among these, Nan and Iav were co-expressed in chordotonal neurons in the TO, thoracic internal organs, and a chordotonal neuron underneath the mouth hook. Besides, Nan was expressed in three external sensory organ neurons in the TO, DO, and VO and these neurons were also *nompC*-positive. Both nan and *nompC* were required for sensing touch on the larval head. Furthermore, by combining RNA-seq and behavioral screening, we identified the novel gene headbutt (*hbt*) that functions in the cells surrounding the DO and TO to regulate the neuronal mechanosensitivity. Taken together, our study demonstrates that the transduction of mechanical force requires a complete cohort of cellular and molecular machinery and provides an entry point to investigate the neural basis of

cephalic mechanotransduction and inter-segmental mechanosensory integration in *Drosophila*.

Acknowledgements We thank Dr. Yuh-Nung Jan (UCSF) for helpful reagents; Dr. Chun Han for reagents for making conditional-knockout flies; and Dr. Zhiqiang Yan for fly stocks. This work was supported by the National Natural Science Foundation of China (31871059), Beijing Municipal Science and Technology Commission (Z181100001518001), and a “Brain+X” seed grant from the IDG/McGovern Institute for Brain Research at Tsinghua University.

References

- Kernan M, Cowan D, Zuker CS. Genetic dissection of mechanosensory transduction: mechanoreception-defective mutants of *Drosophila*. *Neuron* 1994, 12: 1195–1206.
- Yan Z, Zhang W, He Y, Gorczyca D, Xiang Y, Cheng LE, *et al.* *Drosophila* NOMPC is a mechanotransduction channel subunit for gentle-touch sensation. *Nature* 2013, 493: 221–225.
- Hückesfeld S, Niederegger S, Heinzl H-G, Spieß R. The cephalic and pharyngeal sense organs of *Calliphora vicina* 3rd instar larvae are mechanosensitive but have no profound effect on ongoing feeding related motor patterns. *Journal of insect physiology* 2010, 56: 1530–1541.
- Singhania A, Grueber WB. Development of the embryonic and larval peripheral nervous system of *Drosophila*. *Wiley Interdisciplinary Reviews-Developmental Biology* 2014, 3: 193–210.
- Sun Y, Jia Y, Guo Y, Chen F, Yan Z. Taurine Transporter dEAAT2 is Required for Auditory Transduction in *Drosophila*. *Neurosci Bull* 2018, 34: 939–950.
- Zhang W, Yan Z, Jan LY, Jan YN. Sound response mediated by the TRP channels NOMPC, NANCHUNG, and INACTIVE in chordotonal organs of *Drosophila* larvae. *Proc Natl Acad Sci USA* 2013, 110: 13612–13617.
- Rist A, Thum AS. A map of sensilla and neurons in the taste system of *Drosophila* larvae. *J Comp Neurol* 2017, 525: 3865–3889.
- Kernan M, Cowan D, Zuker C. Genetic dissection of mechanosensory transduction: mechanoreception-defective mutations of *Drosophila*. *Neuron* 1994, 12: 1195–1206.
- Miroschnikow A, Schlegel P, Schoofs A, Hueckesfeld S, Li F, Schneider-Mizell CM, *et al.* Convergence of monosynaptic and polysynaptic sensory paths onto common motor outputs in a *Drosophila* feeding connectome. *Elife* 2018, 7.
- Li K, Gong Z. Feeling Hot and Cold: Thermal Sensation in *Drosophila*. *Neurosci Bull* 2017, 33: 317–322.
- Budelli G, Ni L, Berciu C, van Giesen L, Knecht ZA, Chang EC, *et al.* Ionotropic Receptors Specify the Morphogenesis of Phasic Sensors Controlling Rapid Thermal Preference in *Drosophila*. *Neuron* 2019, 101: 738–747.e733.
- Nesterov A, Spalthoff C, Kandasamy R, Katana R, Rankl NB, Andrés M, *et al.* TRP Channels in Insect Stretch Receptors as Insecticide Targets. *Neuron* 2015, 86: 665–671.
- Grueber WB, Jan LY, Jan YN. Tiling of the *Drosophila* epidermis by multidendritic sensory neurons. *Development* 2002, 129: 2867–2878.
- Langenhan T, Piao X, Monk KR. Adhesion G protein-coupled receptors in nervous system development and disease. *Nature Reviews Neuroscience* 2016, 17: 550.
- Winberg ML, Tamagnone L, Bai J, Comoglio PM, Montell D, Goodman CS. The Transmembrane Protein Off-Track Associates with Plexins and Functions Downstream of Semaphorin Signaling during Axon Guidance. *Neuron* 2001, 32: 53–62.
- Pulido D, Campuzano S, Koda T, Modolell J, Barbacid M. Dtrk, a *Drosophila* gene related to the trk family of neurotrophin receptors, encodes a novel class of neural cell adhesion molecule. *The EMBO journal* 1992, 11: 391–404.
- Hartenstein V. Morphological diversity and development of glia in *Drosophila*. *Glia* 2011, 59: 1237–1252.
- Kernan MJ. Mechanotransduction and auditory transduction in *Drosophila*. *Pflugers Arch* 2007, 454: 703–720.
- Grillenzoni N, de Vaux V, Meuwly J, Vuichard S, Jarman A, Holohan E, *et al.* Role of proneural genes in the formation of the larval olfactory organ of *Drosophila*. *Development genes and evolution* 2007, 217: 209–219.



REVIEW

Role of the *C9ORF72* Gene in the Pathogenesis of Amyotrophic Lateral Sclerosis and Frontotemporal Dementia

Zongbing Hao¹ · Rui Wang¹ · Haigang Ren¹ · Guanghui Wang¹

Received: 19 January 2020 / Accepted: 30 April 2020 / Published online: 29 August 2020
© Shanghai Institutes for Biological Sciences, CAS 2020

Abstract Since the discovery of the *C9ORF72* gene in 2011, great advances have been achieved in its genetics and in identifying its role in disease models and pathological mechanisms; it is the most common genetic cause of amyotrophic lateral sclerosis (ALS) and frontotemporal dementia (FTD). ALS patients with *C9ORF72* expansion show heterogeneous symptoms. Those who are *C9ORF72* expansion carriers have shorter survival after disease onset than non-*C9ORF72* expansion patients. Pathological and clinical features of *C9ORF72* patients have been well mimicked *via* several models, including induced pluripotent stem cell-derived neurons and transgenic mice that were embedded with bacterial artificial chromosome construct and that overexpressing dipeptide repeat proteins. The mechanisms implicated in *C9ORF72* pathology include DNA damage, changes of RNA metabolism, alteration of phase separation, and impairment of nucleocytoplasmic transport, which may underlie *C9ORF72* expansion-related ALS/FTD and provide insight into non-*C9ORF72* expansion-related ALS, FTD, and other neurodegenerative diseases.

Keywords Amyotrophic lateral sclerosis · Frontotemporal dementia · *C9ORF72* · Dipeptide repeat proteins · Pathological inclusions

Introduction

Amyotrophic lateral sclerosis (ALS) is a fatal neurodegenerative disease characterized by a deficiency of upper and lower motor neurons in the motor cortex and lumbar spinal cord, respectively [1]. Frontotemporal dementia (FTD) is a devastating disease that mainly involves the frontal and temporal lobes [2]. A GGGGCC (G4C2) hexanucleotide repeat expansion (HRE) in the intron of the *C9ORF72* gene was identified in 2011 and is the most common genetic cause of both ALS and FTD [3–5]. Tens to thousands of G4C2 repeats have been identified in carriers and patients with the *C9ORF72*-related ALS and FTD (c9ALS/FTD) mutation, while only ~30 repeats occur in normal individuals [3, 4]. The HRE can be further transcribed and translated into sense and antisense RNAs, as well as dipeptide repeat proteins (DPRs) that include poly-GA, poly-GP, poly-GR, poly-PA, and poly-PR [6–12].

The underlying mechanisms of c9ALS/FTD can be classified into three prototypes (Fig. 1): (1) loss-of-function of the *C9ORF72* protein [13–17]; (2) formation of sense and antisense RNA foci in the nucleus [18–20]; and (3) gain-of-function caused by repeat-associated non-ATG-initiated translation of DPRs [21–24]. In recent years, several studies have implicated *C9ORF72* in cellular protein transport and that loss of *C9ORF72* impairs autophagy [13, 14, 25–27] and lysosome biogenesis [28]. Despite the fact that *C9ORF72* loss-of-function contributes to microglial activation and a “cytokine storm” in several transgenic mouse models, reducing the expression of *C9ORF72* alone does not induce c9ALS/FTD phenotypes and is dispensable for neuronal survival [15–17, 26, 29]. Thus, we summarize the literature focusing on gain-of-function in this review.

✉ Guanghui Wang
wanggh@suda.edu.cn

¹ Laboratory of Molecular Neuropathology, Jiangsu Key Laboratory of Neuropsychiatric Diseases and Department of Pharmacology, College of Pharmaceutical Sciences, Soochow University, Suzhou 215123, China

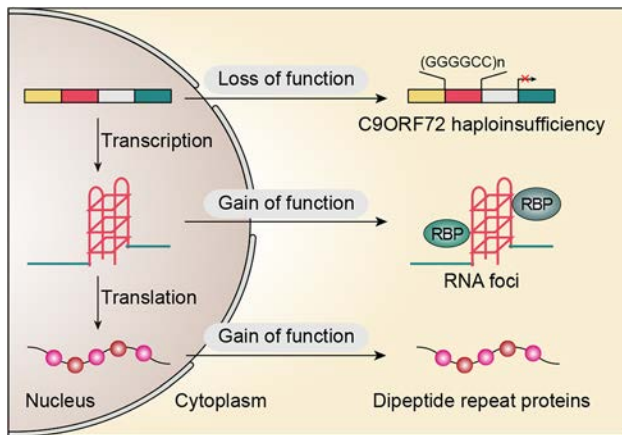


Fig. 1 Mechanisms underlying the GGGGCC hexanucleotide repeat expansion. (1) Loss-of-function: Decreased expression of *C9orf72* mRNA in the frontal cortex of individuals with *C9ORF72* mutation. (2) Gain-of-function caused by RNA foci: The GGGGCC repeat expansion is transcribed into repeat RNA that can interact with DNA to fold into a G-quadruplex structure. The repeat RNA forms RNA foci that sequester RNA-binding proteins in the nucleus of vulnerable neurons. (3) Gain-of-function caused by dipeptide repeat proteins (DPRs): In a repeat-associated non-ATG-initiated manner, the repeat RNA is translated into DPRs that form toxic aggregates in residual neurons.

Clinical Features

Genetics

The G4C2 HRE in the noncoding region of the *C9ORF72* gene contributes to ~25.1% of familial FTD and 37.6% of familial ALS world-wide [30–32]. Strikingly, in the Finnish population, *C9ORF72* repeat expansion accounts for up to 46.0% of familial ALS and 21.1% of sporadic ALS [4], but the frequency of *C9ORF72* repeat expansion is extremely low in Asian populations [33–35]. In recent years, several studies have comprehensively described the clinical and pathological features of *C9ORF72* patients who exhibit wide variation of age at onset and disease duration [36–44]. Most bulbar-onset *C9ORF72* patients exhibit symptomatic heterogeneity [38, 39, 43], including behavioral-variant FTD, progressive non-fluent aphasia, motor neuron disease, ALS, and mild psychosis and anxiety symptoms [41–43]. The ALS patients with *C9ORF72* expansion have shorter survival after disease onset than those without *C9ORF72* expansion [45].

Pathological Features

Neuronal Deficiency

Within a cohort of patients with behavioral variant FTD, compared with patients with mutation in microtubule-associated protein tau (*MAPT*) and progranulin (*GRN*) that

display specific anteromedial temporal atrophy [46, 47] and temporoparietal atrophy [48, 49], respectively, the patients with HRE in *C9ORF72* show a widespread pattern of grey matter loss in the cerebellum and spinal cord, and the extramotor frontal lobes, temporal lobes, and hippocampus, as well as the basal ganglia and occipital lobes [37–44, 50]. Notably, an atrophied cerebellum, which is a characteristic pathology of c9ALS/FTD, is not presented in brain of FTD cases without *C9ORF72* expansion [51, 52], suggesting a specific role of *C9ORF72* in cerebellar pathogenesis. Several other studies using magnetic resonance imaging (MRI) and unbiased voxel-based morphometric analysis have also found broad brain atrophy in *C9ORF72* patients [41, 44], thereby accounting for the clinical heterogeneity of these patients.

Pathological Inclusions

One specific pathological feature of c9ALS/FTD is the presence of G4C2 nuclear RNA foci in both sense and antisense forms [3, 8]; the other is cytoplasmic inclusions of RNA-translated DPRs [9–12, 53]. Notably, intranuclear inclusions of DPRs that co-localize with nucleoli have been identified in the frontal cortex of *C9ORF72* patients [54, 55]. The expression of the five DPRs is predominantly in the form of poly-GA, to a lesser extent poly-GP and poly-GR, compared to poly-PA and poly-PR [53]. However, only slight clinico-pathological correlations of poly-GA, but not other DPRs, have been reported in c9ALS/FTD [53]. It is still unclear how much other DPRs contribute to the pathogenesis, especially arginine-rich poly-GR/PR.

TDP-43 is a major component in the pathological inclusions in the ALS and FTD brain [56–58]. FTD-TDP is classified into four types according to the heterogeneity of TDP-43 inclusions: cytoplasmic inclusions, short neurites in the upper cortical layers (Type A), round TDP-43 inclusions throughout the cortex (Type B), long dystrophic neurites (Type C), and intranuclear inclusions (Type D) [59]. Broad inclusions of TDP-43 have also been identified in the vulnerable neurons of c9ALS/FTD, mainly containing type A, type B, or a combination of both [59–62]. A series of studies have reported that p62-positive, TDP-43-negative cytoplasmic inclusions are present in the cerebellar granular cells of c9ALS/FTD patients, while such inclusions are not found in non-*C9ORF72* mutant individuals [40, 42, 53, 61, 63, 64], indicating a specific role of HRE in the protein degradation pathway. The clinical and pathological features of c9ALS/FTD described elsewhere are summarized in Table 1.

In recent years, impaired nucleocytoplasmic transport has been identified as a common pathological process in *C9ORF72* expansion-induced neurodegeneration [65–68]. Using large-scale unbiased genetic screening, several genes

Table 1 Clinical and pathological features of frontotemporal dementia and amyotrophic lateral sclerosis with *C9ORF72* gene mutation

References	Demographics	Regions	Clinical features	Initiation	Onset*	Duration*	Neuropathology	Inclusions	Refs
2012. Cooper-Knock <i>et al.</i>	563 ALS cases fALS: 43% sALS: 7%	Northern England	ALS and dementia	60% limb, 31% bulbar	57.3	2.5	Motor: UMN and LMN loss Extramotor: Hippocampus and frontal cortex atrophy	TDP-43 type B	[39]
2012. Chio <i>et al.</i>	ALS cases 141 Italian cases 41 German cases	Italy and Germany	ALS, bvFTD, cognitive impairment, psychosis	Bulbar	57.6	3.2	NA	NA	[38]
2012. Simon-Sanchez <i>et al.</i>	353 FTD cases fFTD: 28.7% sFTD: 2.2%	Netherlands	bvFTD, ALS, primary progressive aphasia, memory impairment	5 bulbar 2 limb	56.9	7.6	Temporal, occipital cortex, cerebellum, and SN atrophy	TDP-43 types A, B, and C	[42]
2012. Snowden <i>et al.</i>	398 FTD cases	Manchester/UK	FTD/MND, psychosis, repetitive behaviors	Bulbar	58.3	2.7	Frontal, temporal atrophy, depigmented SN	TDP-43 types A and B	[43]
2012. Mahoney <i>et al.</i>	223 FTD cases	London/UK	60% MND, bvFTD, anxiety, agitation, memory impairment	NA	55.0	8.7	Frontal, temporal, parietal, thalamus, cerebellar atrophy	TDP-43 types A and B	[41]
2012. Boeve <i>et al.</i>	604 FTD/ALS cases	Mayo/USA	bvFTD, 35% PD, ALS, complex executive dysfunction	NA	52	5	Frontal, temporal, parietal atrophy; white matter atrophy	TDP-43 types A and B	[37]
2012. Hsiung <i>et al.</i>	29 FTD/ALS cases	European ethnic origin	bvFTD, progressive non-fluent aphasia, ALS and mild ataxia	NA	54.3	5.3	Motor: Frontal, cerebellar atrophy, LMN loss Extramotor: neo-cortex, hippocampus, SN	TDP-43 types A and B	[40]
2012. Whitwell <i>et al.</i>	76 FTD cases	Mayo/USA	FTD, ALS	NA	NA	NA	Frontal, temporal, parietal, occipital and cerebellar atrophy	TDP-43 types A and C	[44]

bvFTD, behavioral-variant FTD; LMN, lower motor neuron; NA, data not available; PD, Parkinson's disease; SN, substantia nigra; UMN, upper motor neuron; *years

in the nucleocytoplasmic transport process have been identified as major hints in G4C2-expressing *Drosophila* models [66]. Consistently, RanGAP1, a key regulator of nucleocytoplasmic transport [69, 70], is abnormally distributed in the cortex of the G4C2 mouse model and *C9ORF72* ALS patients [67].

Mouse Models with Hexanucleotide Repeat Expansion

It has been reported that overexpression of HRE causes obvious cellular toxicity in cell cultures [18, 19, 23], G4C2 *Drosophila* models [71–73], and a G4C2 zebrafish model

[20]. In addition, Petrucelli and colleagues have developed two G4C2-expressing mouse models using an AAV-packaged hexanucleotide expansion with 66 or 149 repeats [74, 75]. In the 66-repeat model, the mice show evident expression of intranuclear sense RNA foci and DPRs in the central nervous system (CNS), accompanied by motor dysfunction and anxiety-like behaviors, as well as cortical neuronal deficiency [75]. Strikingly, nuclear and cytoplasmic phosphorylated TDP-43 inclusions have been observed in the cortex and hippocampus of (G4C2)66 mice [75]. The 149-repeat mice show similar phenotypes, while antisense RNA foci, in amounts from 10% to 20%, have been found in the hippocampus, cortex, and cerebellum. In addition, the antisense DPRs poly-PA and poly-PR have been

detected in the cortex of 149-repeat mice at 3 months of age [74]. Mis-localization of RanGAP1 and aggregation of stress granule-associated proteins have also been reported in the cortex and hippocampus of 149-repeat mice [74], suggesting that overexpression of HRE is enough to model the neuropathological changes of c9ALS/FTD.

To identify the pathological effects of HRE at lower expression levels, several groups have developed bacterial artificial chromosome (BAC) transgenic mouse models [29, 76–78]. Despite RNA foci and a subset of DPRs in mice containing 500 or 100–1000 repeats of the G4C2 sequence, two BAC models show no behavioral deficiency or neurodegeneration [76, 77]. However, two other transgenic mice show a clear phenotype [29, 78]. One BAC mouse embedded with a patient-derived *C9ORF72* gene harbor either 110 or 450 repeats of G4C2, and the 450-repeat mice display cognitive impairment but not motor deficits, accompanied by size- and dose-dependent expression of RNA foci and DPRs in the CNS [29]. Other transgenic mouse models that have the full-length human *C9ORF72* gene with ~30 and ~500 repeats show obvious gait abnormalities, anxiety-like behavior, and decreased survival, as well as widespread neurodegeneration and TDP-43 pathology [78]. Notably, the antisense RNA foci preferentially accumulate in the c9ALS/FTD-vulnerable cell populations [11, 79, 80]. As both of the latter models have higher expression of human *C9ORF72* mRNA levels than those in the former models [29, 76–78], the expression levels of the human *C9ORF72* gene in mice and the antisense RNA foci and related DPRs may contribute to the phenotypes.

Disease Models with Dipeptide Repeat Proteins

The G4C2 expansion can be translated into five DPRs in a repeat-associated non -ATG-initiated manner (poly-GA, poly-GP, poly-GR, poly-PA, and poly-PR) [7, 9–11]. Among these, poly-GP and poly-GA display higher expression in the c9ALS/FTD brain than the other three DPRs [53]. As poly-GP and poly-PA have been reported to have no cytotoxicity [22, 23, 81], most studies focus on the roles of poly-GA, poly-GR, and poly-PR in neurodegeneration.

Role of Poly-GA in Cytotoxicity

Cell-Culture Models of Poly-GA

Poly-GA forms cellular inclusions and co-localizes with ubiquitin and p62 in GFP-GA50-transfected cultured cells [82]. Poly-GA overexpression induces cytotoxicity, including an increase in caspase-3-positive cells and release of

lactate dehydrogenase, which is also found in cultured primary cortical neurons overexpressing poly-GA [82]. In primary hippocampal neurons, a long repeat length of poly-GA (149 repeats) forms p62-positive inclusions and induces dendrite loss [83]. In addition, GA50 and GA100 cause slight neuronal toxicity in Neuro-2a [81] and NSC-34 cells [84]. However, some studies have reported that 30-repeat lengths of GA have no significant toxicity in NSC-34 and HEK293 cells [24], and that both GA and PA are not neurotoxic even at a length of 200 repeats [23]. To date, it is unclear whether the toxicity of poly-GA depends on the expression levels or cell types.

Drosophila Models with Poly-GA

To determine the role of poly-GA in neurodegeneration, several groups have established poly-GA *Drosophila* models with different repeat lengths [22, 23, 81]. The expression of GA50 and PA50 in *Drosophila* does not induce neurotoxicity, which is consistent with the previous finding in primary hippocampal neurons [23]. Moreover, GA100 and PA100 have no effects on the egg-to-adult viability of *Drosophila* at different temperatures, although GA100 causes a late-onset decrease in survival [22], suggesting a mild toxicity of poly-GA. In addition, overexpression of GA80 does not induce degeneration in *Drosophila* eyes or wing margins [85].

Zebrafish and *Chicken* Models with Poly-GA

Although poly-GA in *Drosophila* does not show cellular toxicity, zebrafishes expressing GA80 show a strong pericardial edema phenotype and dramatically decreased circulation, accompanied by an accumulation of red blood cells, and these phenotypes can be rescued by interfering with the expression of GA80, indicating a toxic property of poly-GA in zebrafish [86]. In addition, poly-GA shows the highest toxicity to neurons in the spinal cord of transgenic chickens as compared to other DPRs [87]. Poly-GA sequesters other DPRs to its aggregates and overexpression of poly-PA inhibits poly-GA aggregation [87], suggesting a role of GA in aggregate formation and the influence of other DPRs on GA aggregation.

Mouse Models with Poly-GA

Given the limitations of cultured cells and *Drosophila* models, several groups have constructed poly-GA transgenic mouse models [88–90]. In poly-GA transgenic mice, in which the expression of poly-GA is controlled by the *Thy1* promoter, poly-GA is mainly distributed in the spinal cord and brainstem [88]. The mice show co-aggregation of poly-GA with p62, Rad23b, and Mif2; this also occurs in

c9ALS/FTD patients [88]. The animals show some behavioral changes, including motor imbalance and hypoactivity, but no defects in muscle strength or spatial memory [88]. Moreover, the mice have no significant motor neuron deficiency in the spinal cord, although microglial activation is present there [88]. With intracerebroventricular injection of adeno-associated virus (AAV)-packaged GFP-GA50, the mice present motor deficits, brain atrophy, neurodegeneration, and neuroinflammation at post-natal day 0 [89]. Poly-GA-induced motor dysfunction has been confirmed using a similar method [90]. Thus, overexpressed poly-GA has neurotoxic effects and induces motor defects in vertebrates, although its effects in cultured cells or *Drosophila* remain controversial.

Roles of Poly-GR and Poly-PR in Cytotoxicity

Cellular Models with Poly-GR and Poly-PR

Within DPRs, poly-GR and poly-PR show strong toxicity in both cellular and animal models, in which several methods have been applied to avoid the toxic effects caused by G4C2 RNA foci. *In vitro* analyses show that synthetic GR20 or PR20 forms nucleolar inclusions and is significantly cytotoxic in U2OS cells and primary astrocytes [21]. In primary cortical neurons, overexpression of PR50 has high neurotoxicity, while poly-GR-induced cell death is repeat-length dependent [23]. Moreover, the cellular toxicity of arginine-rich poly-GR and poly-PR has been reported in multiple cell lines, including Neuro-2a [81], NSC-34 [24, 84], SH-SY5Y [91], and primary cortical neurons [92]. In addition, overexpression of PR100 [93] and GR80 [94] in induced pluripotent stem cell (iPSC)-derived neurons induces significant neuron deficiency and a DNA damage response, further indicating the high toxicity of arginine-rich poly-GR and poly-PR.

Drosophila Models with Poly-GR and Poly-PR

To address whether DPR-induced neurotoxicity depends on repeat RNA, Mizielinska and colleagues have constructed *Drosophila* models in which they use two strategies: (1) a 6 base-pair interruption that contains a stop codon in both the sense and antisense directions is inserted in every G4C2 repeat, which construct produces “RNA-only” repeats without DPR expression; and (2) using alternative codons that encode the same amino-acids but disrupt the G4C2 repeat, which construct expresses “DPR-only” without G4C2 repeats [22]. In *Drosophila*, GR100 and PR100 exhibit strong toxicity, leading to severe neurodegeneration and reduced survival, while GA100 causes late-onset disease [22]. However, “RNA-only” repeats do not induce neurodegeneration and disease phenotypes, suggesting that

DPRs, especially poly-GR and poly-PR, are major factors in *C9ORF72*-induced pathogenesis [22]. Expression of PR50 in motor neurons induces developmental failure in *Drosophila*, despite a normal body morphology [23]. In addition to the neuronal toxicity of arginine-rich DPRs, GR80 exhibits non-neuronal cellular toxicity in *Drosophila*, such as wing margin defects [85], suggesting that PR and GR are highly toxic to both neuronal and non-neuronal cells in *Drosophila*.

Mouse Models with Poly-GR and Poly-PR

Several *C9ORF72* BAC transgenic mice have been established to identify the role of the *C9ORF72* gene in disease [29, 76–78]. Nuclear RNA foci and DPRs have been found in the brain of BAC transgenic mice that have no motor neuron degeneration, although one BAC mouse with an FVB/NJ background shows decreased survival and motor deficits [29, 76–78]. Thus, transgenic mice with long hexanucleotide repeats in the *C9ORF72* gene do not present disease phenotypes, or have only mild phenotypes. Due to the high toxicity of poly-GR and poly-PR in cultured cells, iPSC-derived neurons, and *Drosophila* models, arginine-rich DPR mouse models have been created [95–97]. With intracerebroventricular injections of AAV1 that expresses GFP-GR100, the GFP-GR100 is mainly expressed in the CNS, with a cytoplasmic and diffuse distribution, while there is little expression in the spinal cord [95]. The GR100 mice display progressive motor deficits and memory loss accompanied by age-dependent cortical and hippocampal neurodegeneration. In addition, glial activation occurs at 1.5 months of age [95]. In another mouse model, the spatial and temporal expression of poly-GR is controlled by Tet expression systems, and the expression of GR80 is mainly distributed in the frontal cortex relative to other cortical regions, with diffuse distribution in the cytoplasm and nucleus of 95% of neurons [96]. In addition, the transgenic mice display age-dependent social behavioral deficits, impaired synaptic transmission, cortical neuronal loss, and microglial activation, but no changes in body weight, locomotor activity, and working memory [96]. Thus studies suggest that a long repeat length of poly-GR has a diffuse cytoplasmic distribution and is able to induce severe neurodegeneration and related behavioral deficits *in vivo*.

The poly-PR that shows the highest neurotoxicity in cellular and *Drosophila* models has toxic effects in poly-PR AAV-infected mice and transgenic mice [55, 97]. AAV-infected GFP-PR50 mice show behavioral deficiencies and neurodegeneration at an early stage [55]. Moreover, the overexpression of poly-PR in neurons is highly toxic; up to 60% of GFP-PR50-expressing mice die by 4 weeks of age [55]. Strikingly, in this AAV-mediated poly-

PR expressing mouse, besides a nucleolar distribution, poly-PR mainly exhibits heterochromatic localization, which elicits aberrant post-translational modifications of histone H3 [55]. In the poly-PR transgenic mice with intermediate repeat lengths of poly-PR, the neuronal expression of GFP-PR28 driven by Cre recombinase under control of the *Thy1* promoter is highly toxic [97]. Homozygous transgenic mice develop body weight loss and premature death, similar to GFP-PR50 AAV mice [97]. Heterozygous mice exhibit age-dependent motor dysfunction, decreased survival time, motor-related neuronal deficiency, and neuroinflammation [97]. Unlike the heterochromatic localization of GFP-PR50 in AAV mice [55], GFP-PR28 is mainly distributed in the nucleolus of neurons, as well as a diffuse cytoplasmic distribution in lumbar spinal motor neurons [97]. It is still unknown whether the difference of repeat length in poly-PR between these two models leads to the difference in poly-PR distribution. The animal models of *C9ORF72* with either HRE or dipeptide repeat proteins are summarized in Table 2.

In addition to the difference in cellular localization between poly-GA and arginine-rich DPRs [24], poly-GR and -PR are more neurotoxic than poly-GA in cultured cells [24] and *Drosophila* [22]. Consistent with this, poly-GA mainly influences the cytoplasmic ubiquitin-proteasome system [98], while poly-GR and -PR have effects on nuclear processes. Although all these DPR mice display serious behavioral deficits and neurodegeneration [55, 95–97], they do not develop TDP-43 pathology that is a general neuropathological feature of c9ALS/FTD [56–58]. These data also suggest that the pathogenesis in patients may be complicated. Synergic effects, such as cooperativity between gain- and loss-of-function mechanisms, may be essential for the induction of pathological events.

Pathological Mechanisms

Since the discovery of the non-ATG-initiated translation of *C9ORF72* repeat expansions, a variety of pathological mechanisms linked to DPRs have been identified, ranging from DNA processes to RNA processing to protein translation (Fig. 2).

Shedding Light on DNA Processes

DNA Damage Response (DDR)

Previous studies have demonstrated that an impaired DDR is essential for neuronal deficiency in neurodegenerative diseases [99, 100]. Individuals with mutations in *XRCC1* that encodes a scaffold protein that is involved in DNA

single-strand break repair, present ocular motor apraxia, axon neuropathy, and progressive cerebellar ataxia [101]. Mutations in another ALS/FTD-related gene *FUS* (Fused-in-Sarcoma) lead to a DDR and DNA repair dysfunction [102–106]. Impairment of the DDR can also be induced by mutations in *TDP-43* [107, 108], *ATM* [109], *APTX* [110], and other genes, suggesting a role of the DDR in neurodegeneration.

An essential role of the DDR in the pathogenesis of c9ALS/FTD has been documented in several studies that demonstrated genomic instability as a key event in *C9ORF72*-linked neurodegeneration. In iPSC-derived *C9ORF72* motor neurons, there is increased expression of γ H2AX, a marker of DNA double-strand breaks, and increased tail length in the comet assay, suggesting the presence of DNA damage in c9ALS/FTD [94]. Moreover, the expression of γ H2AX is also increased in the spinal motor neurons of *C9ORF72* patients [90, 93]. In primary cortical neurons and the SH-SY5Y cell line, overexpression of poly-GR and poly-PR induces an accumulation of γ H2AX foci and an increase of phosphorylated ATM, the main kinase for DNA repair [93]. Moreover, in poly-GA and repeat RNA overexpression cellular models, the levels of DNA–RNA hybrids (R-loops), a three-stranded nucleic acid structure produced during the transcription of repeat sequences, are increased, which can lead to genome instability [90]. Furthermore, the ATM signaling pathway is impaired in poly-GA transgenic mice, suggesting that defects in the DNA repair machinery are associated with DPR and RNA repeat-induced DNA damage [90]. DNA damage is increased in iPSC-derived *C9ORF72* motor neurons [94]. Overexpression of poly-GR but not poly-GA in control iPSC-derived motor neurons induces DNA damage [94], further suggesting a role of DPRs in DNA damage.

Heterochromatin and Histone Methylation

Poly-PR is localized to heterochromatin in the cortex of transgenic mice as well as in c9ALS/FTD patients where it causes abnormal histone methylation [55]. In addition, poly-PR reduces the expression levels of HP1 α and disrupts the phase separation of HP1 α , leading to lamin invaginations and double-stranded RNA accumulation [55]. Meanwhile, repetitive elements that make up a large portion of heterochromatin are broadly upregulated in the brains of c9ALS/FTD patients and mice overexpressing poly-PR [55, 111]. The upregulation of abnormal repetitive elements and accumulation of double-stranded RNA induce neurodegeneration. Thus, the abnormality of histone methylation and the dysfunction of heterochromatin and DNA components induced by poly-PR may contribute to the neurodegeneration in c9ALS/FTD.

Table 2 Transgenic mouse models expressing hexanucleotide repeat expansion and dipeptide repeat proteins

References	Constructions	Distributions	Behaviors	Neuropathology	Neuroinflammation	TDP-43	Refs
2015. Chew <i>et al.</i>	AAV2/9-(G4C2) ₆₆ repeats, intracerebroventricular injections	RNA foci: Hippo, MC, cortex, PCs DPRs: GA, GP, and GR in cortex, cereb, hippo and SC	Motor dysfunction, hyperactivity, social abnormality, anxiety-like behaviors	Decreased brain weight, cortical atrophy, MC neuronal loss, PC loss	Activated astrocytes in cortex	Nuclear and cytoplasmic pTDP-43 inclusions in cortex and hippo	[75]
2019. Chew <i>et al.</i>	AAV-2/9-(G4C2) ₁₄₉ repeats, intracerebroventricular injections	RNA foci: Hippo, MC, PCs, thalamus DPRs: GA, GP, and GR in cortex, hippo, cereb and SC; PA and PR in cortex and hippo	Motor dysfunction, hyperactivity, cognitive dysfunction	Cortical neuron loss	Activated astrocytes in cortex	Small cytoplasmic pTDP-43 inclusions in cortex and hippo	[74]
2016. Zhang <i>et al.</i>	AAV-1-GFP-(GA) ₅₀ , intracerebroventricular injections	Cytoplasmic and occasional nuclear inclusions in cortex, hippo, OB, and cereb.	Motor dysfunction, hyperactivity, anxiety, and cognitive defects	Decreased brain weight, cortical and hippo neuron loss, PC loss	Activated microglia and astrocytes in cortex and hippo	Rare cytoplasmic pTDP-43 inclusions	[89]
2017. Sch-ludi <i>et al.</i>	Thy1-(GA) ₁₄₉ -CFP	Most cytoplasmic, rare nuclear GA in the BS, cereb, SC	Motor incoordination, hypoactive	No motor neuron loss	Activated microglia but not astrocytes in SC.	No TDP-43 inclusions, but increased urea-soluble pTDP-43	[88]
2018. Zhang <i>et al.</i>	AAV-1-GFP-(GR) ₁₀₀ , intracerebroventricular injections	Widespread expression of diffuse cytoplasmic GR100 in brain	Motor dysfunction, hypoaffective, memory impairment	Decreased brain weight, hippo cell loss, PC loss	Activated microglia and astrocytes in cortex	Rare cytoplasmic pTDP-43 inclusions	[95]
2019. Chio <i>et al.</i>	Mini-CMV-flag-(GR) ₈₀ , tTA-controlled inducible expression system	Variable distribution, mainly diffuse cytoplasmic form in frontal cortex	Social abnormality, anxiety-like behaviors	Cortical neuronal deficits	Activated microglia and astrocytes in cortex	No TDP-43 inclusions	[96]
2019. Hao <i>et al.</i>	GFP-(PR) ₂₈ , Thy1-cre controlled expression system	Widespread expression of PR in nucleoli of neurons	Motor dysfunction, hyperactivity, anxiety-like behaviors	Decreased brain weight, cortical atrophy, UMN and LMN loss, PC loss	Activated microglia and astrocytes in cereb and SC	No TDP-43 inclusions	[97]
2019. Zhang <i>et al.</i>	AAV-1-GFP-(PR) ₅₀ , intracerebroventricular injections	Nuclear distribution (heterochromatin and nucleoli) in cortex and cereb	Motor dysfunction, cognitive deficits	Decreased brain weight, cortical thinning, hippo atrophy, PC loss	Activated microglia and astrocytes in cereb and cortex	No TDP-43 inclusions	[55]

BS, brainstem; cereb, cerebellum; Hippo, hippocampus; MC, motor cortex; OB, olfactory bulb; PC, Purkinje cell; SC, spinal cord

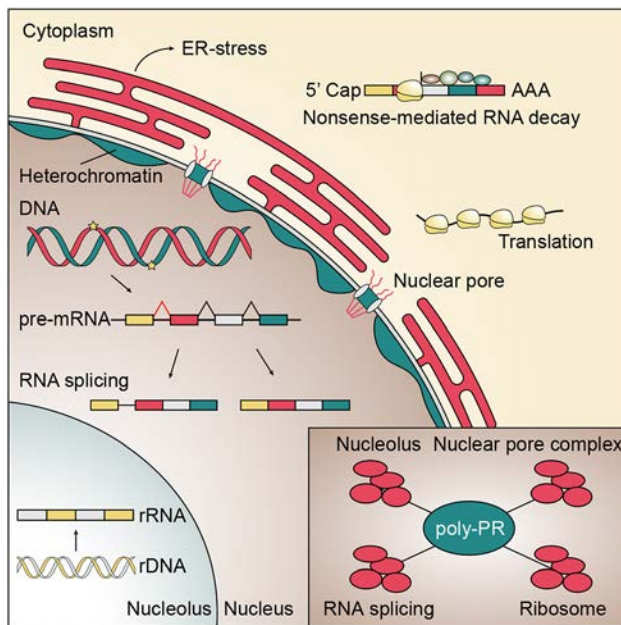


Fig. 2 Potential mechanisms linked to DPR overexpression. DPR overexpression causes neuronal deficiency through mechanisms that range from DNA processes to RNA processing to protein translation. DPRs cause a DNA damage response and poly-PR induces abnormal histone methylation and dysfunction of heterochromatin. Defects in RNA processing such as nonsense-mediated RNA decay, RNA splicing, and ribosomal RNA processing are linked to arginine-rich DPRs. Moreover, these DPRs contribute to dysfunction of protein homeostasis through nucleocytoplasmic transport, the unfolded protein response (ER-stress), and translation. The diagram in the lower right corner summarizes the biological processes related to poly-PR-binding proteins, which mainly include the nucleolus, RNA splicing, the nuclear pore complex, and the ribosome. rDNA, ribosomal DNA; rRNA, ribosomal RNA.

RNA Processing

Nonsense-Mediated RNA Decay (NMD)

NMD, a cellular RNA degradation system that is activated in response to stress, rapidly degrades mRNA containing premature termination codons to prevent the translation of defective proteins [112, 113]. UPF1–3 are master factors for NMD activation in which UPFs interact with each other, the ribosome, and multiple mRNA decay factors [112, 113]. NMD can be inhibited, which is indicated by an overlap of upregulated NMD substrate genes in c9ALS/FTD-derived iPSCs and *UPF3B*^{-/-} lymphocytes [91]. Numerous NMD substrate genes accumulate in PR36 *Drosophila* [91]. In addition, there are significant overlaps in the accumulated NMD genes in flies overexpressing PR36 and those deficient in UPF1 or UPF2 [91]. Furthermore, the NMD substrate genes *Sin3A*, *Gadd45*, *Xrp1*, and *Arc1* do not accumulate in flies expressing α -synuclein, Htt-128Q, or human FUS, although these genes do accumulate in flies overexpressing GR36 or PR36 or with UPF1 knockdown [91]. In contrast,

overexpression of UPF1 significantly inhibits the neurotoxicity induced by GR36 or PR36.

Although the primary cause of NMD by DPRs remains unknown, a reactivation of NMD significantly ameliorates the neurotoxicity in flies expressing DPRs, indicating that impairment of NMD contributes to the pathology of *C9ORF72*.

RNA Splicing

Pre-mRNA splicing and the biogenesis of rRNA are significantly impaired in cultured human astrocytes expressing poly-PR/GR [21]. Notably, FUS and TDP-43, two other ALS-related gene products, have been shown to cause a pre-mRNA splicing dysfunction and reduce downstream gene expression [114–117]. Another study using unbiased quantitative mass spectrometry demonstrated that poly-GR/PR binds to U2 snRNPs (small nuclear ribonucleoproteins) and inhibits spliceosome assembly [118]. Moreover, bioinformatics analysis showed that U2-dependent exons are misspliced in the cortex and cerebellum of *C9ORF72* patients [118]. Previous results have revealed that arginine-rich poly-PR and poly-GR, but not poly-GA, bind to proteins that contain low complexity domains [81, 119]. Consistently, a number of binding proteins with low complexity domains, including several U2 snRNPs, have also been detected [118]. These data suggest that U2 snRNPs sequestered by arginine-rich DPRs contribute to the blocked alternative splicing in *C9ORF72* patients.

Protein Homeostasis

Proteinopathies such as ALS mainly exhibit protein inclusions with impaired quality control systems in cells [13, 14, 120]. Poly-GR and poly-PR interact with proteins that contain low complexity domains and disturb the phase separation of membrane-less organelles, such as the nucleolus, the nuclear pore complex, and stress granules [81, 119, 121, 122]. The function of poly-GR and poly-PR in the nuclear pore complex and stress granules has been systematically described in other reviews [123, 124]. Here, we mainly focus on the role of poly-GR and poly-PR in the protein quality control system, including the unfolded protein response and translation.

Unfolded Protein Response (UPR)

Using unbiased CRISPR-Cas9 screens, TMX2, an endoplasmic reticulum (ER)-resident transmembrane thioredoxin protein, has been identified as a major modifier of neurotoxicity in primary cortical neurons infected with poly-PR [92]. Moreover, RNA-sequencing analysis has demonstrated that the genes in the ER-stress/UPR pathway are significantly upregulated, including *Atf4*, *Bbc3*, and

Chac1. Knockdown of TMX2 ameliorates the neurotoxicity caused by poly-PR overexpression in primary cortical neurons and in motor neurons derived from *C9ORF72* patients [92]. Notably, the ER-stress-related genes *Chac1* and *Atf5* are upregulated in the cerebellum of poly-PR transgenic mice at 2 months of age, before motor dysfunction occurs, suggesting that ER-stress is an early event in the pathogenesis of poly-PR [97, 125]. In addition, poly-GA overexpression induces pathological inclusions, neurotoxicity, and ER-stress [82]. Pharmacological inhibitors of ER-stress decrease the expression of ER-stress markers and alleviate the neurotoxicity caused by poly-GA [62]. Besides c9ALS/FTD, SOD1-mutated ALS and other neurodegenerative diseases also show the presence of ER-stress in the CNS of patients and animal models [126–128]. Interestingly, using techniques that combine translational ribosome affinity purification and high-throughput RNA sequencing, a cascade of cell type-specific dysregulated processes in SOD1-mutated mice has been identified, showing that the UPR starts within neurons, followed by metabolic and inflammatory gene changes in astrocytes and membrane protein gene alteration in oligodendrocytes [126]. Thus, ER-stress is an early reaction occurring specifically in motor neurons in ALS, and maybe a potential target in ALS therapy.

One interesting but still unanswered question is how poly-PR induces the UPR, as arginine-rich poly-PR is localized in the nucleolus, not the ER. Recently, the nucleolus has been identified as a phase-separated protein control compartment [129]. Under stress, nucleoplasmic proteins are transported to the nucleolus, where Hsp70 mediates refolding, preventing the irreversible aggregation of misfolded proteins [129]. In cells expressing poly-PR, disaggregation of misfolded proteins is inhibited and mobile fractions of liquid-separated proteins are significantly reduced, suggesting an inhibition of nucleolar quality control [129]. Thus, misfolded protein aggregation in the nucleolus, which is caused by poly-PR overexpression, may contribute to the misfolded protein response in c9ALS/FTD. However, it remains unknown whether the nucleolus transmits a stress signal to the ER, thereby leading to ER-stress.

Translation

It is well documented that arginine-rich poly-GR and poly-PR interact with ribosomal proteins, and proteins involved in translation [81, 94, 130, 131]. An inhibition of global translation is consistently found in cultured cells expressing poly-PR [132], primary rat cortical neurons [130], adult *Drosophila* [131], and human iPSC-derived motor neurons [131]. Overexpression of the translation initiation factor eIF1A rescues the translational defects and neurotoxicity caused by poly-PR [131]. In addition, overexpression of

poly-GR100 in mice causes significant neurodegeneration with a dysregulation of genes involved in the ribosomal pathway [95]. The impaired canonical translation occurs in neurons of the GR-expressing mouse model; besides, the non-canonical translation (repeat-associated non-ATG-initiated translation, RAN translation) is also found [95], which argues against previous studies suggesting that DPR-induced ER-stress contributes to the selective activation of RAN translation *in vitro* [133–135]. One reason for the difference may be that the expression of DPR-induced ER-stress thereby activates RAN translation at an early stage, while RAN translation is inhibited under chronic stress.

Therapeutic Advances

Due to the high frequency of *C9ORF72* mutation and the urgent requirement for clinical treatment in ALS and FTD, a wide variety of efforts have been put into the identification of promising therapeutic approaches, from DNA to RNA to DPR protein processes.

DNA Processes

DNA methylation plays a pivotal role in regulating the expression of downstream genes. Hypermethylation has been found in the promoter of the *C9ORF72* gene, which contains G4C2 repeat expansions, leading to reduced *C9orf72* mRNA levels [136]. Neurons from carriers of hypermethylated *C9ORF72* repeat expansions display reduced RNA foci and DPR aggregations, suggesting a protective role of hypermethylation in *C9ORF72*-related pathology [136]. Similarly, genetic manipulation using CRISPR-Cas9 technology that targets the promoter region of the *C9ORF72* gene decreases the levels of *C9ORF72* and DPR proteins, and ameliorates neurotoxicity in iPSC-derived neurons [137]. Despite the promising effects, further efforts are needed to avoid the adverse effects of downregulation of *C9ORF72* protein that is essential for immune function [16] and protein trafficking [28].

RNA Processing

Using unbiased large-scale screens, a number of possible remedies for c9ALS/FTD have focused on transcriptional regulation, targeting the transcriptional regulator *PAF1* [138], transcriptional elongation factor *SPT4* [139], and *AFF2/FMR2* [140]. In addition, antisense oligonucleotides (ASOs) that are single-stranded show clear alleviation of nuclear RNA foci and neurotoxicity [19, 141, 142]. Given the essential role of normal *C9ORF72* protein, optimized ASOs exhibiting no *C9ORF72* RNA reduction have been designed and are successful in reducing the number of

sense RNA foci and the expression of DPRs in transgenic mouse models [29], indicating a hopeful outlook for ASOs in the treatment of ALS and FTD. In addition, RNA-targeting Cas9 is also effective in eliminating the G4C2 repeat RNA foci [143].

Protein Homeostasis

As a result of the high toxicity of DPRs, several strategies have been designed to reduce their levels. RPS25 [144], a small ribosomal protein subunit, and DDX3X [145], an RNA helicase, suppress the translation of DPRs and improve the survival of patient-derived induced motor neurons. Moreover, specific antibodies targeting poly-GA significantly reduce GA protein levels, ameliorate neuronal deficiency, and improve motor dysfunction in transgenic mice [146, 147]. Therefore, selective targeting of DPR expression may also be an alternative therapeutic approach.

Conclusions and Perspectives

Despite the broad achievements in exploring the role of DPRs in disease, several key questions remain unanswered. The DPRs form neuronal cytoplasmic inclusions that are widespread in c9ALS/FTD patients, while overexpression of DPRs *in vivo*, especially arginine-rich poly-PR, only show intranuclear inclusions in selective neurons. It remains unknown whether the repeat length of poly-PR, or the localization of other DPRs that may interact with poly-PR, contributes to the cellular distribution. Similarly, the distribution of TDP-43 is inconsistent with the pathological features and a priority is to identify which factors are essential for TDP-43 inclusions, RNA foci, or aggregated DPRs. It will also be interesting to determine whether DPR inclusions in muscle contribute to clinical pathology [148, 149].

Acknowledgements This work was supported by the National Natural Science Foundation of China (31871023 and 31970966), the National Key Scientific R&D Program of China (2016YFC1306000), and a Project Funded by the Priority Academic Program Development of Jiangsu Higher Education Institutions.

References

1. Bruijn LI, Miller TM, Cleveland DW. Unraveling the mechanisms involved in motor neuron degeneration in ALS. *Annu Rev Neurosci* 2004, 27: 723–749.
2. Bang J, Spina S, Miller BL. Frontotemporal dementia. *Lancet* 2015, 386: 1672–1682.
3. DeJesus-Hernandez M, Mackenzie IR, Boeve BF, Boxer AL, Baker M, Rutherford NJ, *et al.* Expanded GGGGCC hexanucleotide repeat in noncoding region of C9ORF72 causes

- chromosome 9p-linked FTD and ALS. *Neuron* 2011, 72: 245–256.
4. Renton AE, Majounie E, Waite A, Simon-Sanchez J, Rollinson S, Gibbs JR, *et al.* A hexanucleotide repeat expansion in C9ORF72 is the cause of chromosome 9p21-linked ALS-FTD. *Neuron* 2011, 72: 257–268.
5. Gijselinck I, Van Langenhove T, van der Zee J, Sleegers K, Philtjens S, Kleinberger G, *et al.* A C9orf72 promoter repeat expansion in a Flanders-Belgian cohort with disorders of the frontotemporal lobar degeneration-amyotrophic lateral sclerosis spectrum: a gene identification study. *Lancet Neurol* 2012, 11: 54–65.
6. Ash PE, Bieniek KF, Gendron TF, Caulfield T, Lin WL, DeJesus-Hernandez M, *et al.* Unconventional translation of C9ORF72 GGGGCC expansion generates insoluble polypeptides specific to c9FTD/ALS. *Neuron* 2013, 77: 639–646.
7. Gendron TF, Bieniek KF, Zhang YJ, Jansen-West K, Ash PE, Caulfield T, *et al.* Antisense transcripts of the expanded C9ORF72 hexanucleotide repeat form nuclear RNA foci and undergo repeat-associated non-ATG translation in c9FTD/ALS. *Acta Neuropathol* 2013, 126: 829–844.
8. Mizielińska S, Lashley T, Norona FE, Clayton EL, Ridler CE, Fratta P, *et al.* C9orf72 frontotemporal lobar degeneration is characterised by frequent neuronal sense and antisense RNA foci. *Acta Neuropathol* 2013, 126: 845–857.
9. Mori K, Arzberger T, Grasser FA, Gijselinck I, May S, Rentzsch K, *et al.* Bidirectional transcripts of the expanded C9orf72 hexanucleotide repeat are translated into aggregating dipeptide repeat proteins. *Acta Neuropathol* 2013, 126: 881–893.
10. Mori K, Weng SM, Arzberger T, May S, Rentzsch K, Kremmer E, *et al.* The C9orf72 GGGGCC repeat is translated into aggregating dipeptide-repeat proteins in FTLD/ALS. *Science* 2013, 339: 1335–1338.
11. Zu T, Liu Y, Banez-Coronel M, Reid T, Pletnikova O, Lewis J, *et al.* RAN proteins and RNA foci from antisense transcripts in C9ORF72 ALS and frontotemporal dementia. *Proc Natl Acad Sci U S A* 2013, 110: E4968–4977.
12. Mackenzie IR, Arzberger T, Kremmer E, Troost D, Lorenzl S, Mori K, *et al.* Dipeptide repeat protein pathology in C9ORF72 mutation cases: clinico-pathological correlations. *Acta Neuropathol* 2013, 126: 859–879.
13. Sellier C, Campanari ML, Julie Corbier C, Gaucherot A, Kolb-Cheynel I, Oulad-Abdelghani M, *et al.* Loss of C9ORF72 impairs autophagy and synergizes with polyQ Ataxin-2 to induce motor neuron dysfunction and cell death. *EMBO J* 2016, 35: 1276–1297.
14. Webster CP, Smith EF, Bauer CS, Moller A, Hautbergue GM, Ferraiuolo L, *et al.* The C9orf72 protein interacts with Rab1a and the ULK1 complex to regulate initiation of autophagy. *EMBO J* 2016, 35: 1656–1676.
15. Burberry A, Suzuki N, Wang JY, Moccia R, Mordes DA, Stewart MH, *et al.* Loss-of-function mutations in the C9ORF72 mouse ortholog cause fatal autoimmune disease. *Sci Transl Med* 2016, 8: 347ra393.
16. O'Rourke JG, Bogdanik L, Yanez A, Lall D, Wolf AJ, Muhammad AK, *et al.* C9orf72 is required for proper macrophage and microglial function in mice. *Science* 2016, 351: 1324–1329.
17. Sudria-Lopez E, Koppers M, de Wit M, van der Meer C, Westeneng HJ, Zundel CA, *et al.* Full ablation of C9orf72 in mice causes immune system-related pathology and neoplastic events but no motor neuron defects. *Acta Neuropathol* 2016, 132: 145–147.
18. Lee YB, Chen HJ, Peres JN, Gomez-Deza J, Attig J, Stalekar M, *et al.* Hexanucleotide repeats in ALS/FTD form length-

- dependent RNA foci, sequester RNA binding proteins, and are neurotoxic. *Cell Rep* 2013, 5: 1178–1186.
19. Donnelly CJ, Zhang PW, Pham JT, Haeusler AR, Mistry NA, Vidensky S, *et al.* RNA toxicity from the ALS/FTD *C9ORF72* expansion is mitigated by antisense intervention. *Neuron* 2013, 80: 415–428.
 20. Swinnen B, Bento-Abreu A, Gendron TF, Boeynaems S, Bogaert E, Nuyts R, *et al.* A zebrafish model for *C9orf72* ALS reveals RNA toxicity as a pathogenic mechanism. *Acta Neuropathol* 2018, 135: 427–443.
 21. Kwon I, Xiang S, Kato M, Wu L, Theodoropoulos P, Wang T, *et al.* Poly-dipeptides encoded by the *C9orf72* repeats bind nucleoli, impede RNA biogenesis, and kill cells. *Science* 2014, 345: 1139–1145.
 22. Mizielinska S, Gronke S, Niccoli T, Ridler CE, Clayton EL, Devoy A, *et al.* *C9orf72* repeat expansions cause neurodegeneration in *Drosophila* through arginine-rich proteins. *Science* 2014, 345: 1192–1194.
 23. Wen X, Tan W, Westergard T, Krishnamurthy K, Markandiah SS, Shi Y, *et al.* Antisense proline-arginine RAN dipeptides linked to *C9ORF72*-ALS/FTD form toxic nuclear aggregates that initiate in vitro and in vivo neuronal death. *Neuron* 2014, 84: 1213–1225.
 24. Tao Z, Wang H, Xia Q, Li K, Li K, Jiang X, *et al.* Nucleolar stress and impaired stress granule formation contribute to *C9orf72* RAN translation-induced cytotoxicity. *Hum Mol Genet* 2015, 24: 2426–2441.
 25. Sullivan PM, Zhou X, Robins AM, Paushter DH, Kim D, Smolka MB, *et al.* The ALS/FTLD associated protein *C9orf72* associates with *SMCR8* and *WDR41* to regulate the autophagy-lysosome pathway. *Acta Neuropathol Commun* 2016, 4: 51.
 26. Ugolino J, Ji YJ, Conchina K, Chu J, Nirujogi RS, Pandey A, *et al.* Loss of *C9orf72* enhances autophagic activity via deregulated mTOR and TFEB signaling. *PLoS Genet* 2016, 12: e1006443.
 27. Yang M, Liang C, Swaminathan K, Herrlinger S, Lai F, Shiekhatter R, *et al.* A *C9ORF72*/*SMCR8*-containing complex regulates *ULK1* and plays a dual role in autophagy. *Sci Adv* 2016, 2: e1601167.
 28. Shi Y, Lin S, Staats KA, Li Y, Chang WH, Hung ST, *et al.* Haploinsufficiency leads to neurodegeneration in *C9ORF72* ALS/FTD human induced motor neurons. *Nat Med* 2018, 24: 313–325.
 29. Jiang J, Zhu Q, Gendron TF, Saberi S, McAlonis-Downes M, Seelman A, *et al.* Gain of toxicity from ALS/FTD-linked repeat expansions in *C9ORF72* is alleviated by antisense oligonucleotides targeting GGGGCC-containing RNAs. *Neuron* 2016, 90: 535–550.
 30. van Blitterswijk M, DeJesus-Hernandez M, Rademakers R. How do *C9ORF72* repeat expansions cause amyotrophic lateral sclerosis and frontotemporal dementia: can we learn from other noncoding repeat expansion disorders? *Curr Opin Neurol* 2012, 25: 689–700.
 31. Rademakers R, van Blitterswijk M. Motor neuron disease in 2012: Novel causal genes and disease modifiers. *Nat Rev Neurol* 2013, 9: 63–64.
 32. Majounie E, Renton AE, Mok K, Dopfer EG, Waite A, Rollinson S, *et al.* Frequency of the *C9orf72* hexanucleotide repeat expansion in patients with amyotrophic lateral sclerosis and frontotemporal dementia: a cross-sectional study. *Lancet Neurol* 2012, 11: 323–330.
 33. Zou ZY, Zhou ZR, Che CH, Liu CY, He RL, Huang HP. Genetic epidemiology of amyotrophic lateral sclerosis: a systematic review and meta-analysis. *J Neurol Neurosurg Psychiatry* 2017, 88: 540–549.
 34. Liu X, He J, Gao FB, Gitler AD, Fan D. The epidemiology and genetics of Amyotrophic lateral sclerosis in China. *Brain Res* 2018, 1693: 121–126.
 35. Liu Q, Liu F, Cui B, Lu CX, Guo XN, Wang RR, *et al.* Mutation spectrum of Chinese patients with familial and sporadic amyotrophic lateral sclerosis. *J Neurol Neurosurg Psychiatry* 2016, 87: 1272–1274.
 36. Boxer AL, Mackenzie IR, Boeve BF, Baker M, Seeley WW, Crook R, *et al.* Clinical, neuroimaging and neuropathological features of a new chromosome 9p-linked FTD-ALS family. *J Neurol Neurosurg Psychiatry* 2011, 82: 196–203.
 37. Boeve BF, Boylan KB, Graff-Radford NR, DeJesus-Hernandez M, Knopman DS, Pedraza O, *et al.* Characterization of frontotemporal dementia and/or amyotrophic lateral sclerosis associated with the GGGGCC repeat expansion in *C9ORF72*. *Brain* 2012, 135: 765–783.
 38. Chio A, Borghero G, Restagno G, Mora G, Drepper C, Traynor BJ, *et al.* Clinical characteristics of patients with familial amyotrophic lateral sclerosis carrying the pathogenic GGGGCC hexanucleotide repeat expansion of *C9ORF72*. *Brain* 2012, 135: 784–793.
 39. Cooper-Knock J, Hewitt C, Highley JR, Brockington A, Milano A, Man S, *et al.* Clinico-pathological features in amyotrophic lateral sclerosis with expansions in *C9ORF72*. *Brain* 2012, 135: 751–764.
 40. Hsiung GY, DeJesus-Hernandez M, Feldman HH, Sengdy P, Bouchard-Kerr P, Dwosh E, *et al.* Clinical and pathological features of familial frontotemporal dementia caused by *C9ORF72* mutation on chromosome 9p. *Brain* 2012, 135: 709–722.
 41. Mahoney CJ, Beck J, Rohrer JD, Lashley T, Mok K, Shakespear T, *et al.* Frontotemporal dementia with the *C9ORF72* hexanucleotide repeat expansion: clinical, neuroanatomical and neuropathological features. *Brain* 2012, 135: 736–750.
 42. Simon-Sanchez J, Dopfer EG, Cohn-Hokke PE, Hukema RK, Nicolaou N, Seelaar H, *et al.* The clinical and pathological phenotype of *C9ORF72* hexanucleotide repeat expansions. *Brain* 2012, 135: 723–735.
 43. Snowden JS, Rollinson S, Thompson JC, Harris JM, Stopford CL, Richardson AM, *et al.* Distinct clinical and pathological characteristics of frontotemporal dementia associated with *C9ORF72* mutations. *Brain* 2012, 135: 693–708.
 44. Whitwell JL, Weigand SD, Boeve BF, Senjem ML, Gunter JL, DeJesus-Hernandez M, *et al.* Neuroimaging signatures of frontotemporal dementia genetics: *C9ORF72*, tau, progranulin and sporadics. *Brain* 2012, 135: 794–806.
 45. Umoh ME, Fournier C, Li Y, Polak M, Shaw L, Landers JE, *et al.* Comparative analysis of *C9orf72* and sporadic disease in an ALS clinic population. *Neurology* 2016, 87: 1024–1030.
 46. Rohrer JD, Ridgway GR, Modat M, Ourselin S, Mead S, Fox NC, *et al.* Distinct profiles of brain atrophy in frontotemporal lobar degeneration caused by progranulin and tau mutations. *Neuroimage* 2010, 53: 1070–1076.
 47. Spina S, Farlow MR, Unverzagt FW, Kareken DA, Murrell JR, Fraser G, *et al.* The tauopathy associated with mutation +3 in intron 10 of Tau: characterization of the MSTD family. *Brain* 2008, 131: 72–89.
 48. Beck J, Rohrer JD, Campbell T, Isaacs A, Morrison KE, Goodall EF, *et al.* A distinct clinical, neuropsychological and radiological phenotype is associated with progranulin gene mutations in a large UK series. *Brain* 2008, 131: 706–720.
 49. Whitwell JL, Jack CR, Jr., Baker M, Rademakers R, Adamson J, Boeve BF, *et al.* Voxel-based morphometry in frontotemporal lobar degeneration with ubiquitin-positive inclusions with and without progranulin mutations. *Arch Neurol* 2007, 64: 371–376.

50. Hodges J. Familial frontotemporal dementia and amyotrophic lateral sclerosis associated with the C9ORF72 hexanucleotide repeat. *Brain* 2012, 135: 652–655.
51. Corcia P, Vourc'h P, Guennoc AM, Del Mar Amador M, Blasco H, Andres C, *et al.* Pure cerebellar ataxia linked to large C9orf72 repeat expansion. *Amyotroph Lateral Scler Frontotemporal Degener* 2016, 17: 301–303.
52. Goldman JS, Quinzii C, Dunning-Broadbent J, Waters C, Mitsumoto H, Brannagan TH, 3rd, *et al.* Multiple system atrophy and amyotrophic lateral sclerosis in a family with hexanucleotide repeat expansions in C9orf72. *JAMA Neurol* 2014, 71: 771–774.
53. Mackenzie IR, Frick P, Grasser FA, Gendron TF, Petrucelli L, Cashman NR, *et al.* Quantitative analysis and clinico-pathological correlations of different dipeptide repeat protein pathologies in C9ORF72 mutation carriers. *Acta Neuropathol* 2015, 130: 845–861.
54. Schludi MH, May S, Grasser FA, Rentzsch K, Kremmer E, Kupper C, *et al.* Distribution of dipeptide repeat proteins in cellular models and C9orf72 mutation cases suggests link to transcriptional silencing. *Acta Neuropathol* 2015, 130: 537–555.
55. Zhang YJ, Guo L, Gonzales PK, Gendron TF, Wu Y, Jansen-West K, *et al.* Heterochromatin anomalies and double-stranded RNA accumulation underlie C9orf72 poly(PR) toxicity. *Science* 2019, 363: eaav2606.
56. Neumann M, Sampathu DM, Kwong LK, Truax AC, Micsenyi MC, Chou TT, *et al.* Ubiquitinated TDP-43 in frontotemporal lobar degeneration and amyotrophic lateral sclerosis. *Science* 2006, 314: 130–133.
57. Sreedharan J, Blair IP, Tripathi VB, Hu X, Vance C, Rogelj B, *et al.* TDP-43 mutations in familial and sporadic amyotrophic lateral sclerosis. *Science* 2008, 319: 1668–1672.
58. Neumann M, Kwong LK, Lee EB, Kremmer E, Flatley A, Xu Y, *et al.* Phosphorylation of S409/410 of TDP-43 is a consistent feature in all sporadic and familial forms of TDP-43 proteinopathies. *Acta Neuropathol* 2009, 117: 137–149.
59. Burrell JR, Halliday GM, Kril JJ, Ittner LM, Gotz J, Kiernan MC, *et al.* The frontotemporal dementia-motor neuron disease continuum. *Lancet* 2016, 388: 919–931.
60. Murray ME, DeJesus-Hernandez M, Rutherford NJ, Baker M, Duara R, Graff-Radford NR, *et al.* Clinical and neuropathologic heterogeneity of c9FTD/ALS associated with hexanucleotide repeat expansion in C9ORF72. *Acta Neuropathol* 2011, 122: 673–690.
61. Stewart H, Rutherford NJ, Briemberg H, Krieger C, Cashman N, Fabros M, *et al.* Clinical and pathological features of amyotrophic lateral sclerosis caused by mutation in the C9ORF72 gene on chromosome 9p. *Acta Neuropathol* 2012, 123: 409–417.
62. Fratta P, Poulter M, Lashley T, Rohrer JD, Polke JM, Beck J, *et al.* Homozygosity for the C9orf72 GGGGCC repeat expansion in frontotemporal dementia. *Acta Neuropathol* 2013, 126: 401–409.
63. Al-Sarraj S, King A, Troakes C, Smith B, Maekawa S, Bodi I, *et al.* p62 positive, TDP-43 negative, neuronal cytoplasmic and intranuclear inclusions in the cerebellum and hippocampus define the pathology of C9orf72-linked FTL and MND/ALS. *Acta Neuropathol* 2011, 122: 691–702.
64. Troakes C, Maekawa S, Wijesekera L, Rogelj B, Siklos L, Bell C, *et al.* An MND/ALS phenotype associated with C9orf72 repeat expansion: abundant p62-positive, TDP-43-negative inclusions in cerebral cortex, hippocampus and cerebellum but without associated cognitive decline. *Neuropathology* 2012, 32: 505–514.
65. Jovicic A, Mertens J, Boeynaems S, Bogaert E, Chai N, Yamada SB, *et al.* Modifiers of C9orf72 dipeptide repeat toxicity connect nucleocytoplasmic transport defects to FTD/ALS. *Nat Neurosci* 2015, 18: 1226–1229.
66. Freibaum BD, Lu Y, Lopez-Gonzalez R, Kim NC, Almeida S, Lee KH, *et al.* GGGGCC repeat expansion in C9orf72 compromises nucleocytoplasmic transport. *Nature* 2015, 525: 129–133.
67. Zhang K, Donnelly CJ, Haeusler AR, Grima JC, Machamer JB, Steinwald P, *et al.* The C9orf72 repeat expansion disrupts nucleocytoplasmic transport. *Nature* 2015, 525: 56–61.
68. Shi KY, Mori E, Nizami ZF, Lin Y, Kato M, Xiang S, *et al.* Toxic PRn poly-dipeptides encoded by the C9orf72 repeat expansion block nuclear import and export. *Proc Natl Acad Sci U S A* 2017, 114: E1111–E1117.
69. Gorlich D, Pante N, Kutay U, Aebi U, Bischoff FR. Identification of different roles for RanGDP and RanGTP in nuclear protein import. *EMBO J* 1996, 15: 5584–5594.
70. Ritterhoff T, Das H, Hofhaus G, Schroder RR, Flotho A, Melchior F. The RanBP2/RanGAP1*SUMO1/Ubc9 SUMO E3 ligase is a disassembly machine for Crm1-dependent nuclear export complexes. *Nat Commun* 2016, 7: 11482.
71. Burguete AS, Almeida S, Gao FB, Kalb R, Akins MR, Bonini NM. GGGGCC microsatellite RNA is neuritically localized, induces branching defects, and perturbs transport granule function. *Elife* 2015, 4: e08881.
72. Celona B, Dollen JV, Vatsavayai SC, Kashima R, Johnson JR, Tang AA, *et al.* Suppression of C9orf72 RNA repeat-induced neurotoxicity by the ALS-associated RNA-binding protein Zfp106. *Elife* 2017, 6: e19032.
73. Xu Z, Poidevin M, Li X, Li Y, Shu L, Nelson DL, *et al.* Expanded GGGGCC repeat RNA associated with amyotrophic lateral sclerosis and frontotemporal dementia causes neurodegeneration. *Proc Natl Acad Sci U S A* 2013, 110: 7778–7783.
74. Chew J, Cook C, Gendron TF, Jansen-West K, Del Rosso G, Daugherty LM, *et al.* Aberrant deposition of stress granule-resident proteins linked to C9orf72-associated TDP-43 proteinopathy. *Mol Neurodegener* 2019, 14: 9.
75. Chew J, Gendron TF, Prudencio M, Sasaguri H, Zhang YJ, Castanedes-Casey M, *et al.* Neurodegeneration. C9ORF72 repeat expansions in mice cause TDP-43 pathology, neuronal loss, and behavioral deficits. *Science* 2015, 348: 1151–1154.
76. O'Rourke JG, Bogdanik L, Muhammad A, Gendron TF, Kim KJ, Austin A, *et al.* C9orf72 BAC transgenic mice display typical pathologic features of ALS/FTD. *Neuron* 2015, 88: 892–901.
77. Peters OM, Cabrera GT, Tran H, Gendron TF, McKeon JE, Metterville J, *et al.* Human C9ORF72 hexanucleotide expansion reproduces RNA foci and dipeptide repeat proteins but not neurodegeneration in BAC transgenic mice. *Neuron* 2015, 88: 902–909.
78. Liu Y, Pattamatta A, Zu T, Reid T, Bardhi O, Borchelt DR, *et al.* C9orf72 BAC mouse model with motor deficits and neurodegenerative features of ALS/FTD. *Neuron* 2016, 90: 521–534.
79. Cooper-Knock J, Higginbottom A, Stopford MJ, Highley JR, Ince PG, Wharton SB, *et al.* Antisense RNA foci in the motor neurons of C9ORF72-ALS patients are associated with TDP-43 proteinopathy. *Acta Neuropathol* 2015, 130: 63–75.
80. Aladesuyi Arogundade O, Stauffer JE, Saberi S, Diaz-Garcia S, Malik S, Basilim H, *et al.* Antisense RNA foci are associated with nucleoli and TDP-43 mislocalization in C9orf72-ALS/FTD: a quantitative study. *Acta Neuropathol* 2019, 137: 527–530.
81. Lee KH, Zhang P, Kim HJ, Mitrea DM, Sarkar M, Freibaum BD, *et al.* C9orf72 dipeptide repeats impair the assembly, dynamics, and function of membrane-less organelles. *Cell* 2016, 167: 774–788 e717.

82. Zhang YJ, Jansen-West K, Xu YF, Gendron TF, Bieniek KF, Lin WL, *et al.* Aggregation-prone c9FTD/ALS poly(GA) RAN-translated proteins cause neurotoxicity by inducing ER stress. *Acta Neuropathol* 2014, 128: 505–524.
83. May S, Hornburg D, Schludi MH, Arzberger T, Rentzsch K, Schwenk BM, *et al.* C9orf72 FTL/ALS-associated Gly-Ala dipeptide repeat proteins cause neuronal toxicity and Unc119 sequestration. *Acta Neuropathol* 2014, 128: 485–503.
84. Suzuki H, Shibagaki Y, Hattori S, Matsuoka M. The proline-arginine repeat protein linked to C9-ALS/FTD causes neuronal toxicity by inhibiting the DEAD-box RNA helicase-mediated ribosome biogenesis. *Cell Death Dis* 2018, 9: 975.
85. Yang D, Abdallah A, Li Z, Lu Y, Almeida S, Gao FB. FTD/ALS-associated poly(GR) protein impairs the Notch pathway and is recruited by poly(GA) into cytoplasmic inclusions. *Acta Neuropathol* 2015, 130: 525–535.
86. Ohki Y, Wenninger-Weinzierl A, Hruscha A, Asakawa K, Kawakami K, Haass C, *et al.* Glycine-alanine dipeptide repeat protein contributes to toxicity in a zebrafish model of C9orf72 associated neurodegeneration. *Mol Neurodegener* 2017, 12: 6.
87. Lee YB, Baskaran P, Gomez-Deza J, Chen HJ, Nishimura AL, Smith BN, *et al.* C9orf72 poly GA RAN-translated protein plays a key role in amyotrophic lateral sclerosis via aggregation and toxicity. *Hum Mol Genet* 2017, 26: 4765–4777.
88. Schludi MH, Becker L, Garrett L, Gendron TF, Zhou Q, Schreiber F, *et al.* Spinal poly-GA inclusions in a C9orf72 mouse model trigger motor deficits and inflammation without neuron loss. *Acta Neuropathol* 2017, 134: 241–254.
89. Zhang YJ, Gendron TF, Grima JC, Sasaguri H, Jansen-West K, Xu YF, *et al.* C9ORF72 poly(GA) aggregates sequester and impair HR23 and nucleocytoplasmic transport proteins. *Nat Neurosci* 2016, 19: 668–677.
90. Walker C, Herranz-Martin S, Karyka E, Liao C, Lewis K, Elsayed W, *et al.* C9orf72 expansion disrupts ATM-mediated chromosomal break repair. *Nat Neurosci* 2017, 20: 1225–1235.
91. Xu W, Bao P, Jiang X, Wang H, Qin M, Wang R, *et al.* Reactivation of nonsense-mediated mRNA decay protects against C9orf72 dipeptide-repeat neurotoxicity. *Brain* 2019, 142: 1349–1364.
92. Kramer NJ, Haney MS, Morgens DW, Jovicic A, Couthouis J, Li A, *et al.* CRISPR-Cas9 screens in human cells and primary neurons identify modifiers of C9ORF72 dipeptide-repeat-protein toxicity. *Nat Genet* 2018, 50: 603–612.
93. Farg MA, Konopka A, Soo KY, Ito D, Atkin JD. The DNA damage response (DDR) is induced by the C9orf72 repeat expansion in amyotrophic lateral sclerosis. *Hum Mol Genet* 2017, 26: 2882–2896.
94. Lopez-Gonzalez R, Lu Y, Gendron TF, Karydas A, Tran H, Yang D, *et al.* Poly(GR) in C9ORF72-related ALS/FTD compromises mitochondrial function and increases oxidative stress and DNA damage in iPSC-derived motor neurons. *Neuron* 2016, 92: 383–391.
95. Zhang YJ, Gendron TF, Ebbert MTW, O’Raw AD, Yue M, Jansen-West K, *et al.* Poly(GR) impairs protein translation and stress granule dynamics in C9orf72-associated frontotemporal dementia and amyotrophic lateral sclerosis. *Nat Med* 2018, 24: 1136–1142.
96. Choi SY, Lopez-Gonzalez R, Krishnan G, Phillips HL, Li AN, Seeley WW, *et al.* C9ORF72-ALS/FTD-associated poly(GR) binds Atp5a1 and compromises mitochondrial function in vivo. *Nat Neurosci* 2019, 22: 851–862.
97. Hao Z, Liu L, Tao Z, Wang R, Ren H, Sun H, *et al.* Motor dysfunction and neurodegeneration in a C9orf72 mouse line expressing poly-PR. *Nat Commun* 2019, 10: 2906.
98. Guo Q, Lehmer C, Martinez-Sanchez A, Rudack T, Beck F, Hartmann H, *et al.* In Situ Structure of Neuronal C9orf72 Poly-GA Aggregates Reveals Proteasome Recruitment. *Cell* 2018, 172: 696–705 e612.
99. El-Khamisy SF, Saifi GM, Weinfeld M, Johansson F, Helleday T, Lupski JR, *et al.* Defective DNA single-strand break repair in spinocerebellar ataxia with axonal neuropathy-1. *Nature* 2005, 434: 108–113.
100. Enokido Y, Tamura T, Ito H, Arumughan A, Komuro A, Shiwaku H, *et al.* Mutant huntingtin impairs Ku70-mediated DNA repair. *J Cell Biol* 2010, 189: 425–443.
101. Hoch NC, Hanzlikova H, Rulten SL, Tetreault M, Komulainen E, Ju L, *et al.* XRCC1 mutation is associated with PARP1 hyperactivation and cerebellar ataxia. *Nature* 2017, 541: 87–91.
102. Wang WY, Pan L, Su SC, Quinn EJ, Sasaki M, Jimenez JC, *et al.* Interaction of FUS and HDAC1 regulates DNA damage response and repair in neurons. *Nat Neurosci* 2013, 16: 1383–1391.
103. Mastrocola AS, Kim SH, Trinh AT, Rodenkirch LA, Tibbetts RS. The RNA-binding protein fused in sarcoma (FUS) functions downstream of poly(ADP-ribose) polymerase (PARP) in response to DNA damage. *J Biol Chem* 2013, 288: 24731–24741.
104. Rulten SL, Rotheray A, Green RL, Grundy GJ, Moore DA, Gomez-Herreros F, *et al.* PARP-1 dependent recruitment of the amyotrophic lateral sclerosis-associated protein FUS/TLS to sites of oxidative DNA damage. *Nucleic Acids Res* 2014, 42: 307–314.
105. Naumann M, Pal A, Goswami A, Lojewski X, Japtok J, Vehlow A, *et al.* Impaired DNA damage response signaling by FUS-NLS mutations leads to neurodegeneration and FUS aggregate formation. *Nat Commun* 2018, 9: 335.
106. Wang H, Guo W, Mitra J, Hegde PM, Vandoorne T, Eckelmann BJ, *et al.* Mutant FUS causes DNA ligation defects to inhibit oxidative damage repair in Amyotrophic Lateral Sclerosis. *Nat Commun* 2018, 9: 3683.
107. Mitra J, Guerrero EN, Hegde PM, Liachko NF, Wang H, Vasquez V, *et al.* Motor neuron disease-associated loss of nuclear TDP-43 is linked to DNA double-strand break repair defects. *Proc Natl Acad Sci U S A* 2019, 116: 4696–4705.
108. Hill SJ, Mordes DA, Cameron LA, Neuberger DS, Landini S, Eggan K, *et al.* Two familial ALS proteins function in prevention/repair of transcription-associated DNA damage. *Proc Natl Acad Sci U S A* 2016, 113: E7701–E7709.
109. Dar I, Biton S, Shiloh Y, Barzilai A. Analysis of the ataxia telangiectasia mutated-mediated DNA damage response in murine cerebellar neurons. *J Neurosci* 2006, 26: 7767–7774.
110. Hirano M, Yamamoto A, Mori T, Lan L, Iwamoto TA, Aoki M, *et al.* DNA single-strand break repair is impaired in aprataxin-related ataxia. *Ann Neurol* 2007, 61: 162–174.
111. Prudencio M, Gonzales PK, Cook CN, Gendron TF, Daugherty LM, Song Y, *et al.* Repetitive element transcripts are elevated in the brain of C9orf72 ALS/FTLD patients. *Hum Mol Genet* 2017, 26: 3421–3431.
112. He F, Jacobson A. Nonsense-mediated mRNA decay: Degradation of defective transcripts is only part of the story. *Annu Rev Genet* 2015, 49: 339–366.
113. Lykke-Andersen S, Jensen TH. Nonsense-mediated mRNA decay: an intricate machinery that shapes transcriptomes. *Nat Rev Mol Cell Biol* 2015, 16: 665–677.
114. Polymenidou M, Lagier-Tourenne C, Hutt KR, Huelga SC, Moran J, Liang TY, *et al.* Long pre-mRNA depletion and RNA missplicing contribute to neuronal vulnerability from loss of TDP-43. *Nat Neurosci* 2011, 14: 459–468.
115. Lagier-Tourenne C, Polymenidou M, Hutt KR, Vu AQ, Baughn M, Huelga SC, *et al.* Divergent roles of ALS-linked proteins FUS/TLS and TDP-43 intersect in processing long pre-mRNAs. *Nat Neurosci* 2012, 15: 1488–1497.

116. Arnold ES, Ling SC, Huelga SC, Lagier-Tourenne C, Poly-menidou M, Ditsworth D, *et al.* ALS-linked TDP-43 mutations produce aberrant RNA splicing and adult-onset motor neuron disease without aggregation or loss of nuclear TDP-43. *Proc Natl Acad Sci U S A* 2013, 110: E736–745.
117. Sun S, Ling SC, Qiu J, Albuquerque CP, Zhou Y, Tokunaga S, *et al.* ALS-causative mutations in FUS/TLS confer gain and loss of function by altered association with SMN and U1-snRNP. *Nat Commun* 2015, 6: 6171.
118. Yin S, Lopez-Gonzalez R, Kunz RC, Gangopadhyay J, Borufka C, Gygi SP, *et al.* Evidence that C9ORF72 dipeptide repeat proteins associate with U2 snRNP to cause mis-splicing in ALS/FTD patients. *Cell Rep* 2017, 19: 2244–2256.
119. Lin Y, Mori E, Kato M, Xiang S, Wu L, Kwon I, *et al.* Toxic PR poly-dipeptides encoded by the C9orf72 repeat expansion target LC domain polymers. *Cell* 2016, 167: 789–802 e712.
120. Wu D, Hao Z, Ren H, Wang G. Loss of VAPB regulates autophagy in a Beclin 1-dependent manner. *Neurosci Bull* 2018, 34: 1037–1046.
121. Boeynaems S, Bogaert E, Kovacs D, Konijnenberg A, Timmerman E, Volkov A, *et al.* Phase separation of C9orf72 dipeptide repeats perturbs stress granule dynamics. *Mol Cell* 2017, 65: 1044–1055 e1045.
122. White MR, Mitrea DM, Zhang P, Stanley CB, Cassidy DE, Nourse A, *et al.* C9orf72 Poly(PR) dipeptide repeats disturb biomolecular phase separation and disrupt nucleolar function. *Mol Cell* 2019, 74: 713–728 e716.
123. Haeusler AR, Donnelly CJ, Rothstein JD. The expanding biology of the C9orf72 nucleotide repeat expansion in neurodegenerative disease. *Nat Rev Neurosci* 2016, 17: 383–395.
124. Gao FB, Almeida S, Lopez-Gonzalez R. Dysregulated molecular pathways in amyotrophic lateral sclerosis-frontotemporal dementia spectrum disorder. *EMBO J* 2017, 36: 2931–2950.
125. Wang R, Xu X, Hao Z, Zhang S, Wu D, Sun H, *et al.* Poly-PR in C9ORF72-related amyotrophic lateral sclerosis/frontotemporal dementia causes neurotoxicity by clathrin-dependent endocytosis. *Neurosci Bull* 2019, 35: 889–900.
126. Sun S, Sun Y, Ling SC, Ferraiuolo L, McAlonis-Downes M, Zou Y, *et al.* Translational profiling identifies a cascade of damage initiated in motor neurons and spreading to glia in mutant SOD1-mediated ALS. *Proc Natl Acad Sci U S A* 2015, 112: E6993–7002.
127. Hetz C, Mollereau B. Disturbance of endoplasmic reticulum proteostasis in neurodegenerative diseases. *Nat Rev Neurosci* 2014, 15: 233–249.
128. Zhao L, Ackerman SL. Endoplasmic reticulum stress in health and disease. *Curr Opin Cell Biol* 2006, 18: 444–452.
129. Frotin F, Schueder F, Tiwary S, Gupta R, Korner R, Schlichthaerle T, *et al.* The nucleolus functions as a phase-separated protein quality control compartment. *Science* 2019, 365: 342–347.
130. Hartmann H, Hornburg D, Czuppa M, Bader J, Michaelsen M, Farny D, *et al.* Proteomics and C9orf72 neuropathology identify ribosomes as poly-GR/PR interactors driving toxicity. *Life Sci Alliance* 2018, 1: e201800070.
131. Moens TG, Niccoli T, Wilson KM, Atilano ML, Birsá N, Gittings LM, *et al.* C9orf72 arginine-rich dipeptide proteins interact with ribosomal proteins in vivo to induce a toxic translational arrest that is rescued by eIF1A. *Acta Neuropathol* 2019, 137: 487–500.
132. Kanekura K, Yagi T, Cammack AJ, Mahadevan J, Kuroda M, Harms MB, *et al.* Poly-dipeptides encoded by the C9ORF72 repeats block global protein translation. *Hum Mol Genet* 2016, 25: 1803–1813.
133. Cheng W, Wang S, Mestre AA, Fu C, Makarem A, Xian F, *et al.* C9ORF72 GGGGCC repeat-associated non-AUG translation is upregulated by stress through eIF2alpha phosphorylation. *Nat Commun* 2018, 9: 51.
134. Tabet R, Schaeffer L, Freyermuth F, Jambau M, Workman M, Lee CZ, *et al.* CUG initiation and frameshifting enable production of dipeptide repeat proteins from ALS/FTD C9ORF72 transcripts. *Nat Commun* 2018, 9: 152.
135. Green KM, Glineburg MR, Kearse MG, Flores BN, Linsalata AE, Fedak SJ, *et al.* RAN translation at C9orf72-associated repeat expansions is selectively enhanced by the integrated stress response. *Nat Commun* 2017, 8: 2005.
136. Liu EY, Russ J, Wu K, Neal D, Suh E, McNally AG, *et al.* C9orf72 hypermethylation protects against repeat expansion-associated pathology in ALS/FTD. *Acta Neuropathol* 2014, 128: 525–541.
137. Krishnan G, Zhang Y, Gu Y, Kankel MW, Gao FB, Almeida S. CRISPR deletion of the C9ORF72 promoter in ALS/FTD patient motor neurons abolishes production of dipeptide repeat proteins and rescues neurodegeneration. *Acta Neuropathol* 2020, 140: 81–87.
138. Goodman LD, Prudencio M, Kramer NJ, Martinez-Ramirez LF, Srinivasan AR, Lan M, *et al.* Toxic expanded GGGGCC repeat transcription is mediated by the PAF1 complex in C9orf72-associated FTD. *Nat Neurosci* 2019, 22: 863–874.
139. Kramer NJ, Carlomagno Y, Zhang YJ, Almeida S, Cook CN, Gendron TF, *et al.* Spt4 selectively regulates the expression of C9orf72 sense and antisense mutant transcripts. *Science* 2016, 353: 708–712.
140. Yuva-Aydemir Y, Almeida S, Krishnan G, Gendron TF, Gao FB. Transcription elongation factor AFF2/FMR2 regulates expression of expanded GGGGCC repeat-containing C9ORF72 allele in ALS/FTD. *Nat Commun* 2019, 10: 5466.
141. Sareen D, O'Rourke JG, Meera P, Muhammad AK, Grant S, Simpkinson M, *et al.* Targeting RNA foci in iPSC-derived motor neurons from ALS patients with a C9ORF72 repeat expansion. *Sci Transl Med* 2013, 5: 208ra149.
142. Lagier-Tourenne C, Baughn M, Rigo F, Sun S, Liu P, Li HR, *et al.* Targeted degradation of sense and antisense C9orf72 RNA foci as therapy for ALS and frontotemporal degeneration. *Proc Natl Acad Sci U S A* 2013, 110: E4530–4539.
143. Batra R, Nelles DA, Pirie E, Blue SM, Marina RJ, Wang H, *et al.* Elimination of Toxic Microsatellite Repeat Expansion RNA by RNA-Targeting Cas9. *Cell* 2017, 170: 899–912 e810.
144. Yamada SB, Gendron TF, Niccoli T, Genuth NR, Grosely R, Shi Y, *et al.* RPS25 is required for efficient RAN translation of C9orf72 and other neurodegenerative disease-associated nucleotide repeats. *Nat Neurosci* 2019, 22: 1383–1388.
145. Cheng W, Wang S, Zhang Z, Morgens DW, Hayes LR, Lee S, *et al.* CRISPR-Cas9 Screens Identify the RNA Helicase DDX3X as a Repressor of C9ORF72 (GGGGCC)_n Repeat-Associated Non-AUG Translation. *Neuron* 2019, 104: 885–898 e888.
146. Zhou Q, Mareljic N, Michaelsen M, Parhizkar S, Heindl S, Nuscher B, *et al.* Active poly-GA vaccination prevents microglia activation and motor deficits in a C9orf72 mouse model. *EMBO Mol Med* 2020, 12: e10919.
147. Nguyen L, Montrasio F, Pattamatta A, Tusi SK, Bardhi O, Meyer KD, *et al.* Antibody Therapy Targeting RAN Proteins Rescues C9 ALS/FTD Phenotypes in C9orf72 Mouse Model. *Neuron* 2020, 105: 645–662 e611.
148. Lynch E, Semrad T, Belsito VS, FitzGibbons C, Reilly M, Hayakawa K, *et al.* C9ORF72-related cellular pathology in skeletal myocytes derived from ALS-patient induced pluripotent stem cells. *Dis Model Mech* 2019, 12: dmm039552.
149. Cykowski MD, Dickson DW, Powell SZ, Arumanayagam AS, Rivera AL, Appel SH. Dipeptide repeat (DPR) pathology in the skeletal muscle of ALS patients with C9ORF72 repeat expansion. *Acta Neuropathol* 2019, 138: 667–670.



REVIEW

Inflammation in Mental Disorders: Is the Microbiota the Missing Link?

Sophie Ouabbou^{1,2,3} · Ying He^{1,4} · Keith Butler⁴ · Ming Tsuang^{4,5}

Received: 23 September 2019 / Accepted: 18 March 2020 / Published online: 27 June 2020
© Shanghai Institutes for Biological Sciences, CAS 2020

Abstract Research suggests that inflammation is important in the pathophysiology of mental disorders. In addition, a growing body of evidence has led to the concept of the microbiota-gut-brain axis. To understand the potential interactions, we begin by exploring the liaison between the immune system and mental disorders, then we describe the evidence that the microbiota impact the immune response in the developing brain. Next, we review the literature that has documented microbiome alterations in major mental disorders. We end with a summary of therapeutic applications, ranging from psycho-biotics to immunomodulatory drugs that could affect the microbiota-gut-brain axis, and potential treatments to alleviate the adverse effects of antipsychotics. We conclude that there is promising evidence to support the position that the microbiota plays an important role in the immunological

pathophysiology of mental disorders with an emphasis on psychotic disorders and mood disorders. However, more research is needed to elucidate the mechanisms.

Keywords Mental disorder · Microbiota · Immunology · Neurodevelopment

Introduction

Mental disorders, among which we mainly focus on schizophrenia (SCZ), autism spectrum disorder, mood disorders, and anxiety, rank among the top causes of years lived with disability worldwide [1]. For SCZ alone, the total cost estimates vary between countries, but are estimated to be ~\$102 billion in the USA [2]. And “psychosis” is a common manifestation of several psychiatric disorders that range from major depressive disorder with psychosis to bipolar disorder type I with psychosis and SCZ [3]. Psychosis is defined by the presence of delusions, hallucinations, disorganized thinking, grossly disorganized or abnormal motor behavior, and negative symptoms such as diminished emotional expression, avolition, and social withdrawal [4].

Efforts toward defining clear mechanisms that explain the pathophysiology of mental disorders, biologically-based diagnoses, and novel treatments are needed [5]. In this context, much has been documented regarding the possible role of inflammation in mental disorders [6]. In parallel, many studies on the human microbiota have accumulated to the point that the microbiota-gut-brain axis is thought to play a role in neuropsychiatric illness [7–9]. As reviewed elsewhere [10], there are several pathways through which the microbiota can modulate the microbiota-gut-brain axis. These include endocrine pathways mediated

Electronic supplementary material The online version of this article (<https://doi.org/10.1007/s12264-020-00535-1>) contains supplementary material, which is available to authorized users.

✉ Ying He
yinghe@csu.edu.cn

- ¹ Department of Psychiatry, and National Clinical Research Center for Mental Disorders, and Hunan Key Laboratory of Psychiatry and Mental Health, The Second Xiangya Hospital of Central South University, Changsha, Hunan 410011, China
- ² Human Microbiome Research Program, Faculty of Medicine, University of Helsinki, 00290 Helsinki, Finland
- ³ Cellular and Molecular Biology Research Centre, University of Costa Rica, San José 11501, Costa Rica
- ⁴ Center for Behavioral Genomics, Department of Psychiatry, Institute for Genomic Medicine, University of California San Diego, La Jolla, CA 92093, USA
- ⁵ Harvard Institute of Psychiatric Epidemiology and Genetics, Harvard School of Public Health, Boston, MA 02115, USA

via cortisol, neural pathways where the vagus nerve and the enteric nervous system are the main routes, metabolic pathways whereby the microbiota produce neurotransmitter precursors like tryptophan but also active substances like short-chain fatty acids (SCFAs), and finally the immune pathway. However, the immune response/inflammation overlaps most with the above pathways, which makes it an almost unavoidable pathway. In the present article, we comprehensively review the reported influence of both the immune system and the microbiota on mental disorders with an emphasis on psychosis. We focus on the pathogenesis of psychosis from a neurodevelopmental perspective, and finally provide perspectives on potential therapeutic applications (Fig. 1).

Inflammation in Mental Disorders and Potential Role of the Microbiota

In this section, we review the evidence, both clinical and from basic science, supporting the existence of a link between mental disorders and inflammation. To date, this link has been explored more than the potential role of the microbiota. We begin by highlighting the epidemiologic data on associations between psychotic and immunologic disorders as well as evidence from the effects of immunomodulatory drugs. Subsequently, we address the mechanisms driven by microorganisms that could alter the

immune response. This is followed by theories of the effects of the immune response on neurodevelopment.

Evidence Linking Mental Disorders to Immunological Disorders

Epidemiological Evidence. Epidemiological evidence links autoimmune and atopic disorders with mental disorders (Table 1). First, a nationwide Swedish study reported an increased risk of affective, personality, and neurotic disorders among individuals hospitalized for systemic lupus erythematosus (SLE), rheumatoid arthritis (RA), and ankylosing spondylitis (AS) [11]. They also found an increased risk of psychosis among women with SLE, RA, and AS but not among men [11]. Subsequently, a Danish study based on the records of 7,704 people, found that individuals with SCZ have a 50% lifetime prevalence of autoimmune disorders and that conversely, given a history of autoimmune disorders, the relative risk for SCZ increases by 45% [12]. Associations have been found for celiac disease, RA, autoimmune thyroiditis, type 1 diabetes mellitus (T1DM), SLE, Guillain-Barré syndrome, psoriasis, multiple sclerosis (MS) and autoimmune hepatitis, among others [13]. The case of celiac disease has been studied more extensively. A higher prevalence among patients with SCZ has been documented and immunological markers for celiac disease or gluten intolerance are present in SCZ patients [14]. Anti-gliadin, transglutaminase, and endomysium antibodies, which all participate in gluten sensitivity, are increased in SCZ [14]. Beyond autoimmune disorders, there is also evidence linking atopic disorders in childhood to the development of psychosis in adulthood [15].

Genetic Evidence. The co-occurrence of immunological disorders and mental disorders might potentially be attributed to common etiological factors. These may be genetic or environmental. Genetic evidence supporting a common link between mental disorders and the immune system has been provided by genome-wide association studies that have identified single-nucleotide polymorphisms associated with SCZ in the major histocompatibility complex on chromosome 6 [25]. Innate immunity has also been mechanistically implicated in the appearance of mental disorders [26]. The environmental evidence may be more complicated, but among others, the microbiota can be influenced by variations in both genetic and environmental conditions [27, 28]. This is one of the reasons why we consider that understanding its role in psychotic disorders is pertinent.

Cross-sectional Evidence. Further evidence of inflammation in mental disorders comes from studies during first-episode psychosis. In these patients, an upregulated inflammatory status has been documented by measuring

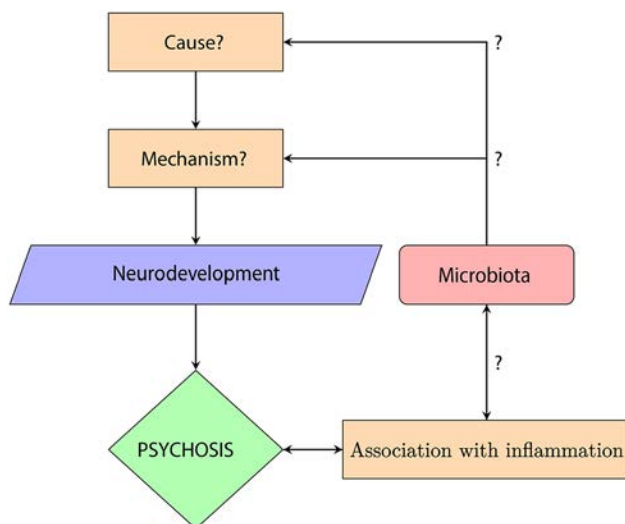


Fig. 1 Summary flowchart. The exact cause and mechanism that explain psychosis remain unknown; however a disruption in neurodevelopment has been documented and is regarded as a pre-stage of psychosis. In parallel, a strong association between psychosis and inflammation has been documented through many sources of evidence. The hypothesis is that the microbiota, which is closely associated with the immune system, may be a piece of the puzzle that explains part of the cause and mechanism of psychosis.

Table 1 Summary of studies that explore an association between immunological disorders and psychosis.

Reference	Country	Sample characteristics	Associations found
Tiosano <i>et al.</i> 2017 [16]	Israel	5,018 SLE patients and 25,090 matched controls	Independent association between SLE and BD
Tiosano <i>et al.</i> 2017 [17]	Israel	5,018 SLE patients and 25,090 matched controls	SCZ and SLE
Jackson <i>et al.</i> 2014 [18]	USA	100 people with SCZ and 100 matched controls	SCZ and gluten antibodies
Khandaker <i>et al.</i> 2014 [15]	UK	6,785 adolescents with psychotic experiences	Atopic disorders prior to psychosis
Benros <i>et al.</i> 2014 [13]	Denmark	3.83 million people; 39,364 with SCZ-like psychosis and 142,328 with autoimmune disease	Autoimmune disorders and psychosis
Kumar <i>et al.</i> 2013 [19]	India	50 patients with pemphigus, 30 with psoriasis, and 30 matched controls	Psychosis with pemphigus and psoriasis
Kota <i>et al.</i> 2012 [20]	India	260 patients with T1DM	Psychosis and T1DM
Sundquist <i>et al.</i> 2008 [11]	Sweden	Entire Swedish population	Psychosis and SLE or RA among women
Sturdy <i>et al.</i> 2002 [21]	UK	533 cases and 533 controls	Psychosis as a risk factor for death certified as caused by asthma
Gilvarry <i>et al.</i> 1996 [22]	UK	101 psychotic and 116 control patients	Family history of psychosis and thyrotoxicosis and T1DM
Nasr <i>et al.</i> 1981 [23]	USA	82 psychiatric patients	Atopic disorders and affective disorders
Osterberg, 1978 [24]	Sweden	58 psychiatric cases	SCZ and either RA or AS

SLE, systemic lupus erythematosus; BD, bipolar disorder; SCZ, schizophrenia; T1DM, type 1 diabetes mellitus; RA, rheumatoid arthritis; AS, ankylosing spondylitis.

cytokines such as interleukins 1 β and 6, and tumor necrosis factor alpha. Also, adiponectin may play a unique pro-inflammatory role in this patient population [29–32]. Variations seem to exist according to the stage of illness. Specific inflammatory cytokines differ between first episodes, psychotic states, and remission states [33]. In the case of bipolar disorder, possible mechanisms have been reviewed elegantly elsewhere [34].

Evidence from Immunomodulatory Drugs. Another source of evidence is the efficacy of immunomodulatory drugs such as minocycline, non-steroidal anti-inflammatory drugs (NSAIDs), dehydroepiandrosterone, dehydroepiandrosterone sulfate, pregnenolone, polyunsaturated fatty acids, N-acetylcysteine, or L-theanine in the treatment of psychosis, which also suggests an underlying inflammatory process [35]. In addition, there is evidence of an anti-inflammatory effect of antipsychotics in inhibiting microglial activation [36].

Potential Role of the Microbiota

Evidence Linking Immunological Disorders and the Microbiota. In this section, we review evidence linking both

atopic and autoimmune disorders to changes in either the normal microbiota or with exposure to infectious agents. According to Okada *et al.* (2010) the “hygiene hypothesis” can be extended from atopic to autoimmune diseases. First, there is epidemiological evidence such as the rise in incidence in places where the sanitation is better, and through migration and geographical distribution studies. Also, a causal relationship has been demonstrated mostly in animal models [37]. Apart from the explanation of T helper 1 (Th1) and Th2 deviation, Okada *et al.* (2010) proposed other explanations such as antigenic competition and bystander suppression by CD4+/CD5+ forkhead box P3 regulatory T cells and mechanisms independent of antigenic stimulation such as the stimulation of Toll-like receptors [37]. Alterations in the microbiota have been documented in autoimmune disorders such as T1DM [38, 39], MS [40], inflammatory bowel disease [41], primary biliary cirrhosis [42], and connective tissue diseases [43, 44] (Table 2).

Signals Driven by Microorganisms. One of the reasons why we consider that the microbiota may play a significant role in mental disorders through modulation of the immune system is because microbial signals drive the balance

Table 2 The hygiene hypothesis: articles on associations between autoimmune disorders and changes in the composition of microbiota.

Reference	Title	Sample characteristics	Associations found
De Groot <i>et al.</i> 2017 [38]	Distinct fecal and oral microbiota composition in human type 1 diabetes, an observational study	53 patients with T1DM and 50 matched controls	Decreased <i>Christensenella</i> and <i>Subdoligranulum</i> are correlated with glycemic control, inflammatory parameters, and SCFAs
Knip <i>et al.</i> 2017 [39]	Modulation of type 1 diabetes risk by the intestinal microbiome	Review	Microbiome protects humans against T1DM
Wekerle, 2017 [40]	Nature, nurture, and microbes: The development of multiple sclerosis	Review	Microbiota may contribute to MS pathogenesis
Kim <i>et al.</i> 2017 [41]	The interplay between host immune cells and gut microbiota in chronic inflammatory diseases	Review	Role of the microbiota in IBD, MS, allergic asthma, and RA
Quigley, 2016 [42]	Primary biliary cirrhosis and the microbiome	Review	Role of a bacterium in the initiation of the autoimmune process that leads to the development of primary biliary cirrhosis
Talotta <i>et al.</i> 2017 [43]	The microbiome in connective tissue diseases and vasculitides: An updated narrative review	Review	The dysbiotic microbiome plays a role in the pathogenesis of SLE, systemic sclerosis, Sjögren's syndrome, and Behçet's disease
Yacoub <i>et al.</i> 2018 [44]	Lupus: the microbiome angle	Review	Mechanisms by which the microbiota affects SLE
Lowry <i>et al.</i> 2016 [45]	The microbiota, immunoregulation, and mental health: Implications for public health	Review	Environmental microbes modify risk for inflammatory disease, with a focus on neurodevelopmental and psychiatric conditions

SCFAs, short-chain fatty acids; T1DM, type 1 diabetes mellitus; MS, multiple sclerosis; IBD, inflammatory bowel disease; RA, rheumatoid arthritis; SLE, systemic lupus erythematosus.

between T helper and T regulatory cells [46, 47]. The signals that drive this balance can be metabolites such as tryptophan or SCFAs, microbial molecules that enhance immune regulatory circuits through stimulation of DC-SIGN (dendritic cell-specific intercellular adhesion molecule-3-grabbing non-integrin) and the Lewis lipopolysaccharide that also binds DC-SIGN, or helminthic molecules such as fucose. These can originate (1) from commensal microbiota, mainly *Firmicutes*, (2) from old infective pathogens such as hepatitis A virus, *Toxoplasma gondii*, *Salmonella spp.*, helminths, nematodes, *Mycobacterium tuberculosis* or *Helicobacter pylori*, and (3) from organisms from the natural environment such as non-tuberculous mycobacteria [45].

Leaky Gut. An altered, more permeable gut barrier has been reported in several disorders such as irritable bowel syndrome [48]. A possible explanation for this increased permeability is a dysbiosis favoring a pro-inflammatory state in the bowel. This allows the passage of inflammatory molecules such as lipooligosaccharide and amino-acids into the bloodstream, causing dysregulation of the immune response and antigen recognition [49]. Thus, we consider that alterations in the microbiota might be both a cause of leaky gut and the leaky gut in turn may be a mechanism

through which dysbiosis exerts its effect on the immune and nervous systems. Gut permeability is thus interesting as a parameter to measure, such as by the presence of *Saccharomyces cerevisiae* or *Candida albicans* antibodies. Also, increased levels of these antibodies have been documented in SCZ [50–52].

Inflammation during Prenatal Life and Neurodevelopment. Finally, another perspective from which to view the impact of the immune system on the brain is neurodevelopmental. There is evidence that pro-inflammatory states during prenatal life, especially in the second trimester, are associated with the development of SCZ [35]. These states can be due to maternal exposure to infection or stressful situations such as the loss of a partner, war, obstetric complications, or starvation [35]. In their review, Suvisaari *et al.* (2013) considered three theories: First, that cytokines play a role in brain development in processes like neurogenesis, gliogenesis, proliferation, axon pathfinding, and microglial development. The second theory hypothesizes that microglia are hyperactive in SCZ. The third theory is based on the finding that auto-antibodies, such as anti-brain and antinuclear antibodies, are elevated in SCZ, and proposes that brain-reactive auto-antibodies participate in the pathophysiology of SCZ [35].

Direct Evidence of a Role of the Microbiota in Immunomodulation and Neuroimmunity

We have discussed evidence for a link between the immune system and mental disorders and in parallel between the microbiota and the immune system. The evidence that links these three elements comes mostly from observational studies which we treat in “[Microbiota and Abnormal Neurodevelopment](#)” section. Jang *et al.* in 2018 reported that exposure of mice to ampicillin causes anxiety and colitis and changes in the microbiota composition [53]. Then they showed that these changes are accompanied by increased blood corticosterone, interleukin-6, and lipopolysaccharide levels. Also, inflammatory cells such as monocytes and dendritic cells were recruited to the hippocampus. Finally, they demonstrated reversal of the changes and the symptoms following administration of *Lactobacillus reuteri* [53]. In a mouse model, it has been shown that altering the microbiome by means of antibiotics diminishes plaque deposition in the brain [54]. Another experiment, by Wilck *et al.*, also demonstrated a link between the microbiota, T-h17 lymphocytes, and neurological health by treating mice with salt, showing compositional changes in the microbiota and reduced aggravation of induced encephalomyelitis, thus demonstrating the existence of what they call a “gut-immune” axis [55]. The presence of this axis is further supported by experiments in animal models of other brain conditions such as stroke [56]. There are even animal models of depression that are constructed by inducing inflammation [57]. It has also been reported that the signaling of the inflammasome associated with anxiety and depression affects the gut microbiota, suggesting that the communication is bidirectional [58].

Microbiota and Abnormal Neurodevelopment

Microbiota and Early Brain Development

The prenatal and postnatal periods are critical neurodevelopmental windows in mammals, and they overlap with the original microbial colonization [59]. Several disruptions of normal development have been described that contribute to the pathogenesis of psychosis and could be mediated by changes in the microbiota (Fig. 2).

Prenatal Period. Though several studies have supported the notion that the mammalian fetus is not germ-free, as once believed [60], the existence of a placental microbiome is still a matter of debate as the positive findings are thought to issue from contamination [61]. However, there is abundant evidence supporting the influence of the microbiota on neurodevelopment in humans and mice [62].

The most direct evidence comes from prenatal infection and antibiotics studies, which include research on both humans and rodents. Reported results from these assays suggest that infections with *Toxoplasma gondii*, human herpesvirus 2, and *Chlamydomphila* have robust links to psychosis in humans [63, 64]. Drawing conclusions about the effects of antibiotics is, in contrast, more complicated and controversial due to the frequent coexistence of infection and the numerous types of antibiotic. Few studies have addressed this in the particular case of psychosis. However, a randomized controlled trial found that macrolide use in pregnant women is associated with an increased risk of childhood cerebral palsy and epilepsy [65], whereas another cohort study did not confirm this result [66].

In rodent studies, maternal exposure to antibiotics increases behavioral abnormalities such as anxiety-like and dissocial behavior in the offspring through perturbations in the microbiota [67, 68].

As well as the above, other factors that have been associated with dysbiotic microbiota and abnormal behavior in the offspring include a high-fat diet [69], maternal immune activation [70], prenatal stress [71, 72], peptidoglycan [73], and propionic acid [74].

Time and Mode of Delivery. The microbiota composition has been shown to differ between preterm and term infants [75]. Preterm infants have an increased risk of psychiatric or behavioral problems later in life [76, 77]. Another aspect that has been studied is the mode of delivery and the results are conflicting. One study reported that cesarean delivery is associated with an increase in psychosis among offspring [78] while another found no significant difference [79]. However, it is known that cesarean delivery is associated with colonization by microbes from the skin instead of the vagina [80]. The mechanisms by which the microbiota is involved in the development of psychosis later in life are not yet fully understood, however its potential involvement makes it worthy of further study.

Postnatal Period. Under normal conditions, infants are exposed to environmental and maternal microbes immediately after birth. As previously stated, the mechanisms by which the microbiota interacts with neurodevelopment remain elusive, the results of potential association studies being very varied. For example, several studies on germ-free animals have shown various abnormalities in behavior, including reduced social behavior and memory deficits [81, 82]; conversely, several studies have indicated that germ-free mice have less anxiety-like behavior and more motor activity than specific pathogen-free mice [9, 83]. In addition, probiotic and antibiotic interventions have been reported to alter neural responses in germ-free mice by mediating the hypothalamic-pituitary-adrenal axis or brain-derived neurotrophic factor [84–86]. Overall, a significant

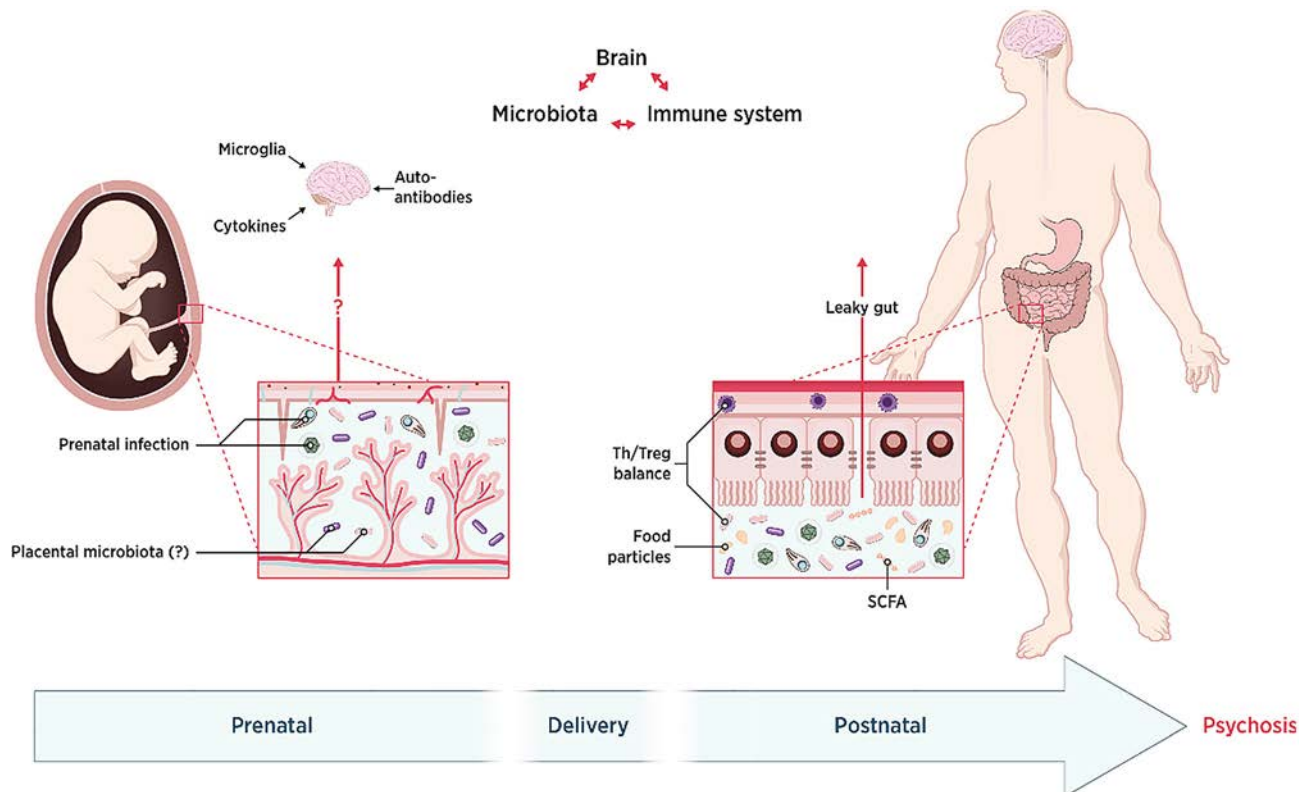


Fig. 2 Role of the microbiota-gut-brain axis during neurodevelopment. We focus on three main critical periods. First, in the postnatal period, although there is consensus about the absence of placental microbiota, microbial disturbance caused by prenatal infection or the administration of antibiotics could impact brain development through diverse pathways. Second, microbial colonization of the newborn

takes place differently depending on the mode and time of delivery and this impacts general health. Finally, during the postnatal period or even adulthood, the microbiota-gut-brain axis still functions through neural, endocrine, and immunological pathways, a particular one being the leaky gut. In the end, abnormal development of the brain might lead to psychosis.

body of documentation supports the idea that the gut microbiota affects neurodevelopment during the postnatal period.

Specific Evidence of an Association between the Microbiota and Mental Disorders

Ultra-high Risk for Psychosis. Our recent study found that the levels of *Clostridiales*, *Lactobacillales*, and *Bacteroidales* are higher in fecal samples from ultra-high risk individuals than genetic high-risk subjects and healthy controls [87]. Combining this with magnetic resonance spectroscopy brain scans we hypothesized that compositional changes of gut microbiota might activate microglia in the brain through the elevation of SCFAs.

Schizophrenia. Unlike the ultra-high risk situation, which only has one related study, there have been many studies investigating the gut microbial composition in SCZ cohorts. Among these are 3 longitudinal studies, with treatments ranging from 6 weeks to 12 months. Two studies found significant changes in the gut microbiota after treatment [88, 89]. However, the other study showed

non-significant results, possibly because of the non-first-episode subjects and the shortest intervention period – only 6 weeks [90]. Also, case-control studies have compared the gut microbiome diversity between SCZ patients and healthy controls [91–94]. Two studies found that SCZ is associated with reduced richness of the gut microbial composition [92, 93], but the other two failed to show consistent results [91, 94]. What is more, the differences in taxonomic composition between SCZ patients and healthy controls are even more complicated and heterogeneous. For example, the abundance of *Clostridium* was found to be increased in SCZ patients from two studies [91, 93], but the situation was just the opposite in another study [94]. All the above cases reflect the dilemma of microbiome studies of mental illness, which display high heterogeneity and difficulties with replicability.

Separately, two oropharyngeal microbiome studies have been conducted on the same population. One found that the level of *Lactobacillus* phage phiadh was significantly higher in SCZ patients than controls [95], and the other showed that *Ascomycota*, *Lactobacilli*, and *Bifidobacterium*, which have been associated with chronic

inflammation, are more abundant in SCZ patients than controls [96].

In addition, several serological studies indirectly support the existence of differences in the microbiome of SCZ patients [97–99]. Torrey *et al.* (2007) conducted a meta-analysis and showed that antibodies to *T. gondii* are increased in individuals with SCZ [97]. Severance *et al.* (2012) detected an elevation of IgG antibodies to *S. cerevisiae* in SCZ compared to controls in 2012, and in 2016 found that *C. albicans* seropositivity increases the odds for SCZ in males [97, 98]. Houenou *et al.* found that higher *Cytomegalovirus* serointensity is related to right hippocampal volume in both SCZ and bipolar disorder patients [99]. A recent systematic review by Nguyen *et al.* (2018) found five microbiome studies and five translocation studies on SCZ, bipolar disorder, or other severe mental illness. Although the authors pointed out limitations in the literature reviewed, they found an association between reduced microbial diversity and other global community differences in patients with SCZ and bipolar disorder [100].

Beyond human studies, Zhu *et al.* and Zheng *et al.* transplanted fecal microbiota from SCZ patients into specific pathogen-free mice and caused SCZ-like behaviors [92, 101]. After that, they suggested that the abnormal behaviors might be induced by subsequently dysregulated kynurenine metabolism or a disrupted glutamate-glutamine-GABA cycle from the morbid gut microbiota.

Autism Spectrum Disorders. At the genus level, *Clostridium* [102–104], *Lactobacillus* [105–107], *Sutterella* [108–110], and *Desulfovibrio* [106, 111] have often been identified in increased proportions in fecal samples from autistic children. And *Prevotella*, *Coprococcus*, and unclassified *Veillonellaceae* have been reported to occur in low abundance in fecal samples from autistic individuals [112]. However, some research data did not show differences in gut microbiota between autistic children and their neurotypical siblings [113]. Like in human samples, the mouse model of autism also showed consensus results that the phyla *Bacteroidetes* and *Firmicutes* and the order *Desulfovibrionales* are associated with autistic behaviors [74, 114, 115]. And interestingly, treatment with *L. reuteri* [116] and *B. fragilis* [114] can reverse some of the core symptoms of autism, such as social deficits and stereotyped behaviors. Also, Chen *et al.* found that deficiency of KDM5 demethylase causes autistic behaviors in flies through gut dysbiosis, and the administration of *Lactobacillus plantarum* restores the behavioral impairments [117]. Compared to adult psychosis, autism usually develops in early life and seems to have fewer psychological factors. Hence, the gut-brain axis is expected to play a role in the etiology and cure of this disabling disease.

Mood Disorders. The topic of gut microbiota and mood disorders has been widely studied. The phylum *Actinobacteria*, the order *Bacteroidales*, and the genus *Oscillibacter* have been consistently reported to be over-represented in association with depression, in both patients and rodent models [118–121]. Perhaps due to the difficulty of establishing animal models of bipolar disorder (especially mania), almost all evidence is from human studies. And increased *Bacteroidetes* and *Clostridiales* and decreased *Faecalibacterium* have been repeatedly reported in individuals with bipolar disorder [122–126]. Furthermore, Hu *et al.* considered that the decreased *Faecalibacterium* and other butyrate-producing bacteria might contribute to bipolar depression, and treatment with Quetiapine could change the microbial composition [123].

Anxiety and Stress-related Disorders. That stressor exposure alters the gut microbiota in rodents and humans has been well studied. The results have shown a decrease of *Lactobacillus* and an increase of *Lachnospiraceae* after stress [81, 127–129]. The fact that both parasite-infected mice and those on an altered diet show anxiety-like behavior strengthens the hypothesis that the microbiota plays a role in anxiety and stress-related disorders [84, 130]. Also, an exploratory study demonstrated that decreased total abundance of *Actinobacteria*, *Lentisphaerae*, and *Verrucomicrobia* is associated with more severe symptoms of post-traumatic stress disorder [131]. Whether germ-free rodents show increased or reduced anxiety-like behavior has not yet been consistently established [9, 132]. The influence of the gut microbiota on anxiety and stress-related disorders warrants further investigation.

Overall, most of the specific evidence either points to the regulation of the immune system or neurotransmitters. And because of all the limitations of animal studies and the conclusions drawn from them, translational studies are critically needed in this field. A summary of studies that explored microbial influence during neurodevelopmental windows and subsequent mental disorders is detailed in the supplementary material (Table S1).

Prospective Therapeutic Applications in Mental Disorders

Probiotic Studies

A probiotic is a live organism that, when ingested in adequate amounts, exerts a health benefit. Their use in mental illness has been reviewed more extensively elsewhere [133]. Several members of the microbiota are known to produce neurotransmitters such as dopamine, gamma-aminobutyric acid (GABA), norepinephrine, serotonin (5-

HT), acetylcholine, and endocannabinoids [134]. The fact that the intestinal microbiota produces neuroactive compounds is one of the reasons why it is pertinent to study and test its therapeutic potential. Dinan *et al.* (2013) define a psychobiotic as such a substance that produces a health benefit in patients suffering from psychiatric illness [134]. It has been reported that 5-HT plasma levels are significantly higher in normal mice than in germ-free mice [135]. This, together with the finding that ingestion of *Bifidobacterium infantis* in rats increases the levels of tryptophan [136], supports the hypothesis that the microbiota plays a role in the modulation of neurotransmitter levels and possibly also mood. Furthermore, the gut microbiota has been shown to affect the levels of brain-derived neurotrophic factor in the brain [84]. It has even been postulated that the microbial colonization of the newborn and infant participates in modulating the development of the hypothalamic-pituitary-adrenal axis [86]. It has also been demonstrated that the regulation of mood by the gut microbiota is mediated by the vagus nerve as it disappears when the vagus is sectioned [137]. The gut microbiota has also been implicated in anxiety regulation in animal models [83, 138].

The use of psychobiotics has been studied in humans in terms of stress [128, 133, 139–142], anxiety [133, 142–145], and mood [133, 142–145]. However, there is little evidence to support the clinical use of psychobiotics and their efficacy. In a systematic review, Romijn *et al.* [146] studied the evidence behind the use of psychobiotics in humans. Their search led to a preselection of ten studies of various mental disorders, none of which showed a statistically significant difference after the administration of probiotics. They selected only one study concerning SCZ in which Dickerson *et al.* (2014) found that repeated-measures analysis of variance showed no significant differences in the total score on the Positive and Negative Symptom Scale (PANSS) between probiotic and placebo supplementation [147]. Romijn *et al.* (2015) concluded that there is little supporting evidence for the use of psychobiotics in humans, and recommended that further research be conducted in affected populations while taking into consideration the duration of the intervention period and the probiotic strain [146]. Nonetheless, a more recent study by Dickerson *et al.* has shown fewer re-hospitalizations after mania with psychobiotic administration [148].

Anti-inflammatory or Immunomodulatory Drugs and Dietary Modifications as Add-on Therapy in Mental Disorders

NSAIDs, aspirin, omega-3 fatty acids, and minocycline have been tested on the symptoms of SCZ, and there is evidence that they are modestly effective [149, 150]. The

second-generation tetracycline minocycline has been tested in humans for the treatment of SCZ. In a systematic review and meta-analysis of six randomized controlled trials by Solmi *et al.* (2017), it was found that minocycline has significant beneficial effects, particularly on improving the negative symptoms. In the PANSS the standardized median difference (SMD) was -0.59 with a confidence interval of $[-0.88, -0.00]$ and a $P = 0.04$. A difference in negative symptoms was also documented (SMD = -0.76 , CI = $[-1.21, -0.31]$, $P = 0.001$). It also has positive effects on cognitive symptoms such as attention and vigilance as well as executive functioning. More trials are necessary to study the effect on positive symptoms [151]. Whether it acts through modification of the microbiota, immunomodulation, or another mechanism remains to be determined [152].

Finally, according to a revision by Kalaydjian *et al.* (2006) there is evidence from ecological studies, prevalence studies, clinical trials that include dietary recommendations, and immunological and genetic findings, that supports the view that SCZ and celiac disease may be heterogeneous presentations of a similar cause and that individuals with SCZ could benefit from dietary modifications [153].

Adjuvant Therapy to Counteract Antipsychotic Side-effects

Antipsychotic medication is known to cause long-term metabolic side-effects such as metabolic syndrome, dyslipidemia, weight gain, insulin resistance, T2MD, and cardiovascular disease [154–160]. In an attempt to assess the mechanisms underlying these adverse effects, Davey *et al.* (2012) studied the consequences of olanzapine administration in rats. Olanzapine-treated rats had an increase in *Firmicutes* and a decrease in *Bacteroidetes* [161] which coincided with the microbiome changes already documented for obesity in humans [162]. To investigate whether the microbiota is directly involved in the metabolic effects of olanzapine, in a second study, Davey *et al.* [163] administered broad-spectrum antibiotics to rats and found that they attenuated the side-effects of olanzapine. Moreover, they found that when antibiotics were administered along with olanzapine the increase in *Firmicutes* and decrease in *Bacteroidetes* no longer occurred. This was later confirmed with risperidone when Bahr *et al.* [164] demonstrated that one of the mechanisms by which risperidone causes weight gain is a decrease in energy expenditure. Interestingly, when they transplanted into naïve mice feces from mice that had suffered weight gain after risperidone administration, these naïve mice also experienced weight gain, demonstrating that changes in the microbiota alone are sufficient to cause weight gain. The

same group also documented changes in the microbiota coherent with those described in obesity among children taking risperidone chronically [165].

It has recently been reported that ~24% of prescription drugs inhibit bacterial growth *in vitro*, and, despite their chemical variability, antipsychotics are one of the groups most notorious for their inhibition of bacterial growth, and it has been proposed that this may be involved in the mechanism of action of these drugs [166].

Although causality and mechanism cannot yet be established, the manipulation of the microbiota by the use of prebiotics, probiotics, dietary modifications, or even antibiotics is a promising tool when it comes to palliating the adverse effects of antipsychotics on energy metabolism. Furthermore, changes in the microbiota may be involved in the mechanism of action of antipsychotics.

Conclusions

Psychotic disorders are highly disabling, hence efforts to understand their pathophysiology are of the utmost importance. It has been extensively documented that inflammation plays a role in these phenomena, as shown by the association between mental disorders and immunological alterations in epidemiological studies.

We have reviewed studies that show an association between prenatal infection and antibiotic use during the windows of development (prenatal, during delivery, and during the postnatal period) that affect the maternal microbiota and might impact brain development. The major drawback of the included studies is that most of them are descriptive of associations and fail to provide insight into the causality and mechanisms of the observed phenomena. Other limitations included small sample sizes and the diversity of differences in the microbiotas of cases and controls. Therefore, there is a clear need for more reports that elucidate the mechanisms by which disturbances in the microbiota cause changes in the gut and the immune system and how these translate into brain pathology. We can still conclude that there is enough evidence to suggest a role for the microbiota and the immune system in the pathophysiology of mental disorders. And further exploration of how suspect microbiota affect the existing psycho-immunology pathway might be a short-cut in this field. In short, investigation of the microbiota-immune-brain axis is a promising field for future study as it may both shed light on one of the mechanisms underlying mental disorders as well as be a source of therapeutic interventions and diagnostic tools such as potential biomarkers. We hope that soon the collective effort in microbiome research will translate into bench interventions and public health recommendations.

Acknowledgments This review was supported by the National Natural Science Foundation of China (81871056). We would like to thank Okko Alitalo, MSc, from the Laboratory of Neurotherapeutics of the Faculty of Pharmacy at the University of Helsinki for designing figure 2. We would also like to thank Dr. Henriette Raventós and her team at the Cellular and Molecular Biology Research Centre of the University of Costa Rica for their corrections and comments on this paper.

Conflict of interest The authors claim that there are no conflicts of interest.

References

1. GBD 2016 Disease and Injury Incidence and Prevalence Collaborators. Global, regional, and national incidence, prevalence, and years lived with disability for 328 diseases and injuries for 195 countries, 1990–2016: a systematic analysis for the Global Burden of Disease Study 2016. *Lancet* 2017, 390: 1211–1259.
2. Chong HY, Teoh SL, Wu DB-C, Kotirum S, Chiou C-F, Chaiyakunapruk N. Global economic burden of schizophrenia: a systematic review. *Neuropsychiatr Dis Treat* 2016, 12: 357–373.
3. Arciniegas DB. Psychosis. *Continuum (Minneapolis)* 2015, 21: 715–736.
4. American Psychiatric Association. *Diagnostic and Statistical Manual of Mental Disorders (DSM-5®)*. Arlington: American Psychiatric Association, 2013.
5. Tamminga CA, Ivleva EI, Keshavan MS, Pearlson GD, Clementz BA, Witte B, *et al.* Clinical phenotypes of psychosis in the Bipolar-Schizophrenia Network on Intermediate Phenotypes (B-SNIP). *Am J Psychiatry* 2013, 170: 1263–1274.
6. García-Bueno B, Bioque M, MacDowell KS, Santabàrbara J, Martínez-Cengotitabengoa M, Moreno C, *et al.* Pro-antiinflammatory dysregulation in early psychosis: results from a 1-year follow-up study. *Int J Neuropsychopharmacol* 2014, 18. <https://doi.org/10.1093/ijnp/pyu037>.
7. Cusotto S, Sandhu KV, Dinan TG, Cryan JF. The Neuroendocrinology of the Microbiota-Gut-Brain Axis: A Behavioural Perspective. *Front Neuroendocrinol* 2018, 51: 80–101.
8. Hong J, Reed C, Novick D, Haro JM, Aguado J. Clinical and economic consequences of medication non-adherence in the treatment of patients with a manic/mixed episode of bipolar disorder: results from the European Mania in Bipolar Longitudinal Evaluation of Medication (EMBLEM) study. *Psychiatry Res* 2011, 190: 110–114.
9. Diaz Heijtz R, Wang S, Anuar F, Qian Y, Björkholm B, Samuelsson A, *et al.* Normal gut microbiota modulates brain development and behavior. *Proc Natl Acad Sci U S A* 2011, 108: 3047–3052.
10. Cryan JF, Dinan TG. Mind-altering microorganisms: the impact of the gut microbiota on brain and behaviour. *Nat Rev Neurosci* 2012, 13: 701–712.
11. Sundquist K, Li X, Hemminki K, Sundquist J. Subsequent risk of hospitalization for neuropsychiatric disorders in patients with rheumatic diseases: a nationwide study from Sweden. *Arch Gen Psychiatry* 2008, 65: 501–507.
12. Benros ME, Nielsen PR, Nordentoft M, Eaton WW, Dalton SO, Mortensen PB. Autoimmune diseases and severe infections as risk factors for schizophrenia: a 30-year population-based register study. *Am J Psychiatry* 2011, 168: 1303–1310.

13. Benros ME, Eaton WW, Mortensen PB. The epidemiologic evidence linking autoimmune diseases and psychosis. *Biol Psychiatry* 2014, 75: 300–306.
14. Cascella NG, Kryszak D, Bhatti B, Gregory P, Kelly DL, Mc Evoy JP, *et al.* Prevalence of celiac disease and gluten sensitivity in the United States clinical antipsychotic trials of intervention effectiveness study population. *Schizophr Bull* 2011, 37: 94–100.
15. Khandaker GM, Zammit S, Lewis G, Jones PB. A population-based study of atopic disorders and inflammatory markers in childhood before psychotic experiences in adolescence. *Schizophr Res* 2014, 152: 139–145.
16. Tiosano S, Nir Z, Gendelman O, Comaneshter D, Amital H, Cohen AD, *et al.* The association between systemic lupus erythematosus and bipolar disorder - a big data analysis. *Eur Psychiatry* 2017, 43: 116–119.
17. Tiosano S, Farhi A, Watad A, Grysman N, Stryker R, Amital H, *et al.* Schizophrenia among patients with systemic lupus erythematosus: population-based cross-sectional study. *Epidemiol Psychiatr Sci* 2017, 26: 424–429.
18. Jackson J, Eaton W, Cascella N, Fasano A, Santora D, Sullivan K, *et al.* Gluten sensitivity and relationship to psychiatric symptoms in people with schizophrenia. *Schizophr Res* 2014, 159: 539–542.
19. Kumar V, Mattoo SK, Handa S. Psychiatric morbidity in pemphigus and psoriasis: a comparative study from India. *Asian J Psychiatr* 2013, 6: 151–156.
20. Kota SK, Meher LK, Jammula S, Kota SK, Modi KD. Clinical profile of coexisting conditions in type 1 diabetes mellitus patients. *Diabetes Metab Syndr* 2012, 6: 70–76.
21. Sturdy PM, Victor CR, Anderson HR, Bland JM, Butland BK, Harrison BDW, *et al.* Psychological, social and health behaviour risk factors for deaths certified as asthma: a national case-control study. *Thorax* 2002, 57: 1034–1039.
22. Gilvarry CM, Sham PC, Jones PB, Cannon M, Wright P, Lewis SW, *et al.* Family history of autoimmune diseases in psychosis. *Schizophr Res* 1996, 19: 33–40.
23. Nasr S, Altman EG, Meltzer HY. Concordance of atopic and affective disorders. *J Affect Disord* 1981, 3: 291–296.
24. Osterberg E. Schizophrenia and rheumatic disease. A study on the concurrence of inflammatory joint diseases and a review of 58 case-records. *Acta Psychiatr Scand* 1978, 58: 339–359.
25. Corvin A, Morris DW. Genome-wide association studies: findings at the major histocompatibility complex locus in psychosis. *Biol Psychiatry* 2014, 75: 276–283.
26. Liu JF, Wu R, Li JX. Toll of mental disorders: TLR-mediated function of the innate immune system. *Neurosci Bull* 2019, 35: 771–774.
27. McDonald D, Hyde E, Debelius JW, Morton JT, Gonzalez A, Ackermann G, *et al.* American Gut: an open platform for citizen science microbiome research. *mSystems* 2018, 3: e00031-18.
28. Goodrich JK, Waters JL, Poole AC, Sutter JL, Koren O, Blekhman R, *et al.* Human genetics shape the gut microbiome. *Cell* 2014, 159: 789–799.
29. Song X, Fan X, Song X, Zhang J, Zhang W, Li X, *et al.* Elevated levels of adiponectin and other cytokines in drug naïve, first episode schizophrenia patients with normal weight. *Schizophr Res* 2013, 150: 269–273.
30. Miller BJ, Buckley P, Seabolt W, Mellor A, Kirkpatrick B. Meta-analysis of cytokine alterations in schizophrenia: clinical status and antipsychotic effects. *Biol Psychiatry* 2011, 70: 663–671.
31. Potvin S, Stip E, Sepehry AA, Gendron A, Bah R, Kouassi E. Inflammatory cytokine alterations in schizophrenia: a systematic quantitative review. *Biol Psychiatry* 2008, 63: 801–808.
32. Tourjman V, Kouassi É, Koué M-È, Rocchetti M, Fortin-Fournier S, Fusar-Poli P, *et al.* Antipsychotics' effects on blood levels of cytokines in schizophrenia: a meta-analysis. *Schizophr Res* 2013, 151: 43–47.
33. Wood SJ, Yung AR, McGorry PD, Pantelis C. Neuroimaging and treatment evidence for clinical staging in psychotic disorders: from the at-risk mental state to chronic schizophrenia. *Biol Psychiatry* 2011, 70: 619–625.
34. Niu Z, Yang L, Wu X, Zhu Y, Chen J, Fang Y. The relationship between neuroimmunity and bipolar disorder: mechanism and translational application. *Neurosci Bull* 2019, 35: 595–607.
35. Suvisaari J, Mantere O. Inflammation theories in psychotic disorders: a critical review. *Infect Disord Drug Targets* 2013, 13: 59–70.
36. Bian Q, Kato T, Monji A, Hashioka S, Mizoguchi Y, Horikawa H, *et al.* The effect of atypical antipsychotics, perospirone, ziprasidone and quetiapine on microglial activation induced by interferon-gamma. *Prog Neuropsychopharmacol Biol Psychiatry* 2008, 32: 42–48.
37. Okada H, Kuhn C, Feillet H, Bach JF. The “hygiene hypothesis” for autoimmune and allergic diseases: an update. *Clin Exp Immunol* 2010, 160: 1–9.
38. de Groot PF, Belzer C, Aydin Ö, Levin E, Levels JH, Aalvink S, *et al.* Distinct fecal and oral microbiota composition in human type 1 diabetes, an observational study. *PLoS One* 2017, 12: e0188475.
39. Knip M, Honkanen J. Modulation of type 1 diabetes risk by the intestinal microbiome. *Curr Diab Rep* 2017, 17: 105.
40. Wekerle H. Nature, nurture, and microbes: The development of multiple sclerosis. *Acta Neurol Scand* 2017, 136 Suppl 201: 22–25.
41. Kim D, Zeng MY, Núñez G. The interplay between host immune cells and gut microbiota in chronic inflammatory diseases. *Exp Mol Med* 2017, 49: e339.
42. Quigley EMM. Primary biliary cirrhosis and the microbiome. *Semin Liver Dis* 2016, 36: 349–353.
43. Talotta R, Atzeni F, Ditto MC, Gerardi MC, Sarzi-Puttini P. The microbiome in connective tissue diseases and vasculitides: an updated narrative review. *J Immunol Res* 2017, 2017: 6836498.
44. Yacoub R, Jacob A, Wlaschin J, McGregor M, Quigg RJ, Alexander JJ. Lupus: The microbiome angle. *Immunobiology* 2018, 223: 460–465.
45. Lowry CA, Smith DG, Siebler PH, Schmidt D, Stamper CE, Hassell JE, *et al.* The microbiota, immunoregulation, and mental health: implications for public health. *Curr Environ Health Rep* 2016, 3: 270–286.
46. Drexhage RC, Hoogenboezem TA, Cohen D, Versnel MA, Nolen WA, van Beveren NJM, *et al.* An activated set point of T-cell and monocyte inflammatory networks in recent-onset schizophrenia patients involves both pro- and anti-inflammatory forces. *Int J Neuropsychopharmacol* 2011, 14: 746–755.
47. de Araujo EG, da Silva GM, Dos Santos AA. Neuronal cell survival: the role of interleukins. *Ann N Y Acad Sci* 2009, 1153: 57–64.
48. Gecse K, Róka R, Séra T, Rosztóczy A, Annaházi A, Izbéki F, *et al.* Leaky gut in patients with diarrhea-predominant irritable bowel syndrome and inactive ulcerative colitis. *Digestion* 2012, 85: 40–46.
49. Dinan TG, Cryan JF. The impact of gut microbiota on brain and behaviour: Implications for psychiatry. *Curr Opin Clin Nutr Metab Care* 2015, 18: 552–558.
50. Severance EG, Alaedini A, Yang S, Halling M, Gressitt KL, Stallings CR, *et al.* Gastrointestinal inflammation and associated immune activation in schizophrenia. *Schizophr Res* 2012, 138: 48–53.

51. Severance EG, Gressitt KL, Stallings CR, Katsafanas E, Schweinfurth LA, Savage CL, *et al.* Candida albicans exposures, sex specificity and cognitive deficits in schizophrenia and bipolar disorder. *NPJ Schizophrenia* 2016, 2: 16018.
52. Severance EG, Gressitt KL, Stallings CR, Origoni AE, Khushalani S, Leweke FM, *et al.* Discordant patterns of bacterial translocation markers and implications for innate immune imbalances in schizophrenia. *Schizophr Res* 2013, 148: 130–137.
53. Jang HM, Lee HJ, Jang SE, Han MJ, Kim DH. Evidence for interplay among antibacterial-induced gut microbiota disturbance, neuro-inflammation, and anxiety in mice. *Mucosal Immunol* 2018, 11: 1386–1397.
54. Minter MR, Zhang C, Leone V, Ringus DL, Zhang X, Oyler-Castrillo P, *et al.* Antibiotic-induced perturbations in gut microbial diversity influences neuro-inflammation and amyloidosis in a murine model of Alzheimer's disease. *Sci Rep* 2016, 6: 30028.
55. Wilck N, Matus MG, Kearney SM, Olesen SW, Forslund K, Bartolomeaus H, *et al.* Salt-responsive gut commensal modulates TH17 axis and disease. *Nature* 2017, 551: 585–589.
56. Singh V, Roth S, Llovera G, Sadler R, Garzetti D, Stecher B, *et al.* Microbiota Dysbiosis Controls the Neuroinflammatory Response after Stroke. *J Neurosci* 2016, 36: 7428–7440.
57. Ma L, Demin KA, Kolesnikova TO, Khatsko SL, Zhu X, Yuan X, *et al.* Animal inflammation-based models of depression and their application to drug discovery. *Expert Opin Drug Discov* 2017, 12: 995–1009.
58. Wong M-L, Insera A, Lewis MD, Mastronardi CA, Leong L, Choo J, *et al.* Inflammasome signaling affects anxiety- and depressive-like behavior and gut microbiome composition. *Mol Psychiatry* 2016, 21: 797–805.
59. Borre YE, O'Keefe GW, Clarke G, Stanton C, Dinan TG, Cryan JF. Microbiota and neurodevelopmental windows: implications for brain disorders. *Trends Mol Med* 2014, 20: 509–518.
60. Kuperman AA, Koren O. Antibiotic use during pregnancy: how bad is it? *BMC Med* 2016, 14: 91.
61. Leiby JS, McCormick K, Sherrill-Mix S, Clarke EL, Kessler LR, Taylor LJ, *et al.* Lack of detection of a human placenta microbiome in samples from preterm and term deliveries. *Microbiome* 2018, 6: 196.
62. Collins J, Borojevic R, Verdu EF, Huizinga JD, Ratcliffe EM. Intestinal microbiota influence the early postnatal development of the enteric nervous system. *Neurogastroenterol Motil* 2014, 26: 98–107.
63. Monroe JM, Buckley PF, Miller BJ. Meta-analysis of anti-*Toxoplasma gondii* IgM antibodies in acute psychosis. *Schizophr Bull* 2015, 41: 989–998.
64. Arias I, Sorlozano A, Villegas E, de Dios Luna J, McKenney K, Cervilla J, *et al.* Infectious agents associated with schizophrenia: a meta-analysis. *Schizophr Res* 2012, 136: 128–136.
65. Meeraus WH, Petersen I, Gilbert R. Association between antibiotic prescribing in pregnancy and cerebral palsy or epilepsy in children born at term: a cohort study using the health improvement network. *PLoS One* 2015, 10: e0122034.
66. Kenyon S, Pike K, Jones DR, Brocklehurst P, Marlow N, Salt A, *et al.* Childhood outcomes after prescription of antibiotics to pregnant women with preterm rupture of the membranes: 7-year follow-up of the ORACLE I trial. *Lancet* 2008, 372: 1310–1318.
67. Tochitani S, Ikeno T, Ito T, Sakurai A, Yamauchi T, Matsuzaki H. Administration of non-absorbable antibiotics to pregnant mice to perturb the maternal gut microbiota is associated with alterations in offspring behavior. *PLoS One* 2016, 11: e0138293.
68. Degroote S, Hunting DJ, Baccarelli AA, Takser L. Maternal gut and fetal brain connection: Increased anxiety and reduced social interactions in Wistar rat offspring following peri-conceptual antibiotic exposure. *Prog Neuropsychopharmacol Biol Psychiatry* 2016, 71: 76–82.
69. Buffington SA, Di Prisco GV, Auchtung TA, Ajami NJ, Petrosino JF, Costa-Mattioli M. Microbial reconstitution reverses maternal diet-induced social and synaptic deficits in offspring. *Cell* 2016, 165: 1762–1775.
70. Pendyala G, Chou S, Jung Y, Coiro P, Spartz E, Padmashri R, *et al.* Maternal immune activation causes behavioral impairments and altered cerebellar cytokine and synaptic protein expression. *Neuropsychopharmacology* 2017, 42: 1435–1446.
71. Jašarević E, Howerton CL, Howard CD, Bale TL. Alterations in the vaginal microbiome by maternal stress are associated with metabolic reprogramming of the offspring gut and brain. *Endocrinology* 2015, 156: 3265–3276.
72. Gur TL, Palkar AV, Rajasekera T, Allen J, Niraula A, Godbout J, *et al.* Prenatal stress disrupts social behavior, cortical neurobiology and commensal microbes in adult male offspring. *Behav Brain Res* 2019, 359: 886–894.
73. Humann J, Mann B, Gao G, Moresco P, Ramahi J, Loh LN, *et al.* Bacterial peptidoglycan traverses the placenta to induce fetal neuroproliferation and aberrant postnatal behavior. *Cell Host Microbe* 2016, 19: 388–399.
74. Foley KA, Ossenkopp KP, Kavaliers M, Macfabe DF. Pre- and neonatal exposure to lipopolysaccharide or the enteric metabolite, propionic acid, alters development and behavior in adolescent rats in a sexually dimorphic manner. *PLoS One* 2014, 9: e87072.
75. Barrett E, Guinane CM, Ryan CA, Dempsey EM, Murphy BP, O'Toole PW, *et al.* Microbiota diversity and stability of the preterm neonatal ileum and colon of two infants. *Microbiolgyopen* 2013, 2: 215–225.
76. Nosarti C, Reichenberg A, Murray RM, Cnattingius S, Lambe MP, Yin L, *et al.* Preterm birth and psychiatric disorders in young adult life. *Arch Gen Psychiatry* 2012, 69: E1–8.
77. Quigley MA, Hockley C, Carson C, Kelly Y, Renfrew MJ, Sacker A. Breastfeeding is associated with improved child cognitive development: a population-based cohort study. *J Pediatr* 2012, 160: 25–32.
78. O'Neill SM, Curran EA, Dalman C, Kenny LC, Kearney PM, Clarke G, *et al.* Birth by caesarean section and the risk of adult psychosis: a population-based cohort study. *Schizophr Bull* 2016, 42: 633–641.
79. Fond G, Bulzacka E, Boyer L, Llorca PM, Godin O, Brunel L, *et al.* Birth by cesarean section and schizophrenia: results from the multicenter FACE-SZ data-set. *Eur Arch Psychiatry Clin Neurosci* 2017, 267: 587–594.
80. Dominguez-Bello MG, Costello EK, Contreras M, Magris M, Hidalgo G, Fierer N, *et al.* Delivery mode shapes the acquisition and structure of the initial microbiota across multiple body habitats in newborns. *Proc Natl Acad Sci U S A* 2010, 107: 11971–11975.
81. Gareau MG, Wine E, Rodrigues DM, Cho JH, Whary MT, Philpott DJ, *et al.* Bacterial infection causes stress-induced memory dysfunction in mice. *Gut* 2011, 60: 307–317.
82. Desbonnet L, Clarke G, Shanahan F, Dinan TG, Cryan JF. Microbiota is essential for social development in the mouse. *Mol Psychiatry* 2014, 19: 146–148.
83. Neufeld KM, Kang N, Bienenstock J, Foster JA. Reduced anxiety-like behavior and central neurochemical change in germ-free mice. *Neurogastroenterol Motil* 2011, 23: 255–264, e119.
84. Bercik P, Denou E, Collins J, Jackson W, Lu J, Jury J, *et al.* The intestinal microbiota affect central levels of brain-derived neurotrophic factor and behavior in mice. *Gastroenterology* 2011, 141: 599–609, 609.e1–3.

85. Desbonnet L, Clarke G, Traplin A, O'Sullivan O, Crispie F, Moloney RD, *et al.* Gut microbiota depletion from early adolescence in mice: Implications for brain and behaviour. *Brain Behav Immun* 2015, 48: 165–173.
86. Sudo N, Chida Y, Aiba Y, Sonoda J, Oyama N, Yu XN, *et al.* Postnatal microbial colonization programs the hypothalamic-pituitary-adrenal system for stress response in mice. *J Physiol (Lond)* 2004, 558: 263–275.
87. He Y, Kosciolk T, Tang J, Zhou Y, Li Z, Ma X, *et al.* Gut microbiome and magnetic resonance spectroscopy study of subjects at ultra-high risk for psychosis may support the membrane hypothesis. *Eur Psychiatry* 2018, 53: 37–45.
88. Schwarz E, Maukonen J, Hyytiäinen T, Kiesepä T, Orešič M, Sabunciyan S, *et al.* Analysis of microbiota in first episode psychosis identifies preliminary associations with symptom severity and treatment response. *Schizophr Res* 2018, 192: 398–403.
89. Yuan X, Zhang P, Wang Y, Liu Y, Li X, Kumar BU, *et al.* Changes in metabolism and microbiota after 24-week risperidone treatment in drug naïve, normal weight patients with first episode schizophrenia. *Schizophr Res* 2018, 201: 299–306.
90. Pełka-Wysiecka J, Kaczmarczyk M, Bąba-Kubiś A, Liśkiewicz P, Wroński M, Skonieczna-Żydecka K, *et al.* Analysis of gut microbiota and their metabolic potential in patients with schizophrenia treated with olanzapine: results from a six-week observational prospective cohort study. *J Clin Med* 2019, 8: 1605.
91. Shen Y, Xu J, Li Z, Huang Y, Yuan Y, Wang J, *et al.* Analysis of gut microbiota diversity and auxiliary diagnosis as a biomarker in patients with schizophrenia: A cross-sectional study. *Schizophr Res* 2018, 197: 470–477.
92. Zheng P, Zeng B, Liu M, Chen J, Pan J, Han Y, *et al.* The gut microbiome from patients with schizophrenia modulates the glutamate-glutamine-GABA cycle and schizophrenia-relevant behaviors in mice. *Sci Adv* 2019, 5: eaau8317.
93. Xu R, Wu B, Liang J, He F, Gu W, Li K, *et al.* Altered gut microbiota and mucosal immunity in patients with schizophrenia. *Brain Behav Immun* 2020, 85: 120–127.
94. Nguyen TT, Kosciolk T, Maldonado Y, Daly RE, Martin AS, McDonald D, *et al.* Differences in gut microbiome composition between persons with chronic schizophrenia and healthy comparison subjects. *Schizophr Res* 2019, 204: 23–29.
95. Yolken RH, Severance EG, Sabunciyan S, Gressitt KL, Chen O, Stallings C, *et al.* Metagenomic sequencing indicates that the oropharyngeal phageome of individuals with schizophrenia differs from that of controls. *Schizophr Bull* 2015, 41: 1153–1161.
96. Castro-Nallar E, Bendall ML, Pérez-Losada M. Composition, taxonomy and functional diversity of the oropharynx microbiome in individuals with schizophrenia and controls. *PeerJ* 2015, 3: e1140.
97. Torrey EF, Bartko JJ, Lun Z-R, Yolken RH. Antibodies to *Toxoplasma gondii* in patients with schizophrenia: a meta-analysis. *Schizophr Bull* 2007, 33: 729–736.
98. Severance EG, Kannan G, Gressitt KL, Xiao J, Alaedini A, Pletnikov MV, *et al.* Anti-gluten immune response following *Toxoplasma gondii* infection in mice. *PLoS ONE* 2012, 7: e50991.
99. Houenou J, d'Albis M-A, Daban C, Hamdani N, Delavest M, Lepine JP, *et al.* Cytomegalovirus seropositivity and serointensity are associated with hippocampal volume and verbal memory in schizophrenia and bipolar disorder. *Prog Neuro-Psychopharmacol Biol Psychiatry* 2014, 48: 142–148.
100. Nguyen TT, Kosciolk T, Eyster LT, Knight R, Jeste DV. Overview and systematic review of studies of microbiome in schizophrenia and bipolar disorder. *J Psychiatr Res* 2018, 99: 50–61.
101. Zhu F, Guo R, Wang W, Ju Y, Wang Q, Ma Q, *et al.* Transplantation of microbiota from drug-free patients with schizophrenia causes schizophrenia-like abnormal behaviors and dysregulated kynurenine metabolism in mice. *Mol Psychiatry* 2019. <https://doi.org/10.1038/s41380-019-0475-4>.
102. Finegold SM, Molitoris D, Song Y, Liu C, Vaisanen M, Bolte E, *et al.* Gastrointestinal microflora studies in late-onset autism. *Clin Infect Dis* 2002, 35: S6–S16.
103. Parracho HMRT, Bingham MO, Gibson GR, McCartney AL. Differences between the gut microflora of children with autistic spectrum disorders and that of healthy children. *J Med Microbiol* 2005, 54: 987–991.
104. Angelis M, Piccolo M, Vannini L, Siragusa S, Giacomo A, Serrazzanetti D, *et al.* Fecal microbiota and metabolome of children with autism and pervasive developmental disorder not otherwise specified. *PLoS One* 2013, 8. <https://doi.org/10.1371/journal.pone.0076993>.
105. Adams JB, Johansen LJ, Powell LD, Quig D, Rubin RA. Gastrointestinal flora and gastrointestinal status in children with autism - comparisons to typical children and correlation with autism severity. *BMC Gastroenterol* 2011, 11: 22–22.
106. Tomova A, Husarova V, Lakatosova S, Bakos J, Vlkova B, Babinska K, *et al.* Gastrointestinal microbiota in children with autism in Slovakia. *Physiol Behav* 2015, 138: 179–187.
107. Strati F, Cavalieri D, Albanese D, De Felice C, Donati C, Hayek J, *et al.* New evidences on the altered gut microbiota in autism spectrum disorders. *Microbiome* 2017, 5: 24–24.
108. Williams BL, Hornig M, Parekh T, Lipkin WI. Application of novel PCR-based methods for detection, quantitation, and phylogenetic characterization of *Sutterella* species in intestinal biopsy samples from children with autism and gastrointestinal disturbances. *mBio* 2012, 3. <https://doi.org/10.1128/mbio.00261-11>.
109. Wang L, Christophersen CT, Soric MJ, Gerber JP, Angley MT, Conlon MA. Increased abundance of *Sutterella* spp. and *Ruminococcus torques* in feces of children with autism spectrum disorder. *Mol Autism* 2013, 4: 42.
110. Zhai Q, Cen S, Jiang J, Zhao J, Zhang H, Chen W. Disturbance of trace element and gut microbiota profiles as indicators of autism spectrum disorder: A pilot study of Chinese children. *Environ Res* 2019, 171: 501–509.
111. Finegold SM, Dowd SE, Gontcharova V, Liu C, Henley KE, Wolcott RD, *et al.* Pyrosequencing study of fecal microflora of autistic and control children. *Anaerobe* 2010, 16: 444–453.
112. Kang DW, Park JG, Ilhan ZE, Wallstrom G, Labaer J, Adams JB, *et al.* Reduced incidence of *Prevotella* and other fermenters in intestinal microflora of autistic children. *PLoS One* 2013, 8: e68322.
113. Gondalia SV, Palombo EA, Knowles SR, Cox SB, Meyer D, Austin DW. Molecular characterisation of gastrointestinal microbiota of children with autism (with and without gastrointestinal dysfunction) and their neurotypical siblings. *Autism Res* 2012, 5: 419–427.
114. Hsiao EY, McBride SW, Hsien S, Sharon G, Hyde ER, McCue T, *et al.* Microbiota modulate behavioral and physiological abnormalities associated with neurodevelopmental disorders. *Cell* 2013, 155: 1451–1463.
115. Theije CGM de, Wopereis H, Ramadan M, Eijndthoven T van, Lambert J, Knol J, *et al.* Altered gut microbiota and activity in a murine model of autism spectrum disorders. *Brain Behav Immun* 2014, 37: 197–206.
116. Sgritta M, Dooling SW, Buffington SA, Momin EN, Francis MB, Britton RA, *et al.* Mechanisms underlying microbial-

- mediated changes in social behavior in mouse models of autism spectrum disorder. *Neuron* 2019, 101: 246–259.e6.
117. Chen K, Luan X, Liu Q, Wang J, Chang X, Snijders AM, *et al.* *Drosophila* histone demethylase KDM5 regulates social behavior through immune control and gut microbiota maintenance. *Cell Host Microbe* 2019, 25: 537–552.e8.
 118. Naseribafrouei A, Hestad K, Avershina E, Sekelja M, Linløkken A, Wilson R, *et al.* Correlation between the human fecal microbiota and depression. *Neurogastroenterol Motil* 2014, 26: 1155–1162.
 119. Jiang H, Ling Z, Zhang Y, Mao H, Ma Z, Yin Y, *et al.* Altered fecal microbiota composition in patients with major depressive disorder. *Brain Behav Immun* 2015, 48: 186–194.
 120. Zheng P, Zeng B, Zhou C, Liu M, Fang Z, Xu X, *et al.* Gut microbiome remodeling induces depressive-like behaviors through a pathway mediated by the host's metabolism. *Mol Psychiatry* 2016, 21: 786–796.
 121. Yu M, Jia H, Zhou C, Yang Y, Zhao Y, Yang M, *et al.* Variations in gut microbiota and fecal metabolic phenotype associated with depression by 16S rRNA gene sequencing and LC/MS-based metabolomics. *J Pharm Biomed Anal* 2017, 138: 231–239.
 122. Evans SJ, Bassis CM, Hein R, Assari S, Flowers SA, Kelly MB, *et al.* The gut microbiome composition associates with bipolar disorder and illness severity. *J Psychiatr Res* 2017, 87: 23–29.
 123. Hu S, Li A, Huang T, Lai J, Li J, Sublette ME, *et al.* Gut microbiota changes in patients with bipolar depression. *Adv Sci (Weinh)* 2019, 6: 1900752.
 124. McIntyre RS, Subramaniapillai M, Shekotikhina M, Carmona NE, Lee Y, Mansur RB, *et al.* Characterizing the gut microbiota in adults with bipolar disorder: a pilot study. *Nutr Neurosci* 2019. <https://doi.org/10.1080/1028415x.2019.1612555>.
 125. Painold A, Mörkl S, Kashofer K, Halwachs B, Dalkner N, Bengesser S, *et al.* A step ahead: Exploring the gut microbiota in inpatients with bipolar disorder during a depressive episode. *Bipolar Disord* 2019, 21: 40–49.
 126. Rong H, Xie XH, Zhao J, Lai WT, Wang MB, Xu D, *et al.* Similarly in depression, nuances of gut microbiota: Evidences from a shotgun metagenomics sequencing study on major depressive disorder versus bipolar disorder with current major depressive episode patients. *J Psychiatr Res* 2019, 113: 90–99.
 127. Zijlmans MAC, Korpela K, Riksen-Walraven JM, de Vos WM, de Weerth C. Maternal prenatal stress is associated with the infant intestinal microbiota. *Psychoneuroendocrinology* 2015, 53: 233–245.
 128. Bailey MT, Coe CL. Maternal separation disrupts the integrity of the intestinal microflora in infant rhesus monkeys. *Dev Psychobiol* 1999, 35: 146–155.
 129. De Palma G, Blennerhassett P, Lu J, Deng Y, Park AJ, Green W, *et al.* Microbiota and host determinants of behavioural phenotype in maternally separated mice. *Nat Commun* 2015, 6: 7735.
 130. Pyndt Jørgensen B, Winther G, Kihl P, Nielsen DS, Wegener G, Hansen AK, *et al.* Dietary magnesium deficiency affects gut microbiota and anxiety-like behaviour in C57BL/6N mice. *Acta Neuropsychiatr* 2015, 27: 307–311.
 131. Hemmings SMJ, Malan-Müller S, van den Heuvel LL, Demmitt BA, Stanislawski MA, Smith DG, *et al.* The microbiome in posttraumatic stress disorder and trauma-exposed controls: An exploratory study. *Psychosom Med* 2017, 79: 936–946.
 132. Crumeyrolle-Arias M, Jaglin M, Bruneau A, Vancassel S, Cardona A, Daugé V, *et al.* Absence of the gut microbiota enhances anxiety-like behavior and neuroendocrine response to acute stress in rats. *Psychoneuroendocrinology* 2014, 42: 207–217.
 133. Bambury A, Sandhu K, Cryan JF, Dinan TG. Finding the needle in the haystack: systematic identification of psychobiotics. *Br J Pharmacol* 2018, 175: 4430–4438.
 134. Dinan TG, Stanton C, Cryan JF. Psychobiotics: a novel class of psychotropic. *Biol Psychiatry* 2013, 74: 720–726.
 135. Collins SM, Surette M, Bercik P. The interplay between the intestinal microbiota and the brain. *Nat Rev Microbiol* 2012, 10: 735–742.
 136. Desbonnet L, Garrett L, Clarke G, Bienenstock J, Dinan TG. The probiotic *Bifidobacteria infantis*: An assessment of potential antidepressant properties in the rat. *J Psychiatr Res* 2008, 43: 164–174.
 137. Bravo JA, Forsythe P, Chew MV, Escaravage E, Savignac HM, Dinan TG, *et al.* Ingestion of *Lactobacillus* strain regulates emotional behavior and central GABA receptor expression in a mouse via the vagus nerve. *Proc Natl Acad Sci U S A* 2011, 108: 16050–16055.
 138. Lyte M, Varcoe JJ, Bailey MT. Anxiogenic effect of subclinical bacterial infection in mice in the absence of overt immune activation. *Physiol Behav* 1998, 65: 63–68.
 139. Bangsgaard Bendtsen KM, Krych L, Sørensen DB, Pang W, Nielsen DS, Josefsen K, *et al.* Gut microbiota composition is correlated to grid floor induced stress and behavior in the BALB/c mouse. *PLoS One* 2012, 7: e46231.
 140. Desbonnet L, Garrett L, Clarke G, Kiely B, Cryan JF, Dinan TG. Effects of the probiotic *Bifidobacterium infantis* in the maternal separation model of depression. *Neuroscience* 2010, 170: 1179–1188.
 141. McKernan DP, Fitzgerald P, Dinan TG, Cryan JF. The probiotic *Bifidobacterium infantis* 35624 displays visceral antinociceptive effects in the rat. *Neurogastroenterol Motil* 2010, 22: 1029–1035, e268.
 142. Messaoudi M, Lalonde R, Violle N, Javelot H, Desor D, Nejd A, *et al.* Assessment of psychotropic-like properties of a probiotic formulation (*Lactobacillus helveticus* R0052 and *Bifidobacterium longum* R0175) in rats and human subjects. *Br J Nutr* 2011, 105: 755–764.
 143. Dapoigny M, Piche T, Ducrotte P, Linaud B, Cardot J-M, Bernalier-Donadille A. Efficacy and safety profile of LCR35 complete freeze-dried culture in irritable bowel syndrome: a randomized, double-blind study. *World J Gastroenterol* 2012, 18: 2067–2075.
 144. Rao AV, Basted AC, Beaulne TM, Katzman MA, Iorio C, Berardi JM, *et al.* A randomized, double-blind, placebo-controlled pilot study of a probiotic in emotional symptoms of chronic fatigue syndrome. *Gut Pathog* 2009, 1: 6.
 145. Benton D, Williams C, Brown A. Impact of consuming a milk drink containing a probiotic on mood and cognition. *Eur J Clin Nutr* 2007, 61: 355–361.
 146. Romijn AR, Rucklidge JJ. Systematic review of evidence to support the theory of psychobiotics. *Nutr Rev* 2015, 73: 675–693.
 147. Dickerson FB, Stallings C, Origoni A, Katsafanas E, Savage CLG, Schweinfurth LAB, *et al.* Effect of probiotic supplementation on schizophrenia symptoms and association with gastrointestinal functioning: a randomized, placebo-controlled trial. *Prim Care Companion CNS Disord* 2014, 16. <https://doi.org/10.4088/pcc.13m01579>.
 148. Dickerson F, Adamos M, Katsafanas E, Khushalani S, Origoni A, Savage C, *et al.* Adjunctive probiotic microorganisms to prevent rehospitalization in patients with acute mania: A randomized controlled trial. *Bipolar Disord* 2018, 20: 614–621.
 149. Keller WR, Kum LM, Wehring HJ, Koola MM, Buchanan RW, Kelly DL. A review of anti-inflammatory agents for symptoms of schizophrenia. *J Psychopharmacol (Oxford)* 2013, 27: 337–342.

150. Sommer IE, de Witte L, Begemann M, Kahn RS. Nonsteroidal anti-inflammatory drugs in schizophrenia: ready for practice or a good start? A meta-analysis. *J Clin Psychiatry* 2012, 73: 414–419.
151. Solmi M, Veronese N, Thapa N, Facchini S, Stubbs B, Fornaro M, *et al.* Systematic review and meta-analysis of the efficacy and safety of minocycline in schizophrenia. *CNS Spectr* 2017, 22: 415–426.
152. Nemani K, Hosseini Ghomi R, McCormick B, Fan X. Schizophrenia and the gut-brain axis. *Prog Neuropsychopharmacol Biol Psychiatry* 2015, 56: 155–160.
153. Kalaydjian AE, Eaton W, Cascella N, Fasano A. The gluten connection: the association between schizophrenia and celiac disease. *Acta Psychiatr Scand* 2006, 113: 82–90.
154. Citrome L, Holt RIG, Walker DJ, Hoffmann VP. Weight gain and changes in metabolic variables following olanzapine treatment in schizophrenia and bipolar disorder. *Clin Drug Investig* 2011, 31: 455–482.
155. Birkenaes AB, Birkeland KI, Engh JA, Faerden A, Jonsdottir H, Ringen PA, *et al.* Dyslipidemia independent of body mass in antipsychotic-treated patients under real-life conditions. *J Clin Psychopharmacol* 2008, 28: 132–137.
156. Chintoh AF, Mann SW, Lam TKT, Giacca A, Remington G. Insulin resistance following continuous, chronic olanzapine treatment: an animal model. *Schizophr Res* 2008, 104: 23–30.
157. Perez-Iglesias R, Mata I, Pelayo-Teran JM, Amado JA, Garcia-Unzueta MT, Berja A, *et al.* Glucose and lipid disturbances after 1 year of antipsychotic treatment in a drug-naïve population. *Schizophr Res* 2009, 107: 115–121.
158. Patel JK, Buckley PF, Woolson S, Hamer RM, McEvoy JP, Perkins DO, *et al.* Metabolic profiles of second-generation antipsychotics in early psychosis: findings from the CAFE study. *Schizophr Res* 2009, 111: 9–16.
159. Cohen D, Correll CU. Second-generation antipsychotic-associated diabetes mellitus and diabetic ketoacidosis: mechanisms, predictors, and screening need. *J Clin Psychiatry* 2009, 70: 765–766.
160. Farwell WR, Stump TE, Wang J, Tafesse E, L'Italien G, Tierney WM. Weight gain and new onset diabetes associated with olanzapine and risperidone. *J Gen Intern Med* 2004, 19: 1200–1205.
161. Davey KJ, O'Mahony SM, Schellekens H, O'Sullivan O, Bienenstock J, Cotter PD, *et al.* Gender-dependent consequences of chronic olanzapine in the rat: effects on body weight, inflammatory, metabolic and microbiota parameters. *Psychopharmacology (Berl)* 2012, 221: 155–169.
162. Turnbaugh PJ, Ley RE, Mahowald MA, Magrini V, Mardis ER, Gordon JI. An obesity-associated gut microbiome with increased capacity for energy harvest. *Nature* 2006, 444: 1027–1031.
163. Davey KJ, Cotter PD, O'Sullivan O, Crispie F, Dinan TG, Cryan JF, *et al.* Antipsychotics and the gut microbiome: olanzapine-induced metabolic dysfunction is attenuated by antibiotic administration in the rat. *Transl Psychiatry* 2013, 3: e309.
164. Bahr SM, Weidemann BJ, Castro AN, Walsh JW, deLeon O, Burnett CML, *et al.* Risperidone-induced weight gain is mediated through shifts in the gut microbiome and suppression of energy expenditure. *EBioMedicine* 2015, 2: 1725–1734.
165. Bahr SM, Tyler BC, Wooldridge N, Butcher BD, Burns TL, Teesch LM, *et al.* Use of the second-generation antipsychotic, risperidone, and secondary weight gain are associated with an altered gut microbiota in children. *Transl Psychiatry* 2015, 5: e652.
166. Maier L, Pruteanu M, Kuhn M, Zeller G, Telzerow A, Anderson EE, *et al.* Extensive impact of non-antibiotic drugs on human gut bacteria. *Nature* 2018, 555: 623–628.



RESEARCH HIGHLIGHT

Microglia Interact with Neurons by Forming Somatic Junctions

Yongjie Wang^{1,2} · Zhihui Huang^{1,2,3}

Received: 24 January 2020 / Accepted: 6 March 2020 / Published online: 24 May 2020
© Shanghai Institutes for Biological Sciences, CAS 2020

Microglia are the main immune cells of the central nervous system that maintain normal neuronal functions. Microglial cells are also linked with major diseases in humans including neurodegenerative disorders such as Alzheimer's disease, stroke, epilepsy, and psychiatric diseases such as schizophrenia [1]. Microglia perform surveillance of the brain microenvironment through their motile processes. Currently, there has been increased attention on the interaction between microglial processes and synaptic elements. At least part of the dynamic motility of resting microglial processes *in vivo* is directed toward neuronal synapses. Resting microglial processes have brief and direct contact with synapses lasting ~5 min and this occurs at a frequency of about once per hour in a neuronal activity-dependent manner. Under the conditions of cerebral ischemia, the duration of these microglia-synapse contacts is significantly prolonged to about an hour, and this is followed by the disappearance of the presynaptic bouton, suggesting that microglia contribute to the subsequent increased turnover of synaptic connections [2]. However, the molecular mechanisms of microglia-neuron communication are not well understood.

Microglial cells are involved in the formation and maintenance of synapses in the brain [3] during development and synaptic plasticity. Researchers have demonstrated that microglial processes interact with axonal terminals and dendritic spines in the visual cortex in a neuronal activity-dependent manner, and for a long time, these were believed to be the main forms of interaction between microglia and neurons [2, 4, 5]. Moreover, the interactions between microglia and synaptic elements, including both axonal boutons and dendritic spines, have also received increased attention. Neuronal cell bodies are relatively stable in most conditions, while the synaptic structures are highly dynamic. The microglial processes actively monitor the surrounding neural parenchyma and respond promptly to brain injury [6]. The interactions between microglia and synapses do not elucidate how microglia monitor and affect neuronal activity spatiotemporally. Therefore, the mechanisms of effective communication between microglia and neuronal somata require investigation. Recently, Cserép and colleagues identified a novel communication site between microglial processes and neuronal cell bodies in both mice and humans. This was based on *in vivo* two-photon imaging, high-resolution light and electron microscopy combined with advanced 3D-analysis. Interestingly, they found that microglia form junctions with most neuronal somata regardless of their cell type in a P2Y₁₂ receptor (P2Y₁₂R)- and neuronal mitochondrial activity-dependent manner. In addition, the study highlighted that microglial junctions are essential for microglia-neuron communication, and for the neuroprotective effects of microglia after acute brain injury [7] (Fig. 1).

Unlike the previous studies showing that the interactions between microglial processes and synaptic elements of neurons are the main configuration [4], this study reported

✉ Zhihui Huang
hzhzju021@163.com

¹ Key Laboratory of Elemene Anti-Cancer Medicine of Zhejiang Province and Holistic Integrative Pharmacy Institutes, Hangzhou Normal University, Hangzhou 311121, China

² Engineering Laboratory of Development and Application of Traditional Chinese Medicine from Zhejiang Province and Holistic Integrative Pharmacy Institutes, Hangzhou Normal University, Hangzhou 311121, China

³ Department of Neurosurgery, The Affiliated Hospital of Hangzhou Normal University, Hangzhou 310015, China

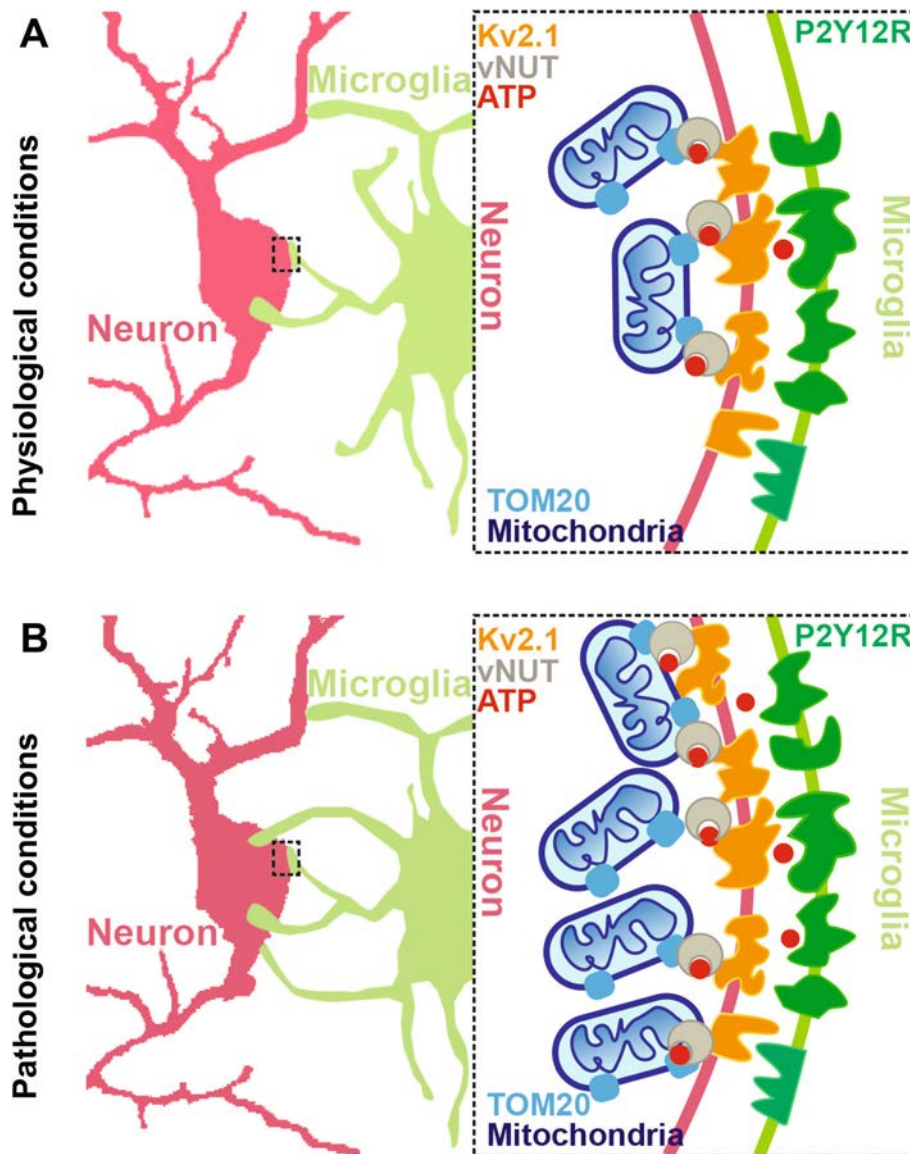


Fig. 1 Schematic of somatic microglial junctions under physiological and pathological conditions. **A** Under physiological conditions, microglia form junctions with most neuronal somata, but not with synaptic elements of neurons, regardless of cell type, in a P2Y12R-dependent manner. Somatic microglial junctions are the main communication sites between neurons and microglia in both mice and humans. They possess a unique nano-architecture within the neuronal somata consisting of Kv2.1 clusters (orange), which are mainly expressed in neurons and are the contact sites of microglia and neurons, TOM20 (sky blue), the main element of the transport protein complex on the outer mitochondrial membrane, and vNUT (brown), an important molecule for the vesicular release of mitochondria-derived ATP from neurons. **B** Under stroke conditions, potentially viable neurons are activated, inducing the release of ATP (red) from

the mitochondria (dark blue), and with the help of vNUT, ATP is released from the neurons. The released extracellular ATP regulates microglial branch dynamics via the purinoceptor P2Y12R (green), expressed specifically in microglia. The microglial processes are recruited to form new microglial-somatic junctions and to protect viable neurons. Somatic microglial junctions are robustly increased in both mice and human post-mortem brain after stroke. In addition, the disintegration of somatic microglial junctions after stroke induces an increase of microglial process coverage in the cell bodies of viable neurons in a P2Y12R- and mitochondrial signaling-dependent manner. This leads to the initiation of protective microglial responses that minimize brain injury. P2Y12R, purinergic receptor P2Y12; TOM20, translocase of outer mitochondrial membrane 20; vNUT, vesicular nucleotide transporter.

that only a small proportion of glutamatergic or GABAergic synapses are associated with microglial processes. In addition, >90% of cortical pyramidal cells, vGluT3⁺ cells, and >80% of PV⁺ interneurons are involved in the formation of somatic microglial junctions in mice. Similar

results were reported in the human neocortex as well. Furthermore, microglia contact neuronal somatic membranes mainly at sites of Kv2.1 clustering, which have been reported to be mainly expressed in neurons [8], in both mice and humans. Extracellular ATP released by neurons

regulates microglial branch dynamics *via* the purinoceptor P2Y12R. P2Y12Rs are expressed specifically in microglia and their activation is required in response to neuronal injury in the brain [9]. Indeed, dense P2Y12R clusters on microglial processes at somatic junction sites were found to directly face neuronal Kv2.1 clusters in pyramidal cells and interneurons (Fig. 1A). Consistent with these results, an *in vivo* imaging study using zebrafish reported that microglia preferentially contact the cell bodies of neurons with higher spontaneous activity, and this results in the reduction of visually-evoked neuronal activity [10]. Given that most studies have shown that the junctions mainly form between microglia and synaptic elements, the underlying mechanisms can be more complex and involve a number of molecules in addition to P2Y12Rs, which requires further investigation. Therefore, understanding the microglial P2Y12R signaling pathway will provide novel candidates for therapeutic interventions in pathologies involving microglial P2Y12Rs such as stroke.

What are the components of somatic microglia-neuron junctions? By using transmission electron microscopy and high-resolution electron tomography with 3D reconstruction, somatic microglial junctions were found to possess unique nano-architecture within the neuronal somata, and the junctions are composed of closely apposed mitochondria, reticular membrane structures, intracellular tethers, and associated vesicle-like membrane structures. However, these features were not observed in perisomatic boutons contacted by microglia. The Kv2.1 clusters were closely associated with the neuronal structures within the junctions. Furthermore, TOM20 (the main element of the transport protein complex in the outer mitochondrial membrane) and vesicular nucleotide transporter (vNUT, an important molecule for vesicular release of mitochondria-derived ATP from neurons) were also reported to be remarkably higher at somatic junctions than adjacent areas (Fig. 1A).

As noted above, mitochondria were close to the junctions, which has been reported to be essential for neuroglial crosstalk [11], so it is important to investigate whether microglial process recruitment to somatic junctions is functionally linked with the activity of mitochondria in neurons. *In vivo* two-photon imaging revealed that the number of mitochondria significantly increases and is accompanied by the formation of somatic microglial junctions in wild-type but not in P2Y12R^{-/-} tissue. This suggests that microglial process recruitment to somatic junctions is linked to neuronal mitochondrial activity and occurs in a P2Y12R-dependent manner. Moreover, neuronal activation induced the release of ATP from the mitochondria, which was inhibited by a vNUT blocker but not a synaptic calcium channel blocker (Fig. 1A). The findings demonstrated that microglia dynamically monitor

neuronal activity at somatic microglia-neuron junctions in a P2Y12R-dependent manner, leading to a rapid increase of somatic coverage by microglial processes. This suggests an interesting possibility that microglia and neurons engage in dynamic communication essential for nervous system health and homeostasis.

The authors examined the interaction between microglia and neurons in the healthy brain. Currently, findings on the roles of microglia in pathological conditions such as stroke are inconsistent across studies [12]. Several studies have explored the contribution of microglia in synaptic functions. In this paper, the somatic microglial junctions were reported to have robustly increased after stroke in both mice and human post-mortem brain tissue (Fig. 1B). Microglial process coverage around the somatic junctions was completely abolished after the administration of a P2Y12R inhibitor or a mitochondrial ATP-sensitive potassium (KATP) channel opener (KATP can prevent mitochondrial injury), which also decreased neuron viability. Stroke-induced disintegration of somatic microglial junctions increased the microglial process coverage of cell bodies in a P2Y12R- and mitochondrial signaling-dependent manner. This led to protective microglial responses hence minimizing brain injury. However, given the limitations of the imaging approach, other methods such as pharmacological and genetic approaches to inactivating or eliminating microglia are needed to further investigate the role of microglia after stroke.

In summary, Cserép and colleagues reported a novel form of interaction between microglia and neurons. Unlike previous results [4], they found that somatic microglial junctions are the main communication sites in both mice and humans under physiological conditions and can respond to brain injury rapidly to protect viable neurons. The injured neurons release ATP which recruits microglial processes to the neuronal somata and protects them in a P2Y12R-dependent manner. However, a number of unanswered questions require further investigations into the mechanism of neuronal protection by microglia. In addition, it is important to investigate whether microglia possess the ability to release certain molecular signals that can alter neuronal behavior following the formation of somatic microglial junctions. Another question to investigate is whether other cell types are involved in neuronal protection such as astrocytes activated through microglia and ATP release in injured tissue. Are there other related molecules important in the formation of microglial somata junctions? Using an epilepsy model, Eyo and colleagues performed *in vitro* and *in vivo* studies and reported that global glutamate sharply increases the numbers of microglial processes. These are involved in the activation of neuronal NMDA receptors, calcium influx, and subsequent ATP release in both a microglial P2Y12R-dependent and

an NMDA receptor activation-dependent manner. P2Y₁₂R-KO mice exhibit reduced seizure-induced increases in microglial process numbers and worsen seizure behaviors [13]. This suggests that both NMDA receptors and P2Y₁₂Rs are key components for junction formation, and P2Y₁₂Rs play an important role in disease. Indeed, a more recent study has shown that microglial P2Y₁₂Rs modulate neuronal excitability and innate fear behaviors in both developing and adult mice [14].

Brain microglial cells display complex phenotypes and roles, and their functions vary based on diverse sites on neurons. Further, they play a vital role in development, learning, and memory in synaptic sites while they play a protective role in stroke. In addition, microglial processes can form junctions with both neuronal somata and synapses, for example in Alzheimer's disease and Parkinson's disease. The communication between microglia and neurons is bidirectional, involving several important factors and signaling axes including P2Y₁₂Rs, ATP, vNUT, and other molecules. Therefore, it is essential to determine the roles of microglia in various neuronal sites. These findings provide novel insights for deep exploration of the crosstalk between microglia and neurons, further advancing knowledge of the mechanisms of brain function.

Acknowledgements This highlight was supported by the Natural Science Foundation of Zhejiang Province (LR18C090001), the National Natural Science Foundation of China (31671071 and 81801102), the National Postdoctoral Science Foundation of China (2018M642413 and 2019T120507), and the Research Start-up Project by Hangzhou Normal University (4125C5021920453).

References

1. Salter MW, Stevens B. Microglia emerge as central players in brain disease. *Nat Med* 2017, 23: 1018–1027.
2. Wake H, Moorhouse AJ, Jinno S, Kohsaka S, Nabekura J. Resting microglia directly monitor the functional state of synapses *in vivo* and determine the fate of ischemic terminals. *J Neurosci* 2009, 29: 3974–3980.
3. Lui H, Zhang J, Makinson SR, Cahill MK, Kelley KW, Huang H-Y, *et al.* Progranulin deficiency promotes circuit-specific synaptic pruning by microglia *via* complement activation. *Cell* 2016, 165: 921–935.
4. Weinhard L, Di Bartolomei G, Bolasco G, Machado P, Schieber NL, Neniskyte U, *et al.* Microglia remodel synapses by presynaptic trogocytosis and spine head filopodia induction. *Nat Commun* 2018, 9: 1228.
5. Tremblay M-È, Lowery RL, Majewska AK. Microglial interactions with synapses are modulated by visual experience. *PLoS Biol* 2010, 8: 1–16.
6. Davalos D, Grutzendler J, Yang G, Kim JV, Zuo Y, Jung S, *et al.* ATP mediates rapid microglial response to local brain injury *in vivo*. *Nat Neurosci* 2005, 8: 752–758.
7. Cserép C, Pósfai B, Lénárt N, Fekete R, László ZI, Lele Z, *et al.* Microglia monitor and protect neuronal function via specialized somatic purinergic junctions. *Science* 2019, 367: 528–537.
8. Fletcher EV, Simon CM, Pagiazitis JG, Chalif JI, Vukojcic A, Drobac E, *et al.* Reduced sensory synaptic excitation impairs motor neuron function *via* Kv2.1 in spinal muscular atrophy. *Nat Neurosci* 2017, 20: 905–916.
9. Haynes SE, Hollopeter G, Yang G, Kurpius D, Dailey ME, Gan WB, *et al.* The P2Y₁₂ receptor regulates microglial activation by extracellular nucleotides. *Nat Neurosci* 2006, 9: 1512–1519.
10. Li Y, Du XF, Liu CS, Wen ZL, Du JL. Reciprocal regulation between resting microglial dynamics and neuronal activity *in vivo*. *Dev Cell* 2012, 23: 1189–1202.
11. Ho MS. Neuroglial crosstalk by mitochondria. *Neurosci Bull* 2017, 33: 111–112.
12. Qin C, Zhou LQ, Ma XT, Hu ZW, Yang S, Chen M, *et al.* Dual functions of microglia in ischemic stroke. *Neurosci Bull* 2019, 34: 1–13.
13. Eyo UB, Peng J, Swiatkowski P, Mukherjee A, Bispo A, Wu LJ. Neuronal hyperactivity recruits microglial processes via neuronal NMDA receptors and microglial P2Y₁₂ receptors after status epilepticus. *J Neurosci* 2014, 34: 10528–10540.
14. Peng J, Liu Y, Umpierre AD, Xie M, Tian DS, Richardson JR, *et al.* Microglial P2Y₁₂ receptor regulates ventral hippocampal CA1 neuronal excitability and innate fear in mice. *Mol Brain* 2019, 12: 1–10.



RESEARCH HIGHLIGHT

The Visual Pathway for Binocular Integration

Na Li¹ · Yu Gu¹

Received: 14 January 2020 / Accepted: 13 February 2020 / Published online: 4 May 2020
© Shanghai Institutes for Biological Sciences, CAS 2020

It is generally believed that the visual pathways from each eye do not integrate to form binocular vision until they reach the primary visual cortex (V1), and individual neurons in the visual thalamus (dorsal lateral geniculate nucleus, dLGN) are thought to receive retinal inputs from either the contralateral or the ipsilateral eye [1]. But recently, many lines of anatomical and functional evidence in mice and marmosets have reported that dLGN neurons have binocular responses and binocularly-modulated responses [2]. It is also generally accepted that monocular deprivation (MD) leads to a series of anatomical and functional changes in V1 during the critical period of development, so the question is whether these changes also occur in the dLGN. Recent studies have reported that MD leads to anatomical changes in thalamocortical projections and impairments of specific dLGN cell types and synapses [3]. A rapid ocular dominance shift in the mouse dLGN has been demonstrated after short-term (6–8 days) MD in both young and adult mice, similar to that reported in V1 long ago [4]. However, using long-term MD, researchers failed to detect changes in the visual responses of dLGN neurons similar to those of V1 [5].

Recently, a report by Huh *et al.* published in the *Journal of Neuroscience* addressed this question [6]. They focused on two points: whether dLGN neuronal properties are chronically altered after long-term MD during the critical period, and whether the long-lasting deficits attributed to MD during the critical period, in V1 originate in the thalamus.

To determine which functional properties of dLGN neurons are changed after long-term MD, the authors injected Cre-dependent GCaMP6s virus (AAV1.Syn.Flex.GCaMP6s virus) into the dLGN of VGLUT2-Cre mice (Vglut2-ires-cre) which restricted GCaMP6s expression specifically to dLGN neurons. After MD for 14 days during the critical period, they tested the changes in visual functions of dLGN boutons projecting to V1 through *in vivo* two-photon calcium imaging. Interestingly, in addition to ocular dominance plasticity, the number and fraction of binocular dLGN boutons were significantly reduced. In other words, the binocular thalamocortical inputs underwent a profound loss after long-term MD. While MD had no evident impact on the overall preferred spatial frequency of dLGN boutons, other visual properties of these boutons, such as binocular matching and binocular modulation, were also evidently changed. Following long-term MD during the critical period, binocular thalamocortical inputs were mismatched in multiple visual response properties, such as the response amplitude, preferred spatial frequency, and preferred orientation. And binocular modulation also underwent substantial impairment. One type of ‘remaining responsive’ bouton, which was visually responsive during monocular and binocular viewing, was also significantly reduced. Binocular facilitation was impaired at the level of both binocular and monocular individual dLGN inputs. In conclusion, long-term MD during the juvenile critical period disrupts binocular integration in mouse visual thalamus.

It is unknown whether these disruptions in the visual thalamus affect the visual properties of V1, the downstream visual pathway. The mouse dLGN can be divided into shell and core regions based on the functional and organizational properties of neurons. The shell region receives inputs from direction-selective retinal ganglion cells and projects to the

✉ Yu Gu
guyu_@fudan.edu.cn

¹ State Key Laboratory of Medical Neurobiology and Ministry of Education Frontiers Center for Brain Science, Institutes of Brain Science, Fudan University, Shanghai 200032, China

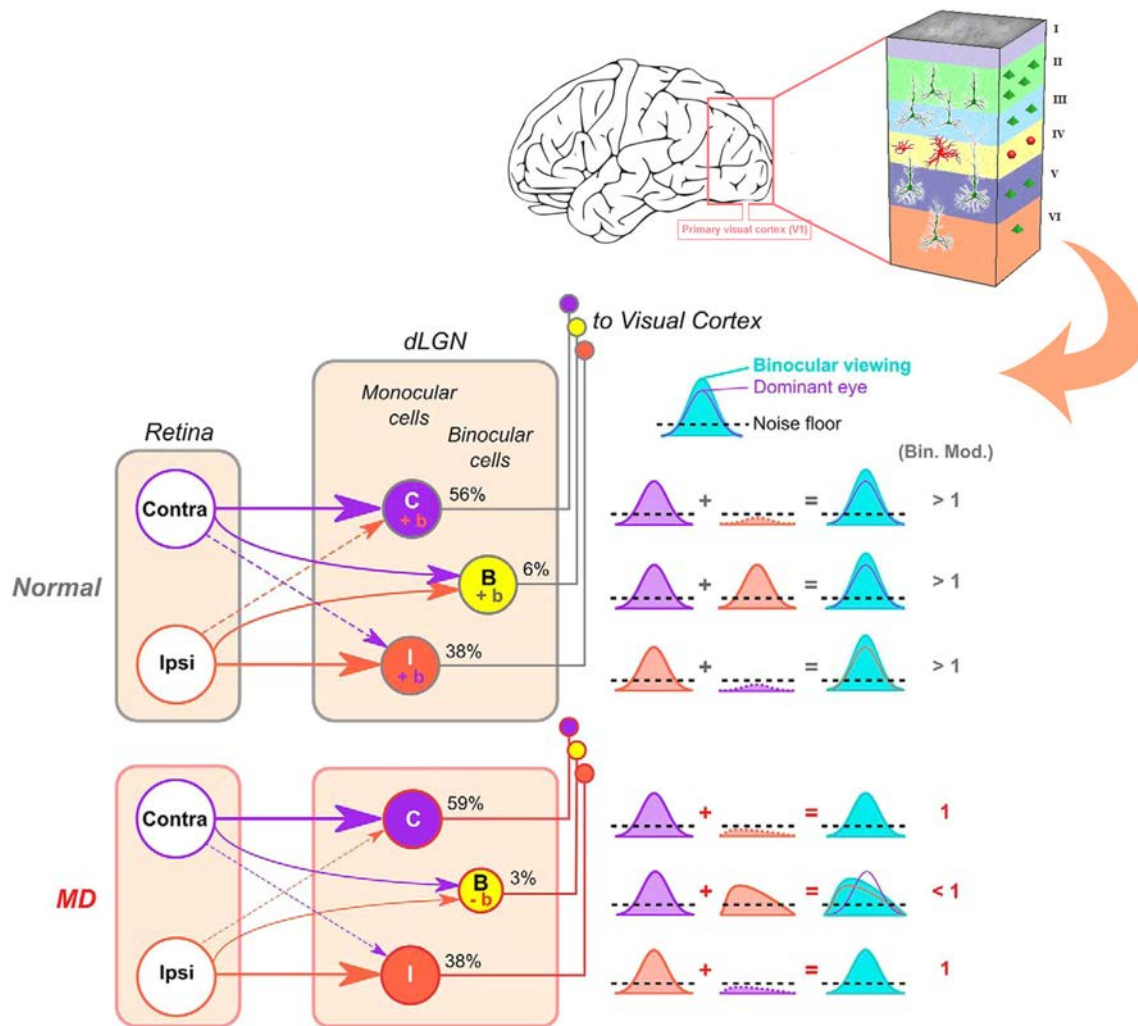


Fig. 1 Schematic model of the visual pathway for binocular integration following long-term critical-period monocular deprivation (MD). In normal mice, besides monocular dLGN neurons, the dLGN also has a few binocular cells which provide inputs to V1. And these neurons display binocular matching similar to V1. Binocular facilitation, larger binocular responses than monocular, also occurs in the

superficial layers (I and II/III) in V1, while the core region receives inputs from non-direction-selective ganglion cells and projects to the middle layer (IV) in V1 [7]. The authors tested the visual properties of layers II/III and layer IV neurons in V1, respectively, using two-photon calcium imaging in two transgenic mouse lines (see below) after long-term critical-period MD. For layers II/III excitatory neuron imaging, a Camk2a-tTa driver line was crossed with a line expressing GCaMP6s under the control of the tetracycline-responsive regulatory element (tetO) to produce CaMK2a-tTA;tetO-GCaMP6s mice. For layer IV excitatory neuron imaging, Scnn1a-Cre mice were bred with GCaMP6f reporter mice (Ai93) to create Scnn1a-Ai93 mice. The authors found that in layers II/III, the numbers and spatial frequency of binocular-responsive neurons were

dLGN. On the other hand, in MD mice the number of binocular dLGN inputs is reduced, and this may originate from retinogeniculate synapses. And the disappearance of binocular facilitation after MD may be caused by V1 feedback. Part of the image was adopted from Huh *et al.*, *J Neurosci* (2020) [6].

significantly reduced. While in layer IV, although long-term MD led to a reduction in the number of binocular cells, the spatial frequency processing was intact, similar to dLGN boutons. Taken together, these findings indicate that the reduction of binocular responses at the level of V1 may originate from the dLGN. On the contrary, the processing for spatial frequency may first appear in V1 layers II/III. Furthermore, the authors found that after long-term critical-period MD, there was no structural loss of thalamocortical connections.

However, the exact location and neuronal mechanisms underlying the loss of binocular-responsive dLGN inputs after critical-period MD remain unclear. Because of the disruption of binocular responses in both the dLGN and V1, and the structural integrity of thalamocortical

synapses, the site that contributes to the loss of binocular responses may originate from upstream of the dLGN, *i.e.* at retinogeniculate synapses. Interestingly, a recent study revealed that retinogeniculate synapses were integrated and fine-tuned quite late during development [8]. Furthermore, other properties of binocular integration may have different visual processing pathways. For example, binocular mismatching has been reported in dLGN boutons after MD, similar to the results previously reported in V1, thus the dLGN may help to shape binocular matching in V1 neurons during development [9]. However, it has also been reported that all ipsilateral components of facilitated cell responses disappear after cortical inactivation, so binocular facilitation may originate from V1 feedback [10]. These findings suggest that the different visual processing pathways may have distinct mechanisms at different levels.

The findings by Huh *et al.* (Fig. 1) also leave some questions that are worth in-depth consideration. First, the timing of monocular deprivation used here is the critical period of V1, rather than that of the dLGN, which may lead to an underestimation of dLGN plasticity. Second, the dLGN boutons' responses by *in vivo* two-photon calcium imaging in the superficial layers of V1 only indirectly reflect a small fraction of all dLGN neurons, so it is uncertain whether the other dLGN neurons that do not project to superficial binocular V1 undergo similar response changes. Last but not least, since the authors did not inactivate V1 feedback to isolate the dLGN responses, the reported results of disrupted binocular integration may be caused by V1 feedback rather than changes in individual dLGN neurons.

To summarize, it is important to determine the visual pathways and mechanisms for binocular integration, especially for amblyopia, a disease due to unbalanced binocular inputs. The current study by Huh *et al.* may provide a novel idea on the experience-dependent maturation of binocular

visual circuits, which may shed light on the clinical treatment of amblyopia.

Acknowledgements This research highlight article was supported by the National Natural Science Foundation of China (31872764 and 81800862), the Shanghai Municipal Science and Technology Major Project (2018SHZDZX01), ZJ Lab, and the Shanghai Science and Technology Committee Rising-Star Program (19QA1401600).

References

1. Casagrande VA, Boyd JD. The neural architecture of binocular vision. *Eye (Lond)* 1996, 10 (Pt 2): 153–160.
2. Rompani SB, Mullner FE, Wanner A, Zhang C, Roth CN, Yonehara K, *et al.* Different modes of visual integration in the lateral geniculate nucleus revealed by single-cell-initiated transsynaptic tracing. *Neuron* 2017, 93: 767–776.e766.
3. Coleman JE, Nahmani M, Gavornik JP, Haslinger R, Heynen AJ, Erisir A, *et al.* Rapid structural remodeling of thalamocortical synapses parallels experience-dependent functional plasticity in mouse primary visual cortex. *J Neurosci* 2010, 30: 9670–9682.
4. Jaepel J, Hubener M, Bonhoeffer T, Rose T. Lateral geniculate neurons projecting to primary visual cortex show ocular dominance plasticity in adult mice. *Nat Neurosci* 2017, 20: 1708–1714.
5. Wiesel TN, Hubel DH. Effects of visual deprivation on morphology and physiology of cells in the cats lateral geniculate body. *J Neurophysiol* 1963, 26: 978–993.
6. Huh CYL, Abdelaal K, Salinas KJ, Gu D, Zeitoun J, Figueroa Velez DX, *et al.* Long-term monocular deprivation during juvenile critical period disrupts binocular integration in mouse visual thalamus. *J Neurosci* 2020, 40: 585–604.
7. Guido W. Development, form, and function of the mouse visual thalamus. *J Neurophysiol* 2018, 120: 211–225.
8. Litvina EY, Chen C. Functional convergence at the retinogeniculate synapse. *Neuron* 2017, 96: 330–338.e335.
9. Gu Y, Cang J. Binocular matching of thalamocortical and intracortical circuits in the mouse visual cortex. *Elife* 2016, 5.
10. Howarth M, Walmsley L, Brown TM. Binocular integration in the mouse lateral geniculate nuclei. *Curr Biol* 2014, 24: 1241–1247.



CORRECTION

Correction to: Microglia Interact with Neurons by Forming Somatic Junctions

Yongjie Wang^{1,2} · Zhihui Huang^{1,2,3}

Published online: 5 June 2020
© Shanghai Institutes for Biological Sciences, CAS 2020

Correction to: Neurosci. Bull.
<https://doi.org/10.1007/s12264-020-00517-3>

The original version of this article unfortunately contained two misunderstandings.

In paragraph 3 of page 3, the sentence starting with “*In vivo* two-photon imaging revealed that the number of mitochondria significantly increases...” should be “*In vivo* two-photon imaging revealed that the activity of mitochondria significantly increases...”;

In paragraph 4 of page 3, the sentence “Microglial process coverage around the somatic junctions was completely abolished after the administration of a P2Y12R inhibitor...” should be “The increased microglial process coverage induced by stroke around the somatic junctions was completely abolished after the administration of a P2Y12R inhibitor ...”.

We are sorry for those mistakes.

The original article can be found online at <https://doi.org/10.1007/s12264-020-00517-3>.

✉ Zhihui Huang
hzhzju021@163.com

¹ Key Laboratory of Elemene Anti-Cancer Medicine of Zhejiang Province and Holistic Integrative Pharmacy Institutes, Hangzhou Normal University, Hangzhou 311121, China

² Engineering Laboratory of Development and Application of Traditional Chinese Medicine from Zhejiang Province and Holistic Integrative Pharmacy Institutes, Hangzhou Normal University, Hangzhou 311121, China

³ Department of Neurosurgery, The Affiliated Hospital of Hangzhou Normal University, Hangzhou 310015, China



CORRECTION

Correction to: Projection from the Anterior Cingulate Cortex to the Lateral Part of Mediodorsal Thalamus Modulates Vicarious Freezing Behavior

Chaowen Zheng^{1,2} · Yanwang Huang^{1,2} · Binshi Bo¹ · Lei Wei¹ · Zhifeng Liang¹ ·
Zuoren Wang^{1,2,3}

Published online: 28 August 2020
© Shanghai Institutes for Biological Sciences, CAS 2020

Correction to: Neurosci. Bull.
<https://doi.org/10.1007/s12264-019-00427-z>

The original version of this article unfortunately contained some mistakes.

The authors found that in this article, the left panel of Figure 6B was a wrong placed figure (it was duplicated with the left panel of Figure 5A), and the corrected Figure 6 was shown as follow.

The original article can be found online at <https://doi.org/10.1007/s12264-019-00427-z>.

✉ Zuoren Wang
zuorenwang@ion.ac.cn

- ¹ Institute of Neuroscience, State Key Laboratory of Neuroscience, CAS Center for Excellence in Brain Science and Intelligence Technology, Chinese Academy of Sciences, Shanghai 200031, China
- ² University of Chinese Academy of Sciences, Beijing 100049, China
- ³ School of Future Technology, University of Chinese Academy of Sciences, Beijing 100049, China

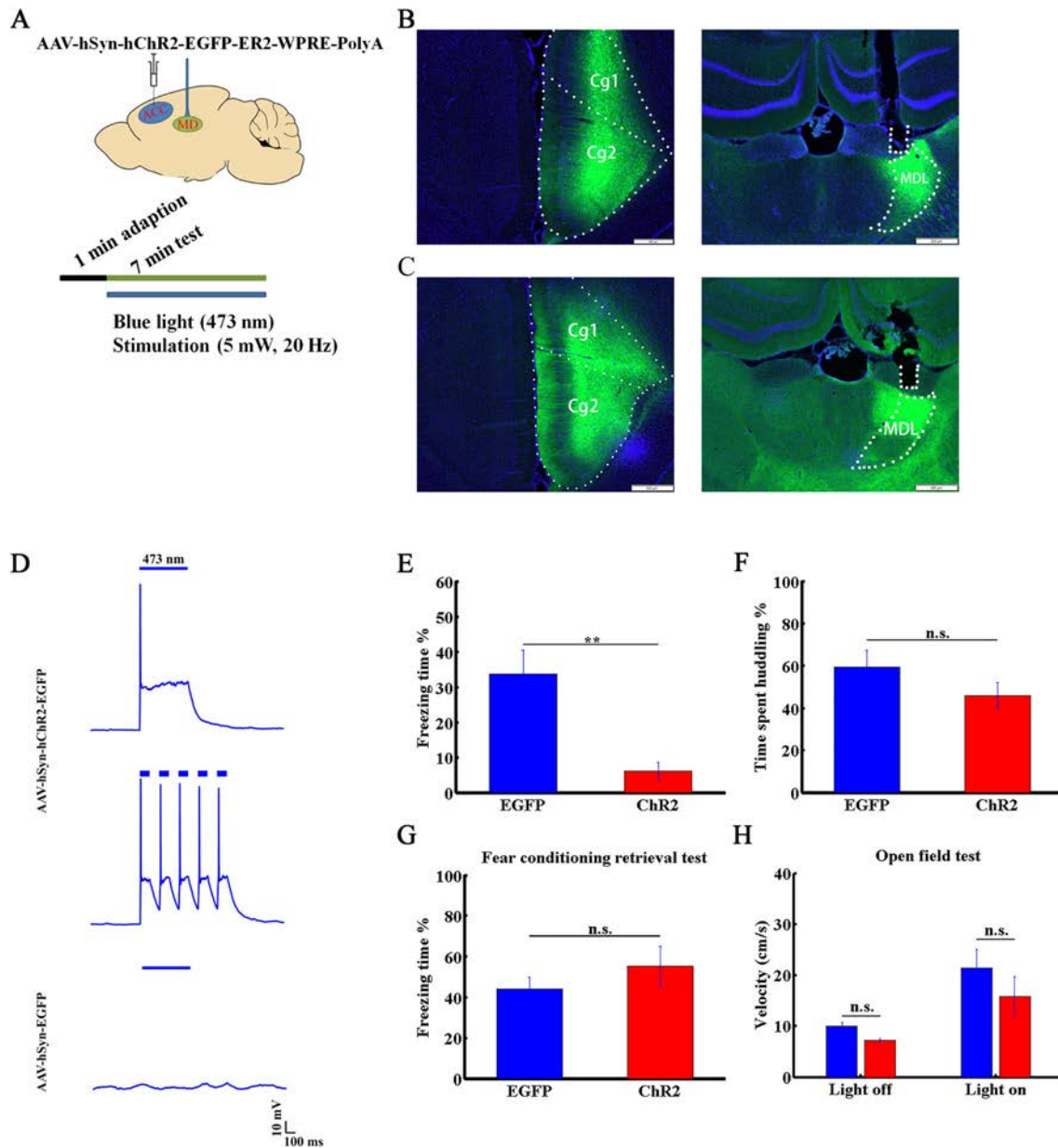


Fig. 6 Activation of the ACC-to-MDL projection decreases vicarious freezing behavior. **A** Diagram showing optogenetic manipulation. **B** Tracing of projection from the ACC to the MDL. Left panel, AAV-hSyn-EGFP virus injection target in the ACC. Cg1, 2, cingulate cortex 1 and 2; right panel, projection terminals and optical fiber position in the MDL. **C** Left panel, AAV-hSyn-hChr2-EGFP virus injection target in the ACC; right panel, projection terminals and optical fiber position in the MDL. Nuclei stained with DAPI. **D** Light pulse-induced response of Chr2-expressing (upper and middle, 10

mW, 1 Hz and 5 Hz, respectively) and EGFP-expressing (lower, 10 mW, 1 Hz) ACC neurons in brain slice. **E**, **F** Freezing (**E**) and huddling (**F**) times of OSs in AAV-hSyn-EGFP (blue) or AAV-hSyn-Chr2 (red) groups. **G** Percentage freezing time of OSs in AAV-hSyn-EGFP- and AAV-hSyn-Chr2-injected groups in the retrieval period after fear conditioning. **H** Locomotor velocity of OSs in AAV-hSyn-EGFP (blue) and AAV-hSyn-Chr2 (red) groups, before and after light stimulation. Data are presented as the mean \pm SEM; $**P < 0.01$, non-parametric rank-sum test, n.s., not significant.



Impact Factor

4.326

**2019 Journal Citation Reports: Q2
(CLARIVATE ANALYTICS, 2020)**

NEUROSCIENCE BULLETIN 神经科学通报 (Monthly)

Vol. 36 No. 9 September 15, 2020

Sponsored by: Shanghai Institutes for Biological Sciences, Chinese Academy of Sciences
Chinese Neuroscience Society
Second Military Medical University

Editors-in-Chief: Shumin Duan, Ru-Rong Ji

Edited by: Editorial Board of *Neuroscience Bulletin*

319 Yueyang Road, Building 31 B, Room 405, Shanghai 200031, China

Phone: +86-21-54922863; Fax: +86-21-54922833

E-mail: nsb@sibs.ac.cn; <http://www.neurosci.cn>

Editors: Bin Wei, Zhi-Rui Liu

Published by: Shanghai Institutes for Biological Sciences, Chinese Academy of Sciences (320 Yueyang Road, Shanghai)

Printed by: Shanghai Shengtong Times Printing Co., Ltd (A6, No. 2888, Caolang Highway, Jinshan District, Shanghai)

Overseas Distributed by: Springer Nature

Home Distributed by: Local Post Offices

ISSN 1673-7067

CN 31-1975/R

Post Office Code Number: 4-608

Permit of Ad. Number: 3100420130051

Price: ¥ 100.00

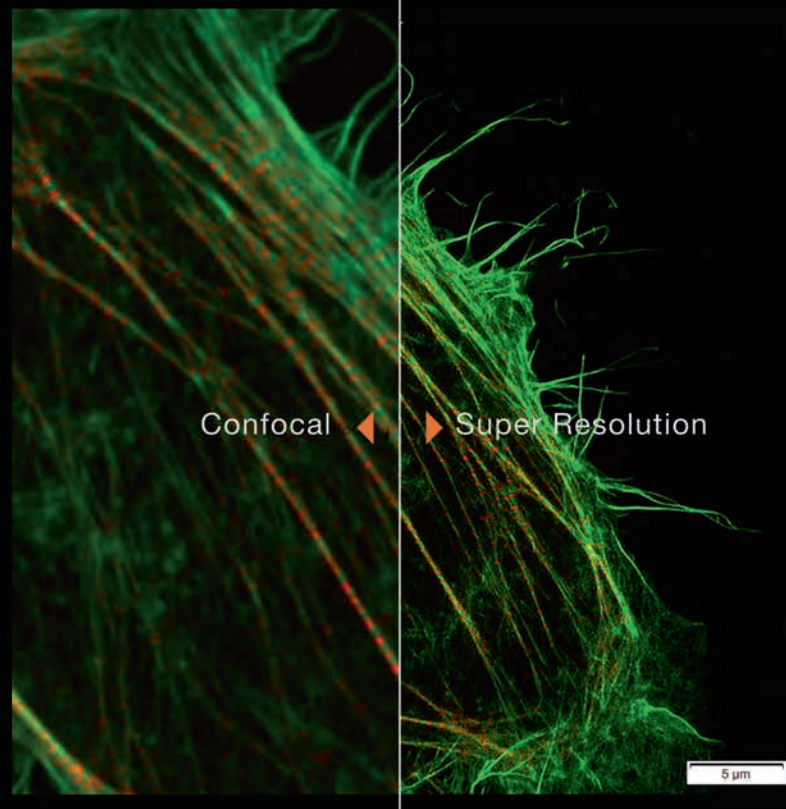
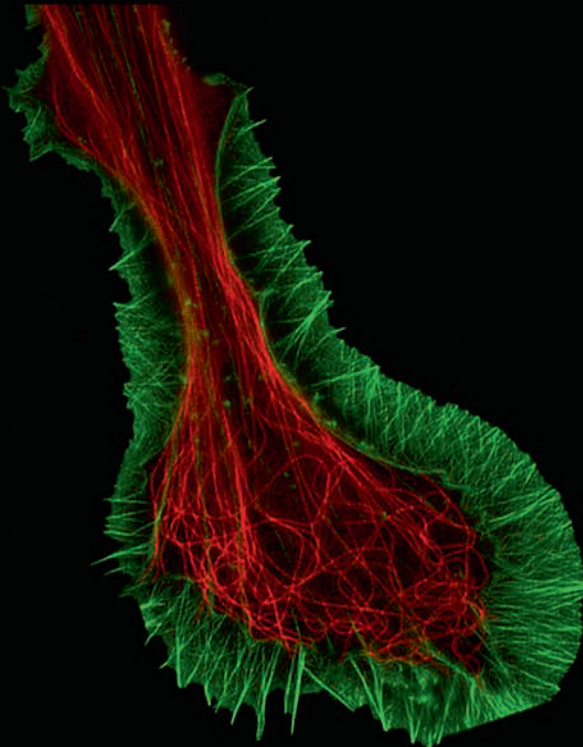
ISSN 1673-7067



9 771673 706209

兼顾分辨率和速度的

转盘共聚焦活细胞超分辨系统 SpinSR10



- 分辨率高达110nm的实时超分辨率成像
- 专有反卷积算法进一步提升图像质量
- 宽视野成像，速度高达 200fps
- 特色硅油物镜可以实现活细胞深层成像
- 宽场、共聚焦、超分辨率模式自由切换
- 功能强大的智能cellSens软件平台



奥林巴斯（北京）销售服务有限公司

北京朝阳区酒仙桥路10号恒通商务园B12C座2F (北京) 010-59756006
上海市徐汇区淮海中路1010号嘉华中心11楼 (上海) 021-51582084
广州市环市东路403号广州电子大厦16楼 (广州) 020-61227171

陕西省西安市新城区尚德路85号太平洋保险大厦8F

湖北省武汉市江岸区中山大道1628号武汉天地企业中心5号7楼701单元
四川省成都市人民南路四段三号来福士广场T1-11楼
辽宁省沈阳市沈河区友好街10号新地中心1号楼3501室

(西安) 029-87206108

(武汉) 027-82718838

(成都) 028-86703700

(沈阳) 024-23342084